Developments for a measurement of the $\beta - \nu$ correlation and determination of the recoil charge-state distribution in ^{6}He β decay

Ran Hong

A dissertation
submitted in partial fulfillment of the
requirements for the degree of

Doctor of Philosophy

University of Washington

2016

Reading Committee:

Alejandro García, Chair

Peter Müller

David Hertzog

Program Authorized to Offer Degree:
UW Physics

University of Washington

Abstract

Developments for a measurement of the $\beta - \nu$ correlation and determination of the recoil charge-state distribution in ^{6}He β decay

Ran Hong

Chair of the Supervisory Committee:
Professor Alejandro García
Department of Physics

The $\beta - \nu$ correlation coefficient $a_{\beta\nu}$ of a pure Gamow-Teller β decay such as the ^{6}He decay is sensitive to tensor-type weak currents predicted by theories beyond the Standard Model. An experiment is developed at University of Washington aiming at measuring the coefficient $a_{\beta\nu}$ of ^{6}He decays to the 0.1% level and looking for its deviation from the Standard-Model prediction $-1/3$ using laser-trapped ^{6}He atoms. The β particle is detected by a scintillator and a multi-wire proportional chamber, and the recoil ion is detected by a microchannel plate with delay-line anodes for position readouts. $a_{\beta\nu}$ is extracted by fitting the measured time-of-flight spectrum of the recoil ions to templates generated by Monte Carlo simulations. This dissertation describes the developments of this experiment for the intermediate goal of a 1% level $a_{\beta\nu}$ measurement, such as the detector design, Monte Carlo simulation software, and data analysis frame work. Particularly, detector calibrations are described in detail. The analysis of a 2% level proof-of-principle run in October 2015 is presented as well.

Shake-off probabilities for decays of trapped ^{6}He atoms matter for the high-precision $a_{\beta\nu}$ measurement. The charge state distribution of recoil ions is obtained by analyzing their time-of-flight distribution using the same experimental setups for the $a_{\beta\nu}$ measurement. An analysis approach that is independent of the $\beta - \nu$ correlation is developed. The measured upper limit of the double shake-off probability is 2×10^{-4} at 90% confidence level. This

result is ∼100 times lower than the most recent calculation by Schulhoff and Drake [1]. This disagreement is significant for the $a_{\beta\nu}$ measurement and needs to be addressed by improved atomic theory calculations.

TABLE OF CONTENTS

ACKNOWLEDGMENTS

The six and a half years of pursuing my PhD degree in physics is coming to an end. My thesis project was full of challenges, and I finally realized how difficult it was to keep all components of the experiment working continuously for four days. However, the joys in my heart were indescribable when I observed the *triple-coincidences* generated by ^{6}He decays for the first time and when I was staring at the computer screen and watching the data accumulating at $\sim$2 Hz during the night shifts in October 2015. Looking back on this wondrous journey, I sincerely thank all people who made these good memories happen, directly or indirectly.

First of all, I must thank my thesis advisor Alejandro García. I learned from him more than physics knowledges and experimental skills. I was deeply moved by his heart for teaching and mentoring his students, enthusiasm of physics, willingness of working shoulder by shoulder with all of us and answering questions whenever we asked. He also encouraged me to participate other research projects and attend summer schools to discover other research areas and get to know more people. He helped me build a solid basis for pursuing my future career as a physicist. Finally, he carefully read every single page of this thesis, gave comments and help me make it better and better.

I thank Peter Müller, our master of laser, for his leadership of the laser trapping system. He brought the discharge source, atomic beam line and the full table of optics at the early days of this experiment, and continued to improve the system for a better performance during the next five years. His persistence in shooting problems of the experiment and finding a reason of any small discrepancy between the observation and prediction is always a good lesson for me. I also thank him for his advising on my thesis writing.

It was my pleasure to work with post-docs Matt Sternberg, Arnaud Leredde, Andreas Knecht and Chris Wrede. From them I learned how to be mature researcher. I thank

Andreas for his initial design of the detector system. He showed me the way and helped me to get my research started in this group. I thank Matt and Arnaud for moving the experiment forward dramatically through the past two years and their leaderships of many sub-projects in this experiment, and Chris for the neutron shield he built.

I am grateful to my fellow PhD students David Zumwalt and Yelena Bagdasarova for their excellent jobs of taking care of the production target, electrode system, vacuum system, laser system and whatever systems that I am not good at. Particularly, I thank Yelena for her development of the COMSOL E-field solver and the ion tracking program, and her help of managing the data analysis software. There would be way more bugs in the code without her contribution. I did enjoy sharing the same office with David and Yelena and talking about subjects well beyond the Standard Topics of physics. As David mentioned in his thesis acknowledgement, I enjoyed the riddle-solving discussions with him. I hope this did not distract Yelena's mind too much from the ion tracking code.

I thank our collaborators Xavier Fléchard and David Etasse from LPC Caen for their contributions to the MCP system and the DAQ system. Particularly, Xavier initiated the idea of calibrating the MCP by putting a mask directly on it. The MCP-position calibration described in this thesis is based on his idea. I thank Oscar Naviliat-Cuncic from NSCL and Derek Storm for their willingness of reading my thesis carefully and giving me comments even though they were not on my reading committee.

I must thank David Hertzog, Peter Kammel, Frederik Wauters and Jarek Kaspar from the UW muon group for their interests in the ^{6}He experiment. Specifically, I thank David for mentoring me and reading my thesis, Peter for letting me join the AlCap experiment in 2013 and get to know people from the muon community, Frederik for sharing me the amplifiers for the MWPC and coauthoring the tensor current analysis paper, and Jarek for sharing the laser equipment and the HV calibration experiences.

I want to thank engineers and faculties from CENPA involved in our experiment. I thank Erik Swanson for teaching me building the first DAQ system, Derek Storm for his help of building the first MWPC, David Peterson and Tim Van Weche for their helps with

electronics, and Gary Holman for his help with computers and networks. I also thank the instrument makers from the machine shop Hendrik Simons, Jim Elms, David Hyde and Tom Burritt for making parts for our experiment. I thank Greg Harper, Eric Smith, Joben Pederson and Doug Will from the accelerator team, for their trainings of using the accelerator, preparing beams for our experiment and maintaining the accelerator. I thank undergraduates Wade Shaffer, Grant Leum and Michael Kossin for their contributions to the auto-stirring system and the valve controlling system that made the experiment way easier to control. I also thank all people from CENPA for making a home away from home for me. CENPA is not only a good place for developing an experiment because of the strong support team, but also a good place for learning because there are so many excellent research groups. I am grateful for the financial supports from CENPA through all these years, and thank all administrative staffs at CENPA.

Again, I thank Alejandro García, Peter Müller, Peter Kammel and Xavier Fléchard for writing reference letters for me and helping me find a post-doc position.

Finally, I thank my wife, Ting Yan, for her persevering love and support. She encouraged me while I was disappointed by low trapping efficiency or sparks in the detectors. I enjoyed telling her about my research and progresses in science.

DEDICATION

To my dear wife, Ting Yan, for her persevering love.

Chapter 1

MOTIVATION FOR PRECISION MEASUREMENTS OF NUCLEAR β DECAYS

Nuclear β decay is the first discovered natural phenomenon governed by the weak interaction. Historically, it played a very important role in developing the theoretical framework of the charged current weak interaction, particularly its chiral properties. For example, Wu *et. al.* [2] discovered the parity violation in the weak interaction by measuring the β asymmetry in the decay of spin-polarized ^{60}Co. Goldhaber *et. al.* [3] discovered that the helicity of neutrino is negative (or left-handed) by observing the γ ray polarization after the electron capture of ^{152m}Eu. In modern days more advanced experimental techniques have been developed and high precision nuclear β-decay experiments are capable of searching for physics beyond the Standard Model (SM) of particle physics.

In this chapter, we overview the basics of the SM. Particularly, theories of charged current weak interaction that governs the nuclear β decay are described within the SM and several models beyond the SM. The interaction Hamiltonians and observables in these theories are presented. Then we introduce several contemporary nuclear β-decay experiments and their impact on searches for physics beyond the SM. Finally, motivations of the new measurements of the $\beta-\nu$ correlation and the recoil charge-state distribution in the ^{6}He decay are discussed.

1.1 Nuclear β-decay and weak interaction theories in the Standard Model and beyond

1.1.1 Overview of the Standard Model of particle physics

The SM of particle physics is a powerful theory that describes the properties of particles and the interactions between particles in a wide range of energies. Detailed descriptions of the SM can be found in many text books like Reference [4]. As shown in Figure 1.1 the set of fundamental particles in the SM consists of three generations of quarks and

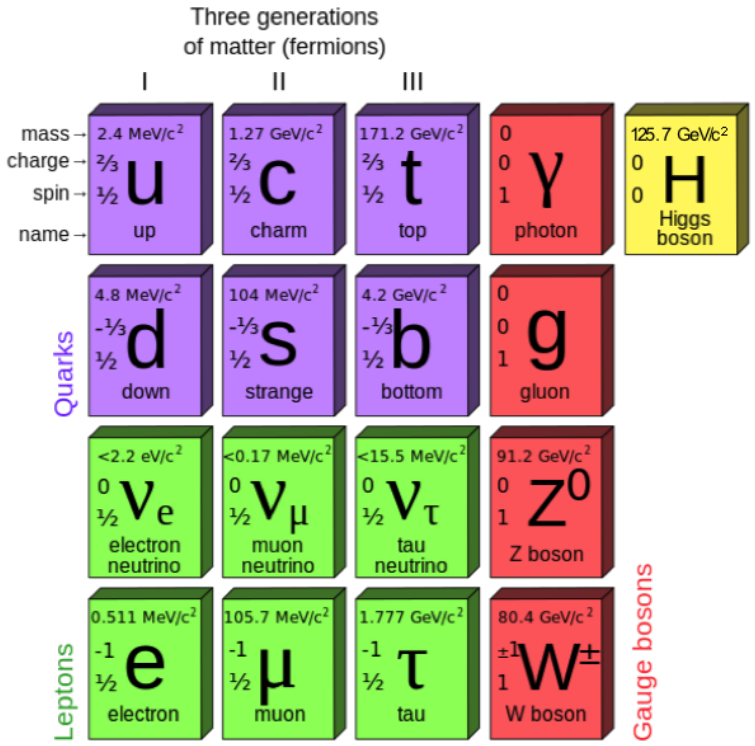

Figure 1.1: The Standard Model fundamental particles

leptons (and their corresponding anti-particles), the gauge bosons (photon, $W^{\pm}$, Z^0 and gluons), and the newly discovered Higgs boson [5][6]. According to this model, the fermions (quarks and leptons) are the fundamental building blocks of matter, and there are four fundamental interactions between them: strong, electromagnetic, weak and gravitational interactions. The SM does not describe gravity adequately, but all the other three forces are generated by coupling fermions to gauge fields and imposing local gauge symmetries to the Lagrangian. The gauge bosons in the SM are the quanta of the gauge fields, and they are also called force carriers or mediators. For example, the dynamic term of a free charged particle is not invariant under $U(1)$ local gauge transformation, but this gauge symmetry is restored if the charged particle is coupled to the electromagnetic field. Photons, quanta of the electromagnetic field, mediate electromagnetic interactions. Similarly, the strong interaction is symmetric under $SU(3)$ gauge transformation and gluons are the mediators

for strong interactions. However, a left-handed $SU(2)$ gauge theory failed to describe the weak interaction because in a gauge invariance theory gauge bosons have to be massless but the weak force carriers are massive. In order to describe the weak interaction within the framework of local gauge invariance, Glashow, Weinberg and Salam developed a theory that unifies the electromagnetic interaction and the weak interaction into a $SU(2)_L \otimes U(1)$ gauge invariance theory and introduced the spontaneous breaking of this symmetry via the Higgs mechanism [7][8][9]. The four fields (W^i (i=1,2,3) and B) of the non-broken $SU(2)_L \otimes U(1)$ gauge mix with each other after the spontaneous symmetry breaking and result in one massless field (photon) and three massive fields ($W^{\pm}$ and Z^0). The Higgs mechanism introduces another boson field called the *Higgs field* whose vacuum expectation value is non-zero, and the massless particles in the $SU(2)_L \otimes U(1)$ invariance theory become massive through interactions with the Higgs field. This model has been rather successful in describing almost all observations in particle physics experiments, but the Higgs mechanism introduced one more particle (the *Higgs boson*) associated with the Higgs field itself and it was not discovered until 2012. The discovery of the Higgs boson in the year of 2012 at the Large Hadron Collider (LHC) vindicated the predictive power of the SM.

1.1.2 Charged-current weak interaction theory in the Standard Model

In the weak interaction sector of the SM, the charged current weak interaction is modeled by the interaction Lagrangian:

$$\begin{aligned}\mathcal{L}_{int} = -\frac{g}{2\sqrt{2}}\{&[\bar{u}(x)_i\gamma^\mu(1+\gamma^5)V_{ij}^{CKM}d(x)_j + \bar{\nu}(x)_i\gamma^\mu(1+\gamma^5)e(x)_i]W_\mu^+ \\ &+[\bar{d}(x)_i\gamma^\mu(1+\gamma^5)V_{ij}^{CKM}u(x)_j + \bar{e}(x)_i\gamma^\mu(1+\gamma^5)\nu(x)_i]W_\mu^-\}, \qquad (1.1)\end{aligned}$$

where the index i goes over all three generations of fermions. In this Lagrangian, u is the field operator of up-like quarks (u, c and t), and similarly d for down-like quarks (d, s and b), ν for neutrinos (ν_e, ν_μ and ν_τ) and e for charged leptons (e, μ, τ). $W_\mu^{\pm}$ are the μ-th ($\mu = 0, 1, 2, 3$) component W boson field operator. γ^μ is the μ-th Dirac matrix. Through out this thesis, the Dirac matrices are in the Weyl representation. We adopt the convention that $\gamma^5 = i\gamma^1\gamma^2\gamma^3\gamma^0$, and thus the left-handed projection operator is $(1+\gamma^5)/2$.

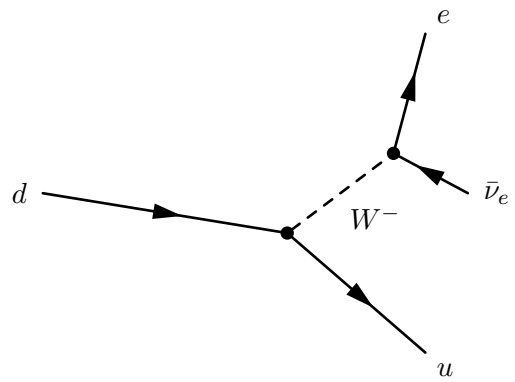

Figure 1.2: Quark level Feynman diagram for the β^- decay with the W^- boson.

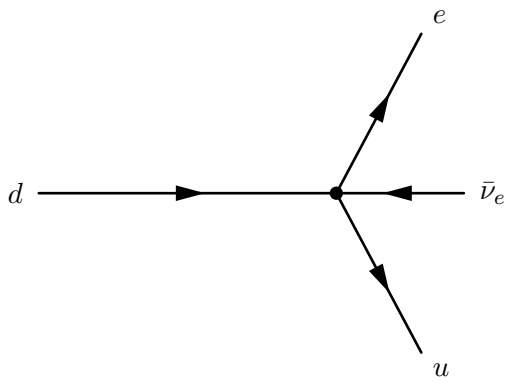

Figure 1.3: Quark level Feynman diagram for the point interaction approximation of the β^- decay.

The $(1+\gamma^5)$ term in this Lagrangian indicates that only left-handed charged currents are involved in weak interactions. V^{CKM} is the Cabibbo-Kobayashi-Maskawa (CKM) quark mixing matrix, which transforms a mass eigenstate of a quark into a weak eigenstate. The factor g is the coupling constant of the charge current weak interaction, and $g = 0.78$.

The quark level process for β^- decay is $d \to ue\bar{\nu}_e$, and its tree-level Feynman diagram is shown in Figure 1.2. The Feynman diagrams for the β^+ decay and electron capture are topologically the same as the one for the β^- decay. The W^- boson propagator for the interaction term associated with the Feynman diagram in Figure 1.2 is

$$\frac{-i(g_{\mu\nu} - (p_\mu p_\nu)/M_W^2)}{p^2 - M_W^2}, \tag{1.2}$$

where the mass of W boson M_W is about 80 GeV/c^2. The typical momenta of the particles involved in nuclear β decays are at the MeV level, much smaller than the W mass. Therefore, we treat the W propagator as a constant and approximate this process as a *point interaction* shown in Figure 1.3, and the interaction Lagrangian becomes

$$\mathcal{L}_{int} = -\frac{G_F V_{ud}^{CKM}}{\sqrt{2}} \left(\bar{u}(x)\gamma_\mu(1+\gamma^5)d(x)\right)\left(\bar{e}(x)\gamma^\mu(1+\gamma^5)\nu_e(x)\right). \tag{1.3}$$

The coupling constant (Fermi coupling constant) in this point interaction Lagrangian is

$$\frac{G_F}{\sqrt{2}} = \frac{1}{8}\left(\frac{g}{M_W}\right)^2 = 1.166 \times 10^{-5}/GeV^2. \tag{1.4}$$

Comparing G_F to the fine structure constant of the electromagnetic interaction, the weak interaction is $\sim$3 orders of magnitude weaker than the electromagnetic interaction. Equa-

tion 1.4 shows that the *weakness* of the weak interaction is due to the large mass of the W boson. One should notice that the original coupling g is dimensionless but the Fermi coupling G_F has a dimension of E^{-2}, which means that the point interaction theory is not renormalizable. When introducing higher order loop corrections, this theory loses its predictive power while dealing with infinities in the correction terms. However, for the tree-level calculation of the weak transition, the point interaction model works well. In this thesis, most calculations are considered up to the tree-level diagram.

Because for all β decays quarks are not in a plane wave single particle state but bounded inside a nucleon with a complicated structure due to strong interactions, it is difficult to calculate observables in nuclear β decays using quarks as fundamental fields. In nuclear β decays there is not enough energy for nucleons to break apart or get into intrinsic excited states, and therefore it is proper to use protons and neutrons as *particles* (or *fundamental fields*) and use the effective field theory Lagrangian

$$\mathcal{L}_{int}^{Eff} = -\frac{G_F V_{ud}^{CKM}}{\sqrt{2}} \left(g_V \bar{p}(x)\gamma_\mu n(x) - g_A \bar{p}(x)\gamma_\mu\gamma^5 n(x)\right) \left(\bar{e}(x)\gamma^\mu(1+\gamma^5)\nu_e(x)\right) \tag{1.5}$$

to calculate differential decay rates. In this effective Lagrangian, the form factors g_V and g_A account for the corrections due to the strong interactions in nucleons, and it is not necessary that $g_V = 1$ and $g_A = -1$ as it is for the quark-level Lagrangian in Equation 1.3. Their values are determined through both theoretical and experimental approaches as shown later in this subsection.

To calculate the leading-order decay amplitude in perturbation theory, Fermi's Golden Rule is used:

$$\mathcal{T}_{fi} = -i2\pi\delta(E_f - E_i) \int \langle f|\mathcal{H}_{int}|i\rangle d^3x, \tag{1.6}$$

where $\mathcal{H}_{int} = -\mathcal{L}_{int}^{Eff}$ and $|i\rangle$ $|f\rangle$ are the initial and final states. Then we rewrite $\mathcal{M} \equiv$

$\int \langle f|\mathcal{H}_{int}|i\rangle d^3x$ as

$$\mathcal{M} = \frac{G_F V_{ud}^{CKM}}{\sqrt{2}} \int (J_{N\mu}^V - J_{N\mu}^A) J_l^\mu d^3x, \tag{1.7}$$

$$J_l^\mu = \langle e\bar{\nu}|\bar{e}(x)\gamma^\mu(1+\gamma^5)\nu_e(x)|0\rangle, \tag{1.8}$$

$$J_{N\mu}^V = \langle f|g_V \bar{p}(x)\gamma_\mu n(x)|i\rangle, \tag{1.9}$$

$$J_{N\mu}^A = \langle f|g_A \bar{p}(x)\gamma_\mu\gamma^5 n(x)|i\rangle. \tag{1.10}$$

$J_{N\mu}^V$ is called the *vector current* and $J_{N\mu}^A$ is called the *axial current* because of their corresponding operator γ_μ and $\gamma_\mu\gamma^5$. In the derivation above, recoil order effects, *i.e.* effects due to the transfer of momentum to nucleons are neglected. In Equation 1.9 and Equation 1.10, the initial state $|i\rangle$ and final state $|f\rangle$ are the nuclear states of the parent and the daughter nucleus. In Equation 1.8, the initial state $|0\rangle$ (vacuum) and final state $|e\bar{\nu}\rangle$ (one outgoing electron and one anti-neutrino) are the leptonic part of the states. If the final states of the leptons are plane waves, the only factor that depends on x is $\exp(i(p_e + p_\nu)x)$ where p_e and p_ν are the momenta of the outgoing electron and anti-neutrino. For MeV scale leptons, their wave lengths are $\sim 10^{-13}$ m, much larger than the size of the nucleus. Thus, the approximation $\exp(i(p_e + p_\nu)x \approx 1$ is used in the following discussions, and the integral in Equation 1.7 only applies to the nuclear currents $J_{N\mu}^V$ and $J_{N\mu}^A$.

The nuclear currents can be further simplified considering that the nucleons are non-relativistic considering that their momenta are small compared to their masses. At the non-relativistic limit,

$$\int J_{N\mu}^V d^3x \to \int \sum_j \langle f|t_j^+|i\rangle d^3x \equiv 2\sqrt{M_i M_r} M_F, \ \mu = 0 \tag{1.11}$$

$$\int \sum_j \langle f|(\mathcal{O}(v_\mu/c))t_j^+|i\rangle d^3x \approx 0, \ \mu = 1,2,3$$

$$\int J_{N\mu}^A d^3x \to \int \sum_j \langle f|\mathcal{O}(v/c)t_j^+|i\rangle d^3x \approx 0, \ \mu = 0 \tag{1.12}$$

$$\int \sum_j \langle f|(\boldsymbol{\sigma}_{j\mu})t_j^+|i\rangle d^3x \equiv 2\sqrt{M_i M_r} M_{GT\mu}, \ \mu = 1,2,3$$

where t_j^+ is the isospin raising operator for each nucleon and σ's are Pauli matrices representing the spin operators of nucleons. The factor $2\sqrt{M_i M_r}$ (M_i and M_r are the masses of

the parent nucleus and daughter recoil nucleus) is from the normalizations of $|i\rangle$ and $|f\rangle$[1]. All terms proportional to v/c are neglected in the following calculations. The non-vanishing matrix elements M_F and M_{GT} are called the Fermi and Gamow-Teller matrix elements respectively. Similarly, the β-decay driven by the vector current is called *Fermi decay* with selection rules: $\Delta J = 0; \Delta T = 0$, and the β decay driven by the axial current is called *Gamow-Teller decay* with selection rules: $\Delta J = 0, \pm 1; \Delta T = 0, \pm 1$, no $J = 0 \to J = 0$ transition. β decays driven by both the vector current and the axial current are called *mixed decays*.

Because nucleons are not elementary particles, the matrix elements calculated above are only the leading order terms. Including recoil order corrections, the vector and axial currents become [10]

$$J^V_{N\mu} = \bar{p}(g_V\gamma^\mu - g_M \frac{i}{m_p + m_n}\sigma_{\mu\nu}q^\nu + g_S \frac{1}{m_p + m_n}q_\mu)n \tag{1.13}$$

$$J^A_{N\mu} = \bar{p}(g_A\gamma^5 + g_T \frac{i}{m_p + m_n}\sigma_{\mu\nu}q^\nu\gamma^5 + g_P \frac{1}{m_p + m_n}q_\mu\gamma^5)n, \tag{1.14}$$

where q is the momentum transfer and $m_p(m_n)$ is the proton(neutron) mass. The form factors g_i $(i = V, A, M, T, S, P)$ all depend on q^2. Except the terms with g_V and g_A, other terms are all *induced* terms with no corresponding ones in the interactions of fundamental quark fields. These induced terms are taken into account in our Monte Carlo simulations described in Chapter 5. For simplicity, these terms are mostly neglected in this chapter.

The value of g_V can be determined using the *conserved vector current* (CVC) hypothesis according which weak currents $\bar{u}\gamma^\mu d$ and $\bar{d}\gamma^\mu u$ are conserved because their isospin analogy electromagnetic currents $\bar{u}\gamma^\mu u$ and $\bar{d}\gamma^\mu d$ are conserved. This hypothesis is based on the assumption that interactions between up and down quarks are invariant under the isospin transformation, *i.e.* changing an up quark into a down quark or vice versa. However, this is not true if the mass difference between the up and down quark and their electromagnetic interactions are taken into account. Using the QCD+QED Lagrangian one can verify that

$$\partial_\mu(\bar{u}\gamma^\mu d) = i(m_u - m_d)\bar{u}\gamma^\mu d - ie\bar{u}\gamma^\mu d A_\mu. \tag{1.15}$$

---

[1]Fermion states are normalized to $\sqrt{2E}$. For nuclei in β decays, $E \approx M$ in the non-relativistic limit.

Although the CVC hypothesis is not exactly true, it is a good approximation provided that the mass difference between the up and down quark is small (∼2.4 MeV) compared to the nucleon mass, and the electromagnetic interaction is also weak compared to the strong interaction inside a nucleon[2]. Therefore, in this thesis we assume the CVC hypothesis is true. Thus, the *weak charge* for the vector current is a conserved quantity like the electric charge, and the coupling constant for a proton is the same as that for an up quark, *i.e.* $g_V = 1$ in the $q^2 \to 0$ limit. The CVC hypothesis in nuclear β decays is verified by the fact that the ft values of all $0^+ \to 0^+$ superallowed β decays are identical [11].

Unlike the vector current, the axial current is not conserved and the strength of the axial-coupling is modified by the decay of charged virtual pions. The value of g_A for the neutron decay is determined from experiments [12][13], and its most up-to-date value is $-1.2723(23)$ [14]. Because its deviation from -1 is small (a ∼27% effect), the axial current is considered partially conserved (PCAC). First principle calculations for g_A using Lattice-QCD are also available [15], but their uncertainties are large compared to that determined from experiments. Furthermore, the PCAC does not guarantee that g_A for other nuclear decays is the same as that for the neutron decay. For nuclei with $A > 10$, the g_A values are *quenched* [16][17] to ~ -1. The reason for the g_A quenching is still not clear. To determine g_A in a decay, its ft-value needs to be measured and its matrix element needs to be calculated. One possible explanation of the g_A quenching is that the matrix elements are not accurately determined due to the finite phase space in the calculation[18]. Others attributed this effect to the meson-exchange currents [19]. At least, in the decays of light nuclei like ^{6}He the g_A value is consistent with that for the neutron decay [20].

As a summary, for nuclear β decays

$$\mathcal{M} = \frac{G_F V_{ud}^{CKM}}{\sqrt{2}} \left(M_F \bar{e}\gamma^0(1+\gamma^5)\nu_e - g_A M_{GT,k} \bar{e}\gamma^k(1+\gamma^5)\nu_e \right), k = 1,2,3 \tag{1.16}$$

and the differential decay rate given by the Standard Model is

$$d\Gamma = \frac{1}{2M_i}|\mathcal{M}|^2(2\pi)^4\delta^{(4)}(p_i - p_f - p_e - p_\nu)\frac{d^3p_e}{(2\pi)^3 2E_e}\frac{d^3p_\nu}{(2\pi)^3 2E_\nu}\frac{d^3p_r}{(2\pi)^3 2E_r}, \tag{1.17}$$

[2]Weak interaction itself also results in non-zero divergence of the weak current, but it is even smaller than the electromagnetic interaction.

where E_r and p_r are the energy and 3-momentum of the daughter (recoil) nucleus. The differential decay rate expressions are discussed in detail in Section 1.2.

1.1.3 Charged-current weak interaction theories beyond the Standard Model

Despite the fact that the SM successfully explained most of experiments done until now, it is still not the ultimate theory of the universe. As discussed above gravity is not fully integrated in this theory. Besides this, it only describes ∼4% of the universe but fails to provide explanations of the rest ∼ 96%, *i.e.* the dark matter and dark energy. Furthermore, the nature of neutrino mass (Dirac or Majorana) is still unknown. It is presently hard to understand why the mass of the Higgs boson is so light given that there are large contributions to it from top quark radiative loops [21]. The SM contains too many parameters which can only be determined by experiments, such as the G_F, CKM matrix, quark masses and so on. Physicists believe that there is possibly a deeper theory, which explains why the parameters have the values they have. Theoretical physicists have proposed many theories, introducing larger symmetry groups and new interactions. These theories predict varieties of new phenomena. On the other hand, experimentalists are searching for non-SM phenomena like new particles or symmetry breaking. The results of these experiments bring about more evidence for certain non-SM theories while putting more stringent limits on the others.

An obvious place to look for new physics via precision experiments is the weak interaction because calculations can be performed with high accuracy using perturbation theory. One can take a phenomenological approach and write all the possible forms of weak currents that satisfy Lorentz invariance but have symmetries different from those of the SM. The most general form of the weak-interaction Hamiltonian is given by Jackson, Treiman and Wyld [22]:

$$\mathcal{H}_{\text{int}} = \sum_{i=S,P,V,A,T} (\bar{p}O^i n)\,(C_i \bar{e} O_i \nu_e + C_i' \bar{e} O_i \gamma^5 \nu_e) + h.c. \tag{1.18}$$

where the C_i's are coupling constants and the operators O_i's are

$$O_S = 1,\ O_P = \gamma^5,\ O_V = \gamma_\mu,\ O_A = i\gamma_\mu\gamma^5,$$
$$O_T = \frac{\sigma_{\mu\nu}}{\sqrt{2}} = \frac{-i\left(\gamma_\mu\gamma_\nu - \gamma_\nu\gamma_\mu\right)}{2\sqrt{2}}. \tag{1.19}$$

The corresponding currents $\bar{p}O^i n$ are called, scalar, pseudo-scalar, vector, axial (or pseudo-vector) and tensor current respectively. In the SM, the constraints of the coupling constants are

- $C_S = C'_S = C_T = C'_T = C_P = C'_P = 0$: no exotic interactions.
- $C_i = +C'_i$ (for $i = V, A$): maximum parity violation, pure left handedness.
- All C_i are real: no time-reversal violation terms besides the CKM matrix.

The values of C_V and C_A are

$$C_V = \frac{G_F V_{ud}^{CKM}}{\sqrt{2}} g_V, \tag{1.20}$$
$$C_A = \frac{G_F V_{ud}^{CKM}}{\sqrt{2}} g_A \tag{1.21}$$

according to the description in the previous subsection.

Any deviations from the descriptions of the coupling constants are generated by physics beyond the SM. This thesis describes an experiment searching for tensor currents. The most important difference between the exotic currents and the SM currents is their chiral property. For the vector and axial currents, the interaction Hamiltonian can be rewritten as

$$\mathcal{H}_{int} = \sum_{i=V,A} (\bar{p}O^i n)\left((C_i + C'_i)\bar{e}^L O_i \nu_e^L + (C_i - C'_i)\bar{e}^R O_i \nu_e^R\right), \tag{1.22}$$

and for the scalar, tensor and pseudo-scalar currents

$$\mathcal{H}_{int} = \sum_{i=S,T,P} (\bar{p}O^i n)\left((C_i + C'_i)\bar{e}^R O_i \nu_e^L + (C_i - C'_i)\bar{e}^L O_i \nu_e^R\right), \tag{1.23}$$

where the superscripts L and R indicate the handedness of the lepton field. In Equation 1.22 and Equation 1.23, only the term with coefficients $C_V + C'_V$ and $C_A + C'_A$ are within the

SM, and both of them have associated lepton fields with identical left handedness. By contrast, the non-SM scalar and tensor currents couple lepton fields with opposite handedness. This difference in the Hamiltonian results in differences in observables like spin-momentum correlations and momentum angular correlations derived from this Hamiltonian. The relationship between the observables to the coupling constants in Equation 1.18 are shown in Section 1.2.

The nuclear matrix elements are calculated for the non-SM currents. In the non-relativistic limit, the leading order matrix element for the scalar current turns out to be the same as that of the vector current (M_F), and the leading order matrix element for the tensor current is the same as that of the axial current (M_{GT}). The non-relativistic form of the pseudoscalar current is at the order of $\mathcal{O}(v/c)$, so the sensitivity to the pseudoscalar current in nuclear β decays is suppressed. Some recent calculations [23] showed that the pseudoscalar form factor is of the order of $\mathcal{O}(10^2)$. The large value of g_P cancels the $\mathcal{O}(v/c)$ suppression in nuclear β decays. However, strong constraints on pseudoscalar couplings are already put by pion decay experiments [24]. Therefore it does not affect the analysis of the tensor currents if the pseudoscalar current is neglected as it is in the scope of this thesis. According to the selection rules described in Subsection 1.1.2, for pure Fermi decays ($0^+ \rightarrow 0^+$ transitions) where $M_{GT} = 0$ only the vector current or the scalar current is involved. For pure Gamow-Teller decays ($\Delta J = \pm 1$ or $\Delta T = \pm 1$) where $M_F = 0$ only the axial current or the tensor current is involved.

The scalar and tensor couplings in the weak interaction described above are purely phenomenological. There are several theories beyond the SM framework describing fundamental interactions that generate tensor and scalar weak currents. One potential source of scalar and tensor couplings is a *leptoquark*-exchange process [25]. In this model, vector or scalar leptoquarks couple to quark-lepton pairs, so they carry lepton numbers, baryon numbers and fractional charges. Example tree-level Feynman diagrams of leptoquark exchange precesses are shown in Figure 1.4, where X-leptoquarks are vector particles and Y-leptoquarks are scalar particles. The terms in the leptoquark-exchange Hamiltonian contain Dirac bilinear currents like $\bar{e}\gamma^\mu u$ which are not included in Equation 1.18, and at the first sight there are no scalar or tensor currents. However, these terms can be rewritten into the forms of terms

in Equation 1.18 through *Fierz rearrangement* [26]. For example, for the scalar leptoquark exchange

$$(\bar{u}\nu_e)(\bar{e}d) = \frac{1}{4}(\bar{u}d)(\bar{e}\nu_e) + \frac{1}{4}(\bar{u}\gamma^\mu d)(\bar{e}\gamma_\mu\nu_e) - \frac{1}{4}(\bar{u}\sigma^{\mu\nu}d)(\bar{e}\sigma^{\mu\nu}\nu_e) - \frac{1}{4}(\bar{u}\gamma^\mu\gamma^5 d)(\bar{e}\gamma_\mu\gamma^5\nu_e) + \frac{1}{4}(\bar{u}\gamma^5 d)(\bar{e}\gamma^5\nu_e). \quad (1.24)$$

After the rearrangement tensor current shows up. Therefore, tensor currents can exist without processes involving spin-2 particles. Vector leptoquarks generate scalar interactions in the point-like interaction level Hamiltonian, while scalar leptoquarks generate both scalar and tensor interactions. A complete set of relationships between the phenomenological coupling constants C_i's and the coupling constants in the leptoquark-exchange theory is summarized in Reference [27]. Theories predicts that leptoquarks may have mass around several hundreds of GeV and some high energy experiments are searching for them as well. Another scenario where scalar and tensor currents emerge is the supersymmetry (SUSY) model [28]. As shown in Figure 1.5 scalar and tensor currents appear at the 1-loop level. SM extensions and their relationship to nuclear β decays are reviewed in References [25], [27] and [24].

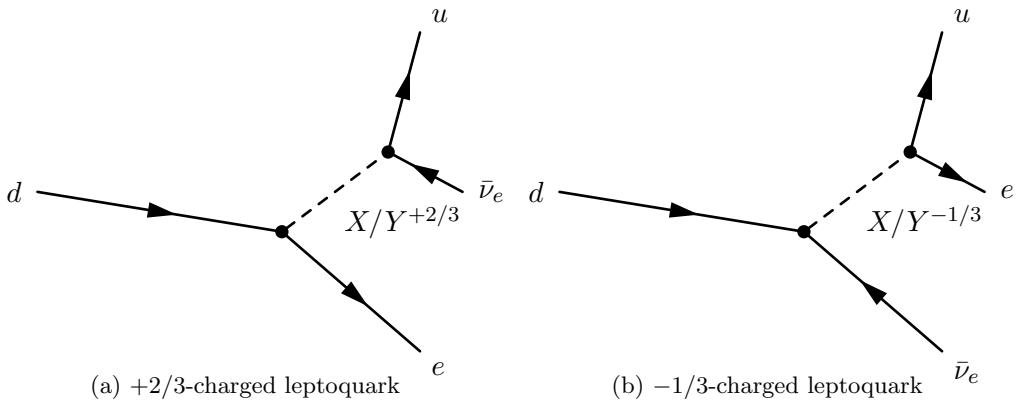

(a) +2/3-charged leptoquark (b) −1/3-charged leptoquark

Figure 1.4: Example Feynman diagrams of leptoquark-exchanging processes that generate scalar and tensor type weak currents. X-leptoquarks are vector particles and Y-leptoquarks are scalar particles.

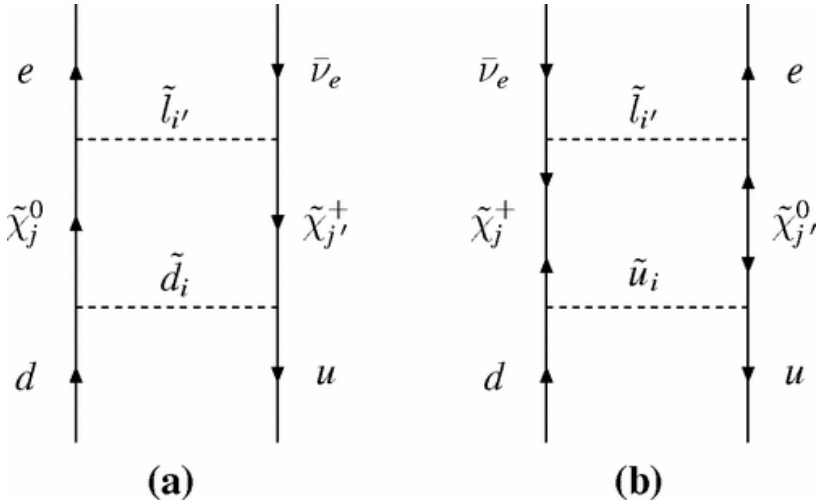

Figure 1.5: Feynman diagrams of processes exchanging particles in the SUSY theory and generating scalar and tensor interactions in the phenomenological Hamiltonian. This figure is taken from Reference [28].

1.2 Differential decay rate and observables in β-decay experiments

1.2.1 Energy spectrum and decay lifetime

Integrating over d^3p_r and dE_ν to eliminate the δ function in Equation 1.17, one gets phase space for the outgoing electron and antineutrino:

$$\begin{aligned} d\Gamma &= \int_{p_r} \frac{1}{2M_i}|\mathcal{M}|^2(2\pi)^4\delta^{(4)}(p_i - p_f - p_e - p_\nu)\frac{d^3p_e}{(2\pi)^3 2E_e}\frac{d^3p_\nu}{(2\pi)^3 2E_\nu}\frac{d^3p_r}{(2\pi)^3 2E_r} \\ &= |\mathcal{M}|^2\frac{1}{(2\pi)^5 16M_iE_eE_\nu E_r}\frac{E_e p_e E_\nu^2}{1+(E_\nu + p_e\cos(\theta_{\beta\nu}))/M_r}dE_e d\Omega_e d\Omega_\nu, \qquad (1.25) \\ E_\nu &= -(p_e\cos(\theta_{\beta\nu}) + M_r) + \sqrt{(p_e\cos(\theta_{\beta\nu}) + M_r)^2 + 2(M_i - M_r - E_e)M_r - p_e^2}, \qquad (1.26) \end{aligned}$$

where $\theta_{\beta\nu}$ is the angle between the momenta of the β particle and antineutrino, and E_ν is determined by the momentum-energy conservation[3] imposed by the δ function. Because the masses of the parent and daughter nuclei are ∼1000 times larger than the energy released in the β decay, in this chapter we make the assumption $M_i, M_r \to \infty$ (but keep $M_i - M_r$ equal to the energy released in the β decay) to simplify the phase space factor in Equation 1.25.

[3]This derivation uses non-relativistic momentum-energy relationship for the recoil nucleus.

Under this assumption, the 2-body phase space for the β particle and antineutrino is

$$d\Omega_{\text{2-body}} = \lim_{M_i, M_r \to \infty} \frac{E_e p_e E_\nu^2}{1 + (E_\nu + p_e \cos(\theta_{\beta\nu}))/M_r} dE_e d\Omega_e d\Omega_\nu$$
$$= p_e E_e (M_i - M_r - E_e)^2 dE_e d\Omega_e d\Omega_\nu. \quad (1.27)$$

The full 3-body phase space expression in Equation 1.25 is used in the Monte Carlo simulation and data analysis of the ^{6}He $\beta - \nu$ correlation measurement (see Chapter 5 and 6).

To derive the β-energy spectrum of a nuclear β decay, one integrates over the directions of the anti-neutrino and the electron and sums over the helicities of the outgoing leptons and initial nuclear spins in Equation 1.25 using the simplified phase space in Equation 1.27. To correct the outgoing β-particle wave function distortion in the Coulomb field of the daughter nucleus, a *Fermi function* $F(\pm Z, E_e)$ ("+" for β^- decay and "−" for β^+-decay) is inserted into the β-spectrum formula. Eventually, one gets the β-energy spectrum

$$W(E_e) \equiv \frac{d\Gamma}{dE_e} = \frac{F(\pm Z, E_e)}{(2\pi)^3} \sqrt{E_e^2 - m_e^2} E_e (E_0 - E_e)^2 \xi (1 + b_{Fierz} \frac{m_e}{E_e}), \quad (1.28)$$

where $E_0 = M_i - M_r$. The *Fermi function* $F(\pm Z, E_e)$ is [29]

$$F(\pm Z, E_e) = \frac{2(1+S)}{\Gamma(1+2S)^2} (2 p_e \rho)^{2S-2} e^{\pi\eta} |\Gamma(S + i\eta)|^2, \quad (1.29)$$

where $S = \sqrt{1 - \alpha^2 Z^2}$ (α is the fine structure constant and Z is the proton number inside the nucleus), $\eta = \alpha Z E_e / p_e$, and ρ is the radius of the nucleus. ξ and b_{Fierz} are functions of the nuclear matrix elements[4] and coupling constants in the Hamiltonian:

$$\xi = |M_F|^2 (|C_S|^2 + |C_V|^2 + |C'_S|^2 + |C'_V|^2)$$
$$+ |M_{GT}|^2 (|C_T|^2 + |C_A|^2 + |C'_T|^2 + |C'_A|^2) \quad (1.30)$$
$$b_{Fierz} \xi = \pm 2 \text{Re} \left(|M_F|^2 (C_S C_V^* + C'_S C'^*_V) + |M_{GT}|^2 (C_T C_A^* + C'_T C'^*_A) \right). \quad (1.31)$$

The factor $16 M_i E_e E_\nu E_r$ in Equation 1.25 is canceled by normalizations of the nuclear and leptonic states[5] in $|\mathcal{M}|^2$.

---

[4] M_{GT} is the reduced matrix element common to the the M_{GTi}'s ($i = 1, 2, 3$).

[5] Approximation $E_r = M_r$ is used.

The term $b_{Fierz}\frac{m_e}{E_e}$ is called the *Fierz interference* term because it comes from the cross terms between the vector (axial) current and the scalar (tensor) current. In the SM, $b_{Fierz} = 0$ because of the absence of the exotic interactions. The shape of the β-energy spectrum is sensitive to scalar and tensor currents through the Fierz interference term. Therefore, by measuring the β spectrum of a certain nuclear β decay and comparing the measured spectrum to the theoretical calculated one in Equation 1.28, one can determine the value of b_{Fierz} and thus the ratio of exotic coupling constants to the SM coupling constants.

The decay lifetime is determined by integrating W_{E_e} over the electron energy:

$$\frac{1}{\tau} = \Gamma = \frac{\xi}{(2\pi)^3}\int F(\pm Z, E_e)\sqrt{E_e^2 - m_e^2}E_e(E_0 - E_e)^2 \times (1 + b_{Fierz}\frac{m_e}{E_e})dE_e. \tag{1.32}$$

The decay lifetime is sensitive to the exotic coupling constants through the Fierz interference, but there are many more quantities like V_{ud}^{CKM}, $|M_F|$ and $|M_{GT}|$, the Fermi function and other corrections affecting the decay lifetime. A lifetime measurement of one β-decay case does not provide good constraints on exotic coupling constants. However, combining all measured lifetimes of $0^+ \to 0^+$ pure Fermi transitions and taking care of all the correction terms the most stringent limit on $C_S + C'_S$ was obtained [11].

1.2.2 $\beta - \nu$ correlation

Besides the energy of the β particle, other aspects of the parent nucleus and the outgoing decay products can be specified and the corresponding differential decay rate can be derived. For example, assuming that the momenta of both outgoing leptons are specified, the differential decay rate is [27]:

$$W(E_e, \Omega_e, \Omega_\nu) = \frac{d\Omega}{dE_e d\Omega_e d\Omega_\nu} = \frac{F(\pm Z, E_e)}{(2\pi)^5}p_e E_e(E_0 - E_e)^2\xi(1 + b_{Fierz}\frac{m_e}{E_e} + a_{\beta\nu}\frac{\boldsymbol{p}_e \cdot \boldsymbol{p}_\nu}{E_e E_\nu}), \tag{1.33}$$

where the $\beta - \nu$ angular correlation coefficient $a_{\beta\nu}$ is

$$\begin{aligned} a_{\beta\nu}\xi = {} & |M_F|^2(-|C_S|^2 + |C_V|^2 - |C'_S|^2 + |C'_V|^2) \\ & + \frac{|M_{GT}|^2}{3}(|C_T|^2 - |C_A|^2 + |C'_T|^2 - |C'_A|^2), \end{aligned} \tag{1.34}$$

and ξ is defined as in Equation 1.30. The expressions for differential decay rates for other specified initial/final states and other correlation coefficients are discussed in great detail in References [22] and [27].

According to Equation 1.34, $a_{\beta\nu}$ is sensitive to scalar and tensor currents as well. For pure Fermi decays, $|M_{GT}| = 0$ so that $a_{\beta\nu} = +1$ if the weak current is of vector type and $a_{\beta\nu} = -1$ if the weak current is of scalar type. For pure Gamow-Teller decay, $|M_F| = 0$ so that $a_{\beta\nu} = -1/3$ if the weak current is of axial type and $a_{\beta\nu} = +1/3$ if the weak current is of tensor type. Compared to b_{Fierz}, $a_{\beta\nu}$ is sensitive to the exotic coupling constants quadratically, while b_{Fierz} is sensitive to them linearly. Therefore, b_{Fierz} is a more sensitive probe if $a_{\beta\nu}$ and b_{Fierz} are measured at the same precision. However, b_{Fierz} is proportional only to $C_S + C'_S$ or $C_T + C'_T$ and thus sensitive to only exotic currents involving left-handed neutrinos as shown in Equation 1.23. By contrast, $a_{\beta\nu}$ is sensitive to exotic currents involving both left-handed and right-handed neutrinos.

The $\beta - \nu$ correlation coefficient is measurable in experiments, but all measured values of $a_{\beta\nu}$ are normalized with respect to the total decay rate. Thus the measured value of the $\beta - \nu$ correlation coefficient is actually

$$\tilde{a}_{\beta\nu} = \frac{a_{\beta\nu}}{1 + b_{Fierz}\langle\frac{m_e}{E_e}\rangle}, \tag{1.35}$$

where $\langle m_e/E_e\rangle$ is the weighted average of m_e/E_e using $W(E_e)$ as the weight. This is true for other correlation coefficients as well. In the following sections and chapters, we use $a_{\beta\nu}$ short for $\tilde{a}_{\beta\nu}$ if not specified.

1.3 Limits on exotic couplings

1.3.1 Limits from nuclear and neutron β-decay experiments and the radiative pion decay experiment

The decay lifetime, shape of the β-energy spectrum, $\beta - \nu$ correlation coefficient $a_{\beta\nu}$ and other correlation coefficients for various nuclear β decays and neutron decays have been measured in many experiments since the 1960s. These measurements put constraints on scalar and tensor couplings. Reviews of the experiments and their individual and combined constraints on the exotic coupling constants can be found in References [27], [30] and [24].

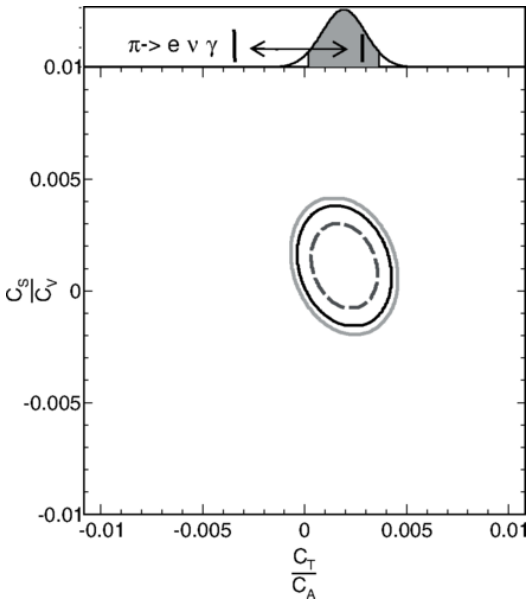

Figure 1.6: 68%, 90%, and 95% confidence level contours of C_T/C_A and C_S/C_V combining neutron and nuclear β-decay data for the three-parameter fit ($C_T = C'_T$, $C_S = C'_S$ and C_A). On top it is shown the probability distribution of C_T obtained by projecting the 2D distribution and the limit of C_T determined from this distribution is compared to the limit from pion decay data [31]. This figure is taken from Reference [32].

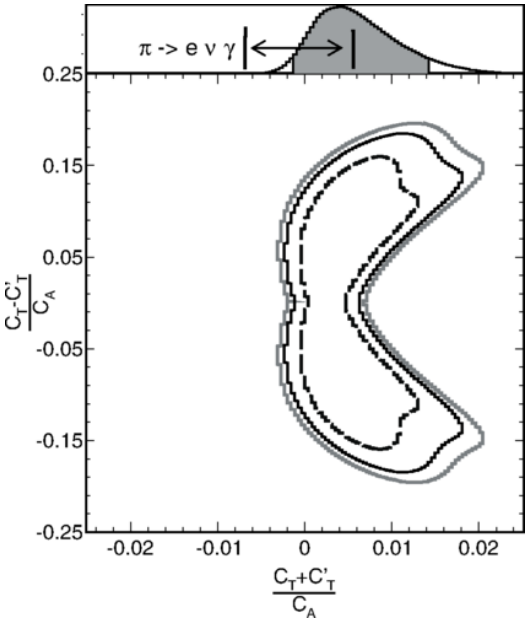

Figure 1.7: 68%, 90%, and 95% confidence level contours of $(C_T + C'_T)/C_A$ and $(C_T - C'_T)/C_A$ from selected nuclear and neutron β-decay data. The top panel shows the 1D projection of the probability distribution, and the shaded area is the 90% confidence level interval for $(C_T + C'_T)/C_A$. The limit determined from this distribution is compared to the limit from pion decay data [31]. This figure is taken from Reference [32].

In Reference [32], Wauters *et. al.* performed a combined analysis of the past experiments of nuclear and neutron β decays and constructed updated limits on tensor coupling constants as shown in Figure 1.6 and Figure 1.7. If maximum parity violation is assumed for the exotic interactions and they only couple to left-handed neutrinos, *i.e.* $C_S = C'_S$ and $C_T = C'_T$, the corresponding 90% confidence level intervals for C_S and C_T are $-0.1 \times 10^{-2} < C_S/C_V < 0.3 \times 10^{-2}$ and $0.0 \times 10^{-2} < C_T/C_A < 0.4 \times 10^{-2}$, and the 68%, 90% and 95% confidence level contours are shown in Figure 1.6. Without the assumption of maximum parity violation, the limits on tensor coupling constants become less stringent. The 90% confidence level intervals are $-0.14 \times 10^{-2} < (C_T + C'_T)/C_A < 1.4 \times 10^{-2}$ and $-0.16 < (C_T - C'_T)/C_A < 0.16$,

and contours at 68%, 90% and 95% confidence levels are shown in Figure 1.7. In both Figure 1.6 and 1.7 horizontal projections of the probability distribution are shown, and limits at 90% confidence level (the shaded area) are compared to the limits set by the pion decay experiment [31].

The limits described above are the combined contribution from many experiments. As for individual experiments, the most stringent limit on $C_S + C'_S$ comes from the b_{Fierz} extracted from the ft-values of the $0^+ \to 0^+$ super-allowed Fermi transitions [11], and the most stringent limit on $C_S - C'_S$ comes from the $a_{\beta\nu}$ measurements in ^{32}Ar decay [33] and ^{38m}K decay [34]. For the tensor currents, the most stringent limit on $C_T + C'_T$ comes from measurements of the relative polarizations P_F/P_{GT} for the positrons emitted in pure Fermi and pure Gamow-Teller decays [35][36]. Besides the experiments on nuclear and neutron β decays, the analysis of the Dalitz plot of the radiative pion decay $\pi^+ \to e^+\nu_e\gamma$ [31] also gives stringent limits on the tensor coupling $C_T + C'_T$, and the limit it sets is compared to the limits from nuclear and neutron β-decay experiments in Figure 1.6 and Figure 1.7. The most stringent limit on $C_T - C'_T$ comes from the measurement of $a_{\beta\nu}$ for the ^{6}He decay in 1963 [37]. This experiment remains the most precise measurement of $a_{\beta\nu}$ for Gamow-Teller decays, while the $a_{\beta\nu}$ for Fermi decays is already measured at the sub-percent level with the help of trapping technologies. Many groups are motivated to employ atomic and ion traps to experiments measuring Gamow-Teller decays, and improve the limits of $C_T - C'_T$. A review of the $a_{\beta\nu}$ measurements is presented in Section 1.4.

1.3.2 Limits from experiments at the LHC

The exotic point-like interactions described by the Hamiltonian in Equation 1.18 can also be probed at high-energy colliders like the Large Hadron Collider (LHC) at CERN. Assuming that the new physics emerges at a higher energy scale than the production threshold of the LHC, *i.e.* the scalar and tensor interactions remain point-like at TeV scale energies, low- and high-energy probes can be compared in a model-independent way. In Reference [38], the Lagrangian for the exotic interactions are written using high-energy physics conventions and the relationships between the coupling constants (ϵ_i and $\tilde{\epsilon}_i$) used in this convention and

the coupling constants used in the low-energy physics convention (C_i and C_i') are given. For the tensor couplings,

$$\epsilon_T = \frac{C_T + C_T'}{8 C_V g_T},$$
$$\tilde{\epsilon}_T = \frac{C_T - C_T'}{8 C_V g_T}, \tag{1.36}$$

where g_T is the tensor current form factor for nucleons. The value of g_S and g_T are calculated using Lattice-QCD. In this section, g_S=0.8(4) and g_T=1.05(35) [15] are used as it is in Reference [38]. The uncertainty of g_S in this calculation is particularly large (∼50%). More recent calculations [39][40][41][23] have been done and the uncertainties of g_S and g_T are improved to ∼15% and ∼4% [42] respectively. These improvements are important when comparing the future higher precision low-energy measurements and higher integrated luminosity experiments at the LHC (see Figure 1.9).

Among the reactions in the LHC experiments, the $pp \to e\nu + X$ channel is directly related to the charged weak interactions and thus β decays, because the parton-level process is $\bar{u}d \to e\bar{\nu}$. The exotic interactions result in excess events at high transverse mass m_T of the lepton pairs, where m_T is defined as

$$m_T \equiv \sqrt{2 E_e^T E_\nu^T (1 - \cos(\Delta\phi_{e\nu}))}. \tag{1.37}$$

E_e^T and E_ν^T are the transverse momenta of the outgoing electron (positron) and anti-neutrino(neutrino). $\Delta\phi_{e\nu}$ is the angle between the lepton momenta in the transverse plane. Because $m_T^2 \sim p_W^2$ where p_W^2 is the square of the 4-momentum of the exchanged virtual mediator, the denominator for the propagator of the virtual mediator is $m_T^2 - m_W^2$ where m_W is the mass of the mediator. In the SM, the mediator is the W boson and at the TeV scale m_W is negligible. Therefore, at large m_T, the propagator scales as $1/m_T^2$. By contrast, if the scale of the exotic interactions is much larger than the TeV scale, *i.e.* $m_W >> m_T$, then the propagator remains constant as m_T varies at the TeV scale. Therefore, the SM propagator is suppressed by $1/m_T^2$ compared to the exotic interactions and the cross section is suppressed by $1/m_T^4$. This makes the cross section of $pp \to e\nu + X$ at high m_T more sensitive to exotic interactions at energy scales much higher than the TeV scale.

	SM propagator	NP propagator	Ratio (NP/SM)
MeV scale (nuclear β decays)	$\sim -\frac{1}{M_W^2}$	$\sim -\frac{1}{M_X^2}$	$\sim \left(\frac{M_W}{M_X}\right)^2$
TeV scale (LHC experiments)	$\sim \frac{1}{m_T^2}$	$\sim -\frac{1}{M_X^2}$	$\sim -\left(\frac{m_T}{M_X}\right)^2$

Table 1.1: Approximate propagators of the SM and new-physics (NP) mediators. The mass scale of the NP mediator (M_X) is assumed much larger than 10 TeV.

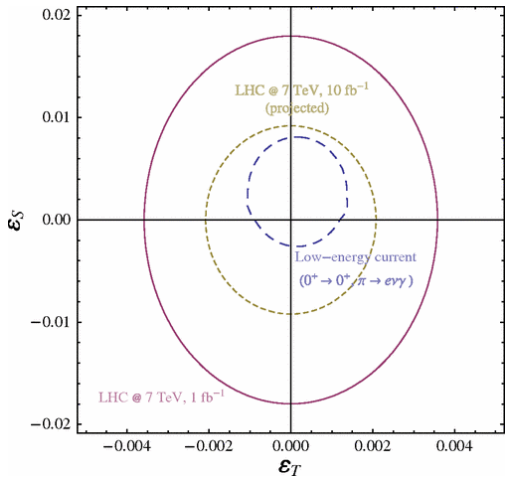

Figure 1.8: Limits on ϵ_T and ϵ_S based on the analysis of the LHC data in the $pp \to e\nu + X$ channel at $\sqrt{s}$ =7 TeV and 1 fb^{-1} (and 5 fb^{-1}) integrated luminosity. Limits from low-energy experiments are plotted as well. This figure is taken from Reference [15].

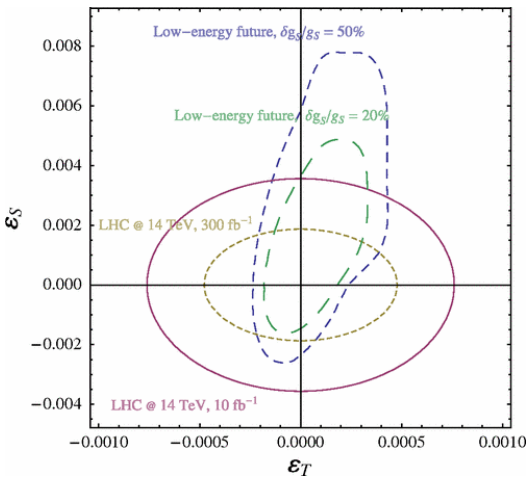

Figure 1.9: Projected limits on ϵ_T and ϵ_S based on the analysis of the future LHC data in the $pp \to e\nu + X$ channel at $\sqrt{s}$ =14 TeV and 10 fb^{-1} (and 300 fb^{-1}) integrated luminosity. Limits from future low-energy experiments assuming 50% and 20% uncertainties for g_S are plotted as well. This figure is taken from Reference [15].

In Reference [15], the LHC data in the $pp \to e\nu + X$ channel at $\sqrt{s}$ =7 TeV and 1 fb^{-1} integrated luminosity are analyzed. The analysis for the data at 5 fb^{-1} integrated luminosity are analyzed in Reference [43]. The limits on ϵ_S, $\tilde{\epsilon}_S$, ϵ_T and $\tilde{\epsilon}_T$ are

$$|\epsilon_S| < 1.3 \times 10^{-2}, |\tilde{\epsilon}_S| < 1.3 \times 10^{-2}$$

$$|\epsilon_T| < 3.0 \times 10^{-3}, |\tilde{\epsilon}_T| < 3.0 \times 10^{-3}.$$

The limits on ϵ_T and ϵ_S are plotted in Figure 1.8, and in this figure the results from

current low-energy experiments are plotted as well. In this comparison, the low-energy experiments still constraint the exotic interactions more stringently than the experiments at the LHC. However, for the $\tilde{\epsilon}_T$ and $\tilde{\epsilon}_S$, the low-energy constraints are $|\tilde{\epsilon}_T| < 3.0 \times 10^{-2}$ and $|\tilde{\epsilon}_S| < 14 \times 10^{-2}$, $\sim$1 order of magnitude larger than the limits put by the LHC experiments. These values depends strongly on the uncertainties of the calculated form factors g_S and g_T. For example, if $g_S = 1.08(28)$ from a more recent calculation [40] is used, the limit on $|\tilde{\epsilon}_S|$ becomes 6.9×10^{-2}. Therefore improvements on the Lattice-QCD calculations are important for translating the limits of coupling constants used in low-energy experiments to the ones used in high-energy physics.

In Figure 1.9 the projected constraints on ϵ_T and ϵ_S from future low-energy experiments and the LHC experiments with $\sqrt{s}$ =14 TeV at higher integrated luminosities are compared. The constraints from low- and high-energy experiments are at a similar scale. However, the limits generated by the LHC experiments depend on the assumption that the new physics appears at a much higher energy than the TeV-scale energies. Besides this, the LHC experiments can put limits on the total cross section of the exotic interactions, but cannot tell the nature of the interaction by itself. High precision low-energy measurements still play an important role throughout the LHC era, because of their independent yet complementary nature.

1.4 Historical and contemporary $a_{\beta\nu}$ measurements

As described in the previous sections, the $a_{\beta\nu}$ measurements played a crucial role in setting limits on $C_T - C_T'$ and $C_S - C_S'$. Experiments that measured $a_{\beta\nu}$ are summarized in Table 1.3 of Reference [44]. Because the momenta of anti-neutrinos (neutrinos) from nuclear β decays are almost impossible to measure directly, $a_{\beta\nu}$ is usually determined by observing the energy spectra of the recoil ions. A positive $a_{\beta\nu}$ value in the differential decay rate enhances the decays with the two leptons going in the same direction and results in more events with-higher energy recoil ions, and vice versa for a negative $a_{\beta\nu}$. The recoil-ion energy spectra were either measured by an ion energy analyzer, or by the Doppler shift of the subsequent decay products (γ ray or proton).

With the help of atomic traps and ion traps, radioactive isotopes can be confined in a

small volume (with size ∼1 mm) so that the decay position is well defined. This makes it possible to use the ion time of flight (TOF) to determine $a_{\beta\nu}$. A typical design of an $a_{\beta\nu}$-measurement setup is shown in Figure 1.10. In this design, a static electric field is applied to increase the recoil ion collection efficiency. The β detector detects the energy and entrance position of the β particle, and the ion detector detects its landing position and time. The trigger time difference between these two detectors gives the TOF of the recoil ion. In this geometry, the β detector and the ion detector are at the opposite sides of the trap, and a positive $a_{\beta\nu}$ enhances decays with shorter TOF, and vice versa for the negative $a_{\beta\nu}$. Furthermore, the momenta of the β particle and the recoil ion are fully determined by the detector readouts, trap position and the strength of the electric field. Assuming the initial momentum of the parent nucleus in the trap is negligible (typically lower than ∼1 eV), the neutrino momentum can be retrieved and the $\beta-\nu$ correlation can be measured directly.

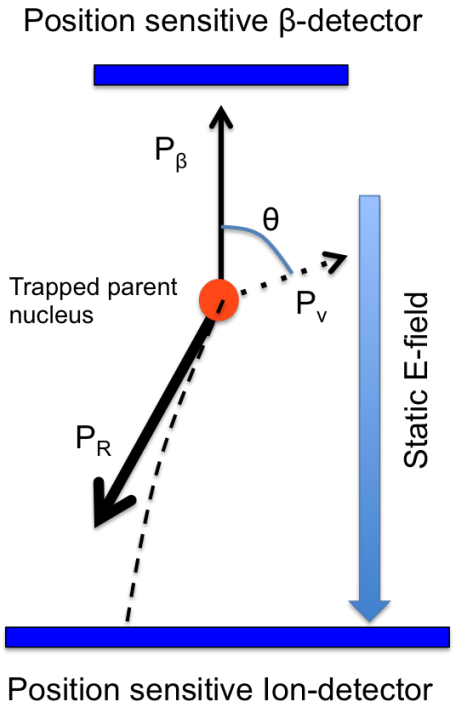

Figure 1.10: A typical design of an $a_{\beta\nu}$ measurement setup using trapped isotopes.

There are variations of the design shown in Figure 1.10. For example, the β detector can be replaced by a low-energy electron detector to detect the shake-off orbital electrons right after the β decay. The TOF is measured by the time difference between the ion detector and the shake-off electron detector. In this case, the shape of the TOF spectrum is still sensitive to $a_{\beta\nu}$ due to the sensitivity of the recoil-ion-energy spectrum to the $\beta - \nu$ correlation.

In the next subsections, examples of one recoil-ion-energy measurement and one TOF measurement using the trap technology are shown. Then the finished and on-going nuclear physics experiments using atomic or ion traps are summarized.

1.4.1 ^{6}He decay recoil-ion-energy measurement (Oak Ridge, 1963)

Johnson *et. al.* designed the experimental setup shown in Figure 1.11 and achieved a 0.9% determination of $a_{\beta\nu}$ through measuring the energy spectrum of the recoil ^{6}Li ions [37]. Briefly speaking, the ^{6}He atoms are produced through $^9\mathrm{Be}(n,\alpha)^6\mathrm{He}$ the reaction using neutrons from the Oak Ridge Research Reactor and 150 g of beryllium oxide powder. The ^{6}He atoms are then transferred to the conical decay volume, and the ^{6}Li recoil ions produced by the decays are collimated through a 0.5 inch aperture at the end of the conical volume. Then their energies are analyzed by magnetic and electrostatic ion energy analyzer and finally the ions are detected by an electron multiplier. The shape of the recoil-ion-energy spectrum (see the right panel of Figure 1.11) is then used to extract $a_{\beta\nu}$. The original result of $a_{\beta\nu}$ from this experiment was $a_{\beta\nu} = -0.3343 \pm 0.0030$. Additional corrections were applied after this experiment, and these corrections are summarized in Table 1.2.

	correction	$a_{\beta\nu}$
Original measurement [37]		-0.3343
Radiative corrections [45]	$+0.0035$	
Shake-off probability update [1]	-0.0017	
Q-value update [46][47]	$+0.00014$	
Combining all corrections	$+0.00086$	-0.3323

Table 1.2: Corrections to the $a_{\beta\nu}$ value determined from Johnson's experiment.

The majority of the uncertainty in this measurement comes from "Random variations in the spectra", amounting to 0.5%, and is said to arise from unknown and unaccounted for systematic variations in the experiment along with statistical uncertainties. The second largest systematic uncertainty arises from the sensitivity to the endpoint of the ion energy spectrum, which amounts to an uncertainty of 0.4% for $a_{\beta\nu}$.

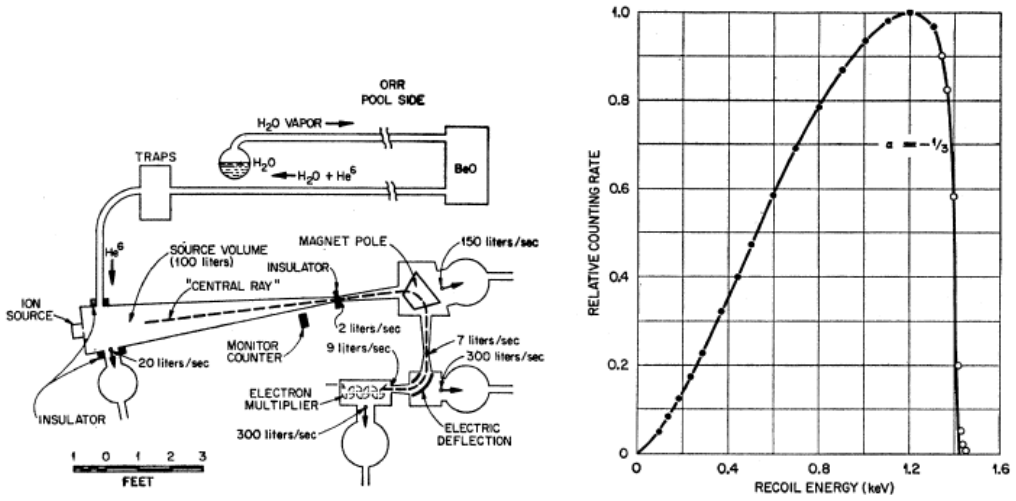

Figure 1.11: (left panel) Apparatus used in the ^{6}He decay experiment by Johnson *et. al.* in 1963. (right panel) Results of the ^{6}He decay recoil-ion-energy spectrum measurement (points) showing consistency with the Standard Model axial vector current expectation (curve). Figures taken from Reference [37].

1.4.2 Recoil ion TOF measurement using trapped $^6He^+$ ions (LPC, 2006)

In 2006, a new measurement of the $a_{\beta\nu}$ of ^{6}He decay was performed using trapped ^{6}He ions by the LPCTrap collaboration. ^{6}He atoms were produced by bombarding a graphite target with a 75 MeV/nucleon beam of ^{13}C at the GANIL-SPIRAL facility in Caen, France. Then the produced ^{6}He atoms were ionized using an electron-cyclotron-resonance (ECR) ion source. After an RF-cooling and bunching stage, the $^6He^+$ ions were injected into a Paul trap. The Paul trap and the detector system around it are shown in Figure 1.12. The recoil $^6Li^{++}$ ions were detected by a micro-channel plate (MCP) in coincidence with the β

particles detected by a double-sided silicon detector (DSSD) and a plastic scintillator. $a_{\beta\nu}$ was extracted by fitting the time-of-flight spectrum of the recoil ion to the template spectra generated by Monte Carlo simulations. The measured value of $a_{\beta\nu}$ from this experiment was $a_{\beta\nu} = 0.3335 \pm 0.0073_{stat} \pm 0.0075_{cyst}$ [48]. While it was not as precise as the older experiment done in 1963 (the Oak Ridge experiment), this result is the most precise determination of $a_{\beta\nu}$ in the ^{6}He decay using β-recoil coincidence measurements, and it paved the way for more precise experiments using trap technologies in the future.

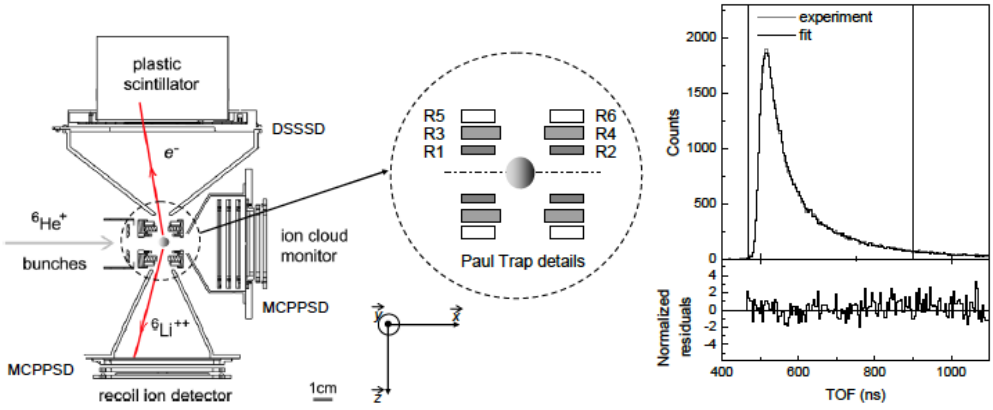

Figure 1.12: (left panel) Ion trap apparatus used in the ^{6}He decay experiment by Flćhard *et. al.* in 2006. (right panel) Results of the recoil ion TOF spectrum measurement fitted to curves generated by Monte Carlo simulations along with residuals. Figures taken from References [48] and [49].

1.4.3 Summary of recent nuclear physics experiments using atomic or ion traps

Some recent measurements of correlation coefficients of nuclear β decays are listed in Table 1.3. Detailed reviews of these measurements and other Standard Model tests using trapped radioactive atoms are discussed in Reference [50][51]. More reviews of laser trapping technologies and laser trapped radioactive isotopes are discussed in Reference [52][53][54]. Among these experiments we highlight the measurement of α-β-$\bar{\nu}$ triple-correlation in the β decay of ^{8}Li and subsequent α-particle breakup of the daughter ^{8}Be* done by Sternberg *et.*

al. [55]. This measurement gives the most stringent limit on tensor currents that couple to right-handed neutrinos (*i.e.* $C_T = -C'_T$): $|C_T/C_A|^2 < 0.011$ at the 95.5% confidence level. This is the first experiment that improves the limit on $C_T - C'_T$ since Johnson's experiment in 1963.

Year	Isotope	Decay type	Trap type	Observable	Reference
2000	^{82}Rb	β^+,GT	Magnetic TOP trap	A_β	[56]
2005	^{38m}K	β^+, F	MOT	$a_{\beta\nu}$	[57][34]
2008	^{21}Na	β^+, F/GT	MOT	$a_{\beta\nu}$	[58][59]
2008	^{80}Rb	β^+, F/GT	MOT	A_T	[60]
2011	^{6}He	β^-, GT	Paul Trap	$a_{\beta\nu}$	[49][48]
2013	^{8}Li	β^-,GT	Paul Trap	α-β-$\bar{\nu}$ correlation	[61]
2014	^{35}Ar	β^+, F/GT	Penning Trap	$a_{\beta\nu}$	[62]
2015	^{8}Li	β^-,GT	Paul Trap	α-β-$\bar{\nu}$ correlation	[55]
On-going	^{6}He	β^-, GT	MOT	$a_{\beta\nu}$	[63]

Table 1.3: Recent nuclear physics experiments using trap technologies.

1.5 ^{6}He experiment with improved precision

^{6}He is the most ideal isotope for searching for tensor couplings. It undergoes a pure Gamow-Teller decay and is thus uniquely sensitive to tensor couplings. It decays to the ground state of ^{6}Li with 100% branch ratio (see decay scheme in Figure 1.13) and half-life ∼807 ms [64]. The nuclear structure of ^{6}He is well understood, and the corrections to the SM predicted observables are small and calculable. The energy released in the decay is 3.5 MeV while the nucleus is light, so the recoil ion gains energy up to 1.4 keV. From the experimentalist's point of view, the large recoil energy makes the effect of the $\beta - \nu$ correlation easier to detect. Besides this merit, the ∼807 ms half-life is long enough for producing, transferring and manipulating the atoms, especially for experiments using traps.

The past measurements of $a_{\beta\nu}$ were discussed in Section 1.4, and in the most recent

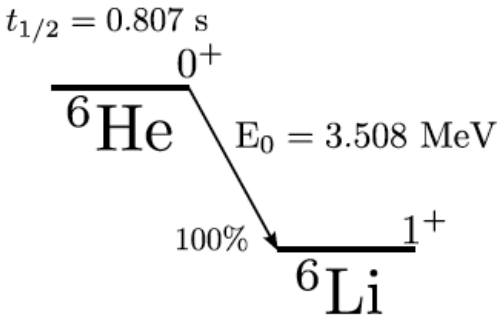

Figure 1.13: ^{6}He decay scheme.

experiment [48] an ion trap was used. Though ion traps are applicable to varieties of isotopes, the temperature of the ions is high enough and the spatial distribution of the ions is broad enough to result in significant systematic uncertainties in the $a_{\beta\nu}$ extraction. These are the dominating sources of systematic uncertainties in the previous $a_{\beta\nu}$ measurement of the ^{6}He decay. By contrast, neutral atom traps like the magneto-optical trap (MOT) are colder and better localized than ion traps, and the systematic uncertainties discussed above become less important. MOTs were already used in the $a_{\beta\nu}$ measurements of the ^{38m}K decay at TRINAT [34] and the ^{21}Na decay at Laurence Berkeley National Lab [59]. The MOT techniques were proven to be successful in measuring $a_{\beta\nu}$ to sub-percent precision for pure Fermi and mixed transitions. Therefore, we proposed a new $a_{\beta\nu}$ measurement of the ^{6}He decay using a MOT, in order to achieve a sub-percent level determination of $a_{\beta\nu}$ of a pure Gamow-Teller decay and thus improve the current limits on $C_T - C_T'$ by a factor of $\sim$3.

The apparatus construction of the proposed experiment for measuring the $a_{\beta\nu}$ of the ^{6}He decay (the ^{6}*He experiment*) was started in 2009. The ^{6}He production system [63] was developed in 2010. Since then, a trapping system and a detector system based on the scheme drawn in Figure 1.10 were developed and improved. In this thesis, a general description of the ^{6}He experiment is presented in Chapter 2. The current design (see Chapter 3), calibration (see Chapter 4) and Monte Carlo simulation (see Chapter 5) of the detector system are presented. The plan is to repeat the 1% level measurement of

$a_{\beta\nu}$ with the current design, and then make improvements to achieve the goal of a 0.1% level measurement of $a_{\beta\nu}$. The results from a proof-of-principle run with ∼2% statistical uncertainty in $a_{\beta\nu}$ are presented as well (see Chapter 6).

1.6 Orbital electron shake-off and recoil charge-state distribution after nuclear β decay

Orbital electron shake-off is the process in which orbital electrons are excited into the continuum after a sudden change of the nucleus generated electric potential. Due to the change of the electric potential the wave functions of the bound states and continuous states are different from those before the potential change. In the *sudden approximation* which assumes that the change of potential takes no time, the probability of transitions from a bound state to a state in the continuum is the square of the wave function overlap between the bound state and the state in the continuum. The shake-off effect is common to nuclear β decays because both the charge and momentum of the nucleus change suddenly in the decay. In nuclear β decays, the nuclear potential changes in $\sim 10^{-18}$ s which is the time for the β particle to leave the electron cloud of the atom. Comparing to the orbital period of orbital electrons ($\sim 10^{-16}$ s), the time for potential change is short, and therefore the sudden change approximation is valid.

The shake-off process results in different charge states in the recoil ions from the β decays. For all experiments that measure the recoil ions, the ion charge state is crucial for ion energy determination. Particularly, for $a_{\beta\nu}$ measurements using traps the recoil-ion-energy dependency of the shake-off probability is important because it affects the shape of the TOF spectrum and thus results in systematic offset in the extracted $a_{\beta\nu}$. Therefore, many of the nuclear β-decay experiments were accompanied by measurements of charge-state distributions of recoil ions and thus shake-off probabilities [65][66][67]. On the other hand, shake-off probabilities of many β decays were calculated [68][65][66][67]. By comparing these calculated results to measured ones, the validities of the algorithms were tested.

For the ^{6}He decay, the shake-off probabilities were calculated for both ground state neutral atoms [68] and ground state $^6He^+$ ions [66]. The measured charge state distribution of the recoil ions from the decays of $^6He^+$ ions agrees well with the calculation [66]. For

neutral atoms, the calculated single electron shake-off probability agrees well with the measurement [69], but the double shake-off probability was overestimated by almost one order of magnitude. In 2015, a new calculation [1] was performed for the shake-off probabilities for ^{6}He atoms in both ground state and the metastable state 2 $^3S_1$. For the ground state ^{6}He atom, this calculation also overestimates the double shake-off probabilities, and the recoil energy dependency of the single shake-off probability deviates from the measurement described in Reference [69]. Until now, there are no measurements of the charge state distribution of the recoil ions after the decay of ^{6}He in the 2 $^3S_1$ metastable state, which is important for experiments with MOT-trapped ^{6}He atoms. Therefore, we planned to perform this measurement using the facilities developed for the $a_{\beta\nu}$ measurement, so that the calculation described in Reference [1] has a measurement to compare to. Furthermore, for most of the measurements of the recoil energy dependency of the shake-off probability, the comparisons to the calculations were performed using Monte Carlo simulations assuming $a_{\beta\nu}$ has the SM predicted value. This analysis method weakens the future analysis on $a_{\beta\nu}$ using the same decay. We developed an analysis method that is insensitive to the value of $a_{\beta\nu}$ at the leading order. The measurements and analysis of the charge-state distribution of recoil ions in the ^{6}He decay are described in Chapter 6.

Chapter 2

THE ^{6}HE EXPERIMENT IN A NUTSHELL

2.1 ^{6}He Production

The typical efficiency of the atomic trapping system is approximately 1×10^{-7}. In order to accumulate enough ^{6}He atoms in the trap so that the required statistics can be achieved in a reasonable period of time, the ^{6}He production rate is desired to be at least 10^{10} atoms per second. We designed and constructed the ^{6}He production system based on the ^{7}Li(^{2}H, ^{3}He)^{6}He reaction [70], using a deuteron beam bombarding a lithium target.

The deuteron beam is provided by the tandem Van de Graaff accelerator available at CENPA, University of Washington. This tandem accelerator delivers a deuteron beam at 18 MeV to the lithium target with current up to 15 μA. As shown in Figure 2.1 the lithium is held in a stainless steel cup with a 7.5 μm thick tantalum front window exposed to the deuteron beam. The lithium holder is mounted inside the target station shown in Figure 2.2. The produced ^{6}He atoms diffuse out from the molten lithium and then are transferred to the lower-background experimental area through a 6 inch diameter tube. The experimental area is separated from the production room by a $\sim$1.5-m thick concrete wall with additional neutron shielding on both sides.

In order to maximize and stabilize the production of ^{6}He, several additional functions of the production target were developed. The most important one is the temperature control system. The melting point of lithium is 180.5 °C, and usually the target is operated at 250 °C in order to achieve a higher yield of ^{6}He. While the 18 MeV deuteron beam is bombarding the target at 15 μA, 270 W power is being dumped into the target system continuously. Therefore, the target needs active cooling when running at the full beam current ($\sim$15 μA). On the other hand, while running at low current during beam tuning and production testing, the beam power is not enough to melt the lithium, so active heating is needed. The temperature control system is housed inside a copper block which is silver-

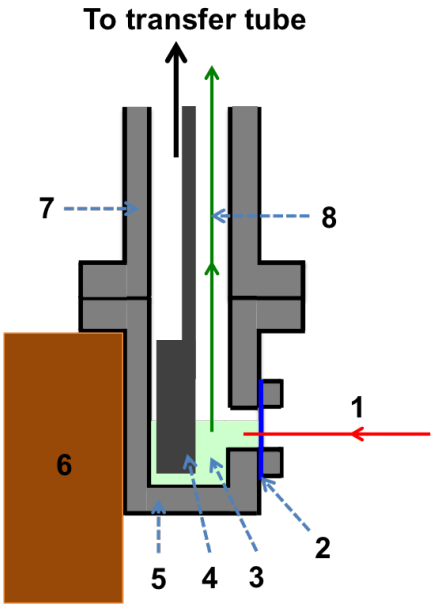

Figure 2.1: Lithium target configuration. 1) Deuteron beam. 2) 7.5 μm tantalum foil. 3) Molten lithium. 4) Half-cylinder shape stirring paddle. 5) Stainless steel cup 6) Temperature controlled copper block. 7) Cup mount. 8) ^{6}He diffusion path.

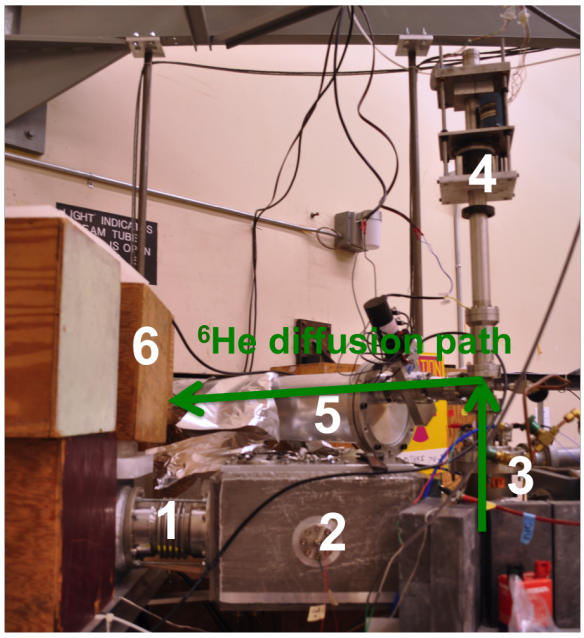

Figure 2.2: Target station mounted at the end of the beam line. 1) Beam line. 2) Beam collimator box. 3) Target chamber. 4) Auto-stirring motors. 5) 6 inch diameter extraction tube to low background experimental area. 6) Neutron shielding. The ^{6}He diffusion path is labeled in green.

soldered onto the stainless steel cup that holds the lithium. A 300 W electric heater is mounted inside the copper block for heating. Cooling channels inside the copper block allows compressed air flowing through the copper and lowering the temperature. A thermocouple temperature sensor is mounted on the copper block to monitor its temperature. The switch of the electric heater and the valve of the cooling nitrogen are controlled by an OMEGA CN7500 PID temperature controller that also reads the thermocouple temperature sensor. This unit regulates the target temperature around a preset value.

Another important feature of the target system is the *auto-stirring* system. The only process that extracts the produced ^{6}He from the lithium is diffusion. In order to minimize the diffusion distance inside the lithium, the beam should be tuned so that it hits just below the top surface of the molten lithium. A half-cylinder shape tantalum stirring paddle is in-

serted into the lithium. By changing the vertical position of the stirring paddle, the surface level of the lithium is adjusted. In practice, we adjust the stirring paddle vertical position and the deuteron beam position to maximize the observed ^{6}He production rate. Furthermore, the beam penetrates through the front window and dumps energy over an area of less than 1 mm^2 on the window. The window is so thin that thermal conductivity is too low to conduct the heat away efficiently. If there is no lithium at the back of the window at the beam-hit position, this point on the window will be overheated and eventually the window is melted at this point. Therefore, about every 30 minutes we insert the stirring paddle to the deepest position and then stir the lithium for five revolutions so that the lithium wets the entire front window and conducts the heat produced in the window efficiently. The vertical and azimuthal motion of the stirring paddle are powered by two stepper motors through a magnetic transporter, and these stepper motors are controlled by an Arduino micro-controller. Both the temperature control system and the stepper motor controllers are located outside the target room for easy accessibility during irradiation times.

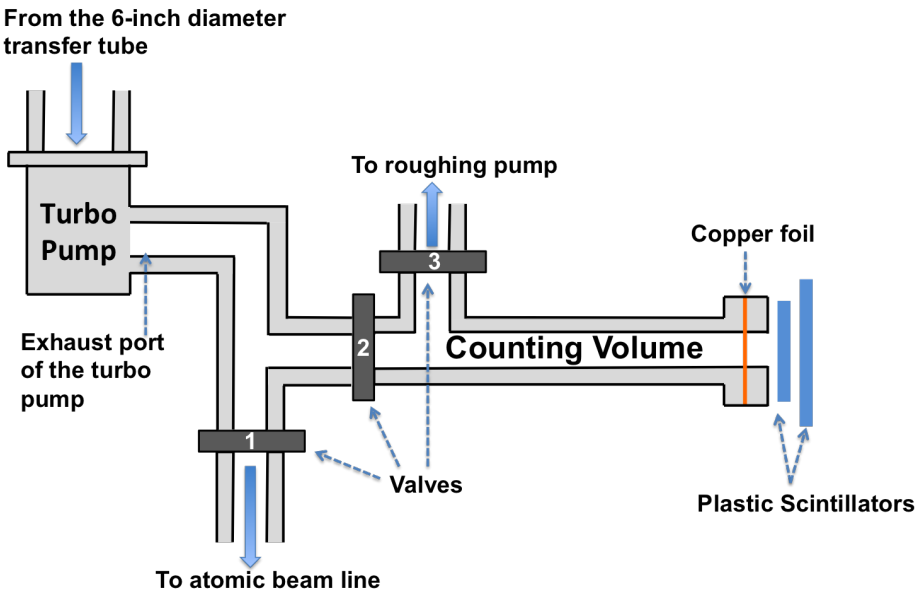

Figure 2.3: Schematic of ^{6}He production monitor system.

In the low-background experimental area, the 6 inch transfer tube is connected to a 360

l/s turbo-molecular pump which delivers the ^{6}He atoms to its exhaust port. The vacuum configuration connected to the exhaust port of the turbo pump is shown in Figure 2.3. During the production measurement period, "Valve-1" and "Valve-3" in Figure 2.3 are closed and "Valve-2" is open so that all of the extracted ^{6}He atoms fill the counting volume which is used for ^{6}He production test. The counting volume is a 30-cm long 5-cm diameter tube with a 1-mil thick copper foil sealed at the far end away from the transfer turbo pump. The decays of the ^{6}He in the counting volume are detected by two plastic scintillators mounted right against the flange at the end of the counting volume. The light from these scintillators is read out by photo-multiplier tubes. A coincidence trigger from these two scintillators is required in order to reduce the radiation background generated by the production target and the accelerator. We performed a simulation using GEANT4 [71] to study the relationship between total number of ^{6}He atoms inside the counting volume and the number observed decays by the two scintillators.

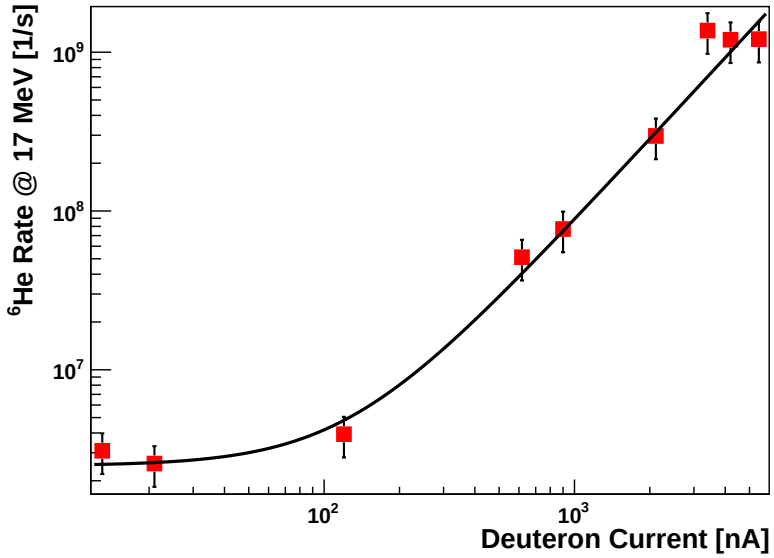

Figure 2.4: Extracted ^{6}He rate in the low-background experimental area as a function of deuteron beam current at an energy of 17 MeV. The data are fit with an empirical model: $R \approx 2.5 \times 10^6 + 656 \times I^{1.7}$where the rate R is in decays/s and the current I in nA. The exponential factor of 1.7 hints at a somewhat improved extraction of ^{6}He at higher beam currents. This figure is taken from Reference [63].

During the early stage of the production target development, we measured how the production rate scales as a function of the beam current, which is shown in Figure 2.4 [63]. After the auto-stirring system and temperature monitor system were developed and the 18 MeV deuteron beam current is maximized to around 15 μA, the ^{6}He production rate reached 2×10^{10}/s. Throughout the measurement of the $\beta - \nu$ correlation, the ^{6}He production rate can be maintained stably at 60% to 70% of this peak production rate.

More detailed descriptions of the design and construction of the lithium target and the ^{6}He production monitor system can be found in Reference [44].

2.2 Atomic beam-line and magneto-optical traps

During the $\beta - \nu$ correlation measurement period, the ^{6}He atoms are delivered to the atomic beam line by opening "Valve-1" in Figure 2.3 while the valve to the counting volume ("Valve-2" in Figure 2.3) remains sealed. Meanwhile, "Valve-3" in Figure 2.3 is open so that the counting volume is pumped by the roughing pump. A 50-l/s turbo pump is mounted downstream of the valve to the atomic beam line. This turbo pump pressurizes the ^{6}He atoms into the starting point of the atomic beam line, the "RF discharge tube" inside the "Transverse-cooling chamber" (see Figure 2.5).

The principles of laser cooling and trapping are described in more details in References [72] and [73], and the detailed operations of the trapping system of this experiment are described in Reference [44]. In this thesis, the laser cooling and trapping systems are described in a brief way in order to facilitate the description of the rest part of this experiment.

2.2.1 RF discharge source

When using laser to cool and trap neutral atoms, the laser frequency needs to be tuned near the transition frequency corresponding to a resonance in the atom being handled. For helium atoms, it is very difficult to use any transition from the ground state because it requires continuous vacuum ultraviolet laser (with photon energy above 20 eV) which is not available. However, the metastable state 2^3S_1 of helium has a sufficiently long lifetime (7870 seconds [74]), and the transition wavelength between 2^3S_1 and 2^3P_2 (1083 nm) is

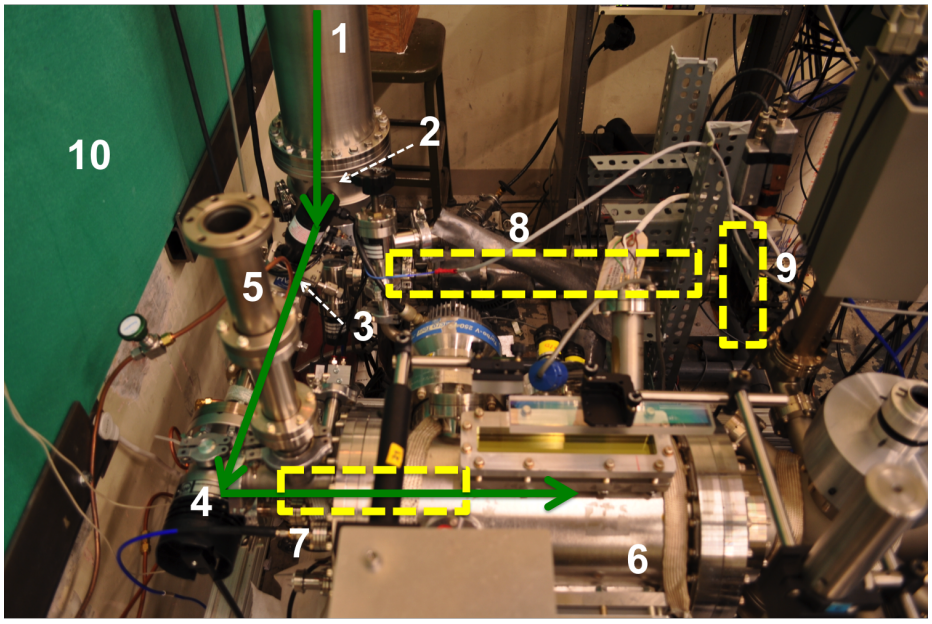

Figure 2.5: Head section of the atomic beam line. 1) 6 inch diameter transfer tube. 2) 360-l/s turbo pump. 3) Valve to the atomic beam line. 4) 50-l/s turbo pump. 5) Liquid nitrogen reservoir. 6) Transverse-cooling chamber. 7) RF discharge tube(inside the chamber). 8) Counting volume. 9) Scintillators for ^{6}He production counting. 10) Borated plastic neutron shielding. ^{6}He transfer path is labeled by green arrows.

achievable with sufficient power by commercial laser systems [72]. Therefore, we chose this pair of states for cooling and trapping.

The helium atoms are excited to the 2^3S_1 metastable state from the ground state in a low-pressure radio-frequency (RF) discharge source. Driven by the RF field, the electrons in the plasma oscillate and collide with neutral helium atoms, exciting the atoms to various atomic states. Most of the excited helium atoms de-excite back to the ground state, but some atoms de-excite to the metastable state 2^3S_1. Eventually only $\sim 10^{-5}$ of the total helium atoms end up in the metastable state. The schematic of the RF discharge source is shown in Figure 2.6. The helium atoms are mixed with ~1-mTorr xenon carrier gas before entering the discharge tube. The discharge tube is cooled by liquid nitrogen so that through colliding with the tube wall the incoming gas is cooled to ~100 K. The RF resonator running at ~50 W and ~300 MHz creates the plasma inside the tube. The carrier gas helps create

higher electron density in the plasma to increase the production of the metastable helium atoms. When the metastable helium atoms collide with the wall or other gas molecules, they quench to the ground state. Therefore, the pressure of the carrier gas cannot be too high, and only the forward-going metastable atoms are preserved in the rest of the atomic beam line.

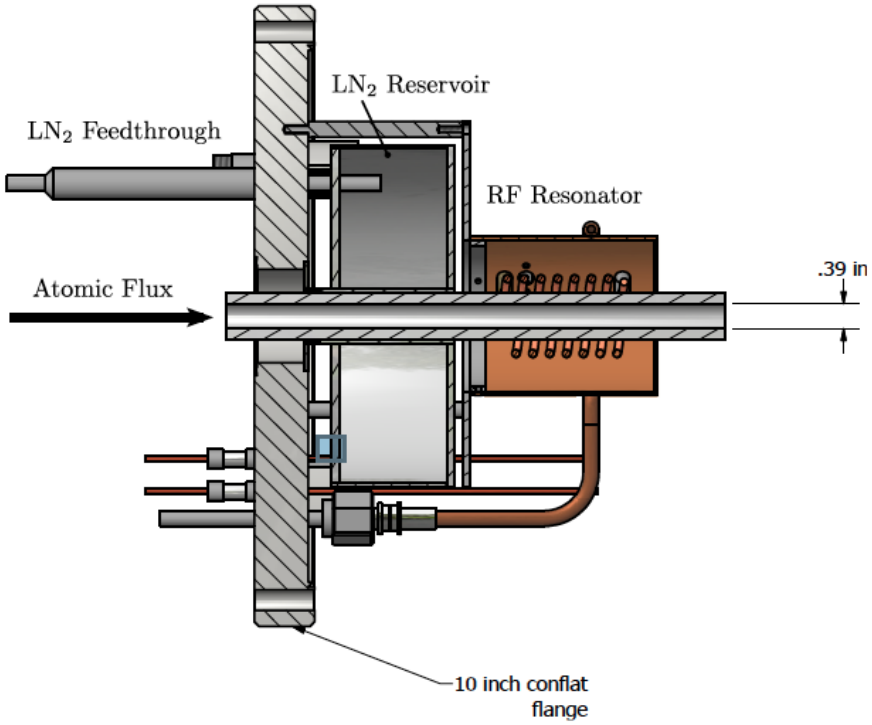

Figure 2.6: Schematic of the RF discharge assembly used in the experiment. This figure is taken from Reference [44].

2.2.2 Laser cooling and trapping system

At the exit of the discharge tube, four beams of laser red-detuned from the $2^3P_2 \rightarrow 2^3S_1$ transition frequency shine towards the atomic beam from the transverse directions. In this laser field, the metastable helium atoms are slowed down in the transverse directions, so this procedure is called *transverse cooling*. After the transverse cooling, the atomic beam is more focused towards the forward direction, and therefore the capture efficiency of the MOT

increases by a factor of ∼80. Exiting the transverse cooling chamber through an aperture, the atomic beam enters the Zeeman slower. A beam of red-detuned laser propagates against the direction of the atomic beam and the atoms slow down by absorbing photons. The magnetic field along the atomic beam keeps the atoms on resonance with the laser through the Zeeman effect so that the atoms feel the slowing force everywhere along their path in the Zeeman slower. The Zeeman slower decelerates the helium atoms from ∼500 m/s to ∼10 m/s well matched to the MOT capture velocity of also ∼10 m/s. Near the exit of the Zeeman slower, a 2D MOT is installed to focus the atomic beam and thus increase the capture efficiency of the MOT.

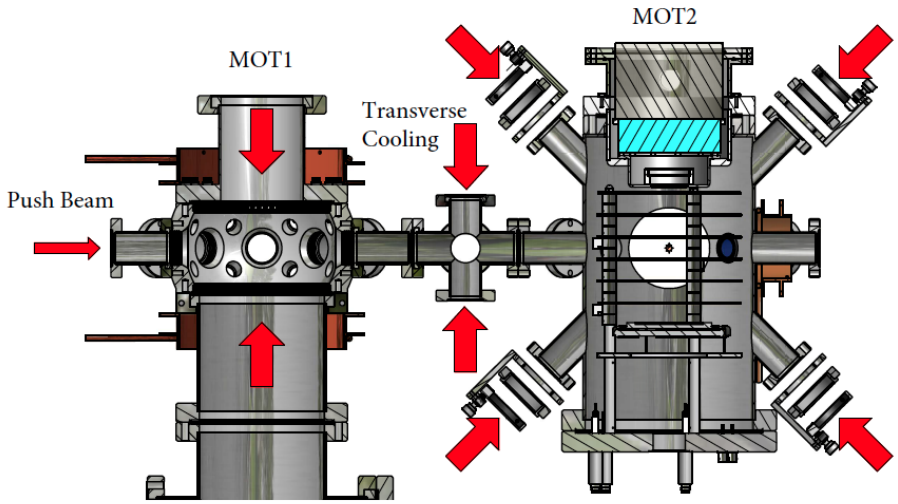

Figure 2.7: Cross-section view of the two MOTs. This figure is taken from Reference [44].

In this experiment, there are two MOTs. The first MOT (MOT-1) captures the atoms exiting the Zeeman slower, and at the second MOT (MOT-2) the $\beta - \nu$ correlation measurement is conducted (see Figure 2.7). In each MOT, three pairs of counter-propagating red-detuned laser beams cool the atoms down to approximately 100 μK, and one pair of anti-Helmholtz coils create a quadrupole magnetic field that traps helium atoms at the B=0 region with the help of the laser field. Periodically, an additional laser beam pushes the trapped helium atoms from MOT-1 to MOT-2. Typically, the MOT-1 to MOT-2 transfer efficiency is ∼30%. Besides the trapped helium atoms, the non-trapped helium atoms also

diffuse into MOT-1. When trapping ^{6}He atoms, the number of non-trapped ^{6}He atoms in the MOT-1 chamber is approximately 100 times more than the trapped ones. The non-trapped ^{6}He atoms also decay in the MOT-1 chamber so they create a huge background for the experiment, and therefore it is impossible to measure the $\beta - \nu$ correlation at MOT-1. Also, it is essential to limit the diffusion of non-trapped ^{6}He atoms from MOT-1 chamber to MOT-2 chamber. A 10 mm diameter, 100 mm long aperture tube and a shutter are installed in between the two MOT chambers. The shutter only opens for ∼5 ms during the MOT-1 to MOT-2 transfer period. In this way, the non-trapped ^{6}He atoms are reduced greatly in the MOT-2 chamber. A signal-to-background ratio of ∼12 has been achieved in the detector system at MOT-2.

All laser power, frequency, polarization, alignment, and magnetic fields need to be optimized to achieve the best trapping efficiency. Usually, we first optimize the system to trap the stable isotope ^{4}He and then switch the laser frequency by the accurately known isotope shift to the ^{6}He configuration. We also use the trapped ^{4}He cloud to determine the position of the MOT and other systematic effects of the detection system.

2.2.3 MOT imaging

Cameras are mounted on the view ports of both MOTs and they image the MOTs using the fluorescence 1083 nm light from the MOTs. The position and the shape of the MOTs can be determined from the image. The number of trapped atoms is determined by the brightness of the image. For ^{6}He, the trapped atoms are very few (∼500) and the fluorescence of 1083 nm light is too dim for cameras. We shine a beam of 706 nm laser to the MOT and drive the transition between $2\ ^3P_2$ and $3\ ^3S_1$ states. The fluorescence of the 706 nm light is detected by a photo-multiplier, and this probing scheme is sensitive to a few tens of atoms in the trap. Throughout the experiment, we trapped ∼500 ^{6}He atoms in MOT-1 and ∼150 in MOT-2.

Besides the optical imaging system, the MOT is also imaged in the X-Y plane by a micro-channel plate described in Chapter 3. The micro-channel plate detects penning ions or photoions from the MOT for both ^{4}He and ^{6}He. This enables us to directly compare the

MOT position for ^{4}He and ^{6}He in the X-Y plane. Details of the MOT-position determination methods are described in Chapter 4.

2.3 Detector system overview

2.3.1 Detectors

In order to realize the detection scheme described in Section 1.5, we constructed the detector system mounted on the MOT-2 chamber whose cross-section view is shown in Figure 2.8. The ^{6}He atoms are trapped at the center of the MOT-2 chamber. A β telescope is mounted above the ^{6}He trap. The β telescope consists of a multi-wire proportional chamber (MWPC) close to the entrance window and a scintillator-photomultiplier assembly above the MWPC. The scintillator and the photomultiplier tube (PMT) are connected by a cylindrical acrylic light guide. The MWPC reads the entrance position of the β particle from the ^{6}He decay and the scintillator-PMT assembly reads the full energy of the β particle. The coincidence trigger between the PMT and the MWPC also suppresses the background caused by γ rays from the accelerator and the production target. Below the ^{6}He trap a micro-channel plate (MCP) detector system is installed to detect the recoil ^{6}Li ions. The MCP reads the landing position of the recoil ion. The time of flight (TOF) of the recoil ion is started by the PMT signal and stopped by the MCP signal. A stack of electrode plates create an electric field that accelerates the recoil ions towards the MCP so that the ion detection solid angle reaches close to 4π. The vacuum feed-throughs for the electrodes and the MCP system are mounted in the bottom flange. Besides the MOT lasers, one beam of high-intensity pulsed nitrogen laser is aligned to the MOT. This laser can photoionize the atoms in the MOT, which can be used for calibration of the electric field. Detailed descriptions of the design and construction of the detectors are described in Chapter 3 and the detector calibrations are described in Chapter 4.

2.3.2 Additional features

Besides the detectors mentioned above, the MOT-2 chamber has additional features that maintain the detector system in a good condition or facilitate varieties of calibration exper-

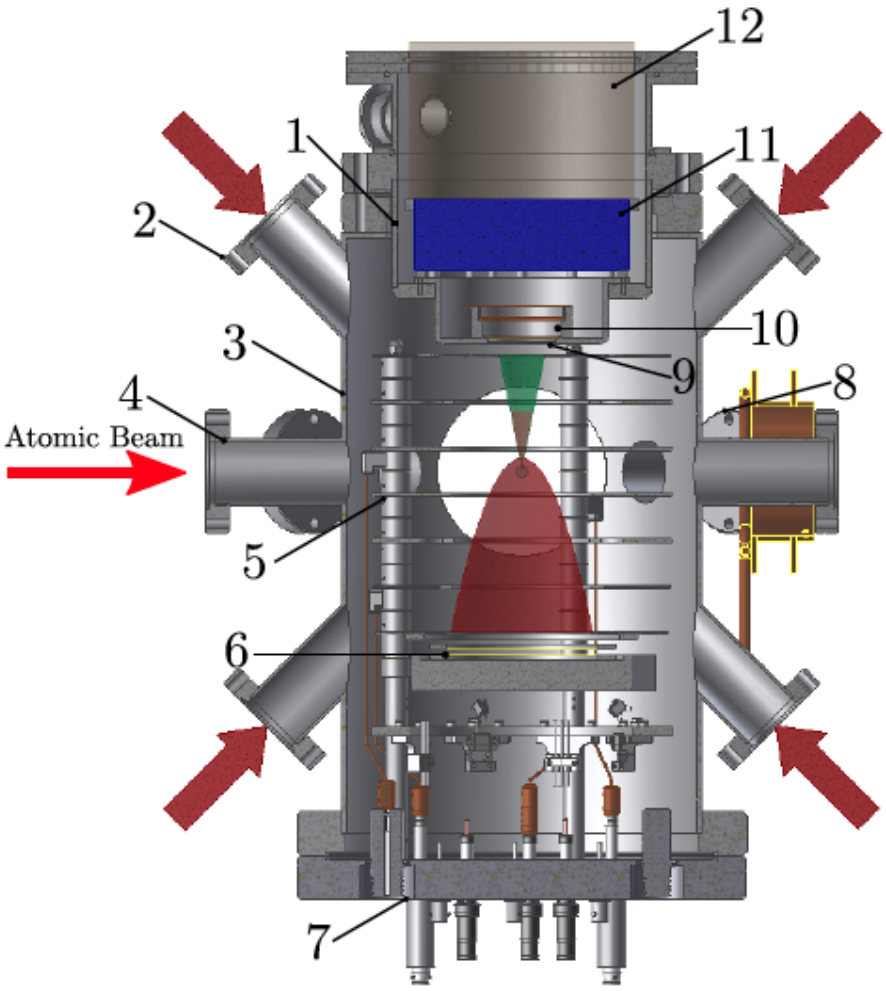

Figure 2.8: Cross-section view of the detector system mounted on the MOT-2 chamber. 1) re-entrant telescope housing, 2) trapping-laser ports, 3) main chamber, 4) ^{6}He transfer port, 5) electrode assembly, 6) micro-channel plate (MCP) recoil-ion detector, 7) 10 inch custom feedthrough flange for HV and MCP connections, 8) trap-monitoring ports, 9) 127 μm Be foil, 10) multi-wire proportional chamber (MWPC), 11) plastic scintillator, 12) light guide. This figure is taken from Reference [44].

iments.

One source of non-trapped ^{6}He atoms in the MOT-2 chamber is the back stream from the rough vacuum through the turbo pump on the MOT-2 chamber. To prevent the back stream, we added another 50-l/s turbo pump (the "isolation pump" shown in Figure 2.9)

that isolates the MOT-2 turbo pump from the rough vacuum which contains ^{6}He atoms that come from the exhaust of the MOT-1 turbo pump.

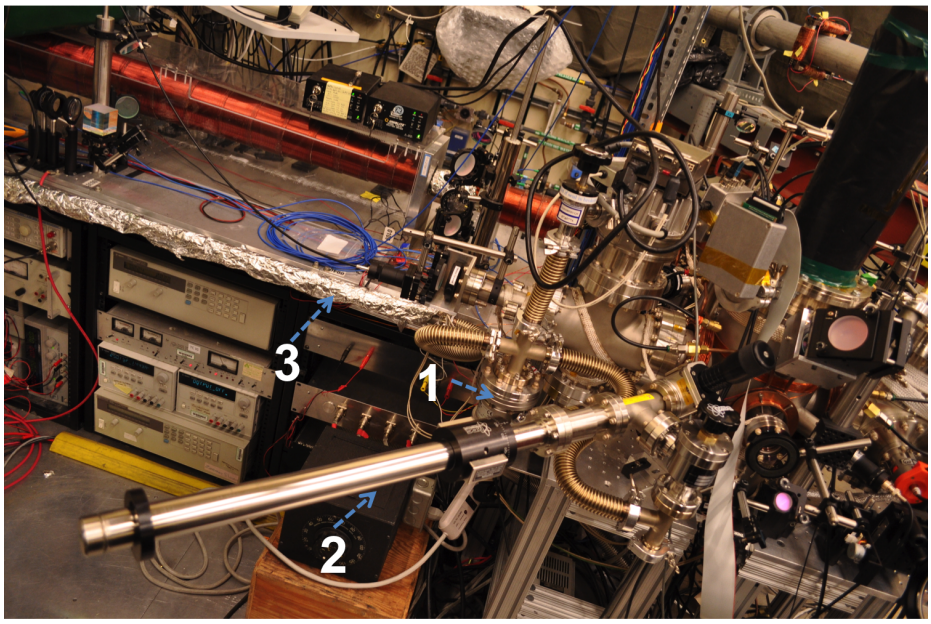

Figure 2.9: Photo of the MOT-2 chamber and some of its additional features. 1) 50 l/s isolation turbo pump. 2) Magnetic transporter for inserting calibration sources. 3) Diffuse ^{6}He transfer tube.

For calibration purposes, radioactive sources need to be placed at the position of the MOT. We use a magnetic transporter to move the calibration sources into/out from the MOT-2 chamber and rotate them inside the MOT-2 chamber. The calibration sources are mounted on an aluminum holder and then attached to the end of the inner rod of the magnetic transporter. In order to maintain the ultra-high vacuum ($\leq 10^{-9}$ Torr) in the MOT-2 chamber while changing the sources, the volume of the magnetic transporter is separated from the MOT-2 chamber by a gate valve. This volume is also connected to the volume between the MOT-2 turbo pump and the isolation pump through an angle valve. After changing calibration sources, the magnetic transporter is pumped by the isolation pump for at least 6-hours before connecting to the MOT-2 chamber.

As shown in Figure 2.9, the volume between the two turbo pumps is also connected to the exhaust line of the turbo pump on the transverse cooling chamber through a valve. This

allows for releasing high flux of non-trapped ^{6}He atoms into the MOT-2 chamber through the entrance of the magnetic transporter. The diffuse ^{6}He source plays an important role in calibrations and the background subtraction as described in Chapter 4.

2.4 $\beta - \nu$ angular correlation extraction and systematic uncertainty determination

As mentioned in Section 1.5, the $\beta - \nu$ correlation coefficient $a_{\beta\nu}$ is extracted by fitting the measured recoil ion TOF spectrum to templates generated by the Monte Carlo simulation. Realistic descriptions of the experimental system are taken into account in the simulation, for example, the size of the MOT, response functions of the detectors and uniformity of the electric field. The fitting templates for the $a_{\beta\nu} = -1/3$ and $a_{\beta\nu} = +1/3$ cases are shown in Figure 2.10. The two TOF peaks correspond to the two charge states of the recoil ^{6}Li ions. The ion-energy dependency of the shake-off probability is taken into account in the Monte Carlo simulation. The detailed fit procedure and the extraction of $a_{\beta\nu}$ are described in Chapter 6.

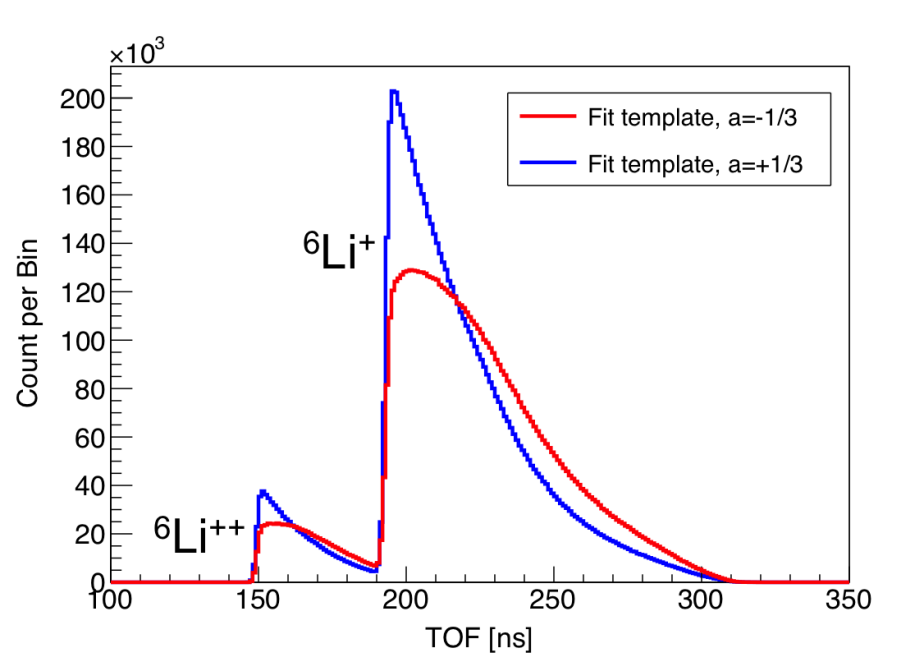

Figure 2.10: TOF fitting templates with $a_{\beta\nu} = -1/3$ (red) and $a_{\beta\nu} = +1/3$ (blue).

The shape of the TOF spectrum is sensitive to $a_{\beta\nu}$. However, it also depends on the β phase space and the recoil-ion phase space. Therefore, anything that affects the TOF or the collection of the β particles or the recoil ions becomes a potential source of systematic uncertainty. The sensitivities of the systematic effects are studied through the Monte Carlo simulation described in Chapter 5. The detector system is calibrated as described in Chapter 4. The systematic uncertainty of the $a_{\beta\nu}$ is determined by the calibration results and the Monte Carlo simulated sensitivities of systematic effects.

2.5 Summary

In this chapter the entire experiment was briefly overviewed. The flowchart of this experiment is shown in Figure 2.11. In the rest of this thesis, the detector system, Monte Carlo simulation and data analysis will be discussed in detail.

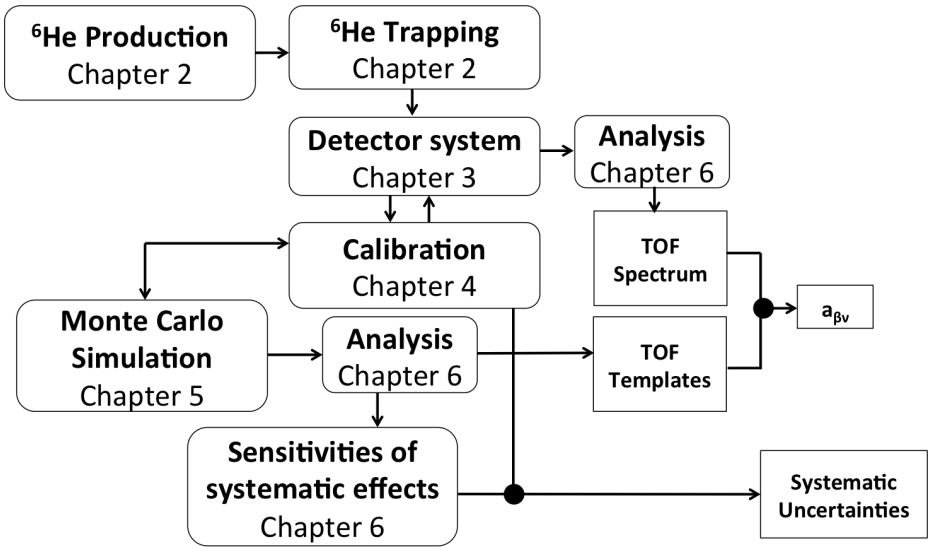

Figure 2.11: Flowchart of the measurement of the $\beta - \nu$ correlation in the ^{6}He decay. For each component the most relevant chapter in this thesis is indicated.

Chapter 3

DETECTOR SYSTEM DESIGN AND CONSTRUCTION

In this chapter, the design and construction of the main detector system: the MWPC, scintillator-PMT assembly, electrode system that generates the ion-accelerating field, and the MCP ion detector are described. Then the cycle control system and the nitrogen laser that is used for ionizing the trapped atoms are introduced. Finally, the data acquisition system *FASTER* is described.

3.1 β *telescope*

A section view of the β telescope is shown in Figure 3.1. The chamber enclosing the β telescope consists of three parts: the top, the body, and the bottom window holder. The top part seals against the light guide body with an O-ring, and provides four ports with ISO-25 flanges for the gas inlet/outlet and cable feed-throughs. The gas for the MWPC fills the whole empty space inside the chamber. The body part is mounted at the top of the MOT-2 chamber, and supports the weight of the scintillator-light guide-PMT system. The bottom window holder is sealed against the body part with an indium wire. The front window, which is a beryllium foil with a 127 μm thickness and a 38.1 mm diameter, is fusion bonded to the bottom window holder. The beryllium window holds against the 1 atm pressure difference between the MWPC gas and the ultra-high vacuum below 2×10^{-9} Torr on the other side. Its thickness and diameter are chosen to minimize the β straggling while maintaining its mechanical strength. The sizes and positions of the body part and the bottom window holder are designed to provide as much space for the detectors as possible while avoiding the laser beams for the MOT. As a result, the inner space of the bottom window holder is 91.4 mm in diameter and 38.1 mm deep, and the beryllium window is 70.9 mm above MOT-2.

The two components of the β telescope are described in Section 3.1.1 and Section 3.1.2.

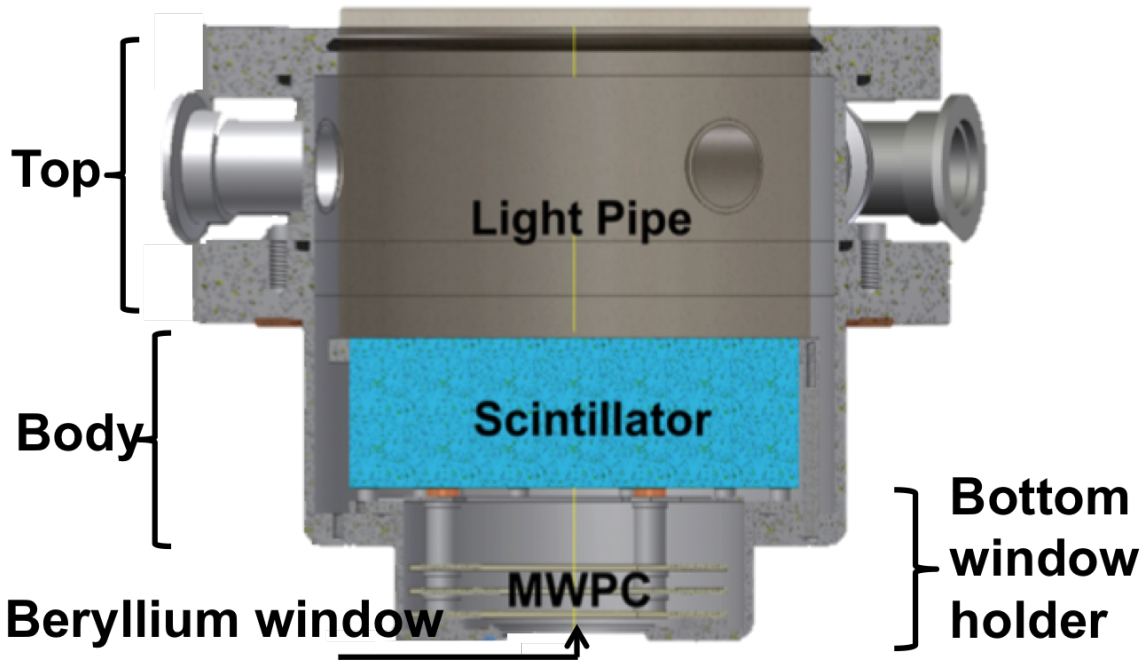

Figure 3.1: Section view of the β telescope

3.1.1 Multi-wire proportional chamber

3.1.1.1 MWPC design overview and principle of operation

We chose to use the MWPC to detect entrance position of the β particle because the efficiency of the MWPC is above 90% for β particles from ^{6}He decay, while the β-energy loss is about 4 keV, smaller than thin silicon detectors or scintillator sheets. The straggling of the β particle is also very small, even including the front window. A position resolution of 1 mm has been easily achieved in many other cases [75].

The MWPC assembly and its 3D model are shown in Figure 3.2. The MWPC has three wire planes strung on 1.575 mm thick FR4 glass epoxy printed circuit boards (PCB). The center wire plane acts as the anode and the top and bottom wire planes act as cathodes. The electrode boards are cut into round-corner square shape. There are four holes at the corners

for mounting. The center square open area is for wire stringing. The three electrode boards are tightened to the threaded rods on a 0.125 mm thick stainless steel base plate. The distance between adjacent electrodes is set by the thickness of the spacer nuts (6.35 mm). The whole assembly is inserted into the bottom window holder of the enclosing chamber. The top of the threaded rods are fixed to the bottom window holder so that the position of the MWPC is fixed relative to the chamber.

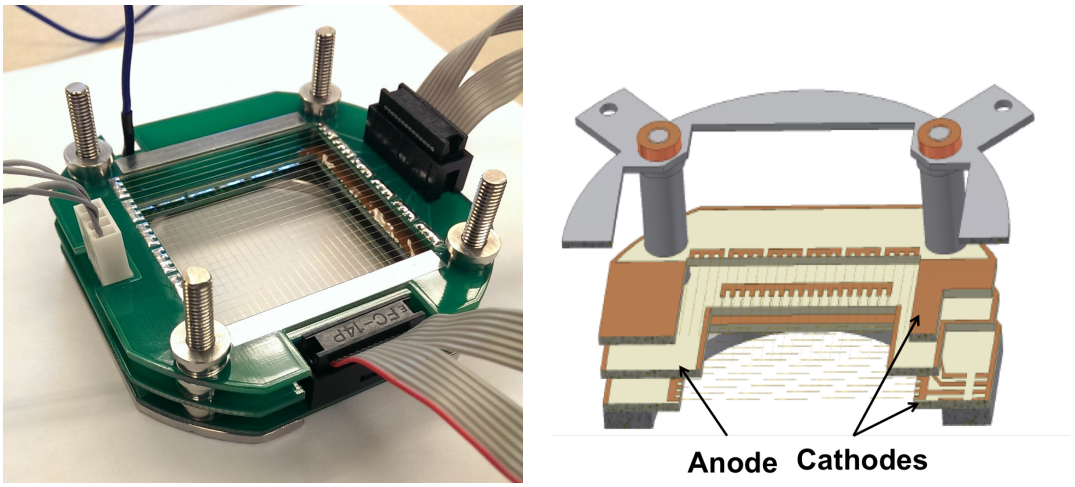

(a) (b)

Figure 3.2: (a) Photo of the MWPC. The electrodes are mounted on the supporting frame. The HV cable and signal cables are connected. (b) MWPC 3D model

During the operation, the thin wires on the anode board are biased at positive high voltage while the cathode wires are held at ground potential. Incident particles (β particles, X-rays, etc.) ionize the gas molecules, and then the electrons from these ionizations drift close to the anode wires, getting multiplied in the strong electric field. The final electron cloud in the avalanche is collected by the anode wire, while the positive ion cloud is pushed away and induces charges on the cathodes [76]. The collected charges on the anode and the induced charges on the cathodes are read out through charge-sensitive amplifiers. The electrode design and position reconstruction algorithm are described in Section 3.1.1.2.

The main challenge in our experiment concerning the MWPC is the geometry limitations due to the chamber size. With all the supporting structures, electronic components and

connectors on the MWPC electrode boards, the active area is limited to a ∼40 mm × 40 mm square. The detection solid angle defined by the collimator corresponds to a 16 mm-radius fiducial area on the MWPC, which is only ∼4 mm away from the edge. The position distortion and gain non-uniformity inside the fiducial area are not negligible. The methods of dealing with these difficulties are described in Section 4.3 and Section 4.4.

3.1.1.2 MWPC electrode design and position reconstruction algorithm

10 μm diameter gold-plated tungsten wires are used for the anode. The anode wires are first wound onto a metal frame using a wire-winding machine. A brush motor is used to keep the tension on the wires. The wire-winding machine keeps a 2 mm space between wires. Then 20 of the wires on the metal frame are soldered onto the anode PCB, giving a 4.8 cm×4.0 cm active area. At one end of each anode wire, it is connected to the HV conductor track individually through a 22 MΩ resistor, and on the HV track there is a pin where the HV cable is plugged. Capacitors are soldered in between adjacent wires as indicated in Figure 3.3b, forming a charge divider for position reconstruction. Each end of the capacitor chain is connected to a pin through a decoupling capacitor, and the signal cables are plugged on to the pins. All exposed HV conductors on the anode PCB are covered by Amstrong-12 epoxy to prevent sparking (see Figure 3.3a).

Conventionally, thin conductor strips are used for MWPC cathodes, but they introduce more electron energy loss and scattering. In order to minimize these effects, we chose to use 50 μm diameter gold-plated tungsten wires for the cathodes instead. The procedure to string wires onto the cathode boards is the same as that for the anode. The wire spacing for the cathodes is also 2 mm. Because there is no electronic components on the cathode boards, the active area is 48 mm×48 mm, larger than the anode's. More sensing wires give better position reconstruction and less distortion near the edges. On each cathode board, four adjacent wires are connected together by a conductor strip, forming six groups of wires in total as in Figure 3.4. Each group is connected to one pin of the connector on the edge of the board, where flat ribbon signal cables are plugged in. The cut-outs in the top cathode board provide space for connectors from the lower electrodes.

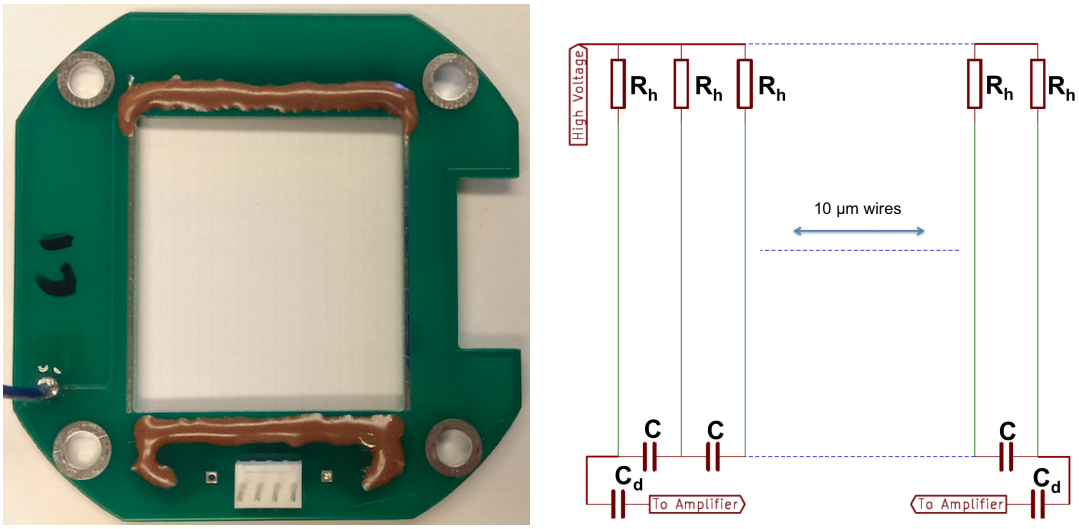

(a) (b)

Figure 3.3: (a) Photo of the MWPC anode board. Electronic components are covered under epoxy. (b) Schematic of the capacitive charge divider on the anode board. The 10 μm wires for gas multiplication are connected to the high voltage power supply through 22 MΩ resistors(R_h) . All capacitors in the charge division chain have the same capacitance of 470 pF. The decoupling capacitors C_d also have the same capacitance as C.

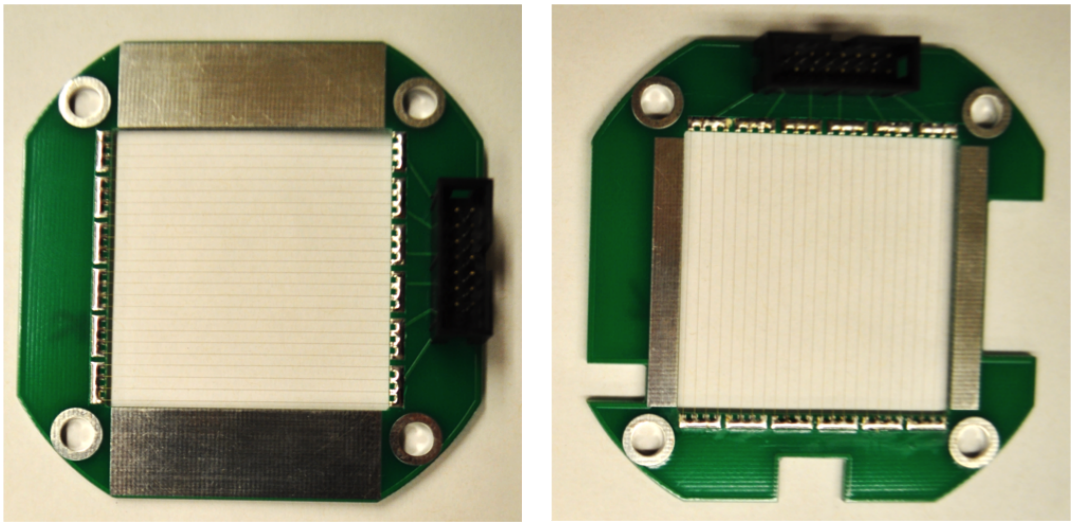

(a) Bottom cathode (b) Top cathode

Figure 3.4: Top view of the MWPC cathodes.

The wire direction of the top electrode is parallel to the anode wire direction, while the bottom one is perpendicular to the anode wire direction. In the MWPC coordinate system, the X axis is parallel to the anode wires and the Y axis is parallel to the bottom cathode wires. All signal cables and the HV cable run from the MWPC to the top part of the chamber in the space between the light guide and the chamber wall. The upper end of the anode signal cables are plugged to a 26-pin sub-D feed-through connector mounted at the top part of the chamber, and the cathode signal cables are plugged to another 26-pin sub-D feed-through. The HV cable is plugged to a SHV feed-through. Amplifiers are plugged on the outside of the sub-D feed-throughs for signal readout.

The position of the avalanche can be reconstructed by calculating the "Center-of-gravity" of the induced charges on the two cathodes [77]. For example, the X coordinate of the avalanche is given by

$$X_{rec} = \frac{\sum_{i=1}^{6} Q_i X_i}{\sum_{i=1}^{6} Q_i} \tag{3.1}$$

where Q_i's are the charges on the i-th strip (the 4-wire group) on the bottom cathode board and X_i's are the center coordinate of that strip. The Y coordinate of the avalanche can be reconstructed in the same way using the signals from the top cathode. The anode-to-cathode distance and the wire grouping scheme are optimized for this position reconstruction algorithm [77].

The charge divider on the anode can also give the position of the wire on which the avalanche happens, and this provides another way to reconstruct the Y coordinate of the avalanche. All capacitors (including the decoupling capacitors) in the charge division chain have the same capacitance, so the position of the triggered wire is given by

$$Y_{rec} = \frac{N_w + 1}{2} d_w \left(\frac{Q_L - Q_R}{Q_L + Q_R}\right) \tag{3.2}$$

where Q_L and Q_R are the charges collected at the left and right end of the charge divider, d_w is the anode wire spacing which is 2 mm for our anodes, and N_w is the total number of anode wires which is 20 in our case. Equation 3.2 is valid for the ideal case. Obviously, deviations from the nominal capacitance values result in distortions in the position reconstruction. Additionally, a non-linear relationship between avalanche position and the charge ratio

arises if the non-zero capacitance between anode wires and ground are taken into account [78]. The non-linear effects are reduced if the capacitance of each capacitor in the charge divider chain is sufficiently larger than the parasite capacitance from an individual wire to ground. According to Reference [78], the capacitance of each capacitor should be at least $N_w^2 C_w$, where N_w is the number of wires and C_w is the capacitance between an individual wire to ground. In other words, the total capacitance of the divider capacitors in series is greater than all parasite capacitance in parallel. We chose $C = 470\ pF$ as C_w is less than $1\ pF$. Since all anode wires are held at the same potential during normal operation, the divider capacitors do not need to be HV capacitors. However, sparks on the wires may drop the potential of that wire to zero instantly, resulting in a large potential difference across the adjacent capacitors much higher than their breaking voltage. Therefore, spark preventing techniques are crucial when using capacitive charge dividers. Fortunately, by covering the HV conductors with epoxy, we didn't see any sparks on the wires throughout the experiment[1].

The Y coordinate of the avalanche position are determined with two different methods. This redundancy gives us additional information to study properties of the chamber. In this experiment, we chose to use the bottom cathode reconstructed X coordinate and the anode reconstructed Y coordinate as the MWPC position readout. The cathode reconstructed Y coordinate is used as an auxiliary tool.

3.1.1.3 Counting gas for the MWPC

We use 1 atm Ar-10%CO_2 mixture as the counting gas (or proportional gas). We chose this gas mainly for convenience. It is inexpensive and nonflammable. No pump is needed for operating at 1 atm. The average energy needed to create an electron-ion pair in this mixture is approximately 26 eV [79]. Thus around 38 electron-ion pairs are created per keV energy loss of the incident particle. Before using the MWPC, the chamber is purged with the proportional gas at flow rate 6.0 scfh for ten minutes as the gain is stabilized. During normal operation, the proportional gas flows at 3.0 scfh through the chamber. The

[1]There were sparks from the HV strip on the other side of the resistors, and in this case there are no large potential differences between wires.

gas outlet is connected to the atmosphere directly through a ∼1-m long 0.25 inch diameter plastic tube.

3.1.1.4 Electronics for the MWPC

The MWPC anode is biased typically at +2850 V using a Bertan model 375X power supply, and its output voltage is monitored by a LabView program. The anode signals are read by a home made 4-channel amplifier. 2 channels are being used and the other 2 spare ones are for possible future development of a 5-layer MWPC with two anode boards. For each channel, the first stage is a charge-sensitive pre-amplifier, and it is followed by a differential shaping amplifier and a voltage amplifier that drives the 50 Ω load. This amplifier is constructed based on the design of the time-projection chamber pre-amplifiers for the MuSun experiment [80]. The cathode signals are amplified by a 16-channel amplifier. The custom-made amplifier chip [81] was previously used by the STAR experiment [82] and the MuCap experiment [83] for the electron proportional chamber cathodes. The amplifier chip integrates the charge-sensitive pre-amplifier and a differential shaper together for each channel. We modified the MuCap version of the amplifier board by removing the following discriminators and taking the chip outputs via AC-coupling capacitors. Both anode and cathode amplifiers are enclosed in aluminum boxes and plugged into the sub-D connectors on the β detector chamber wall. The properties of these amplifiers are listed in Table 3.1. The output signals of these amplifiers are fed to the data acquisition system.

	Gain	Shaping Time	Driving 50 Ω
Anode Amp.	4 V/pC	200 ns	Yes
Cathode Amp.	16 V/pC	150 ns	No

Table 3.1: Basic properties of anode and cathode amplifiers

3.1.2 Scintillator-PMT assembly

The total energy of the β particle is measured by the total amount of light generated in the scintillator and subsequently measured by the PMT. The scintillator is cut into a cylinder 38.1 mm in height and 119.38 mm in diameter. The outer diameter of the PMT is 133 mm. The residual magnetic field from the MOT-2 coils is high enough to affect the gain of the PMT substantially if the PMT locates right above the top flange of the enclosing chamber shown in Figure 3.1. Instead, we use a 34.29-cm long PMMA light guide to connect the PMT to the scintillator, so that the PMT stays farther from the coils. The scintillator is glued to one end of the light guide concentrically, and the PMT is coupled to the light guide by EJ-550 optical grease from Eljen Technology. The diameter of the light guide is 127.0 mm, slightly bigger than the scintillator. The whole assembly is supported vertically at the shoulder of the light guide by a stainless steel ring with three legs, and these legs are inserted into holes in the floor of the body part of the enclosing chamber. When the scintillator-PMT assembly is mounted in position, the distance from the beryllium window to the front surface of the scintillator is 41.3 mm.

For the ion TOF measurement, it is desirable to have a fast response β detector to start the TOF measurement. Therefore, we chose to use the EJ-200 plastic scintillator from Eljen Technology with 0.9 ns rise time and 2.1 ns decay time. The PMT model is Hamamatsu R1250 with a typical rise time of 2.5 ns and typical transit time of 54 ns. The spectral response of the PMT also matches the light emission spectrum of the scintillator. Both of them center around 420 nm.

In order to achieve a better energy resolution, the scintillator and the light guide are wrapped with reflective material to reduce the escaping of scintillation light. The front surface of the scintillator is covered with 6 μm aluminized mylar foil, and the sides of the scintillator and the light guide are wrapped with 10 μm thick teflon tape. For the section below the top flange of the enclosing chamber there is one layer of teflon, and above the flange there are layers. All ports of the enclosing chamber are light-tight and the section of the light guide above the top flange are further wrapped with three layers of black plastic sheets to prevent room light from leaking into the light guide. The wrapped scintillator,

light guide and PMT are shown in Figure 3.5.

Figure 3.5: Photo of the scintillator, light guide and PMT with wrappings.

The power supply for the PMT is a Model N1470 from CAEN. The PMT is biased at -1700V so that the signal size for the event with highest β energy from the ^{6}He decay is about 70% of the dynamic range of the data acquisition system. The dynode output and one of the two anode outputs from the PMT base is sent to the data acquisition system, while the other anode output is terminated by a 50 Ω terminator. In the PMT base, one 1000 pF capacitor is added from the anode signal outputs to ground. This capacitor makes the signal less sharp ($\sim$10 ns rise time and $\sim$100 ns fall time) and filters out high-frequency noises. Without this capacitor, our data acquisition system with a 500 MHz sampling rate does not calculate the charge integration accurately using the current algorithm.

The gain of the PMT is monitored by its response to external LED pulses. The LED pulses are generated in a home-made LED driving circuit. The LED pulses are sent to the PMT through a light fiber, coupled to the light guide with optical grease right above the

top flange and wrapped inside the teflon layers. The LED pulses are also sent to a silicon photo diode for reference. The detailed procedure of LED gain stabilization is described in Section 4.7.

3.1.3 Detection solid angle of β particles from trapped ^{6}He atoms

The detection solid angle of the β telescope is defined by the collimator (the top electrode for generating the ion-accelerating field) 9.94 mm below the beryllium window. This collimator is made of 2 mm thick stainless steel that is enough to stop a 3.5 MeV β particle. The inner radius of the collimator is 13 mm, giving a $0.91\% \times 4\pi$ detection solid angle relative to the MOT. This solid angle corresponds to 27.9 mm diameter on the beryllium window, 32.3 mm diameter on the MWPC anode board, and 46 mm diameter on the front of the scintillator. Therefore, both the MWPC active area and the scintillator cover larger solid angles than the collimator.

3.2 Ion-accelerating field

The ion-accelerating field is generated by a stack of seven electrodes shown in Figure 3.6. These electrodes are 2 mm thick, 170 mm outer diameter stainless steel plates. The inner diameter of the top electrode is 26 mm and it serves as the collimator of the β telescope as well. The inner diameter of all the other electrodes is 80 mm. The separation between adjacent electrodes is 24 mm. The detail mechanical inspection of the electrode system after assembled is described in Section 4.13.1. The MCP ion detector and its calibration mask are mounted on the lower side of the bottom electrode, which is described in Section 3.3. Cut-outs are made on the electrodes for the trapping laser beams. The electrodes are supported by four insulated columns. Each column is constructed from the ceramic separators shown in Figure 3.7. They are tightened to each other through set-screws. Electrodes are clamped between the separators. Each separator is covered by two metal sleeves from each side and these sleeves are in contact with the electrodes. There is a 1 mm gap between the metal sleeves (see Figure 3.7) so that the electrodes are still insulated from each other. These sleeves prevent static charges from building up on the surface of the ceramic separators.

Each electrode is connected to a high-voltage feed-through on the bottom flange via a 2 mm diameter copper wire.

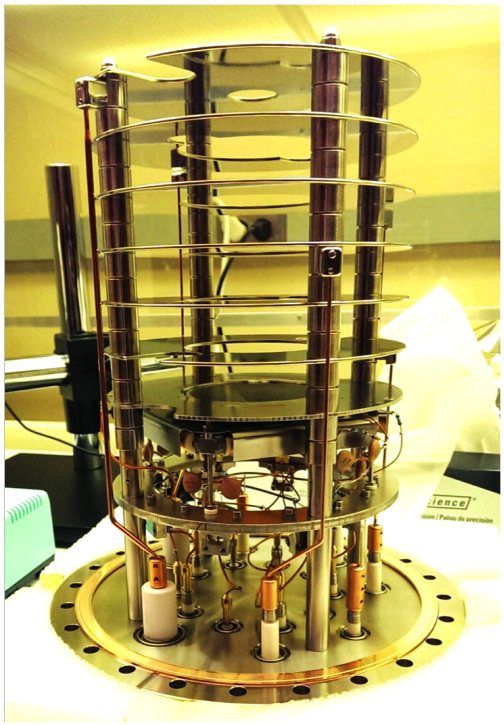

Figure 3.6: Fully assembled electrode structure for generating the ion-accelerating field. The MCP ion detector is also mounted to the bottom electrode.

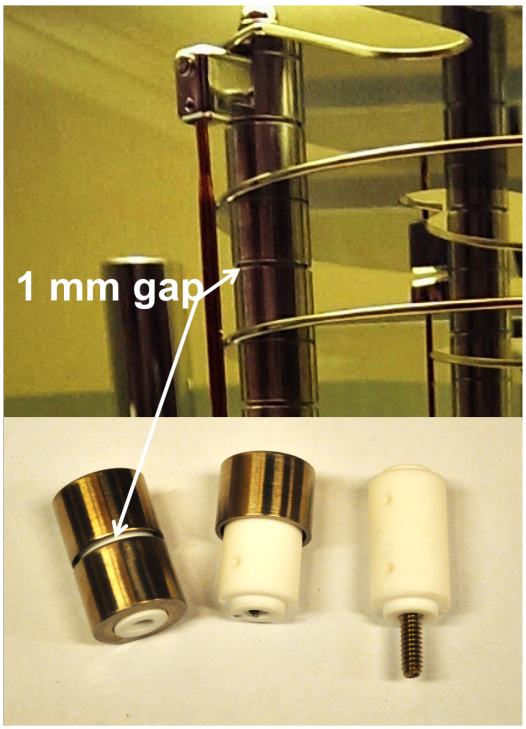

Figure 3.7: Zoomed-in view of the supporting column (top) and the ceramic separators with and without the metal sleeves (bottom).

Because the bottom electrode is in direct contact with the front of the MCP ion detector, its voltage is set by the power supply for the ion detector. The other six electrodes are individually biased by daisy-chained Spellman MP5 high-voltage (HV) power supplies shown in Figure 3.8 and the connections between the electrodes and the power supplies are shown in Figure 3.9. Each power supply can output 0 to 5 kV and is controlled by a 0 to 10 V input voltage. Because these power supplies are in series, except the first power supply all the other ones are at high voltage. In order to control the HV power supplies at high voltages, we use five Ultravolt EFL30 isolated power supplies to deliver 24 V power voltages to the HV power supplies from the ground level. Through these isolators one can control

the HV power supplies and read out their monitoring voltages and currents. In between the electrodes and the power supplies, low-pass filters are installed to filter out the high-frequency noise from the power supplies because this noise can be picked up by the MCP read out system.

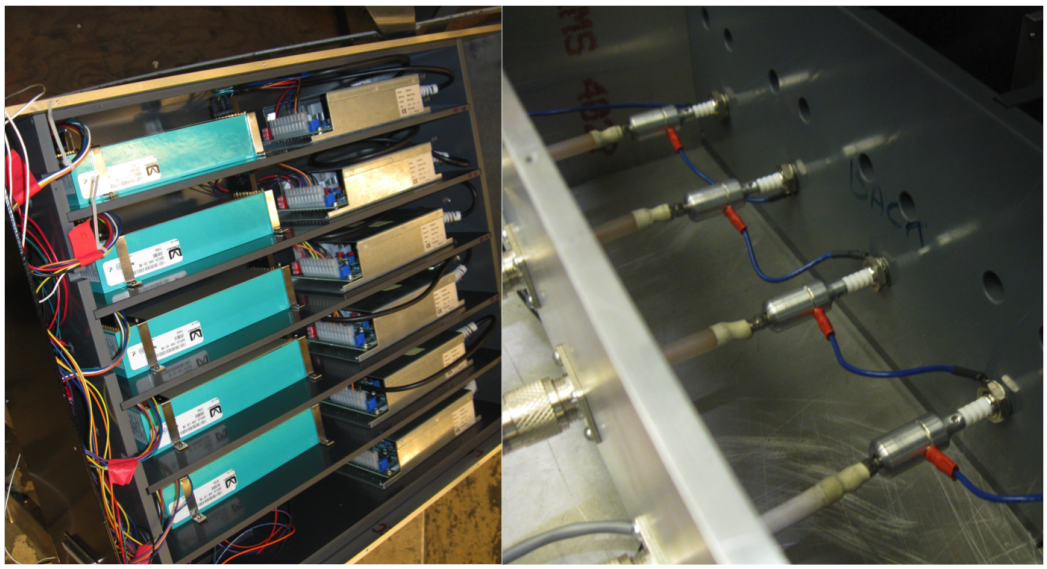

Figure 3.8: (Left panel) Power supply box for the E-field electrodes. The six aluminum boxes are the Spellman MP5 power supplies and the five green boxes are the Ultravolt EFL30 isolated power supplies. The lowest HV power supply is at the ground level, so there is no isolator for it. (Right panel) The HV power supplies are daisy-chained at the output compartment of the power supply box.

The HV system is controlled by a LabView program which sets the final voltages and ramping speeds for the HV power supplies. This program also monitors the leakage current from each power supply and trips the high voltage when the current level is above the threshold (typically set to 20 μA). The bias voltage on each electrode is set so that the electric field in the ion flight region is as uniform as possible. The calculation and optimization of the electric field is described in Section 4.13. The voltage of the bottom electrode (and the MCP front surface) is set at -2 kV, and typically the top electrode is biased at $+22$ kV.

To prevent the electrode system from sparking, all metal parts are machined with rounded corners and edges and the electrodes are electro-polished. The system is con-

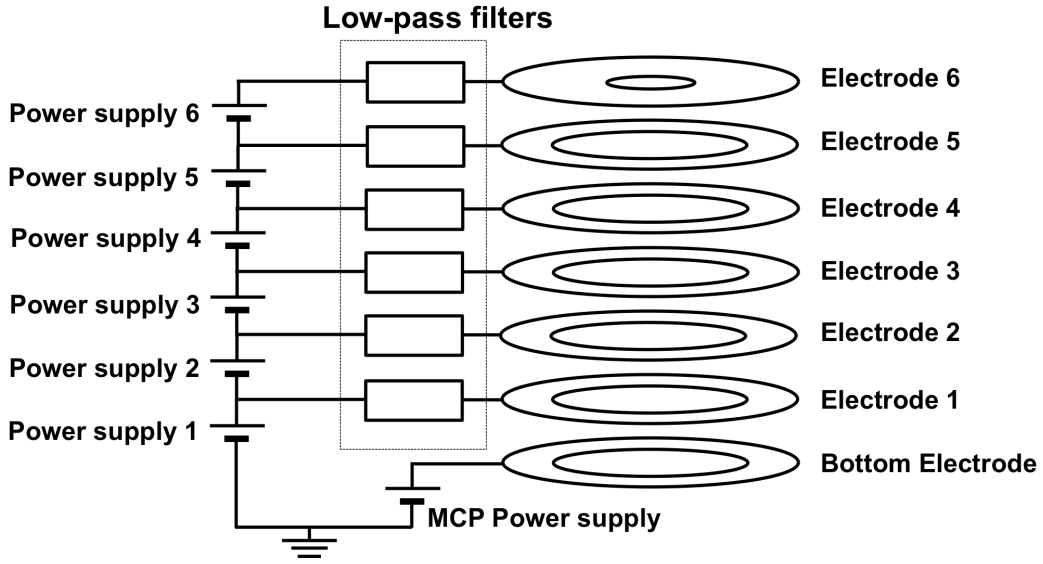

Figure 3.9: Schematics of the connections between the electrodes and the power supplies.

ditioned in argon plasma for 2.5 hours with the MCP detector's base turned off.

3.3 Recoil Ion detector

A micro-channel plate (MCP) stack made by Photonis [84] is mounted on the MCP holder. The MCP stack consists of 2 MCPs in the so-called Chevron configuration. The outer diameter of the MCP is 84 mm and the active area has a diameter of 75 mm. The pore diameter is 25 μm and the thickness of one MCP plate is 1.5 mm, so that the length-diameter ratio of each channel is 60 : 1. The MCP stack is held by a ceramic ring at the bottom, and the ceramic ring is bolted to the MCP holder. A 50 μm thick nickel grid mask is clamped between the MCP stack and the MCP holder. The width of each grid line is 250 μm and the pitch is 4 mm, and therefore the open area is 88%. This pattern provides the reference for calibrating the position response of the MCP. The inner diameter of the mask is 75 mm which sets the hardware fiducial cut on the MCP position spectrum. A photo of the MCP stack with the mask and the MCP holder is shown in Figure 3.10a. Between the front and the back of the MCP stack, 2000 V $\sim$ 2400 V bias[2] is applied. There

[2]The MCP works properly in this range of bias voltage. In our experiment, we bias MCP at 2371.2 V.

is a $\sim 8^\circ$ angle from the micro-channel to the normal direction of the surface. When the recoil ^{6}Li ions hit the entrance section of a micro-channel, it generates a few electrons on the channel surface. Due to the bias, the strong electric field accelerates these electrons down along the micro-channel, and each time the electrons hit the channel wall the number of electrons multiplies. When the electron cloud leaves the back surface of the MCP stack, the overall gain is $\sim 10^7$. Due to the loss of electrons, a positive signal is formed on the back surface of the MCP stack. This signal is read out and stops the TOF measurement. The front of the MCP stack is held at the same potential as the MCP holder and their potential is the lowest in the whole chamber. Therefore, if the ^{6}Li ion doesn't hit the micro-channels, the electrons it generates at the surface will fly upward without going into the channel, and thus no signal is generated. The total pore-opening area is about 50% of the MCP active area, so the efficiency of ion detection is typically 50%.

The delay-line anode made by Roentdek [85] is placed 8 mm below the MCP back surface for position read out. As shown in Figure 3.11 the delay-line anode consists of two sets of bare copper wires wound on a ceramic holder and perpendicular to each other. The outer one is for Y-coordinate read out and the inner one is for X-coordinate read out. The winding pitch is 1 mm for both set of wires and for each set there is a signal wire and a reference wire parallel to each other and separated by 0.25 mm. Both the signal wire and the reference wire are held at a potential $\sim$300 V more positive than the back of the MCP. Therefore, the electron cloud from the back of the MCP keeps flying towards the delay-line anode wires, and get collected by the two sets of signal wires. The potential of the signal wires is typically 20 V to 50 V higher than the potential of the reference wires in order to make sure the electrons are mostly collected by the signal wires. The charge collected on a signal wire propagates in both directions and eventually is read out at the two ends of the wire. The signal wire and the reference wire are coupled to a passive transformer at each end, and the transformer forms a differential signal between the two wires. Because the electrons are mostly collected on the signal wire, this differential signal is proportional to the charge that propagates to the input of the transformer. Any noise generated on both the signal wire and the reference wire is suppressed in the transformer. It takes $\sim$1 ns for the collected charge to propagate through one turn of the winding. Therefore 1 mm in the

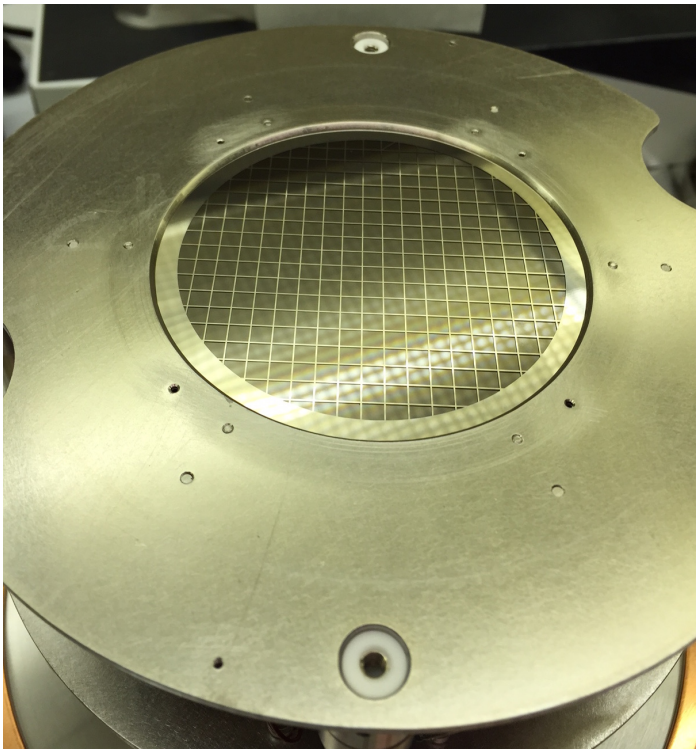

(a)

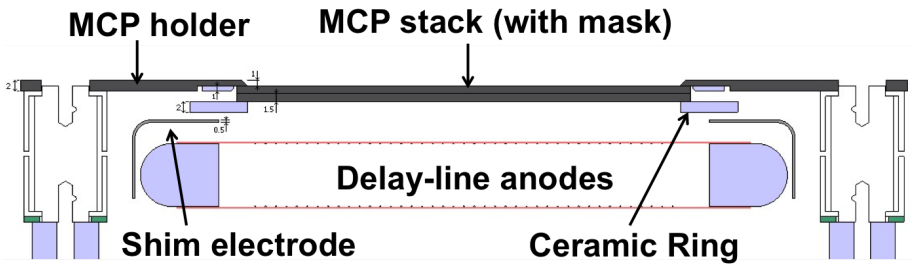

(b)

Figure 3.10: (a) Photo of the micro-channel plate with the calibration mask placed on top of it. (b) Section view of the MCP system schematics.

direction perpendicular to the delay-line wire corresponds to ∼2 ns time difference between the two signals read at the ends of the wire. The position where the electron cloud hits the

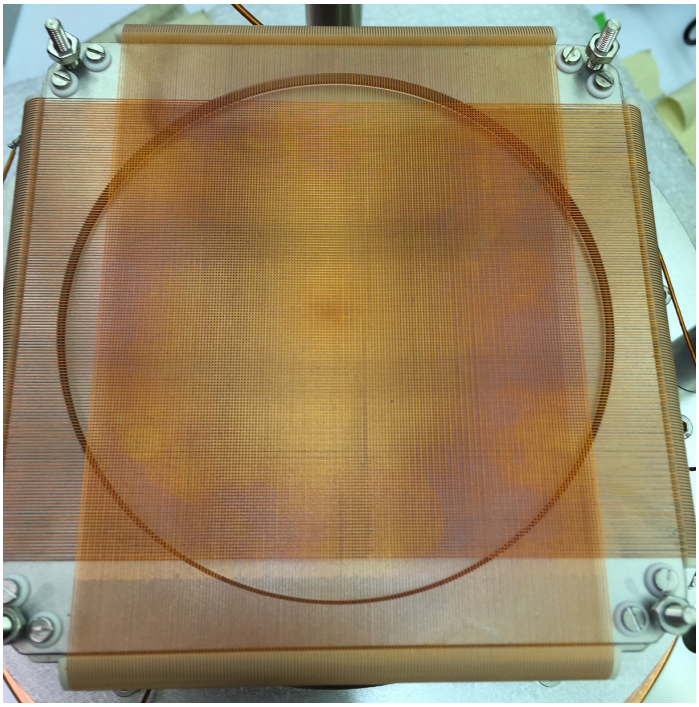

Figure 3.11: Delay line anodes.

delay-line anodes is reconstructed by

$$X = \frac{TX_1 - TX_2}{2 \text{ ns/mm}},$$
$$Y = \frac{TY_1 - TY_2}{2 \text{ ns/mm}}, \tag{3.3}$$

where X and Y are the electron cloud position in millimeter and TX_1, TX_2, TY_1, TY_2 represent the time of each signal readout in nanosecond.

The distance between the back of the MCP and the delay-lines are chosen so that the electron cloud expands to a few millimeters before it hits the delay-lines, so that the electrons are collected on three winding loops on average. The signal time read at the end of the wires is therefore the average time of the hits on the multiple winding loops. This averaging gives a better timing resolution and thus a better position resolution. The typical position resolution of the delay-line anodes is better than 100 μm. Also, it is desirable to make the electric field between the back of the MCP stack and the delay-line anodes uniform so that the electron cloud is flying perpendicularly to the delay-line anode surface without

deviation. However, the electric field near the edge of the MCP stack is not uniform, so an extra electrode is placed in between the back of the MCP stack and the delay-line anodes in order to shim the fringe field. The non-perfect shimming of the field can cause distortion in the position reconstruction near the edge of the MCP. These distortions can be corrected by the calibration procedure described in Chapter 4.

The MCP holder is fixed at -2000 V as required by the ion-accelerating field. The voltages applied to the components of the ion detector system is listed in Table 3.2. The voltages of the front of the MCP stack, the back of the MCP stack, the shim electrode, the delay-line signal wires and the delay-line reference wires are supplied by a two-channel HV power supply NHQ-203 through a voltage divider. All MCP signals are read through decoupling capacitors, because they are at high voltage. The signal from the back of the MCP stack is inverted and then amplified by a fast amplifier Ortec 200C. The four anode signals are amplified by a four channel fast amplifier Ortec 420C. The gain of all these amplifiers is 20. Then the output signals from the amplifiers are sent to the data acquisition system.

Electrode	Voltage (V)
MCP Front	-2000
MCP Back	371.2
Shim Electrode	400.0
Reference Wire	761.5
Signal Wire	815.8

Table 3.2: Voltages of the ion detector system.

3.4 Cycle control system

In order to measure the background from the non-trapped ^{6}He decays *in situ*, we separate each measurement cycle into foreground period and background period[3]. During the fore-

[3]This development was not implemented in the run in October 2015, *i.e.* the background period is 0.

ground period the MOT-2 trapping lasers are turned on, and during the background period the MOT-2 trapping lasers are turned off. The push beam is pulsing at 4 Hz during the whole cycle. Therefore, the amount of non-trapped ^{6}He stays similar during the background period. At the first push beam pulse in a cycle, a time-reference (Time Ref.) pulse is sent to the DAQ system. The time difference between the decay-event triggering and the time stamp of the latest time-reference signal determines the temporal position of this event in the cycle. The cycle scheme is shown in Figure 3.12.

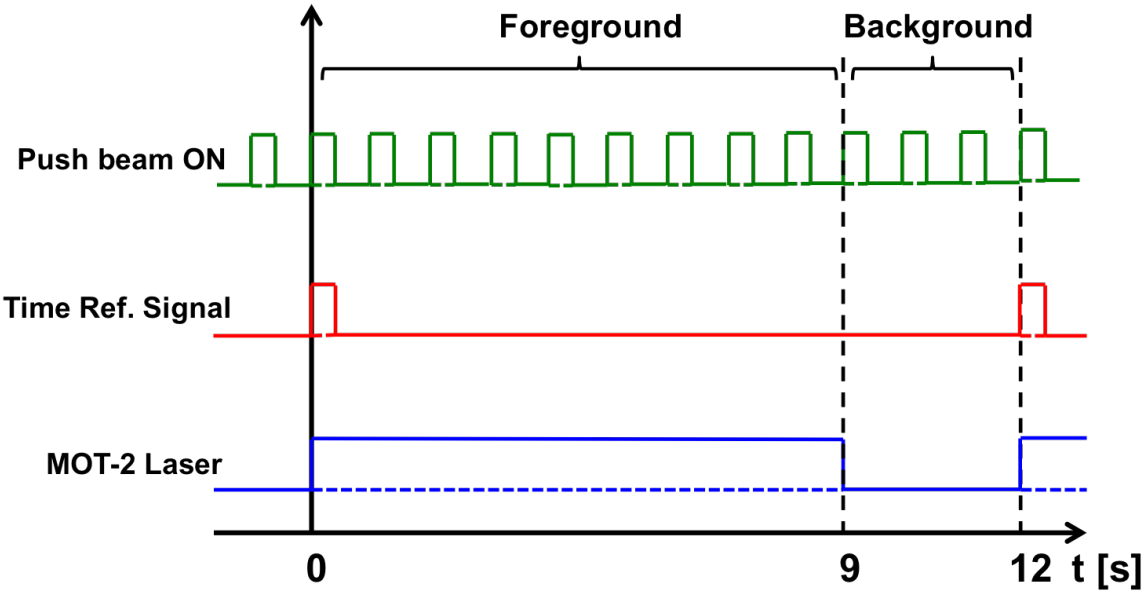

Figure 3.12: Cycle scheme of the pushing beam, time-reference signal and MOT-2 laser. High-level in each square wave indicates ON status. This example scheme assumes 9 s foreground and 3 s background period.

The cycling is controlled by a LabView program that sends TTL signals to the controller of the push beam, MOT-2 beam, etc. This program also controls the detailed timing of the pushing procedure, like opening the shutter between MOT-1 and MOT-2, pre-cooling of the MOT-1 before pushing, etc. A detailed description of this system can be found in Reference [44]. Concerning the data analysis, the events that happen when the transferred atoms are still in flight before being captured are blocked in the data analysis. Typically, the blocked period starts from the push beam pulse and lasts for 30 ms.

3.5 Nitrogen-laser for ionizing the trapped atoms

It is useful to ionize the trapped neutral atoms in the MOT and measure the TOF of the photoions. By comparing the TOF values of the photoions in different voltage settings to the simulated results, the accuracy of the electric-field calculation and the MOT Z coordinate determination can be tested (see Section 4.13.5). The photoions can also be used in MCP response calibrations (see Section 4.10.2).

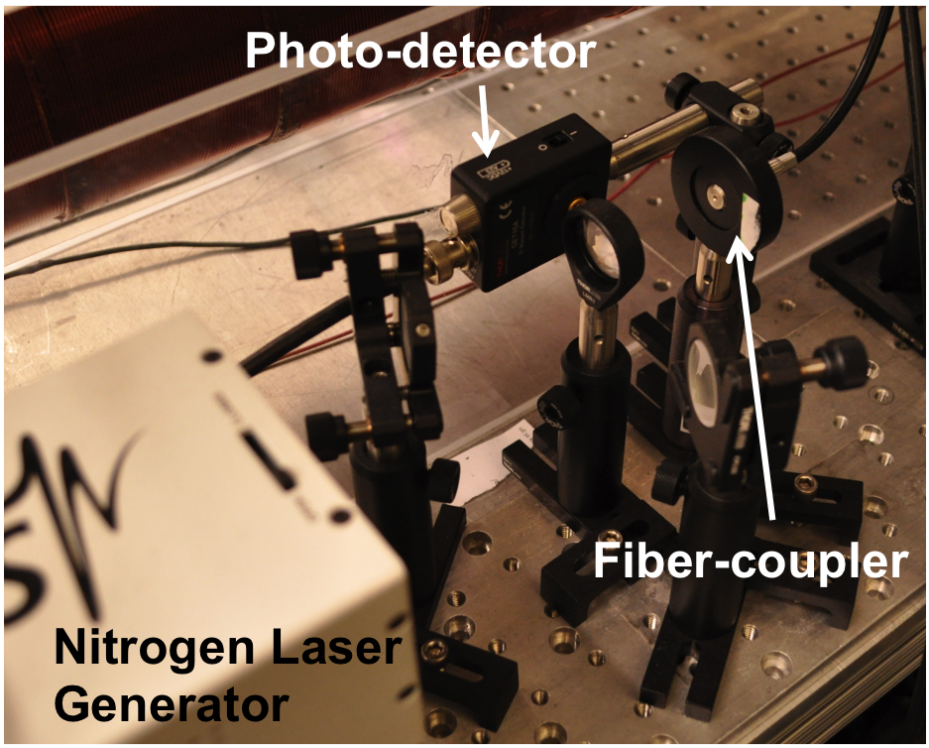

Figure 3.13: Nitrogen laser generator.

We use a pulsed beam from a 337.1 nm nitrogen laser to ionize the trapped helium atoms. The nitrogen laser system is shown in Figure 3.13. The nitrogen laser pulses are generated by a NL-100 laser made by Stanford Research Systems (SRS). The nitrogen laser has a beam profile 3 mm $\times$ 7 mm, and it is focused into an optical fiber and then delivered to one view port on the MOT-2 chamber. At the view port, the light output from the optical fiber is re-focused to the MOT position using a lens. The width of the laser beam

is about 2 mm at the MOT position. The angle of the optical fiber output is adjusted so that the output laser beam intercept with the atom cloud in the MOT. A photodetector (Thorlab Det10A Si Detector) is mounted near the fiber coupler at the input side of the optical fiber to detect the scattered photons from the nitrogen laser. The signal from the photo-detector is read by the data acquisition system and it starts the TOF measurement for the photoions.

The pulse width (FWHM) of the nitrogen laser is less than 3.5 ns, and the rising edge of the photo-detector pulse is ∼8 ns. The laser wavelength is 337.1 nm, so the photon energy is not enough to ionize the metastable ^{6}He atoms in the 2^3S_1 state but enough to ionize the helium atoms in the 2^3P_2 state. Therefore, the photoionization rate depends on the population of the 2^3P_2 state helium atoms. When the helium atoms are trapped, they are constantly cycling between the 2^3S_1 state and the 2^3P_2 state in the trapping-laser field, so there is always some atoms in the 2^3P_2 state, depending on the trapping-laser power and frequency detuning. When the number of atoms in the 2^3P_2 state is high, multiple ionizations are observed (see Section 4.10.2). During the experiment, the nitrogen laser is pulsed at 20 Hz.

3.6 Data acquisition (DAQ) system

3.6.1 Introduction to the FASTER system

We use the Fast Acquisition System for nuclEar Research (FASTER) [86] developed at LPC Caen[4] as our data acquisition system. FASTER is a modular digital data acquisition system based on a synchronized tree model. Briefly speaking, the incoming signal is continuously sampled by the *daughter board* at its sampling rate, and then the daughter board sends this stream of time stamped samples to the *mother board* for software filtering, shaping and trigger-decision making. Then the mother board sends the calculated information of the signal to the front-end computer, like integrated charge, trigger time and peak value of a pulse. The computer uses these time stamped data packets to build grouped events from different channels according to a given group window and logic scheme, and these data

[4]Laboratoire de Physique Corpusculaire de Caen

are subsequently written to the hard drive. One can also by-pass the grouping building module and write all data. FASTER is a gate-free system because each channel makes its own decision on triggering and the coincidence is built later at the front-end computer. There is no need to change the hardware if the coincidence scheme is changed. Moreover, the polarity, dynamic range, and filtering parameters are also tuned by software, so more versatile algorithms can be developed to improve the data quality while some of these algorithms are very difficult to implement by hardware.

In this experiment, we used six FASTER modules mounted on a microTCA[5] crate. A controlling module communicates to the front-end computer through an ethernet cable and provides a 500 MHz clock to all boards in the crate. All modules in the same microTCA crate are synchronized. Each FASTER module has one SYROCO-AMC [86] mother board, and each mother board has two CARAS [86] daughter boards, and each daughter board has two channels. A CARAS board samples the input signal at the clock frequency and digitizes it into a 12-bit integer. The CARAS boards on the first two modules are configured as QDC-TDCs[6] [87] and assigned for fast signals like the MCP signals and the PMT signals. The rest of the CARAS boards are configured as ADCs[7] [88] and assigned for slower signals like the MWPC signals. The detailed signal assignment at the DAQ crate is shown in Table 3.3.

	QDC		ADC			
	Module 1	Module 2	Module 3	Module 4	Module 5	Module 6
Ch1	PMT Dynode	MCP X1	MWPC X1	MWPC X5	MWPC Y3	MWPC A1
Ch2	N_2-Laser	MCP X2	MWPC X2	MWPC X6	MWPC Y4	MWPC A2
Ch3	MCP Back	MCP Y1	MWPC X3	MWPC Y1	MWPC Y5	LED
Ch4	PMT Anode	MCP Y2	MWPC X4	MWPC Y2	MWPC Y6	Time Ref.

Table 3.3: Signal assignment at the DAQ crate.

[5]Telecommunications Computing Architecture

[6]QDC: charge-to-digital converter. TDC: time-to-digital converter.

[7]ADC: analog-to-digital converter

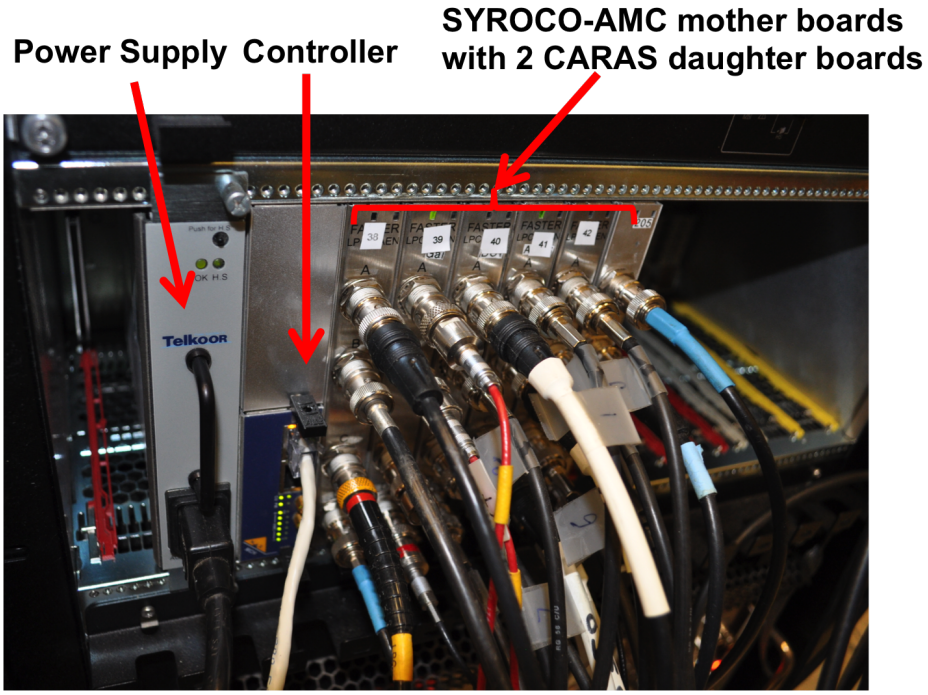

Figure 3.14: The microTCA crate and the FASTER acquisition system. Installed modules (from left to right) are power supply, controller, and six FASTER modules with one SYROCO-AMC mother board and two CARAS daughter boards.

3.6.2 QDC channels

The signal processing is done on the mother board by the FPGA[8] firmware. The firmware consists of several data processing software modules. The digitized wave forms are sent to a dynamic baseline restoration (BLR) module. This module has three important setup parameters: the threshold, the blocking gate length, and the low-pass filter frequency cut. In this module, the *pulse range* is defined as the period when the input signal is above the threshold plus the time corresponding to the blocking gate immediately after this period. During the pulse range the baseline restoration module is disabled. Outside the pulse range, the wave form is processed by the low-pass filter and its output is set as the baseline. The wave form with the baseline subtracted is fed into the trigger module and the charge

[8]Field-programmable gate array

integration module. The trigger module applies the Constant Fraction Discriminator (CFD) algorithm and sends the trigger time into the output data stream. The charge integration module integrates the wave form in a given window and outputs the result. Up to four integration windows can be used, and thus one can determine four integrated charges from one pulse. During the charge integration windows, the trigger module is disabled, and thus it cannot re-trigger. We used the first charge integration window for the charge measurement and the second charge integration window to set a dead time for that channel.

The input impedance of each QDC channel is set to 50 Ω. Because the coincidence event builder reduces most of the noises in single channels, we set the trigger threshold of each channel right above the electronic noise. The details about the setups of the baseline restoration, the constant discriminator, and the charge integration windows are discussed in Chapter 4.

3.6.3 ADC channels

Similar to the QDCs, the digitized waveforms after the baseline restoration are sent to the trigger module and a peak-sensing module. For the trigger module, a high pass filter is applied to the input waveform, and then a leading-edge discriminator algorithm determines the trigger time from the filtered waveform. No CFD algorithm is applied to the ADC modules, so the timing resolution is limited to the sampling period, which is 2 ns in this experiment. For the peak-sensing module, a CR-RC^4 shaping algorithm[9] is applied to the input waveform and the peak value of the result waveform is sent to the output stream.

Since the cathode amplifier cannot drive 50 Ω load, the input impedances of channels for cathode signals are set to 1 kΩ. The input impedance of other channels are set to 50 Ω. The detail setups of ADC channels are discussed in Chapter 4.

---

[9] A CR-RC^4 shaping circuit consists of one CR circuit (differentiator) and four following RC circuit (integrator). The CR-RC^4 shaping algorithm calculates the output waveform based on the principle of the CR-RC^4 circuit.

3.6.4 Data structure and the online histogram viewer

Trigger times and integrated charges (or peak values) are sent to the front-end computer to build grouped events. The group scheme can be configured using a boolean expression. For the measurement of $a_{\beta\nu}$ in ^{6}He decay, the group scheme is

(PMT Anode and MWPC Anode-1 and MWPC Anode-2)
or (MWPC Anode-1 and MWPC Anode-2)
or MCP Back or N_2-Laser or Time Ref. or (PMT Anode and LED),

which means that the PMT-MWPC coincidence signal or the MWPC signal or the MCP-back signal $\cdots$ can trigger the grouping. The group window is set to 300 ns, meaning within any 300 ns window the above boolean expression is *true* it is considered as a grouped event. One can also set a *follower list* and a *follower window*. Provided the group boolean expression is true, all channels in the follower list and the boolean expression are also grouped if they are triggered within the follower window. The follower window extends on both sides of the group window. In our experiment, the channels in the follower list are:

four MCP delay-line anodes and 12 MWPC cathode strips,

and the follower window is set to 2000 ns.

All grouped data are written to the hard drive in binary format. C libraries are provided for programmers to read out and decode the data file. Meanwhile, the data collected by FASTER are also sent to the program Root Histogram Builder (RHB), which is an online data analysis tool. The RHB can be used as an oscilloscope displaying the waveforms of not only the raw signal from each channel but also the filtered waveforms from different shapers. One can also use script files to configure the RHB and calculate derived quantities, construct histograms, and apply conditions for histogram filling. Important histograms like the TOF histogram, β spectrum and MCP image are constructed in the online histogram builder, so that it is easy to monitor the status of the experiment and discover anomalies.

Chapter 4

DETECTOR PERFORMANCE AND CALIBRATION

In order to make sure that the detectors described in Chapter 3 have fulfilled the design requirements, calibration experiments are conducted before, during, and after the $a_{\beta\nu}$ measurements.

In this chapter, the performance tests for each detector are described first, and then detailed detector responses are discussed. Based on the behaviors of the detectors, high-precision calibration schemes are developed. The β telescope is described first, and then the MCP ion detector. Following them, the ion-accelerating field measurements, MOT position measurements and absolute timing calibrations are discussed. Finally, measurements of the TOF spectral shape for the background generated by non-trapped ^{6}He decays are introduced.

4.1 MWPC performance test

4.1.1 Overall gain measurement

The anode of the MWPC is biased at +2850 V during normal operation, while the cathodes are grounded through amplifiers. We simulated the electric field using GARFIELD [89]. The equipotential surfaces near the center wire are drawn in Figure 4.1. The electron multiplication only happens if the electric field is stronger than the threshold for the counting gas ($\sim 4.8 \times 10^4$ V/cm for the gas we use), and in our case the radius of the region of multiplication is $\sim$30 μm. Within the region of multiplication the electric field is cylindrically symmetric, and therefore the gain formula for a *single-wire proportional tube* [90] is still valid. The calculated gain for our MWPC is about 8×10^4.

The actual gain is difficult to measure by pulse height analysis as is done in Reference [75]. The reason is that the avalanche also induces opposite signals on the adjacent anode wires, and these signals also propagate to the ends of the charge division chains, canceling part of

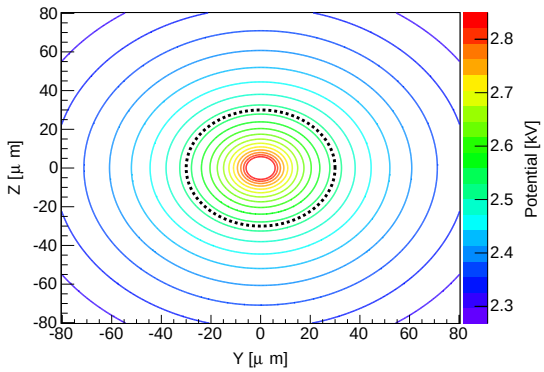

Figure 4.1: Simulated equipotential surfaces near the center wire and the region of multiplication (dashed line).

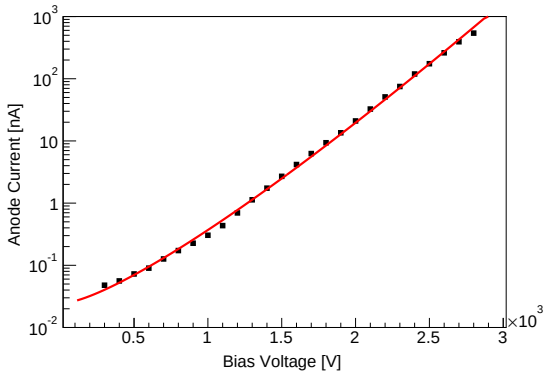

Figure 4.2: Measured $I_A - V$ data (black squares), fit to Equation 4.1 (red curve).

the main signal. This cancelation ratio is hard to measure directly. Instead, we measured the anode current at different bias voltages, and fit the curve to [90]

$$ln(I_A) = c_1 V(ln(V) + c_2) + c_3 \tag{4.1}$$

where I_A is the anode current, V is the anode bias voltage, and c_i's $(i = 1, 2, 3)$ are fitting parameters. The gain (multiplication factor) M is given by $M = I_A \times exp(-c_3)$. We put the MWPC assembly shown in Figure 3.2 into a test enclosure and place a 100 μCi ^{90}Sr source right next to the front window. The measured $I_A - V$ data in Figure 4.2 fits very well to Equation 4.1 and the fit value for c_3 is -3.68, thus we estimate $M \sim 4.48 \times 10^4$ at a 2850-V bias.

The measured gain and the calculated gain are on the same order of magnitude but the measured gain is lower than the calculated one. It is not surprising because the calculation assumes the gain is uniform across the whole MWPC. In fact, near the end of the wires the electric field is weaker, so the gain is lower. A high precision determination of the absolute gain of the MWPC is not needed in this experiment as long as it is high enough so that the detection efficiency is high. The non-uniformity of the MWPC gain is accounted for in Section 4.4 in order to perform energy deposition measurements.

4.1.2 MWPC signal processing

The MWPC signals (2 from anode amplifiers and 12 from cathode amplifiers) are read out by FASTER ADC modules. Signals from each channel are shaped by a high-pass filter with 60 ns shaping time (fast shaper) and a $CR - RC^4$ shaper with 500 ns shaping time (slow shaper). The timing of the signal is determined by a leading-edge discriminator applied to the fast shaper, while the signal size is determined by the peak value of the slow shaper output. The pulse shapes for the fast and slow shapers measured by the FASTER oscilloscope module are shown in Figure 4.3.

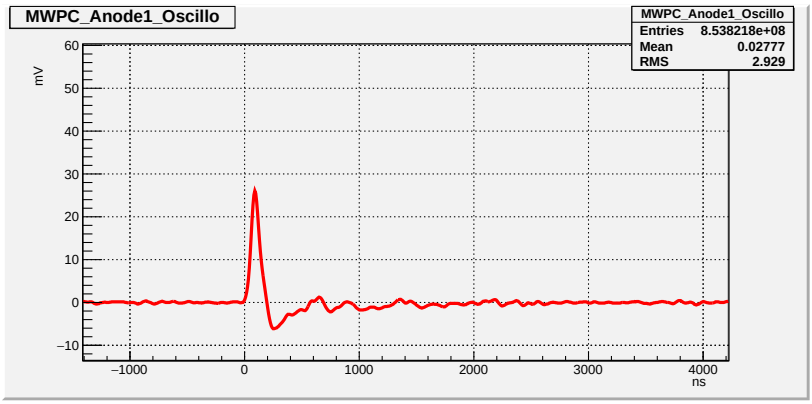

(a) High-pass filter channel.

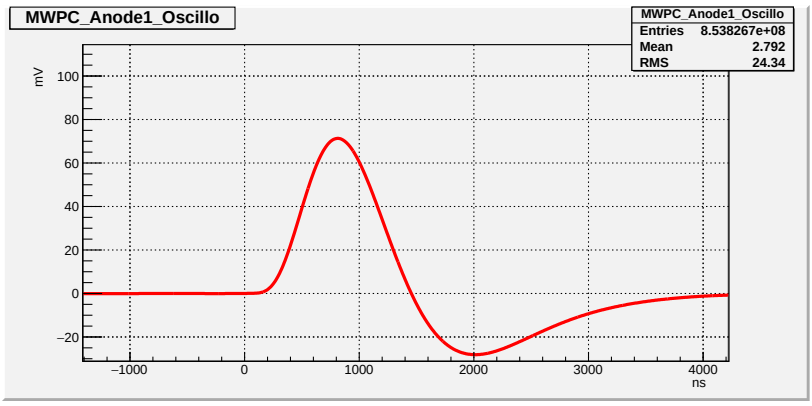

(b) $CR - RC^4$ shaper channel.

Figure 4.3: Typical pulse shapes from the MWPC-anode $CR - RC^4$ shaper channel.

In order to achieve a high detection efficiency, the trigger threshold for each channel

is set just above its electronic noise so that the noise trigger rate is below ∼100 Hz. The energy deposition readout is given by the sum of the anode signals. The hit position readout is calculated based on Equation 3.1 and Equation 3.2.

4.1.3 Energy deposition and position response test

The energy and position response of the MWPC are tested using a ^{55}Fe source. Its 5.9 keV K_α X-ray following the electron capture generates a localized ionization cloud in the MWPC gas, and it is ideal for both energy and position calibrations of the MWPC. The anode signal sum spectrum is plotted in Figure 4.4a. The broad peak at $x = 70$ in Figure 4.4a corresponds to the full energy of the X-ray from the source, and the bump near $x = 40$ corresponds to the argon escape peak. At first look, the resolution is not high enough to resolve these two peaks. As can be seen in this figure the electronic noise level is below $x = 4$. There is no need to apply software threshold in order to remove the electronic noise, because the coincidence between the anode signals and cathode signals are always applied when reconstructing its energy deposition and position readout, and the electronic noise is further suppressed. The cathode signal sum spectrum (Figure 4.4b) looks similar to the anode signal sum. Figure 4.4c shows a linear correlation between the anode-signal sum and the cathode-signal sum, which agrees with the fact that the total charge induced on the cathodes should be proportional to the total charge collected on the anode. There are two bands in the correlation plot of the top cathode-signal sum and the bottom-cathode signal sum (Figure 4.4d). The ion cloud produced by the avalanche is not symmetric, but skewed to the position of the initial ionization generated by incoming high-energy particles. Therefore, the ion cloud induces less signal on the farther cathode because of the shielding effect of the anode wires. Therefore, the double-band structure in Figure 4.4d is expected.

The position spectrum of the MWPC (MWPC Image) is shown in Figure 4.5a, where the X coordinate is reconstructed by the bottom cathode and the Y coordinate is reconstructed by the anode. The most striking feature of the MWPC image is its granular structure. The projections onto Y and X axes are plotted in Figure 4.5b and Figure 4.5c. The peaks in the Y direction are expected because the avalanches only happen on the wires, and the charge

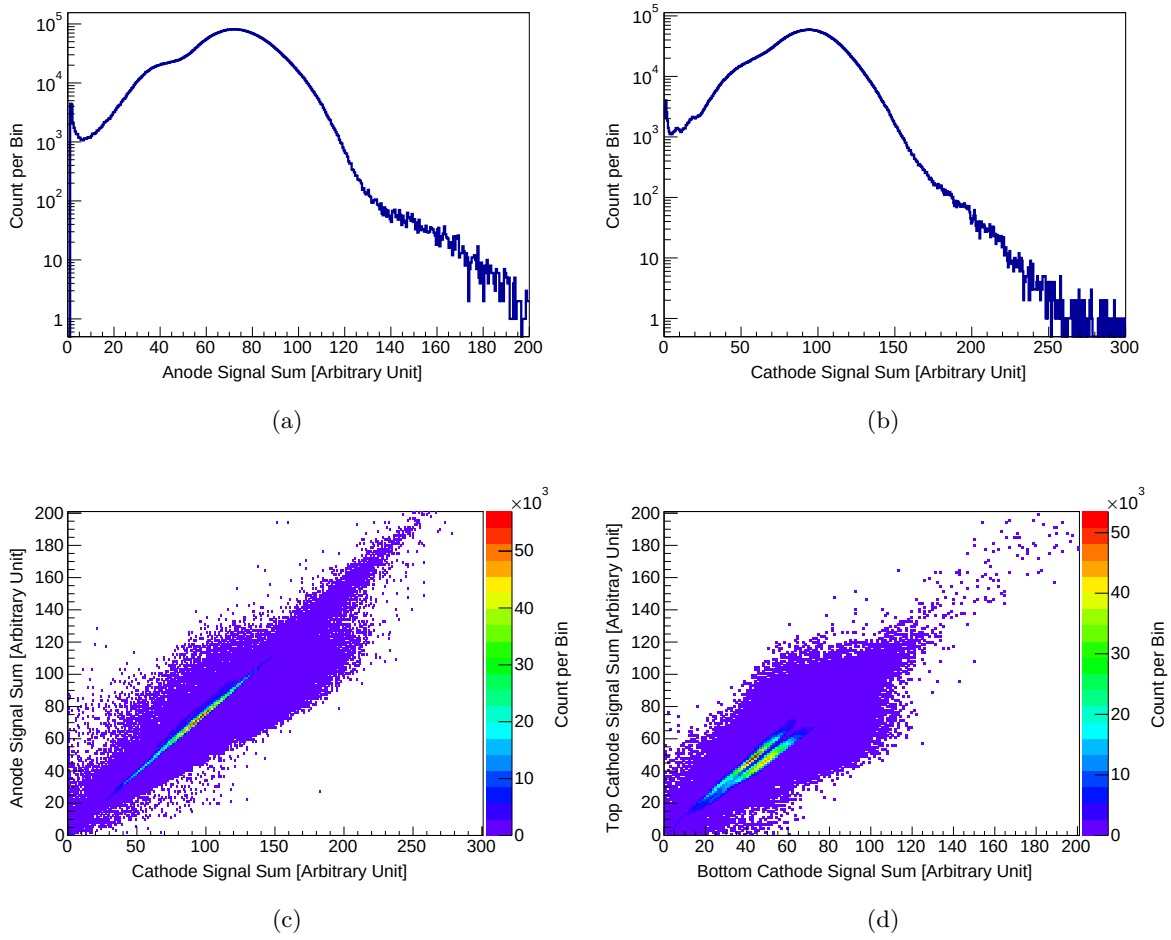

Figure 4.4: (a) MWPC anode-signal sum. (b) MWPC cathode-signal sum. (c) Correlation between cathode-signal sum and anode-signal sum. (d) Correlation between the bottom cathode-signal sum and top cathode-signal sum. See text for the explanation of the double-band structure in (d).

divider on the anode is supposed to give the position of the triggered wire, which is discrete. In fact, the peaks in the center region of the MWPC image Y projection are close to the real wire positions (*i.e.* ± 1 mm, ± 3 mm,$\cdots$). When the incoming X-ray hits the space between two anode wires, the initial ionization may drift to two wires and trigger both of them, then the charge divider may give a position readout at the center of two wires. This model can explain the minor peaks in between the major peaks in the MWPC image Y projection.

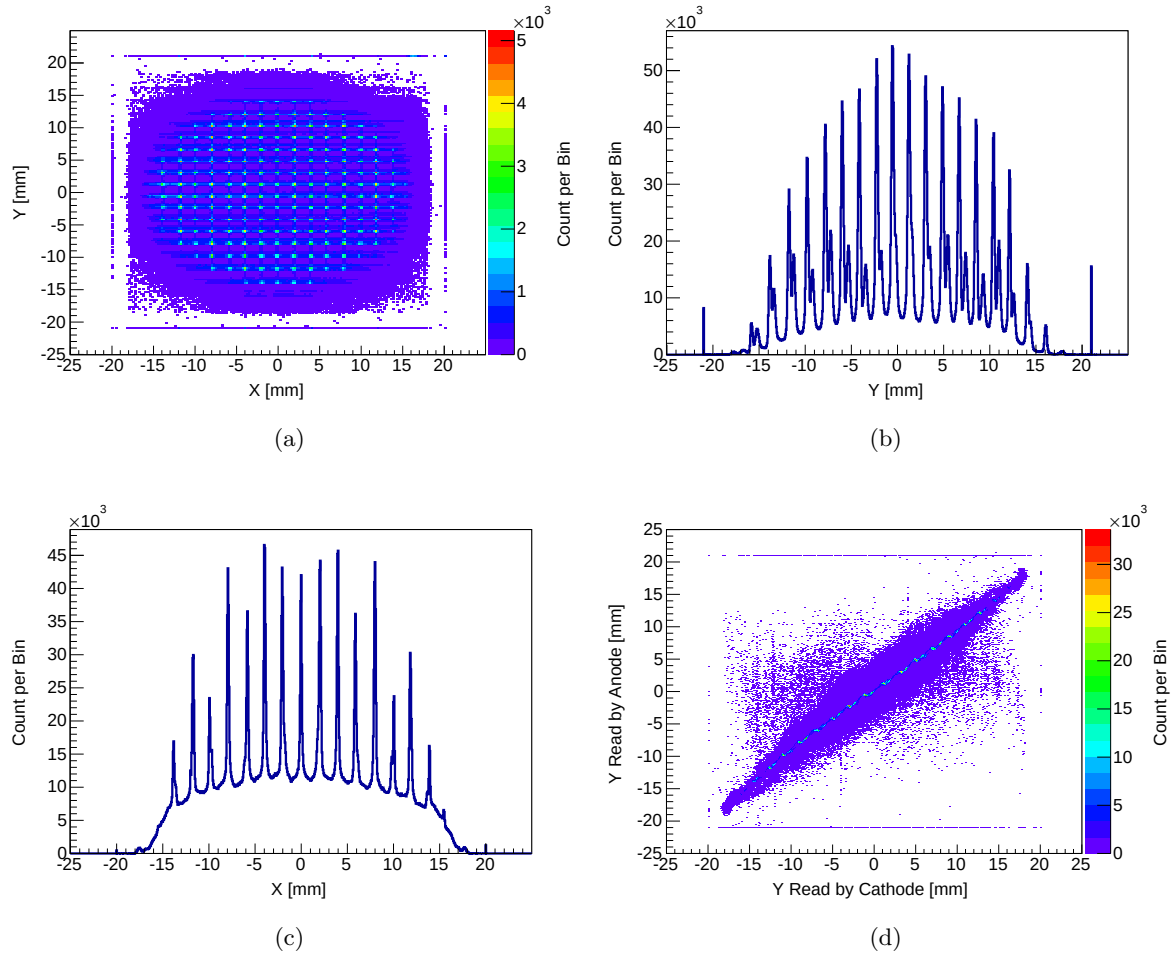

Figure 4.5: (a) Uncalibrated MWPC-position spectrum (b) Uncalibrated MWPC-Image Y projection (c) Uncalibrated MWPC-Image X projection (d) Correlation between the anode-reconstructed Y and the cathode-reconstructed Y

This effect can be reproduced in the Monte Carlo simulation described in Chapter 5.

Peak structure also exists in the MWPC-image X projection. The peak positions are at 0 mm, ± 2 mm, ± 4 mm, $\cdots$, which are the centers of the cathode wire spacings. In the naive model of the MWPC the electric field of the drift region (from the cathodes to the planes $\sim$1 mm away from the anode) is uniform and there is no electric field outside the cathodes. The X-ray source uniformly illuminates the whole MWPC volume and the multiplication can happen at any position along each wire, so the event distribution along

the wire direction (X direction) should be uniform. This contradicts with the peak structure in the MWPC-image X projection. This inconsistency lead to our discovery of the cathode focusing effect. The detailed explanation of the peak structure and a more realistic modeling of the electric field in the MWPC are discussed in Section 4.2.

Finally, Figure 4.5d shows the correlation between the anode-reconstructed Y coordinate and top cathode-reconstructed Y coordinate. The overall relationship between the two readings are proportional, and this validates both methods. In principle, the cathode reading is sensitive to the ion cloud distribution and it can tell the different initial ionization positions even though these ionization electrons eventually all hit the same wire. By contrast, the anode charge divider cannot tell this difference. This explains the step structures in Figure 4.5d near wire positions. However, the smearing from the main proportion band in Figure 4.5d is caused by the incorrect reconstruction by the cathode if some cathode wire groups are below the trigger threshold.

4.2 Cathode focusing effect of the MWPC

Since the cathode wires are held at ground potential, one may expect no electric field outside the cathode due to static electric shielding. However, in reality the wires are so thin and sparse that the field is not fully shielded. We use GARFIELD [89] to calculate the electric field and the equipotential surfaces are shown in Figure 4.6 (wires are all at their rated positions in the GARFIELD simulation). Clearly, the 100 V equipotential surface is below the bottom cathode wires, and the electric field there is still as strong as $\sim$100V/cm. The field near the cathode is far from being uniform. Therefore, electrons produced outside the cathodes are attracted towards the anode and their drift lines are focused towards the center between two cathode wires by the non-uniform field around the cathode wires. The electron drift lines are also simulated using GARFIELD. In this simulation, the initial electron positions are uniformly distributed on the plane 4 mm away from the bottom cathode wire plane. The electron drift lines and the final positions distribution are plotted in Figure 4.7. This focusing effect causes the peaks in Figure 4.5c. The initial electrons generated in between the cathodes and the anode do not drift across the cathodes and thus do not experience the focusing field. They form the smooth pedestal in Figure 4.5c. Similar

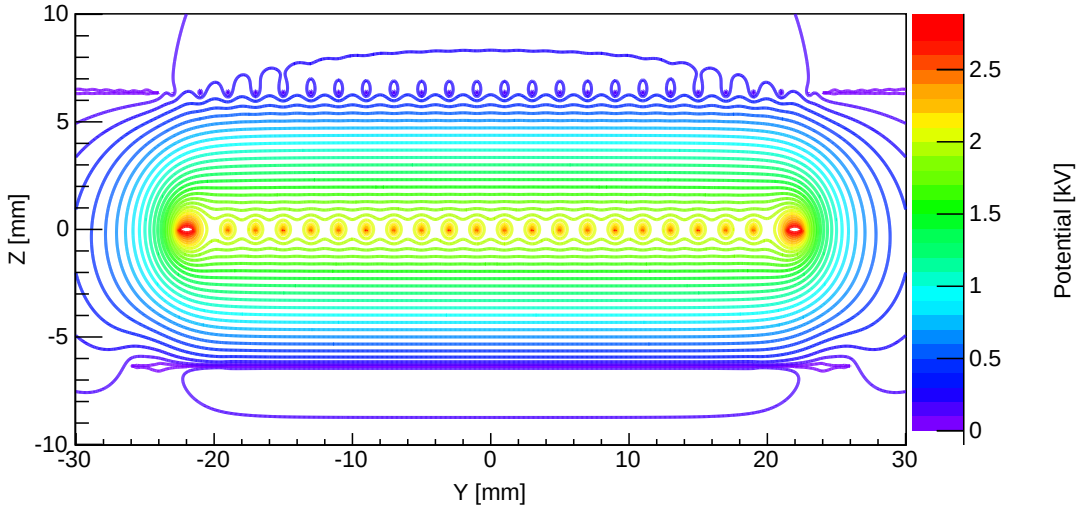

(a) Y-Z Plane, X=1 mm.

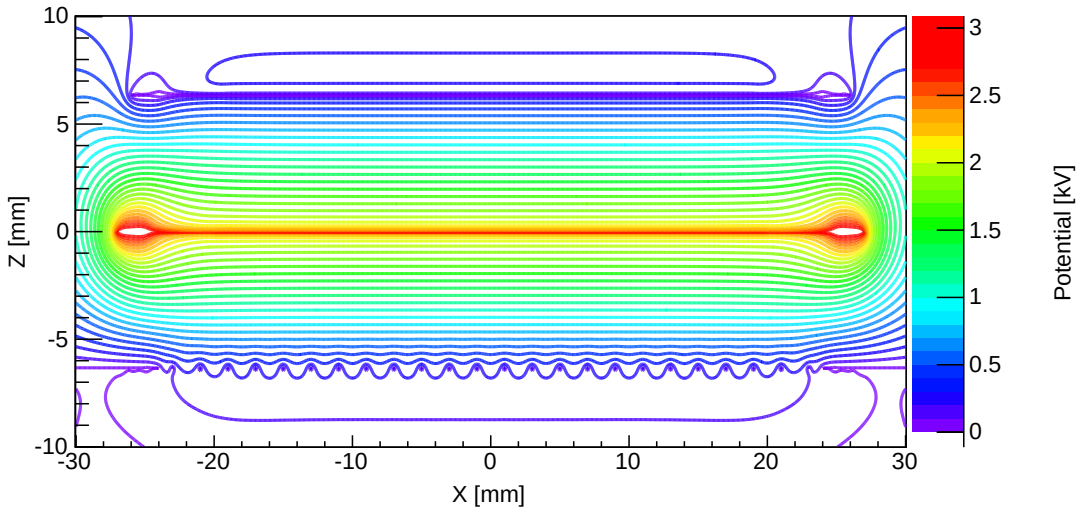

(b) X-Z Plane, Y=1 mm.

Figure 4.6: Equipotential surfaces from calculation using GARFIELD. Each line represents a change of 100 V.

effect also happens on the other cathode, but it focuses electrons to the center between two adjacent anode wires. When the electrons approach the anode wires, they are either collected all by one wire or split into the two adjacent wires. This doesn't affect the peak

structures in Figure 4.5b.

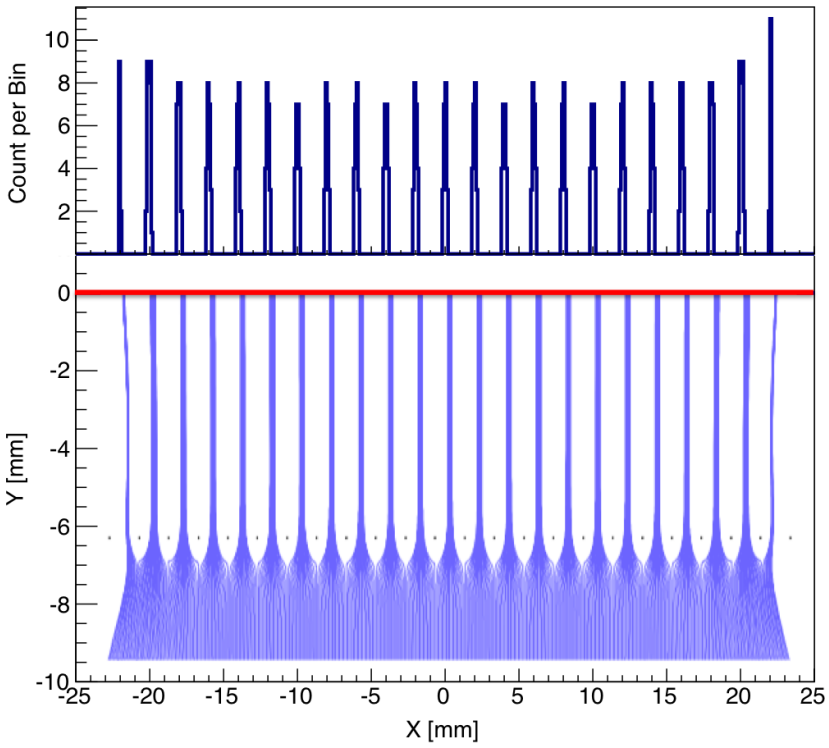

Figure 4.7: Electron drift lines and the distribution of final positions calculated with GARFIELD. The anode wire is indicated by the red line and cathode wires perpendicular to the plane are indicated by the black dots at $y = -6.35$ mm.

In order to confirm this explanation of the peaks in the X-coordinate spectrum, we covered half of the bottom cathode with a 0.5 mil thick mylar foil, which blocks the focused electrons generated below the cathode. This mylar foil doesn't attenuate the X-ray substantially or affect the electric field around the cathode wires. In this case, only the ionizations generated in between the cathode and the anode are detected. We did the same measurement and observed that on this half of the plane, the peak diminished. This phenomenon confirmed that the cathode focusing effect is the cause of the peaks in the X-coordinate spectrum. Furthermore, this cathode focusing effect of MWPC was also observed by the MuCap group and explained the high cathode transparency of back-drift ions in their Time Projection Chamber [91]. However, we provided a more direct observation and confirmation

of this effect.

The cathode focusing effect provides an easy way to calibrate the position response of the MWPC. As shown in Figure 4.7, in the region of interest [−14 mm,+14 mm], the electron drift lines after focusing are very straight, so the hit positions on the anode wire are well defined. In the GARFIELD simulation the hit positions of the focused drift lines are no farther than 10 μm away from wire spacing centers. The wire positions are accurate up to 250 μm. Thus, we used the peak positions in the MWPC position spectrum and the wire positions to correct the position reconstruction algorithm. Eventually, the position reading accuracy is limited by the wire position accuracy (250 μm).

4.3 MWPC position response calibration

In Figure 4.5a, the events at the edges of the MWPC image correspond to events in which only one anode(cathode) channel is triggered. These are considered invalid events and need to be ruled out. Moreover, if the number of triggered cathode wire groups is too few, the position reconstruction accuracy is poor. For the calibration run using ^{55}Fe source, the spectra of triggered wire number for both cathodes are plotted in Figure 4.8. Over 98% of the total events triggered at least 3 wire groups on the bottom cathode. Therefore, to validate one event we require that both anode channels and at least 3 wire groups on the bottom cathode are triggered in coincidence. The position of each valid event is corrected using the algorithm described below.

For the Y coordinate, the peak positions are determined and then their distances from the peak positions to their corresponding wire positions (peak-wire distance) are calculated. On an event-by-event basis, the Y coordinate readout is shifted by a distance which is a linear interpolation of the peak-wire distances for its adjacent peaks. After this correction, all peaks should line up with their corresponding wire positions. The correction is only done to events with non-corrected Y coordinate in the range [−15 mm,15 mm]. Events beyond this region are ruled out in the analysis.

For the X coordinate, different numbers of triggered wire groups result in different distortions in position reconstruction. Figure 4.9 shows the X-coordinate spectrum for each case where certain number of wire groups are triggered. For example, the 12 mm

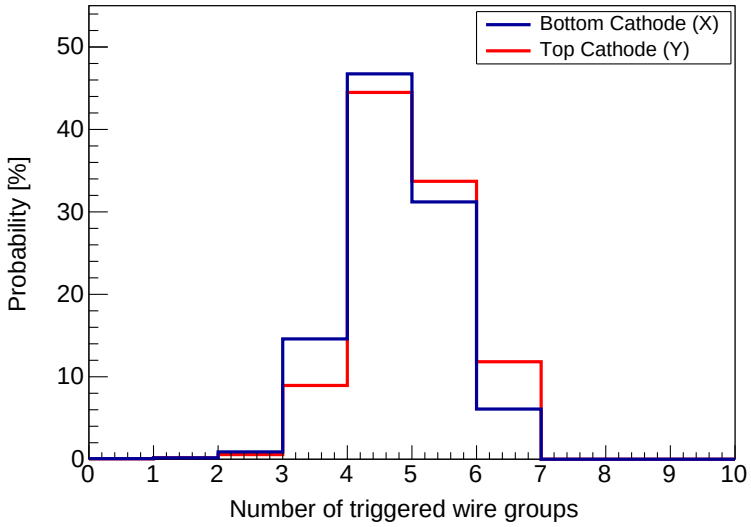

Figure 4.8: Probability distribution of triggered wire groups for the bottom and top cathodes.

peaks in the 4-triggered case and the 3-triggered case deviate from each other by 200 μm. Besides the differences in peak positions, the pedestal envelopes for these cases also have different shapes. The oscillations of the pedestal envelopes are due to a geometrical effect. Events that occur at the center of a wire group are more likely to trigger odd numbers of groups. On the contrary, events that occur in between two wire groups are more likely to trigger even number of groups. For example, one event occurring near -4 mm (the center of the third wire group) induces similar size of signals on wire groups 1 and 5. It's more likely for them to be both above the threshold, or both below the threshold. Therefore either five groups or three groups are triggered. This explains the trough at -4 mm for the 4-trigger case pedestal envelope.

Due to the envelope, there are missing peaks in the case where three wire groups are triggered, which makes the calibration difficult. Because in the trough region of the 3-trigger X-coordinate spectrum most of the events trigger four or more wire groups. Therefore, by removing the contribution from the wire group with the smallest signal size, one can turn a 4-trigger case to a 3-trigger case without affecting the position reconstruction algorithm

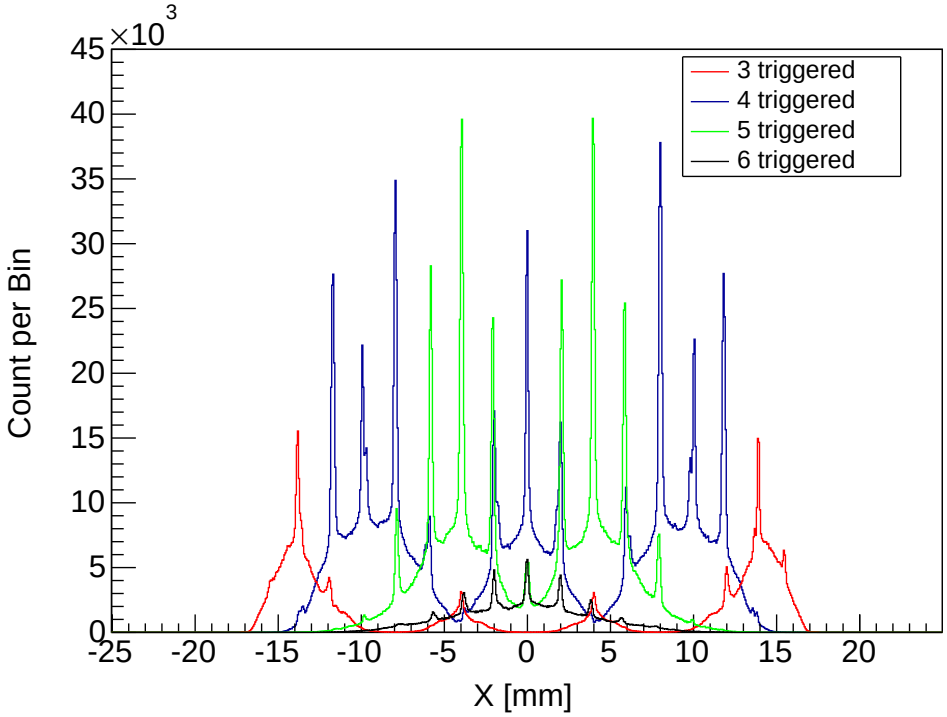

Figure 4.9: X-coordinate spectrum of the MWPC in the cases where 3, 4, 5, or 6 wire groups are triggered.

of the 3-trigger case. In this way, all events are using their first 3 largest-signal wire groups for the X-coordinate reconstruction, and the resulting X-coordinate spectrum is shown in Figure 4.10a. In the original trough regions (*i.e.* around -8 mm, 0 mm and 8 mm) of Figure 4.10a, one peak splits into two and there are gaps between the split peaks. To explain this effect, we take the gap at 0 mm as an example. If one event happens near this position, the induced charges on the wire group-3 and 4 are large while the ones on the wire group-2 and 5 are small but with similar sizes. It is not possible to conclude which of them is larger due to fluctuations. If only the first three largest-signal wire groups are kept, missing the wire group-2 or wire group-5 results in a large distortion in the X-coordinate reconstruction towards the negative direction or positive direction. These two cases correspond to the two split peaks near 0 mm which are supposed to be both at 0 mm. Similarly, Figure 4.10b and Figure 4.10c show the X-coordinate spectra for the cases where the four or five largest-signal

wire groups are used. Peak splitting also happens at -4 mm and 4 mm in Figure4.10b, which can be explained by the same mechanism. The wire splitting at 0 mm in Figure4.10c is too small to be observed so that it is ignored in the analysis.

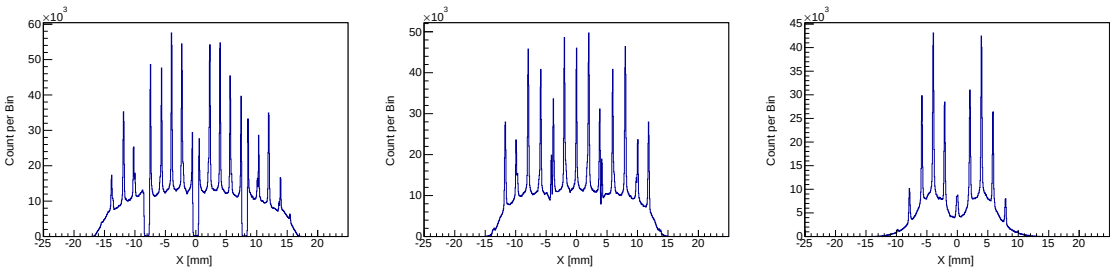

(a) (b) (c)

Figure 4.10: X coordinate spectrum of the MWPC in the cases where 3 (a), 4 (b), or 5 (c) wire groups are kept.

Based on Figure 4.11, a correction algorithm similar to that is used for the Y-coordinate correction is constructed for each case (with 3 or 4 or 5 triggered wire groups). The target positions for the peaks to move to are 0 mm, ± 2 mm, $\pm$ 4mm, $\cdots$. For those events with non-corrected X-coordinate reconstructions which fall in the gaps between split peaks, the corrected X coordinate will be exactly the target position. During the event-by-event based X-coordinate correction, we first determine the number of triggered wire groups, and then apply the correction algorithm associated with that number of triggered wire groups. We don't construct the algorithm for the 6-trigger case, and therefore if in the experiment one event triggered all 6 wire groups, we keep the first five largest-signal wire groups and treat this event as a 5-trigger case. Furthermore, in Figure 4.10c there are no peaks outside the range [-8 mm, 8 mm], so that these events cannot be corrected using the algorithm described above. Therefore, for these events we keep the first four largest-signal wire groups and treat them as a 4-trigger case. The same action is also applied to the events in the 4-trigger case beyond the range [-12 mm, 12 mm]. Eventually, in the 3-trigger case, events beyond the range [-14 mm, 14 mm] are rejected. This defines the cathode effective region.

After the calibration, the X-coordinate and Y-coordinate spectra are plotted in Fig-

ure 4.11a and Figure 4.11b. The peak positions are all aligned well with the expected positions. The deviations from the peaks to their expected positions are shown in Figure 4.11c and Figure 4.11d, and they are all less than 100 μm. Therefore, the position reconstruction accuracy is dominated by the wire position accuracy, which is 250 μm. Because the calibration is only done in the range [−14 mm, 14 mm] for the X direction and [−15 mm, 15 mm] for the Y direction, events outside this region should not be used in any analysis including the MWPC energy deposition calibration. This also defines the largest fiducial area of the MWPC. The calibrated MWPC image is drawn in Figure 4.12. Furthermore, in order to generate the cathode signals in the MC simulation as close to the measured one as possible, we saved the induced charge (signal size) distribution for every X coordinate (with a 0.125 mm spacing). For example, the induced charge distribution on the bottom cathode for $X = -0.1875$ mm is shown in Figure 4.13.

This calibration method is convenient since no collimated beams are needed. We only need to insert a radioactive source at the MOT position without changing other parts of the detector system or break the vacuum. Even for β particles that do not generate localized initial ionizations, these peaks are still visible, so the monitoring of the calibration is built into the data from the real measurement.

As a summary, most of the features of the MWPC position spectrum are explained. However, it is difficult to use a single number to quantify the resolution of the MWPC. For example, the incoming β particles generate many initial ionizations along their tracks and the position reconstruction for them can be very different depending on whether they are above or below the bottom cathode. Therefore, in the Monte Carlo simulation we take into account the detail physical processes like initial ion generation, cathode focusing effect, charge division and charge induction (see Chapter 5).

4.4 MWPC energy deposition calibration

In order to investigate the gain uniformity of the MWPC we plotted the 2D histograms of the event counts versus the anode signal sum and the X coordinate (Y coordinate) as in Figure 4.14. The signal size distribution for each position is revealed at the same time. At each wire position in Figure 4.14b the hottest spot corresponds to the full energy deposition

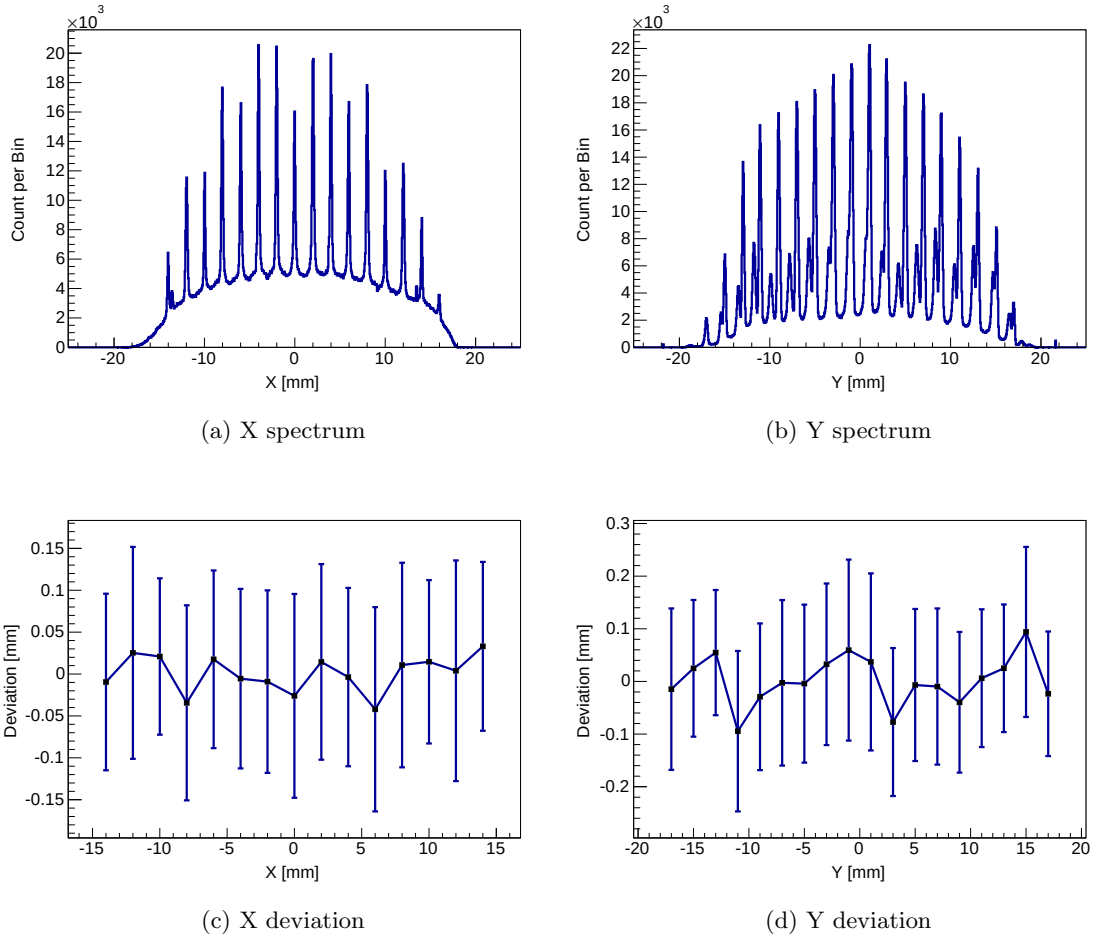

(a) X spectrum

(b) Y spectrum

(c) X deviation

(d) Y deviation

Figure 4.11: Calibrated X-coordinate and Y-coordinate spectra of the MWPC and the deviations of the peak positions.

of the 5.9 keV X-ray, and the vertical position of this hottest spot indicates the gain of that wire. Obviously, the gain is not the same from wire to wire. Figure 4.14a shows that the gain is also not uniform along the wire direction. Consistently, the gain is lower near the ends of the wires.

To correct the gain non-uniformity of the MWPC, a position-dependent energy calibration algorithm is developed, so that the MWPC energy readout is calibrated on an event-by-event basis. We divide the MWPC into *cells*, and each cell is a 2 mm×2 mm square centered at the peak positions in Figure 4.12, for example (2 mm, −3 mm). The

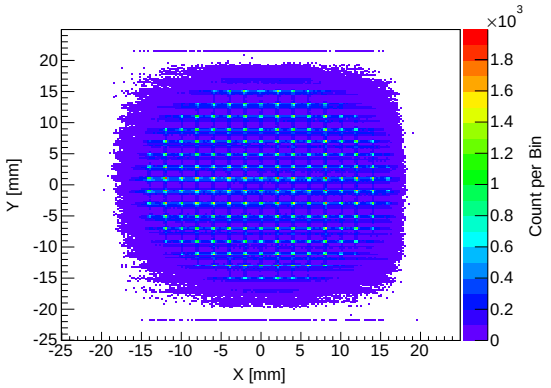

Figure 4.12: Calibrated MWPC image.

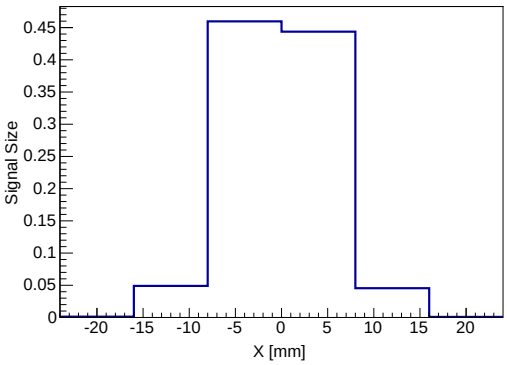

Figure 4.13: MWPC bottom cathode signal distribution for an event happening at $X = -0.1875$ mm. The horizontal axis in this figure is for the X coordinate of the center of each bottom-cathode wire group.

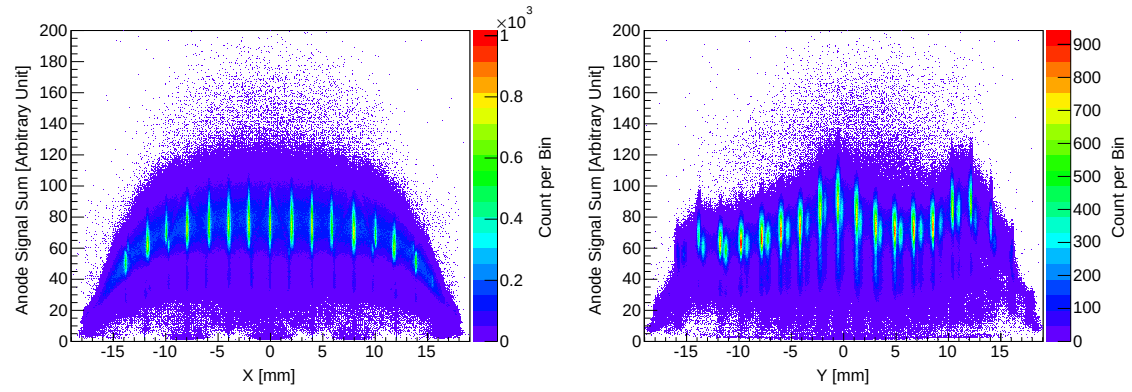

(a) (b)

Figure 4.14: (a) Anode signal sum versus X coordinate. (b) Anode signal sum versus Y coordinate.

^{55}Fe-calibration data are processed again with the event-by-event based position calibration implemented, and the anode sum spectrum for each cell is constructed. The energy-peak position of each spectrum is determined through a Gaussian fit in the energy-peak region, and the relative peak position (the energy-peak position of the center cell is the reference) versus the cell position is plotted in Figure 4.15 which is effectively the gain distribution of

the MWPC. For each cell, a scaling factor is defined as the relative peak position. During the event-by-event energy calibration, the original energy readout is divided by the scaling factor associated with the cell in which the event falls, so that the energy-peak positions of all cells are aligned at the same position. Then this corrected energy-peak position is calibrated to 5.90 keV.

The energy deposition spectrum of the MWPC is shown in Figure 4.16 after the position calibration and energy deposition calibration are implemented. The FWHM of the 5.90 keV peak is 1.4 keV, and the argon escape peak is more distinguishable than in Figure 4.4a. Therefore, the bad energy resolution of Figure 4.4a is caused by the gain non-uniformity, not the electronic noise or the initial ionization fluctuation.

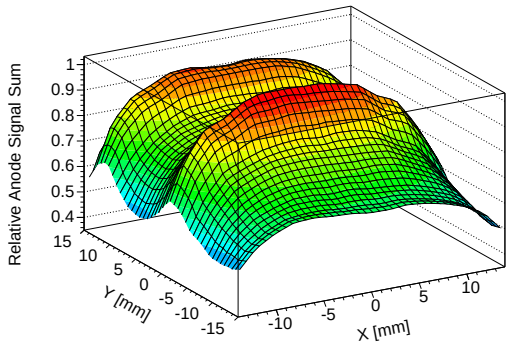

Figure 4.15: MWPC gain distribution normalized to the peak value of the (0 mm,1 mm).

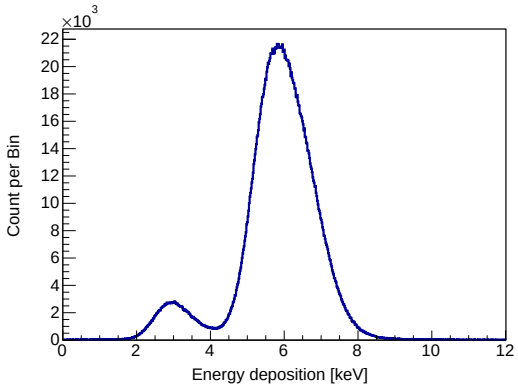

Figure 4.16: Calibrated MWPC energy deposition spectrum.

After the energy response of the MWPC was calibrated, we tested its response to minimal ionizing β particles. A ^{207}Bi source is inserted at the center of the MOT-2 chamber for this test. Coincidence trigger with the scintillator-PMT assembly is imposed so that only the MWPC responses to the 481.7 keV and 975.7 keV conversion electrons are kept while the contributions from the ^{207}Pb X-rays are ruled out. The MWPC energy deposition spectrum for this test is plotted in Figure 4.17. The spectral shape is "Landau-like" and the most probable value (peak position) for the energy deposition is 3.3 keV. The hardware threshold for the MWPC anode channels corresponds to $\sim$0.2 keV, which is well below the low-energy

tail of this spectrum. Because the dynamic range of the FASTER CARAS card is only up to 2.1 V, the large size signals saturate the ADCs and result in an incorrect MWPC position reconstruction. The saturation voltage of each anode channel corresponds to 15 keV, and therefore we imposed a 15 keV upper limit for the MWPC energy readout. The data loss due to saturation is $\sim 1\%$.

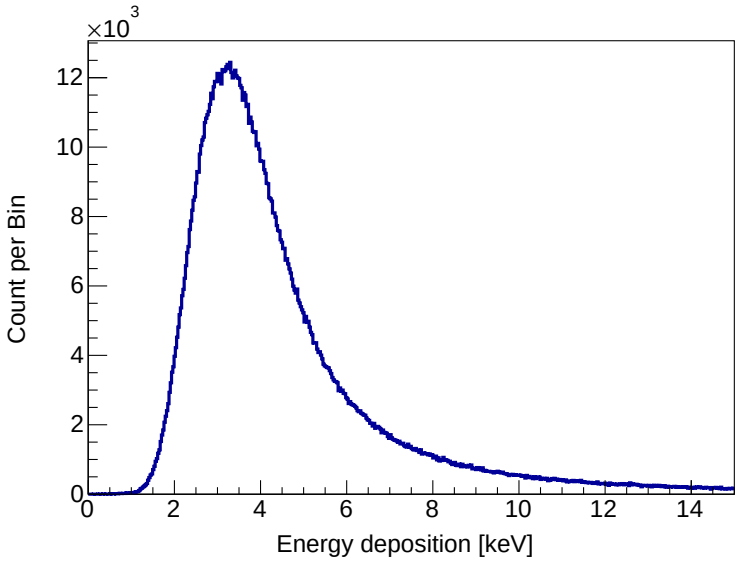

Figure 4.17: Calibrated MWPC energy deposition spectrum for conversion electrons from the ^{207}Bi source.

4.5 MWPC efficiency and uniformity calibration

The MWPC efficiency for detection of minimal ionizing β particles was studied using a ^{90}Sr source, which was placed at the center of the MOT-2 chamber. It emits β particles with energy from 0 to 2.28 MeV. We imposed a 1 MeV threshold on the energy deposition in the scintillator, and we observed that $\sim$98% of the events trigger both MWPC anodes. According to Figure 4.8 98% of the events that trigger the anodes also trigger three or more wire groups on the bottom cathode. Furthermore, the data loss due to saturation is $\sim$1% mentioned in the previous subsection. After taking all these effects into account, the efficiency of the MWPC should be approximately 95%.

The center 14 mm radius circle of the MWPC is approximately uniformly illuminated by the ^{90}Sr source, and a uniform distribution of events is expected. The distribution of events over the MWPC cells is plotted in Figure 4.18. Within the 14 mm radius circle, the number of counts per cell varies up to ±30%. This can be caused by efficiency non-uniformity. Figure 4.18 shows that the efficiency near X=−4 mm and X=4 mm is smaller. This is caused by rejecting those events that triggers less than 3 wire groups on the bottom cathode. The efficiency non-uniformity of the MWPC is studied by Monte Carlo simulation discussed in Chapter 5 and Chapter 6.

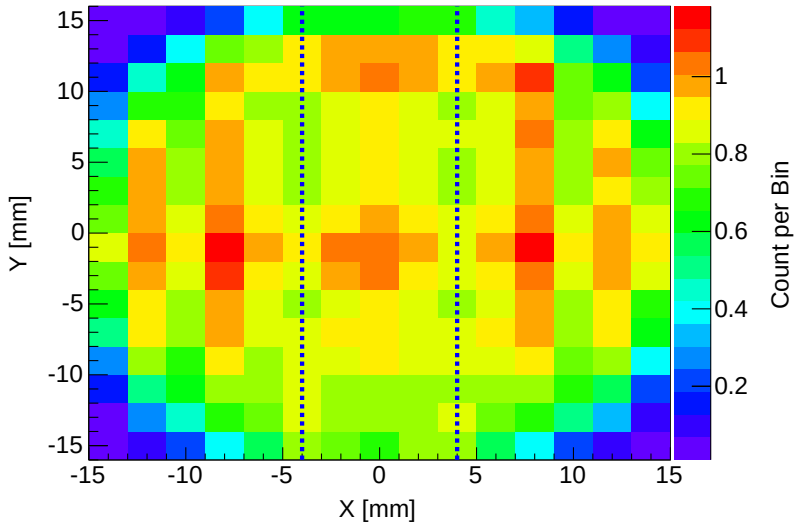

Figure 4.18: Distribution of events over the MWPC cells in a run with ^{90}Sr source. Count in cell at (0 mm,1 mm) is normalized to 1.

4.6 Scintillator-PMT assembly performance test

The Scintillator-PMT assembly was also tested with the ^{207}Bi source. The detailed FASTER settings for the PMT anode and dynode channels are listed in Appendix A. After the baseline restoration and the low-pass filter, a sample pulse shape measured by the FASTER oscilloscope module is shown in Figure 4.19. The typical rising time (bottom to top of the pulse) is 20 ns and the typical decay time (decay life-time) is 100 ns. The typical noise is

below 2 mV. The two charge integration windows are set to [−30 ns, 500 ns] and [−30 ns, 2000 ns]. The first window is for total scintillation light readout and the second one is for setting a dead time. With these settings, the triggering rate of the PMT is about 8 kHz with ∼100 ^{6}He atoms present in the MOT-2 chamber. The high counting rate is caused by the γ ray or neutron background induced by the accelerator, which is confirmed by comparing the PMT triggering rate when the beam is on and when the beam is off. At this rate, the loss due to dead time is ∼1.6%. After-pulses around 1000 ns after the main pulse are observed, but the 2000 ns long dead time blocks all after pulses happening within this window. No after-pulses are observed beyond 2000 ns.

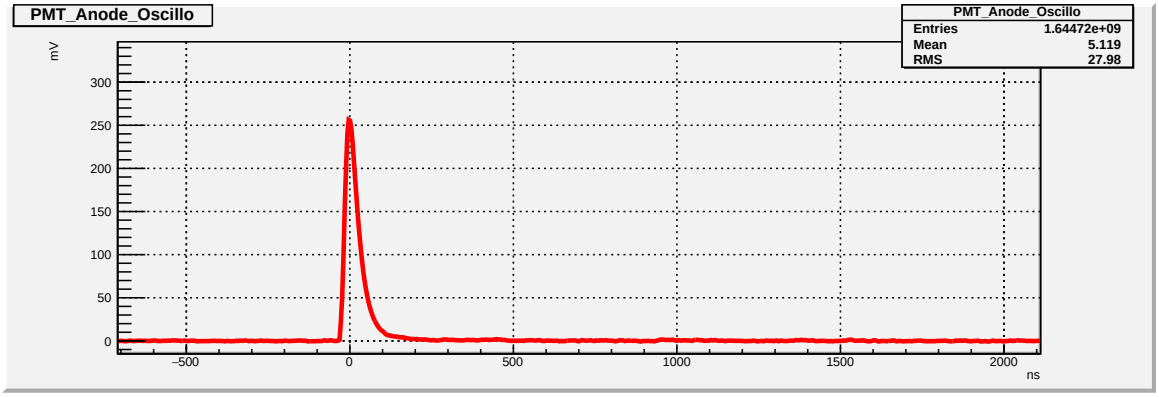

Figure 4.19: Typical pulse shape of the PMT anode signal (from RHB oscilloscope). This pulse sample does not have the after-pulse mentioned in the text.

The non-calibrated spectra of the PMT anode readout with and without the MWPC trigger in coincidence are shown in Firgure 4.20. The total conversion electron yield from the ^{207}Bi source is 6.4% of the γ ray yield. Without the MWPC trigger in coincidence, the scintillator-PMT assembly also detects γ rays through Compton scattering and photo-electric effect. The MWPC selects only the events generated by incoming electrons. In the coincidence spectrum, there are two major peaks near $Q_{int} = 500$ and $Q_{int} = 1000$ corresponding to the two strongest conversion electron lines from the ^{207}Bi source at 481.7 keV and 975.7 keV. These two spectral lines are used in the following studies and calibrations.

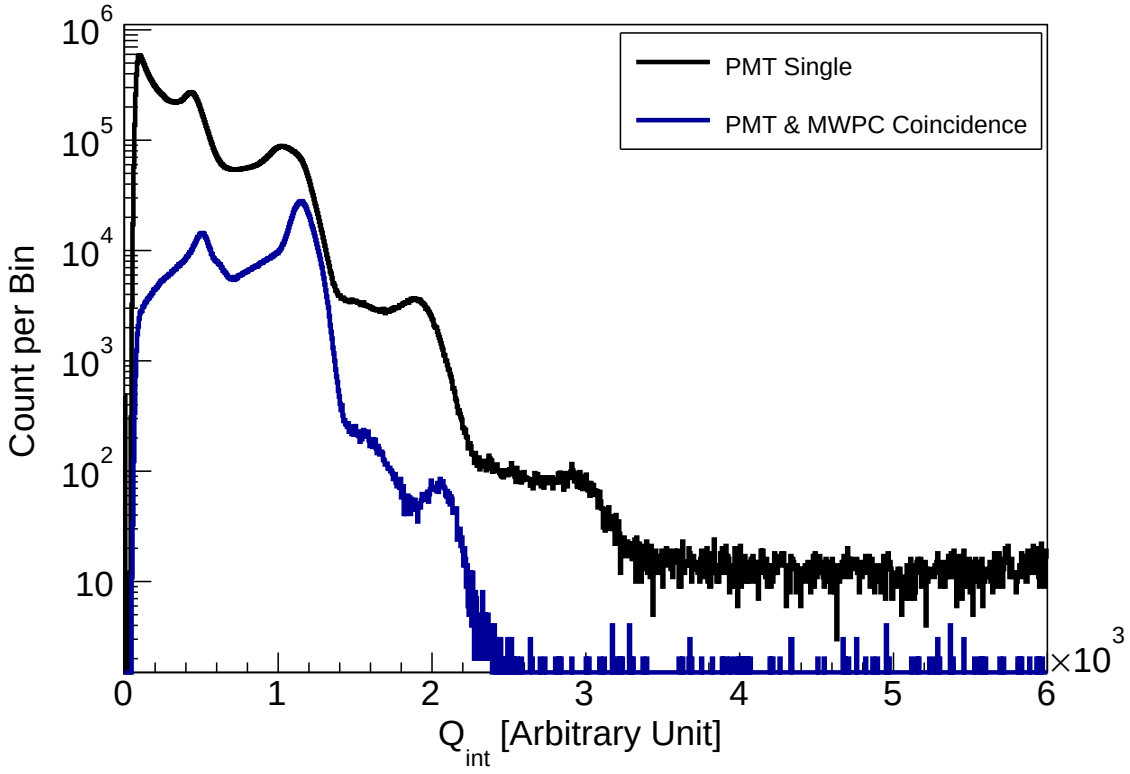

Figure 4.20: Non-calibrated spectrum of the Scintillator-PMT assembly. Black curve: triggered on PMT alone. Blue curve: triggered in coincidence with the MWPC anodes.

4.7 Scintillator-PMT assembly energy response calibration

In Figure 4.21, the physics processes through which the energy of the original particle is measured are shown. All response functions $D(E_d, E_0)$, $S(I_{scint}, E_d)$, $P(N_e, I_{scint})$, $A(N_{ef}, N_e)$ and $I(Q_{int}, N_{ef})$ are conditional probability distribution functions. Ideally, all of them are δ functions, for example $S(I_{scint}, E_d) = \delta(I_{scint} - (aE_d + b))$, and all processes are linear and there is no smearing. In the ideal case the final readout of the integrated charge from the PMT anode is expected to be linear with the energy of the original particle. However, the stochastic nature of the scintillation and the PMT photoelectron generation yields finite resolution. Besides this, the original particle may lose energy in dead layers of the detectors, or back-scatter after leaving only part of its energy in the active region of the

detector. Quenching happens during the process of scintillation. The quantum efficiency of the PMT photo-cathode may not be uniform, and the multiplications of the photoelectrons may be affected by many factors like rate and current, so that the linearity of the gain may be undermined. The gain of the PMT also drifts over time. The DAQ system may also introduce non-linear effects if it is not well tuned. Among all these issues mentioned above, the energy deposition process is studied via Monte Carlo simulation, which is described in Chapter 5. The distortions caused by the other effects are usually small or can be reduced by improved construction and tuning of the system. The long light guide together with its reflective wrapping make the luminescence on the PMT cathode less dependent on where the original scintillation occurs. In this section, we fold response functions S, P, A, and I into one position independent total response function $F(Q_{int}/M(x,y,T), E_{dep})$, where Q_{int} is the readout from the PMT anode, E_{dep} is the energy deposition in the scintillator, and $M(x,y,T)$ is a correction factor that depends on the hit-position (x,y) and time. In other words, the $M(x,y,T)$ corrects the non-uniformity and non-stability of the detector. The detail estimation of the correction factor M is described in Subsection 4.7.1 and then the approximation of the response function F is described in Subsection 4.7.2.

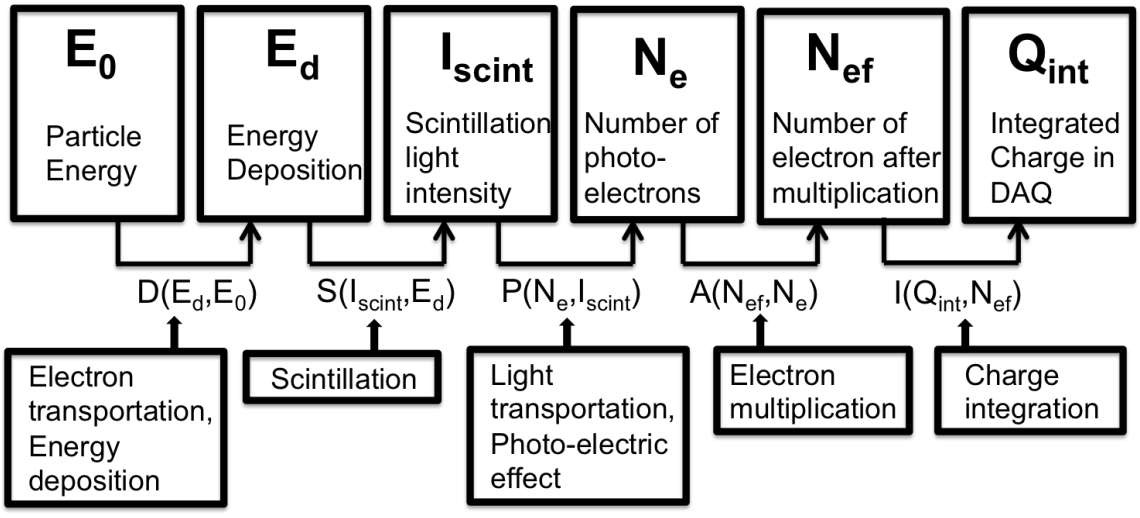

Figure 4.21: Physical processes through which the energy of the original particle is converted into the integrated charge measured by the DAQ system

4.7.1 Stability and uniformity

The stability of the scintillator-PMT assembly is affected by many factors. The multiplication of the PMT depends on the supply voltage. Besides this, the residual MOT-2 magnetic field also affects the gain of the PMT. The μ-metal shield extends to only the front surface of the PMT, so it doesn't shield the field along the PMT axis completely. With the previous configuration, the light guide was only 89 mm long, and the gain of the PMT decreased by over 90% when the MOT-2 magnetic field was turned on. This motivated us to make a longer light guide which ended up being 343 mm in the present configuration. In such configuration, the MOT-2 magnetic field only affects the PMT gain by ∼10% as shown in Figure 4.22. Because during the experiment the MOT-2 magnetic field is needed, the calibrations are all done when the magnetic field is on and kept stable.

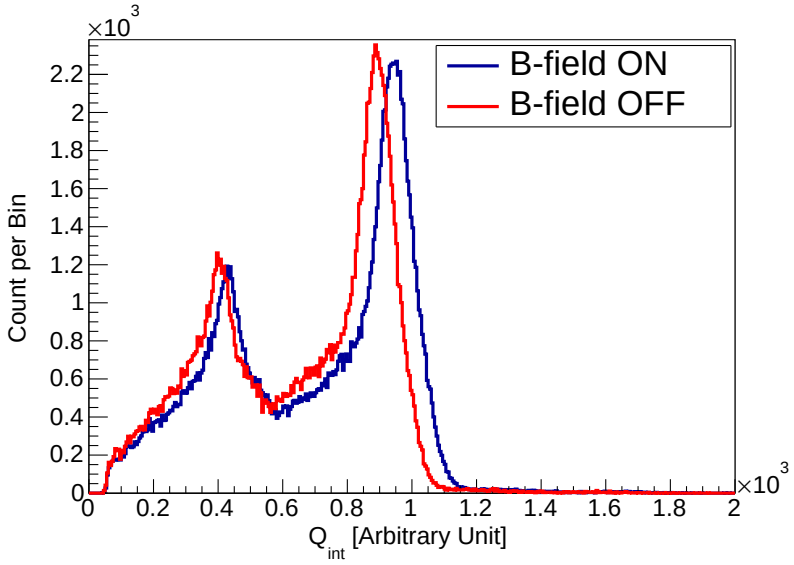

Figure 4.22: Energy spectrum of the ^{207}Bi radiation detected by the β telescope. Blue curve: MOT-2 magnetic field off. Red curve: MOT-2 magnetic field on.

In order to determine the behavior of the detector over a 12 hour period of time (the typical time in-between calibrations during the experiment) dedicated calibrations were performed. The ^{207}Bi source was used and the PMT was triggered in coincidence with the MWPC. Every 5 minutes the data were collected and the position of the 975.7 keV peak

was determined through a gaussian fit. The plot of the peak positions (normalized to the peak position of the first period) versus time is shown in Figure 4.23a, and the statistics of the peak positions is shown in Figure 4.23b. The error bar of each point in Figure 4.23a is 1.00×10^{-3}, and the RMS of the distribution in Figure 4.23b is 1.84×10^{-3}, greater than 1.00×10^{-3}. The extra RMS comes from the drift, and therefore the peak position drift RMS is 1.54×10^{-3}.

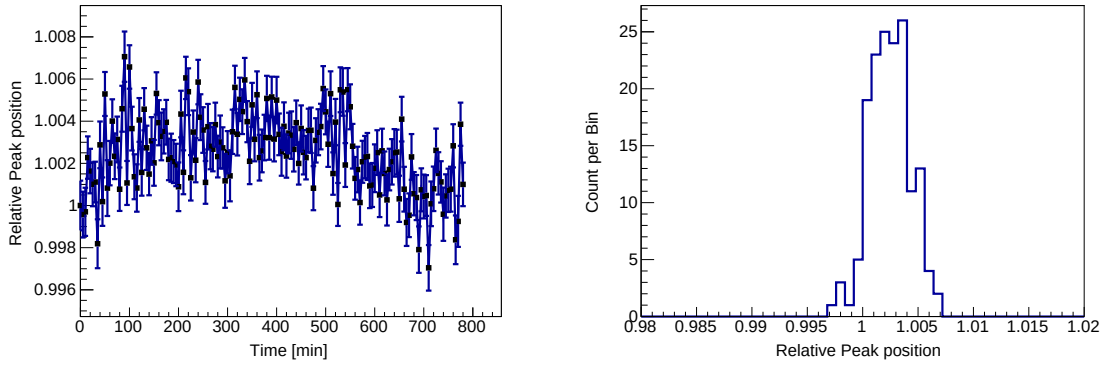

(a) (b)

Figure 4.23: (a) Time spectrum of the ^{207}Bi 975.7 keV peak position. (b) Statistics of the ^{207}Bi 975.7 keV peak positions.

While using the ^{207}Bi source to study the energy response drift, the LED pulses described in Section 3.1.2 are triggered at 100 Hz. Both the responses of the silicon photo-detector and the PMT are recorded. Every 5 minutes the peak positions of the spectra read by the PMT and the photo-detector are determined. In order to rule out drift caused by the LED light source, the peak position of the spectrum read by the PMT is corrected by dividing it with the peak of the photo-detector spectrum. The corrected peak positions versus time are shown in Figure 4.24a, and the statistics of the corrected peak positions is shown in Figure 4.24b. The error bar of each point in Figure 4.24a is 9×10^{-5}, and the RMS of the distribution in Figure 4.24b is 5.95×10^{-4}, and therefore the peak position drift RMS in this case is 5.88×10^{-4}.

The drift determined by the ^{207}Bi spectrum is 2.6 times larger than that determined

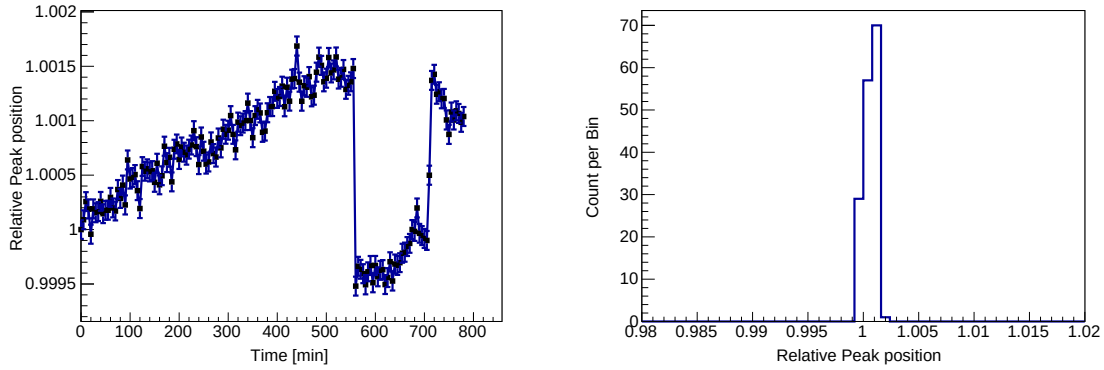

(a) (b)

Figure 4.24: (a) Time spectrum of the corrected LED pulse peak position. Jumps in the spectrum are shown in this example. (b) Statistics of the corrected LED pulse peak positions.

by the LED pulser spectrum. There are several reasons that can cause this discrepancy. First of all, the LED pulser study doesn't include the drift of the scintillator light yield. Secondly, the LED pulser shape is quite different from the scintillator pulser. The LED pulse has a longer rising edge and a longer tail (∼300 ns). In addition, the stability of the light transfer (optical fiber and fiber connectors) was not thoroughly tested. Therefore, the drift determined by the ^{207}Bi spectrum is more trustworthy. On the other hand, the LED pulses can be used during the measurement of the ^{6}He decays, but the ^{207}Bi source cannot. Therefore, we use the LED pulse spectrum as a monitor of the PMT gain in order to make sure there is no drift or sudden jumps larger than 1×10^{-3}. For example, in Figure 4.24a, two jumps at the order of $\sim 2 \times 10^{-3}$ were observed at 560 min and 720 min from the beginning of the calibration run. The reason for these jumps is not known. They might be caused by someone turning on and off some magnetic coils nearby. No matter what causes the jump, data runs with jumps like these are rare and thus discarded during the $a_{\beta\nu}$ measurement.

To test the spatial uniformity of the energy response of the scintillator-PMT assembly, the ^{207}Bi spectrum is constructed for every 2 mm×2 mm cell of the MWPC within a 15 mm radius from the center. For each spectrum, the position of the 975.7 keV peak was

determined through a gaussian fit. The peak positions (normalized to the peak position of the center cell) are plotted in the spatial 2D graph shown in Figure 4.25a, and the statistics of the peak positions is shown in Figure 4.25b. The average error bar size of each point in Figure 4.25a is 1.51×10^{-3}, and the RMS of the distribution in Figure 4.25b is 2.43×10^{-3}. Therefore, the RMS of the uniformity is 1.90×10^{-3}.

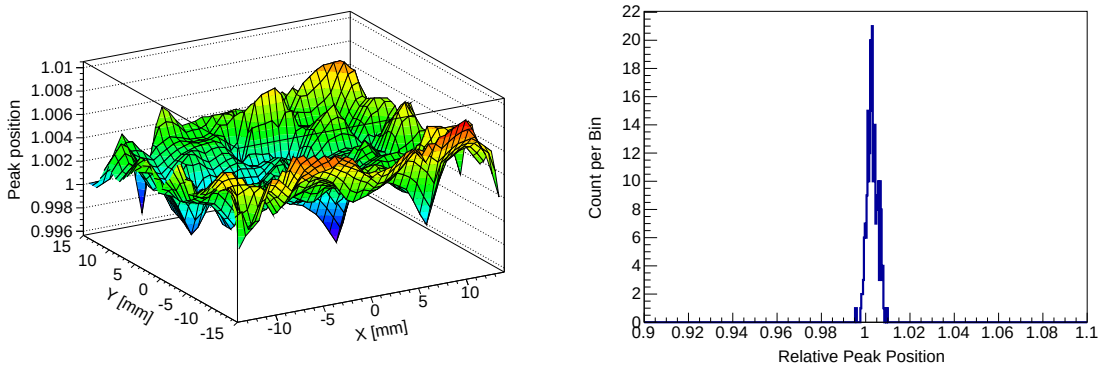

(a) (b)

Figure 4.25: (a) The ^{207}Bi 975.7 keV peak positions versus MWPC position readout. (b) Statistics of the ^{207}Bi 975.7 keV peak positions.

After all, the 1.54×10^{-3} drift in the energy response and the 1.90×10^{-3} spatial non-uniformity of the scintillator-PMT assembly is not a substantial contribution to the systematic error according to the study in Chapter 6. Therefore, we don't apply corrections for the drift or non-uniformity. The correction function $M(x, y, T)$ is set to unity. The drift and non-uniformity are directly treated as sources of systematic uncertainties.

4.7.2 Energy response function

Because in the final analysis of the ^{6}He $\beta - \nu$ correlation measurement a 14 mm radius cut on the MWPC position readout is imposed, we impose the same cut for the scintillator-PMT assembly energy response calibration. With this cut imposed, the Q_{int} spectrum is plotted in Figure 4.26. Besides the 2 major conversion electron lines, the ^{207}Bi source also has a weak conversion electron line at 1682.2 keV, which is about 0.3% as strong as the

conversion electron line at 975.7 keV. It is distinguishable after over about 1 hour of data taking. One striking feature of the coincidence spectrum in Figure 4.26 is the low-energy tail of each peak. We found through Monte Carlo simulations that these tails are caused by the photoelectrons from the substrate of the source, and the detail study of this effect is discussed in Chapter 5.

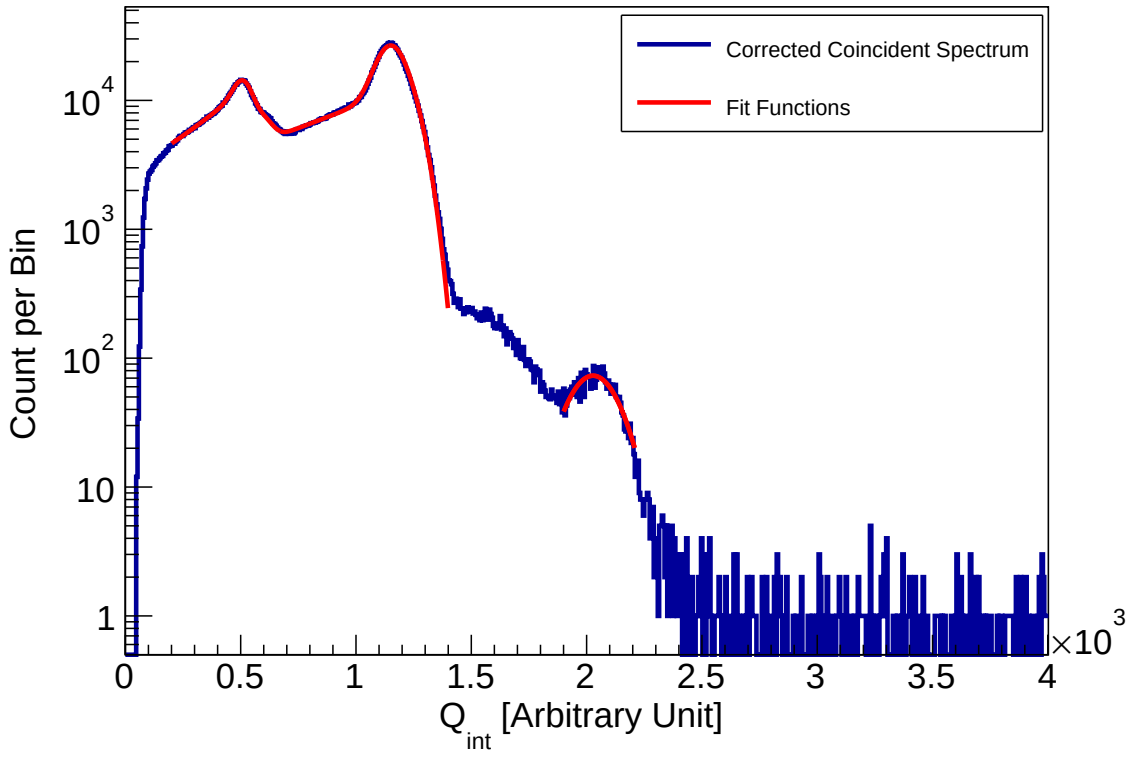

Figure 4.26: Analytical fit of the peaks in the coincidence spectrum of the corrected PMT readout.

For the calibration purpose, we fit the spectrum in Figure 4.26 with analytical functions to extract the peak positions and width. The conversion electron lines are fitted to gaussian functions, while the tails are fitted to an exponential function convoluted with a gaussian function. We first fit the entire region of the two lower-energy peaks and their tails, which is from $Q_{int} = 150$ to $Q_{int} = 1500$. We take into account the L-shell and M-shell conversion

electron lines, and we fix their intensity ratios and energies relative to the K-shell conversion electron line. Therefore, the fit function for the entire region is

$$\begin{aligned} f(Q_{int}) = p_0 \left(P_1(Q_{int}, p_1, p_2) + T(Q_{int}, p_1, p_2, p_3, p_4)\right) \\ + p_5 \left(P_2(Q_{int}, p_6, p_7) + T(Q_{int}, p_6, p_7, p_8, p_9)\right) \end{aligned} \tag{4.2}$$

where the peak functions $P_1(x, p_1, p_2)$, $P_2(x, p_6, p_7)$ and tail functions $T(x, p_i, p_j, p_k, p_l)$ are

$$\begin{aligned} P_1(x, p_1, p_2) &= \exp(\frac{(x-p_1)^2}{2p_2^2}) + 0.26\exp(\frac{(x-1.074p_1)^2}{2p_2^2}) + 0.062\exp(\frac{(x-1.086p_1)^2}{2p_2^2}) \\ P_2(x, p_6, p_7) &= \exp(\frac{(x-p_6)^2}{2p_7^2}) + 0.29\exp(\frac{(x-1.15p_6)^2}{2p_7^2}) + 0.072\exp(\frac{(x-1.175p_6)^2}{2p_7^2}) \\ T(x, p_i, p_j, p_k, p_l) &= p_k \times \mathrm{Erfc}(\frac{x - p_i + p_l p_j^2}{\sqrt{2}p_j}) \times \exp(\frac{p_l}{2}(2x - 2p_i + p_l p_j^2)) \end{aligned} \tag{4.3}$$

and the parameter definitions and the fit values of them are shown in Table 4.1. The function $\mathrm{Erfc}(x)$ is the complementary error function[1]. The fit function is overlaid on top of the coincidence spectrum in Figure 4.26. There are excess events around $Q_{int} = 350$ and $Q_{int} = 1350$ because both of the two particles from the ^{207}Bi cascade decay enter the scintillator and deposit energy in the scintillator. This effect is also taken into account and explained in detail in Chapter 5. Secondly, we fit the 1682.2 keV peak with a Gaussian function, and the peak position is at $Q_{int} = 1750$. The fit function is also shown in Figure 4.26.

We ran Monte Carlo simulations with the ^{207}Bi calibration source, and the peak positions of the three conversion electron lines are also determined in the spectrum of the β telescope energy readout, which is the energy deposition (E_{depsim}) spectrum folded with Gaussian smearing. The relationship between the three conversion electron-energy peak values ($E_{\beta sim-p}$ and Q_{int-p}) in the simulated β telescope energy readout spectrum and the measured PMT anode readout spectrum are plotted in Figure 4.27. The three data points fits very well to a linear function

$$E_{\beta sim-p} = a \times Q_{int-p} + b, \tag{4.4}$$

where a and b are fit parameters. Finally, we define $E_\beta = a_{fit} \times Q_{int} + b_{fit}$ as the calibrated energy readout of the Scintillator-PMT assembly, where a_{fit} and b_{fit} are the fitted values

[1]The relationship between $\mathrm{Erfc}(x)$ and $\mathrm{Erf}(x)$ defined in Equation 4.10 is $\mathrm{Erfc}(x)$=1−$\mathrm{Erc}(x)$.

Parameter	Definition	Value	Error
p_0	Norm of the 975.7 keV peak	1.838e+4	50.5
p_1	Position of the 975.7 keV peak	1.154e+3	0.194
p_2	Width of the 975.7 keV peak	6.183e+1	0.146
p_3	Ratio of the tail of the 975.7 keV peak	3.101e−1	2.31e−3
p_4	"Length" of the tail of the 975.7 keV peak	1.525e−3	1.64e−5
p_5	Norm of the 481.7 keV peak	5.211e+3	77.6
p_6	Position of the 481.7 keV peak	5.153e+2	0.531
p_7	Width of the 481.7 keV peak	4.096e+1	0.406
p_8	Ratio of the tail of the 481.7 keV peak	7.387e−1	1.90e−02
p_9	"Length" of the tail of the 481.7 keV peak	4.146e−03	6.75e−05

Table 4.1: Definition of parameters in Equation 4.3 and the fit values of these parameters.

of parameter a and b in Equation 4.4. This calibration procedure is carried out periodically throughout the experiment and update the parameter a_{fit} and b_{fit} for data analysis.

After the linear calibration, E_{dep} should be the expectation value of E_β. Then we fold in a Gaussian smearing to account for the resolution of the detector, the total response function $F(E_\beta, E_{dep})$ can be approximated as

$$F(E_\beta, E_{dep}) = \frac{1}{\sqrt{2\pi\sigma^2}} \exp(-\frac{(E_\beta - E_{dep})^2}{2\sigma^2}), \tag{4.5}$$

where σ is the gaussian width which also depends on E_{dep}. Ideally, this width is only due to the fluctuation of the number of photoelectrons generated from the PMT cathode. In this case, σ is proportional to $\sqrt{N_e}$. The width for the 975.7 keV peak is the parameter p_2 in Equation 4.3, and the fitted value is 61.83 ± 0.146 keV. Therefore, the energy dependency of σ is:

$$\sigma(E_{dep}) = \sigma(975.7 \text{ keV}) \times \sqrt{\frac{E_{dep}}{975.7\ keV}} \tag{4.6}$$

Equation 4.5 and Equation 4.6 are used in the Monte Carlo simulation to generate the β-telescope energy readout. Furthermore, the parameter $\sigma(975.7)$ is fine tuned in the sim-

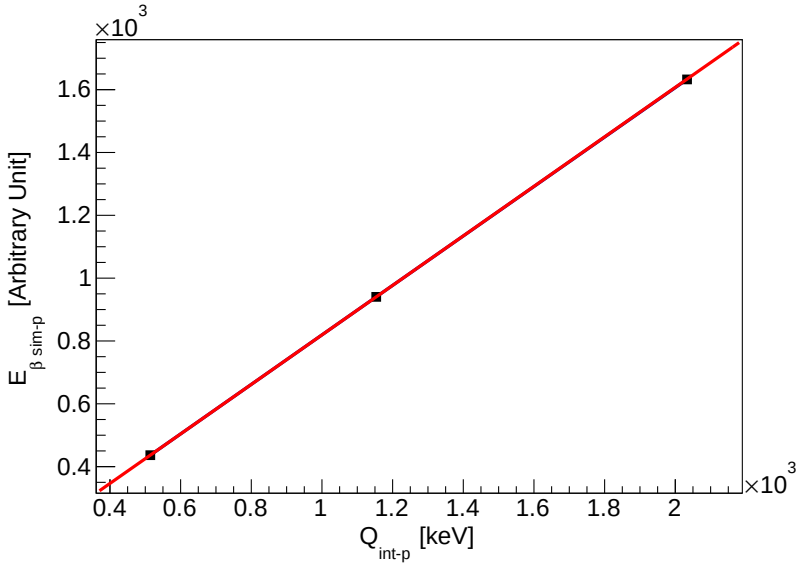

Figure 4.27: Linear fit of the relationship between $E_{\beta sim-p}$ and Q_{int-p}. Error bars are included but too small to be seen in this graph.

ulation to give the best match to the measured E_β spectrum. However, under this change the peak values of the simulated spectrum of the β-telescope energy readout may change as well, and this results in a different fit in Equation 4.4. Therefore, we perform a recursive calibration procedure and eventually get a stabilized calibration. The detail about this procedure is described in Chapter 5.

The linear fit in Equation 4.4 only extends to 1682.2 keV, and we extrapolate this linear relationship to the end-point of ^{6}He decay. The goodness of the whole-spectrum matching is discussed in Chapter 5.

4.8 MCP performance test

The basic performance of the MCP is tested using the 5.5 MeV α-particles from an ^{241}Am source. Low-pass filters with 13 ns shaping time are applied to the MCP-back signal channel and all delay-line anode channels. After the baseline restoration (BLR) and the low-pass filters, typical pulse shapes for the MCP-back signal (MCP signal) and the delay-line anode signals are shown in Figure 4.28. In order to achieve the best timing performance, the CFD

delay time for the MCP channel is set to 2 ns while the CFD delay times for the delay-line anode channels are set to 6 ns. The MCP signal channel has an undershoot and ringings after the prompt pulse. These features also appear in pulses from the delay-line anode channels. Therefore, for all these channels the charge integration windows are set so that only the prompt pulses are integrated.

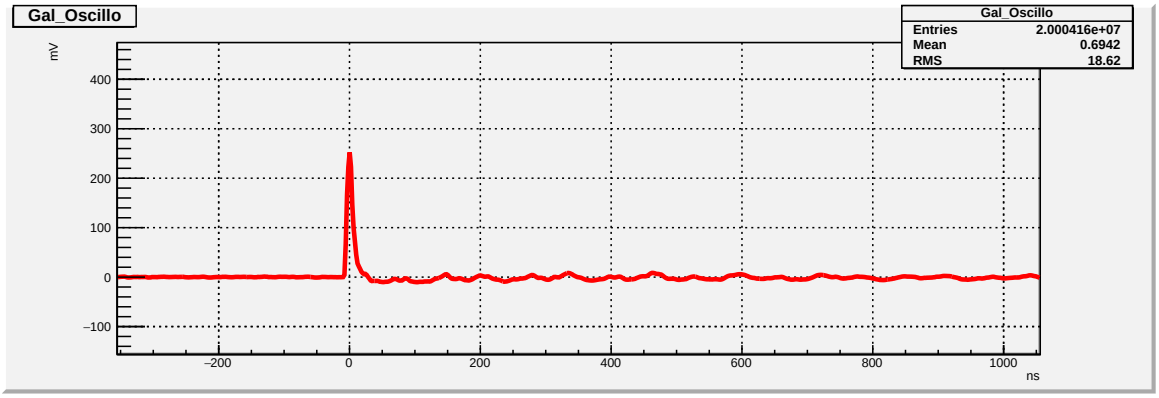

(a)

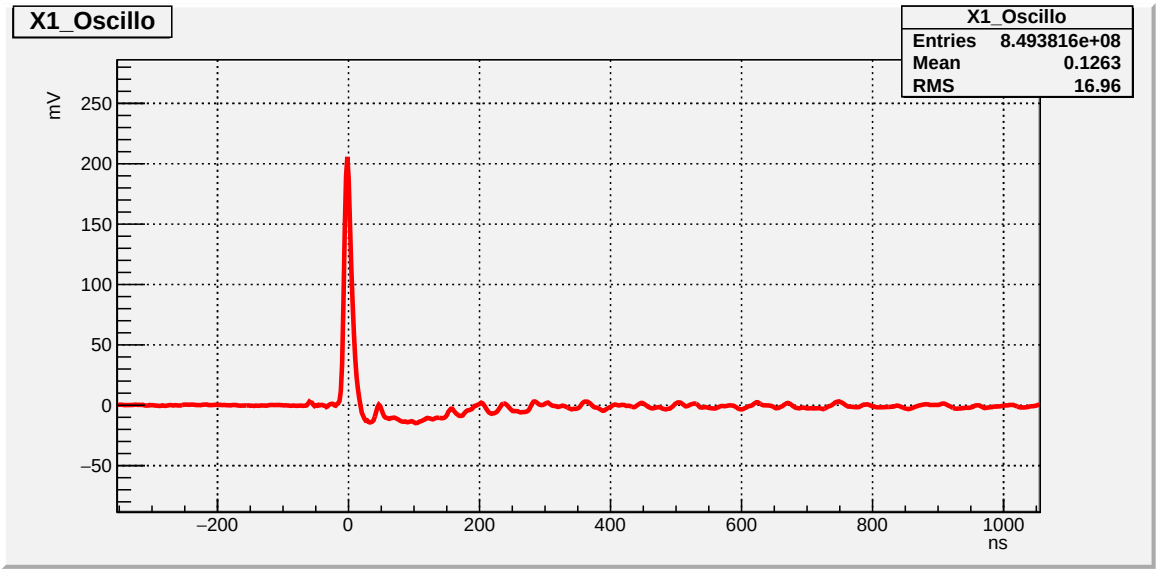

(b)

Figure 4.28: (a) Typical pulse shape of the MCP signal. (b) Typical pulse shape of the Delay-line anode signals.

The spectra of the integrated charge of the MCP signal (Q_{MCP}) and the delay-line anode channels (QX_1,QX_2,QY_1 and QY_2) are plotted in Figure 4.29. The QY_2 spectrum is significantly different from the other ones, but we haven't observed severe efficiency non-uniformity or position distortion in the Y direction. Furthermore, correlations between these integrated charges are shown in the 2D plots in Figure 4.30. All these relationships are positive proportional. This indicates that the resolution of the charge-readout system is very good. The strong positive correlation between the two channels of the same delay-line wire shows that there is no severe attenuation along the delay-line wires. Therefore, the delay-line doesn't make the MCP detection efficiency worse near the edge.

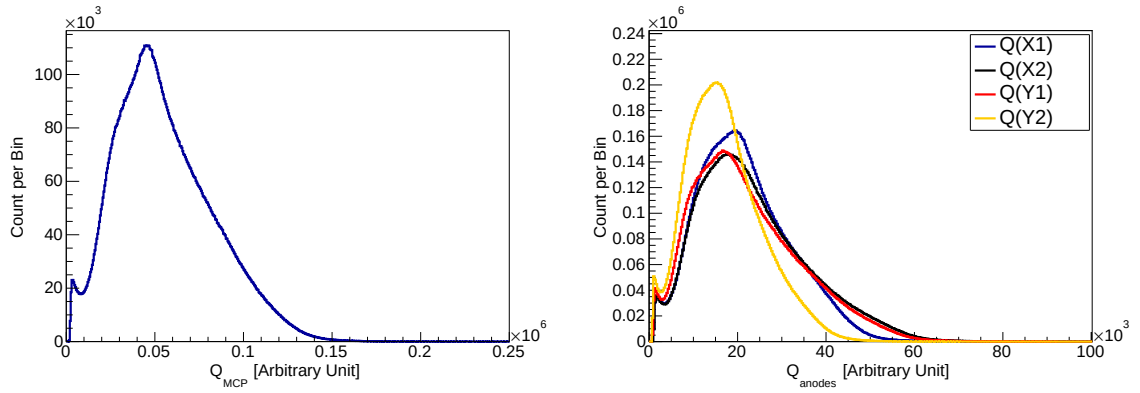

(a) (b)

Figure 4.29: Spectra for (a) Q_{MCP} and (b) QX_1,QX_2,QY_1 and QY_2.

The particle-landing position is reconstructed using Equation 3.3. The non-calibrated MCP position spectrum is shown in Figure 4.31. The grid structure is clearly seen, and the rim of the mask is also obvious. Because the total length of delay-line wires are fixed, the sum of the period of time during which the signal propagates from the charge collection position to each end of the delay-line should be the same no matter where the event happens. The difference between the time of the MCP signal (T_{MCP}) and the time of the signal of the X-anode wire (TX_1 or TX_2) equals the signal propagating time plus a constant shift including delays in cables and amplifiers. During this test, the cabling, amplifiers, and DAQ

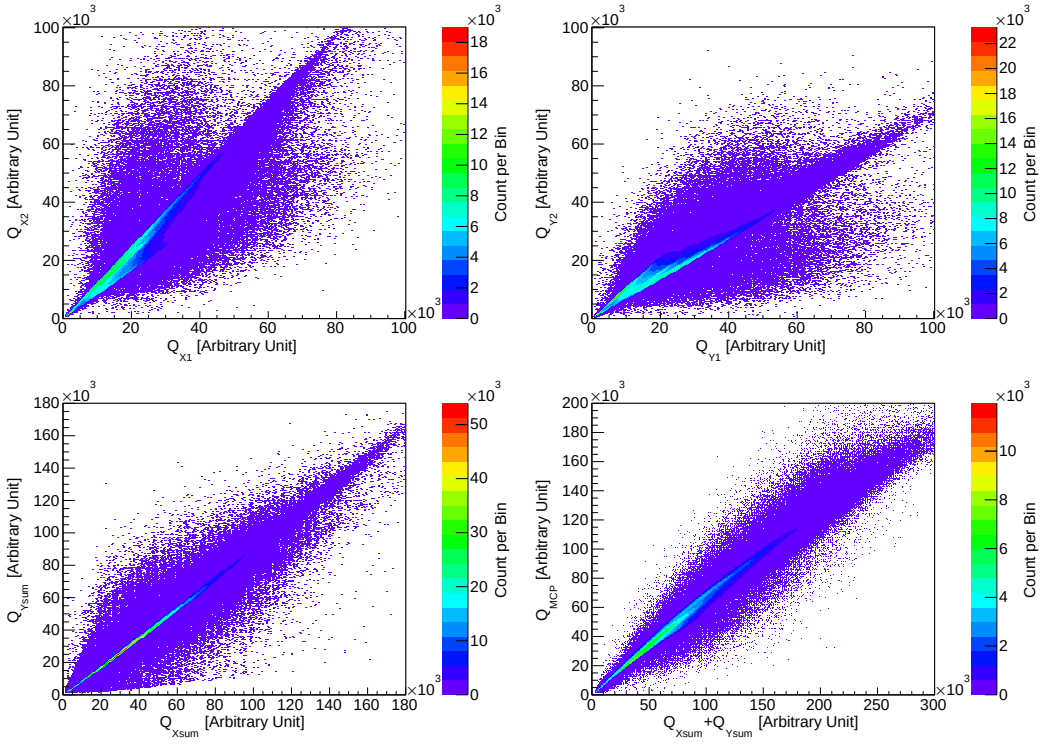

Figure 4.30: Correlations of integrated charges of the MCP signal and the delay-line anode signals.

settings are not changed, and thus the time sums TX_{sum} and TY_{sum} defined as

$$TX_{sum} = (TX_1 - T_{MCP}) + (TX_2 - T_{MCP}),$$
$$TY_{sum} = (TY_1 - T_{MCP}) + (TY_2 - T_{MCP}), \tag{4.7}$$

should be constant. If any signal among the MCP signal and the delay-line anode signals is triggered by random noise, another incoming particle, or spurious pulses, Equation 4.7 may not hold. Therefore, a strict condition on TX_{sum} and TY_{sum} can rule out many false coincidence triggers and noise. The spectra of TX_{sum} and TY_{sum} are shown in Figure 4.32. The cut applied on TX_{sum} is [88 ns, 96 ns], and the cut applied on TY_{sum} is [85 ns, 93 ns]. After application of these cuts, the MCP position spectrum becomes clearer, and 5.5% of the original events are ruled out.

The primary purpose of the MCP is to detect the ^{6}Li ions at about 13 keV. Besides

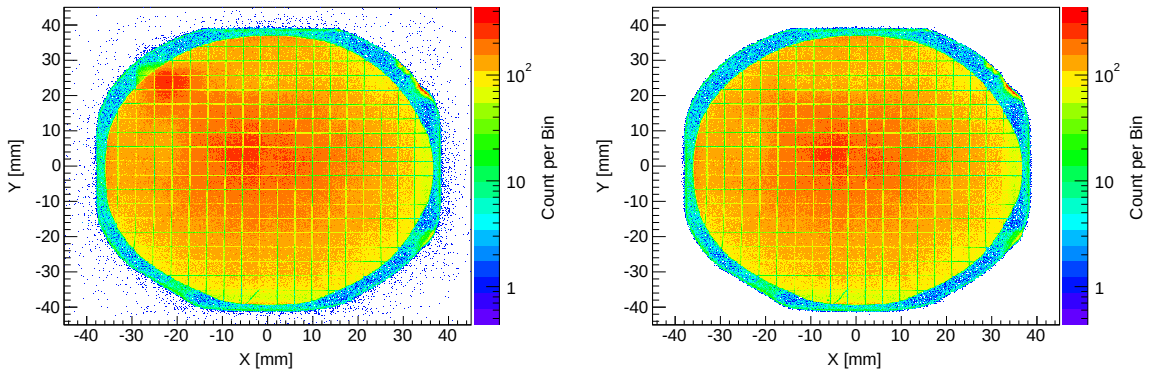

Figure 4.31: MCP position spectra, without (a) and with (b) cut on TX_{sum} and TY_{sum}. The shadow outside the illuminated area is caused by background events (spontaneous emission, cosmic rays, etc.).

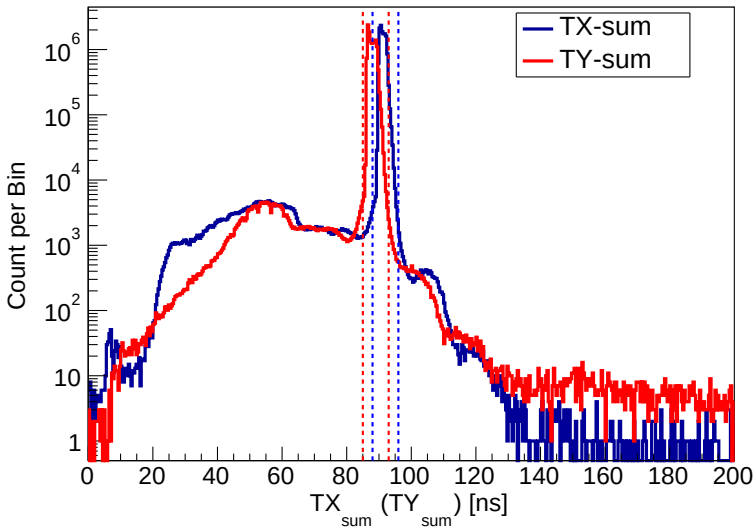

Figure 4.32: TX_{sum} (Blue) and TY_{sum} (Red) spectra with cut region indicated.

that, the MCP is also used for other calibration purposes. For example, the MCP detects β particles in the timing calibration and ^{4}He ions in the electric field calibration. The MCP signal spectra of these cases are different from that of the α-particles from the ^{241}Am source.

These differences are discussed in Section 4.12. During the tests with the ^{241}Am source, we kept the ion-accelerating electric field turned on in order to maintain a similar environment where the recoil ^{6}Li ions are detected.

4.9 MCP position calibration

We use the shadow of the grid on the MCP image to calibrate the position reconstruction. The 50 μm thick mask with the grids is directly attached to the front surface of the MCP, so the shadow created by the mask has the same shape of the mask itself[2]. After the mask and the MCP stack are mounted to the MCP holder, the whole assembly is brought to a laser-scanning microscope and the front surface of the mask is scanned. In this way the straight edges of the grids and the circular edge of the whole opening region are determined at an accuracy of $\sim$2 μm. The photo of the mask and the image produced by the microscope are shown in Figure 4.33. The diagonal line of the square at the top is to break the axial symmetry of the pattern to make obvious the positive directions of the axes of the MCP position spectrum.

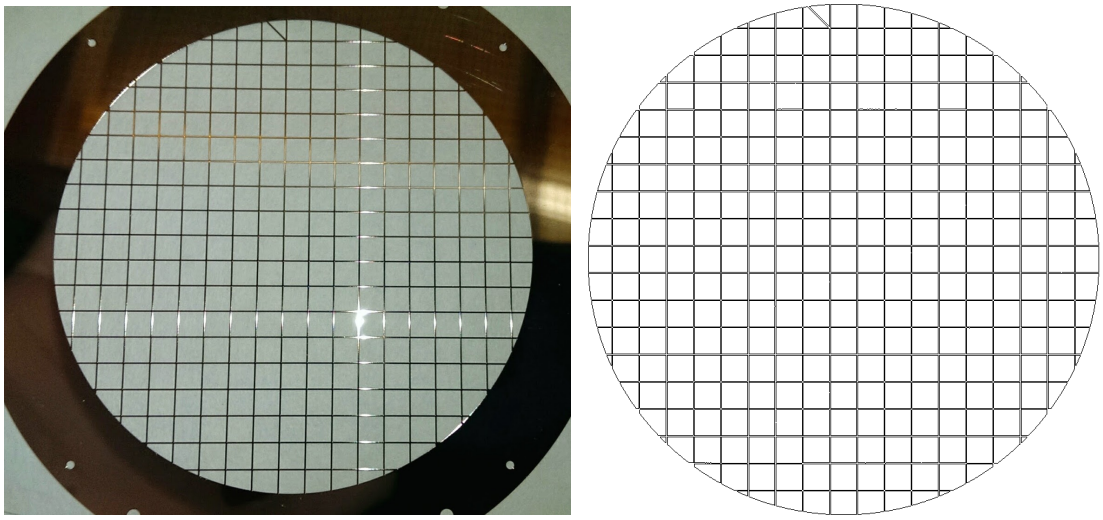

Figure 4.33: Photo and the scanned image of the mask.

[2]Edges of grid lines are cut at 45° relative to the bottom surface in order to avoid blocking incoming particles before they reach the MCP surface.

In the following subsection, the algorithm that determines the grid positions in the MCP position spectrum and the algorithm that corrects the deviation from the measured grid positions are described. The calibration accuracy and position resolution of the MCP are discussed. Potential differences in the MCP position responses to 5.5 MeV α-particles and $\sim$13 keV ^{6}Li ions are discussed in Subsection 4.11.2.

4.9.1 Grid-line determination

As shown in Figure 4.31 besides the shadow beyond the opening area of the mask, the circular shape of the illuminated area is distorted near the edge and it also has an overall elliptical distortion. For the convenience of the grid-line determining algorithm, the image is scaled first to make the illuminated area close to a circle and then a radius cut of 38.5 mm is applied so that the shadow beyond the cut is eliminated. An algorithm is designed and programmed to determine the positions of the grid lines in the MCP position spectrum. The positions of grid-line crossings are determined first, and then for each complete squares with all corner-points determined three more points on each edge are determined, as is shown in Figure 4.34. All these determined points should stay at the center of the shadow created by the grid lines. The detail description of this algorithm is presented in Appendix C.

Obviously, the mask edge is very distorted from its circular shape. In the scope of this thesis, only the complete squares are included in the analysis. The grid lines on the MCP position spectrum are less distorted than the edge. The statistics of the deviation of all the determined points is shown in Figure 4.35. The mean deviation is 278 μm and the maximum deviation is 1.1 mm. In general, the farther the position is from the center, the larger deviation it has.

4.9.2 Correction algorithm

Comparing the determined points on the grid lines in the MCP position spectrum and their real positions, we found that there is a global offset, stretching and rotation. However, we also observed bowing of the grid-line segments up to several hundreds of micrometers happening only to several adjacent squares. A global correction function cannot take care

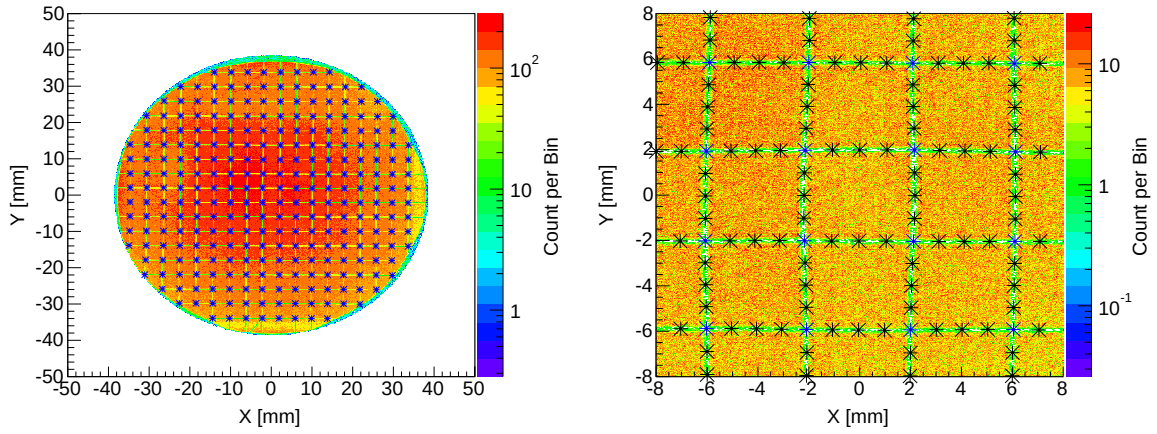

(a) (b)

Figure 4.34: (a) Determined grid-line crossings along the grid shadow in the MCP position spectrum. (b) Zoomed-in center region of (a) with additional three points added along each edge.

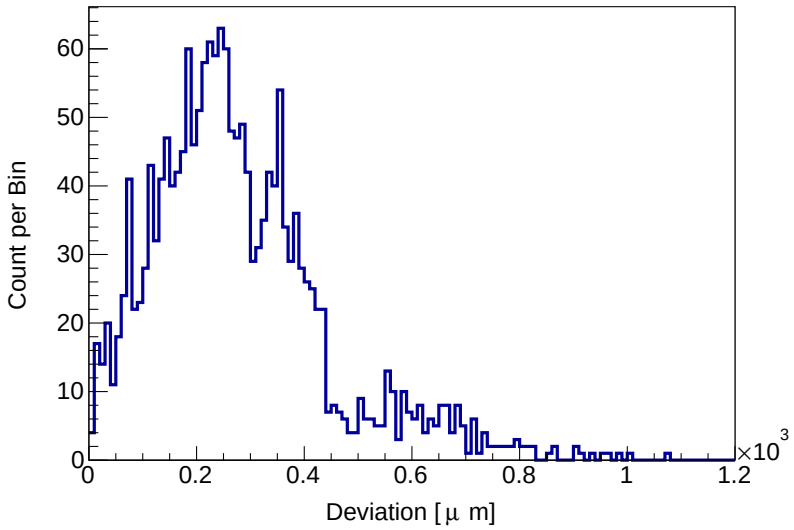

Figure 4.35: Statistics of the deviations of all determined points.

of these local distortions. Therefore, in order to achieve higher calibration accuracy, we correct the distortions square by square.

Take the square region centered at [0.0 mm, 4.0 mm] as an example. Two functions are constructed in order to move those determined points (black points labeled in Figure 4.36) to their physical coordinates:

$$X_C = p_0X^2 + p_1XY + p_2Y^2 + p_3X + p_4Y + p_5,$$
$$Y_C = q_0X^2 + q_1XY + q_2Y^2 + q_3X + q_4Y + q_5, \tag{4.8}$$

where X and Y are the coordinates of the determined points from the MCP position spectrum, X_C and Y_C are their corrected coordinates, and the p's and q's are 12 parameters to be determined. We fit these two functions to their physical positions (red points labeled in Figure 4.36) and extract the 12 unknown parameters in Equation 4.8. These correction functions are constructed for each complete square, and their parameters are saved to a calibration file, which will be used for position corrections in other analyses.

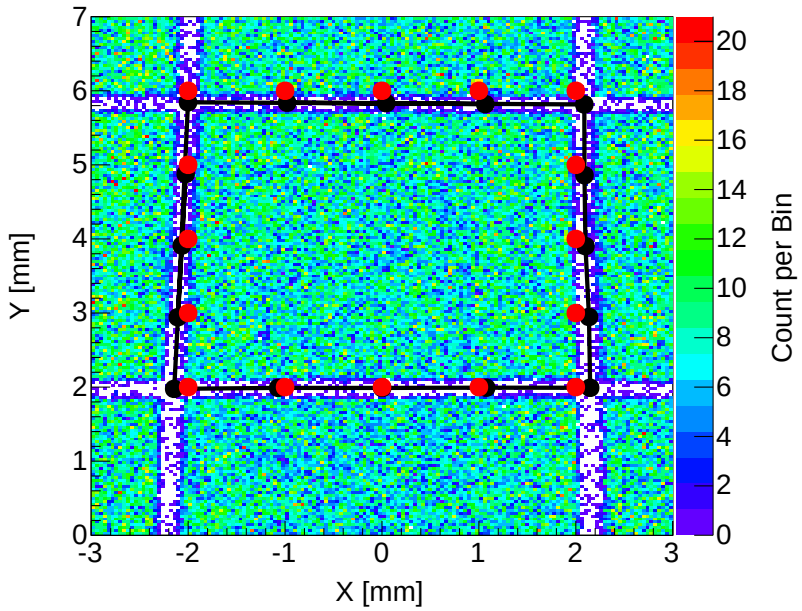

Figure 4.36: The square region centered at [0.0 mm, 4.0 mm] with the determined points at the corners and on the edges (labeled in black and joined with black lines). The physical positions of these points are labeled in red. The black loop indicates the boundary of this region.

For the event-by-event position correction, an algorithm is developed to determine which square an event belongs to. Given the event position reconstructed by the DAQ readings and a square region, the algorithm outputs whether the event position is within the boundary of the square region. For a square region, all determined points at the corners and on the edges are connected into a loop using straight lines, and this loop is defined as the boundary of the square region as is shown in Figure 4.36. This procedure insures that the right set of correction functions are applied to each event.

4.9.3 Position calibration accuracy and resolution

The calibration data are re-processed and an event-by-event correction is applied. The corrected MCP position spectrum is shown in Figure 4.37. Events outside the fiducial cut, *i.e.* the complete squares, are ruled out. Using the same algorithm described in Appendix C we determined the grid-line crossings and three more points along each grid-line segment on the corrected MCP position spectrum. The statistics of deviations of these points from their physical positions are shown in Figure 4.38a. After the position correction, the average deviation becomes 7.6 μm with a root-mean-square 3.4 μm. Therefore, we estimate that the position-calibration accuracy is 7.6 μm. Positions of the grid-line crossings are plotted in Figure 4.38b on top of the dashed lines indicating the physical positions of the grid lines.

The resolution of the MCP position response is related to the sharpness of the grid lines. To study this, we project the center region of each grid-line segment to the axis perpendicular to the grid line. For example, the region enclosed by the blue rectangle in Figure 4.39a is projected onto the X axis, forming the 1D histogram in Figure 4.39b. Ideally, the event count should be zero in the region covered by grid lines, while the event count distribution should be uniform in the exposed region. If the MCP position response has a finite Gaussian resolution, the sharp edges of the ideal spectrum are smeared, *i.e.* convoluted with a Gaussian function. Therefore, we fit the projection histogram to a function:

$$F(x) = N_1 \times \left(1 - \mathrm{Erf}\left(\frac{x-\mu_1}{\sqrt{2}\sigma_1}\right)\right) + N_2 \times \left(1 + \mathrm{Erf}\left(\frac{x-\mu_2}{\sqrt{2}\sigma_2}\right)\right) + B, \qquad (4.9)$$

where N_1 and N_2 are normalization factors, B is a constant background, μ_1 and μ_2 are

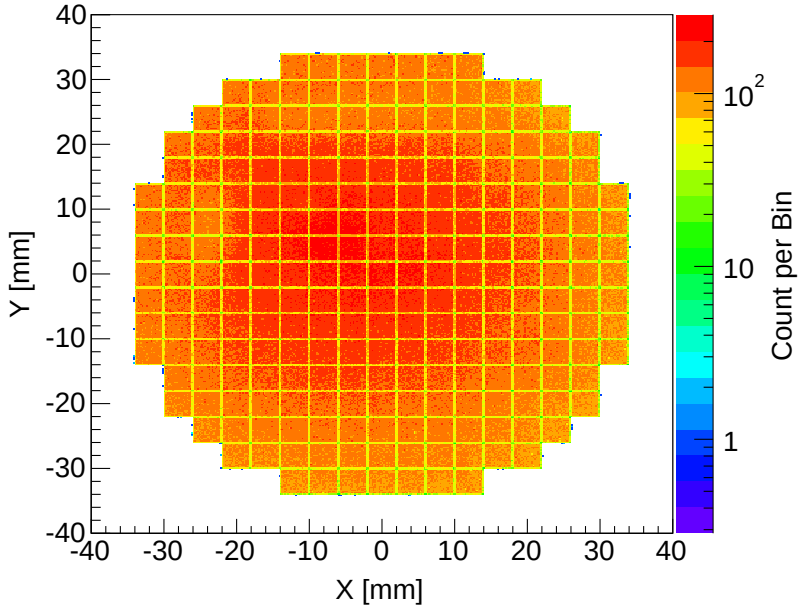

Figure 4.37: MCP position spectrum with event-by-event position correction.

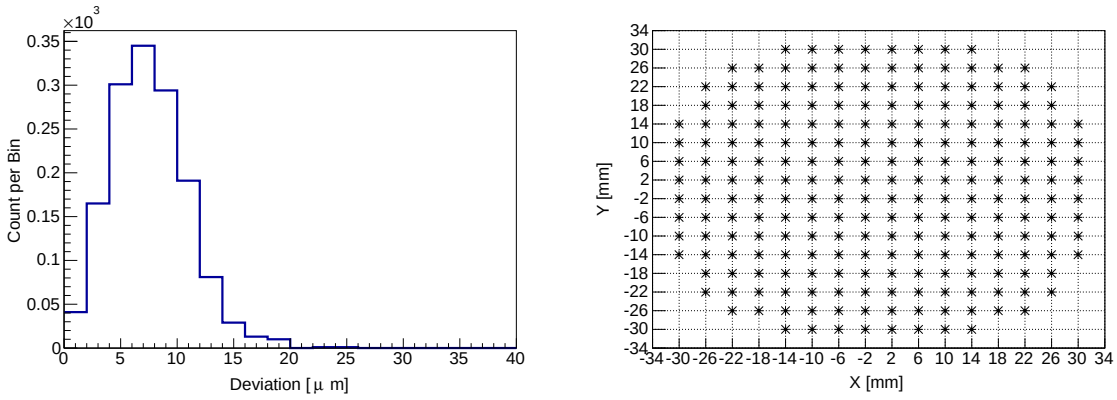

(a) (b)

Figure 4.38: (a) Statistics of the deviations of all determined points from the corrected MCP position spectrum. (b) Positions of the corners of the square regions. Dash-lines are at the physical positions of the grid lines.

positions of the falling edge and the rising edge, σ_1 and σ_2 are the Gaussian smearing

widths of the edges, and the error function Erf(x) is defined as:

$$\mathrm{Erf}(x) = \frac{2}{\sqrt{\pi}} \int_0^x \exp(-t^2) dt. \tag{4.10}$$

The resulting fitted function of the projection is also shown in Figure 4.39b. The statistics of the falling and rising edge widths for all the horizontal grid segments and the vertical grid segments are shown in Figure 4.40. All these distributions have a similar shape, with mean around 36 μm and root-mean-square around 8 μm. The root-mean-squares of these width distributions are also comparable to the fit uncertainties of σ_1 and σ_2 in Equation 4.9, which are around 6 μm. This indicates that the widths of distributions in Figure 4.40 are mainly due to statistical uncertainties of the fits.

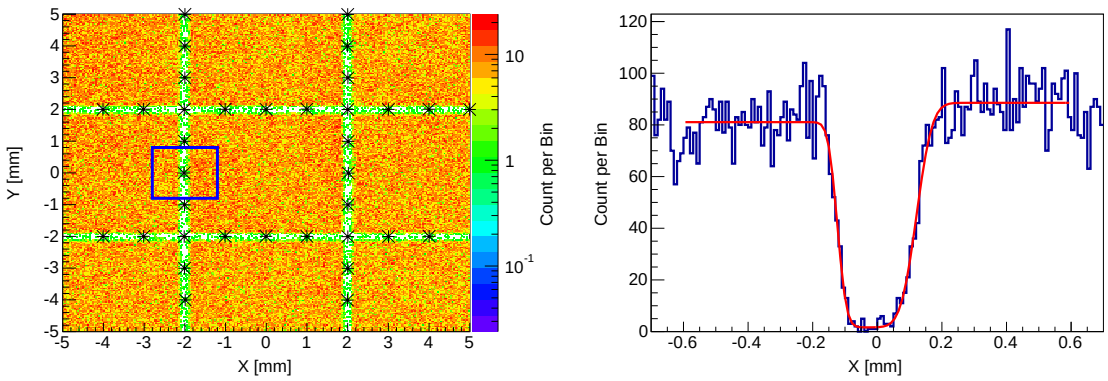

(a) (b)

Figure 4.39: (a) Region for MCP position resolution study, enclosed by the blue rectangle. (b) Projection of the region shown in the left figure onto the X axis. The red line is the fit-function defined in Equation 4.9.

Furthermore, the fitted value of $\mu_2 - \mu_1$ corresponds to the width of the grid lines. The distributions of the widths of horizontal and vertical grid-line segments are shown in Figure 4.41. The mean values of both the horizontal and vertical grid-line widths are consistent with their physical width of 250 μm.

To summarize, we developed a program that finds the grid lines on the MCP position spectrum and constructed correction functions for each complete square region. The correction functions are applied on an event-by-event basis, and a position-calibration accuracy

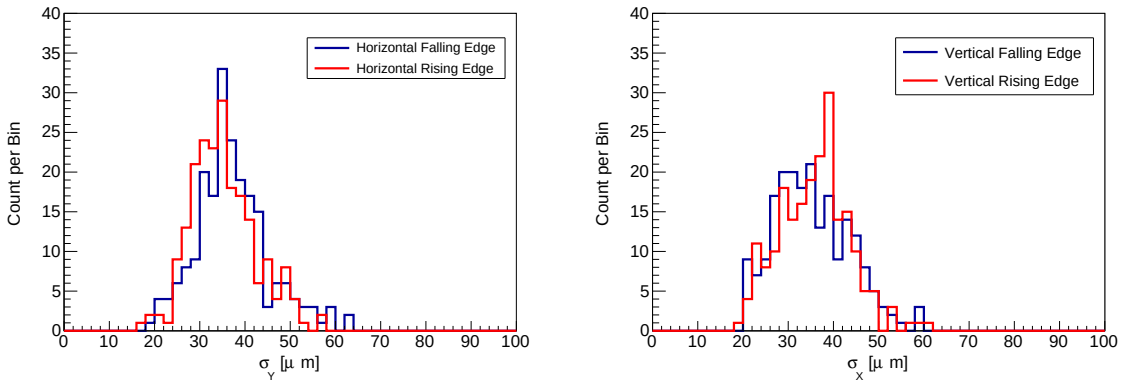

(a) Horizontal grid-line segments

(b) Vertical grid-line segments

Figure 4.40: Distributions of Gaussian smearing widths (σ_X and σ_Y) of falling edges and rising edges.

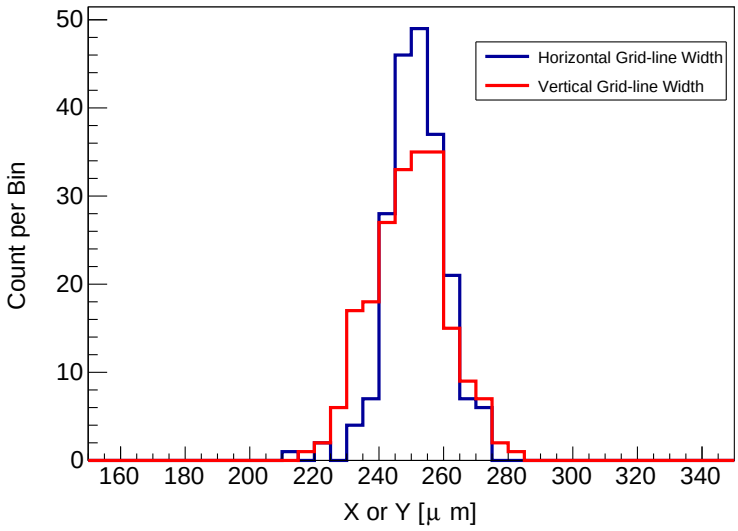

Figure 4.41: Statistics of the widths of grid-line segments.

of 7.6±3.4 μm is achieved. Combining all statistics in Figure 4.40, the position resolution of the MCP is 35.9±7.9 μm. The measured grid-line width is consistent with its physical value. In this calibration data set there are 1.34×10^7 events, which is required to achieve the calibration accuracies mentioned above.

4.10 MCP signal size study

In this section, we discuss factors that affect the MCP signal size (Q_{MCP}) spectrum: particle type, ion energy, position and incident angle. It is important to understand these factors because the MCP signal size affects the efficiency of the MCP.

4.10.1 Q_{MCP} spectra for different types of particles

Three types of particles are studied in this section: 1) α-particles from the ^{241}Am source are used in the MCP position calibration; 2) β particles with $\sim$2 MeV energy generate background whenever there are ^{6}He atoms in the MOT-2 chamber; 3) Ions with $\sim$10 keV kinetic energy are the dominant particles detected by the MCP for the ^{6}He $a_{\beta\nu}$ measurement. For the Q_{MCP} spectrum study, we introduced the α-particles and β particles by inserting the ^{241}Am source and the ^{90}Sr source, and introduced the ^{6}Li ions by filling the MOT-2 chamber with non-trapped ^{6}He and applying the ion-accelerating field.

However, there are usually other species of particles introduced together with the particles of interest, and they can trigger the MCP as well. The α-particles from ^{241}Am source kick out surface ions from the source substrate. The non-trapped ^{6}He atoms emit β particles and ^{6}Li recoil ions. In order to study the MCP response for one specific species of particle, it is important to find techniques to isolate the contribution from the particles of interest. For the ^{241}Am source, the ion-accelerating field prevents the ions kicked out by the α-particles from reaching to the MCP, because the source is held at ground while the nearest two electrodes are all biased >5 kV. For the non-trapped ^{6}He, the β-particle contribution is ruled out by imposing the coincidence trigger with the β telescope and a proper TOF cut. Details of the TOF cut is described in Section 4.10.2.

In the study of the Q_{MCP} spectrum, the MCP position readout is calibrated based on a run with ^{241}Am, and then the center square region is chosen to be the fiducial area. In this case, the gain of the MCP is approximately uniform in this 4 mm by 4 mm area. The Q_{MCP} spectra for α-particles, β particles and ^{6}Li ions are plotted in Figure 4.42. During these measurements, all coils on the MOT-2 chamber were kept on so that the magnetic field is the same as that for the experiment with trapped ^{6}He.

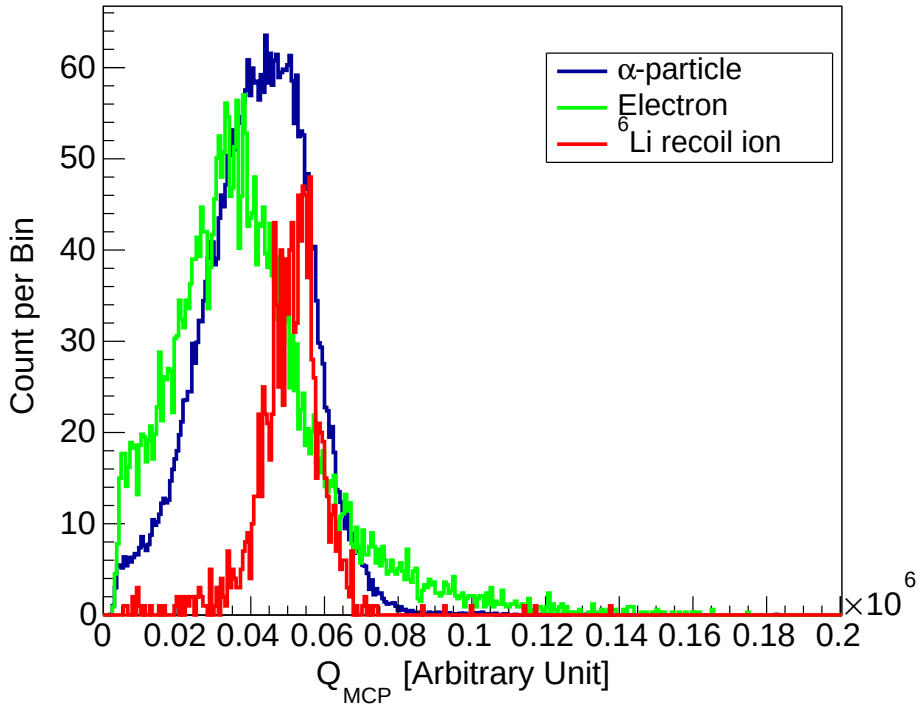

Figure 4.42: Q_{MCP} spectra for different incoming particles. The spectrum for ^{6}Li ions is measured using non-trapped ^{6}He source. For the measurement of ^{6}Li a coincidence trigger with the β telescope is imposed to rule out contributions from β particles.

According to the plots in Figure 4.42, the shape of the spectra for ^{6}Li ions is Gaussian-like while the spectral shapes for α-particles and electrons are peak-like but asymmetric. Compared to the spectrum for ^{6}Li ions, the α-particle spectrum has a larger low-Q_{MCP} component. The reason is that the 5.5 MeV α-particles are more likely to impact into the MCP substrate and generate fewer surface electrons. In the same way, the β particles impact even deeper so that the average signal size is smaller than the cases for α-particles and ^{6}Li ions. The threshold of Q_{MCP} corresponds to ~3% of the ^{6}Li-ion or α-particle spectrum peak position, and near the threshold the event count is also low. Therefore, the MCP efficiency of detecting ^{6}Li-ions or α-particles is insensitive to gain variations. The electronic noise is completely under the threshold.

Besides using the non-trapped ^{6}He, the MCP response to ions is also probed using

Penning ions and photoions from trapped ^{4}He atoms. Penning ions are generated through collisions between the trapped metastable helium atoms and the residual gas (predominantly hydrogen) in the chamber. Photoions from MOT-2 are generated by nitrogen laser pulses. Events caused by the photoions are selected by imposing the coincidence with the nitrogen laser pulses. The ion-accelerating electric field is turned on during these measurements. Because the thermal energy of the Penning ions or photoions is negligible compared to the energy they gain from the electric field, the initial velocity of the ions is neglected, and the ions hit only the center of the MCP. The fiducial area used for the previous studies still works. Because all events are concentrated inside the fiducial area and the event rates for Penning ions and photoions are about 300 Hz and 15 Hz respectively, it is easier to achieve high-statistics Q_{MCP} spectra during a short period of time.

Similar to the ^{6}Li ion spectrum, the Q_{MCP} spectra for Penning ions and photoions also have Gaussian-like shapes as shown in Figure 4.43. For the photoion Q_{MCP} spectrum, there are also peaks with higher Q_{MCP} values. The position of the second peak shown in the right figure of Figure 4.43 is almost twice the first peak position. These higher peaks are caused by multiple photoions hitting the MCP and generating the same pulse. The temporal pulse width of the nitrogen-laser that ionizes the ^{4}He atoms is less than 3.5 ns. Therefore if multiple atoms are ionized, the separation of the times when they hit the MCP is less than 3.5 ns, which is smaller than the rising edge of the pulse and cannot be resolved. When multiple incoming ions hit the MCP within the charge-integration window, the integrated charge of the MCP signal is proportional to the number of incoming ions. The dominant case is that two ^{4}He ions hit the MCP together, which generate the second peak in the Q_{MCP} spectrum. The number of events in the second peak depends on the density of atoms in the trap. We did find that the more atoms are in the trap, the more events are in the higher peaks of the Q_{MCP} spectrum. In order to reduce the multiple hits by the photoions and avoid damage to the MCP due to high-intensity Penning ions, the number of atoms in MOT-2 is kept below 10^4.

Obviously the Q_{MCP} spectra for both Penning ions and photoions have tails on the low Q_{MCP} side. Empirically we fit these spectra to an Exponentially-modified Gaussian (EMG)

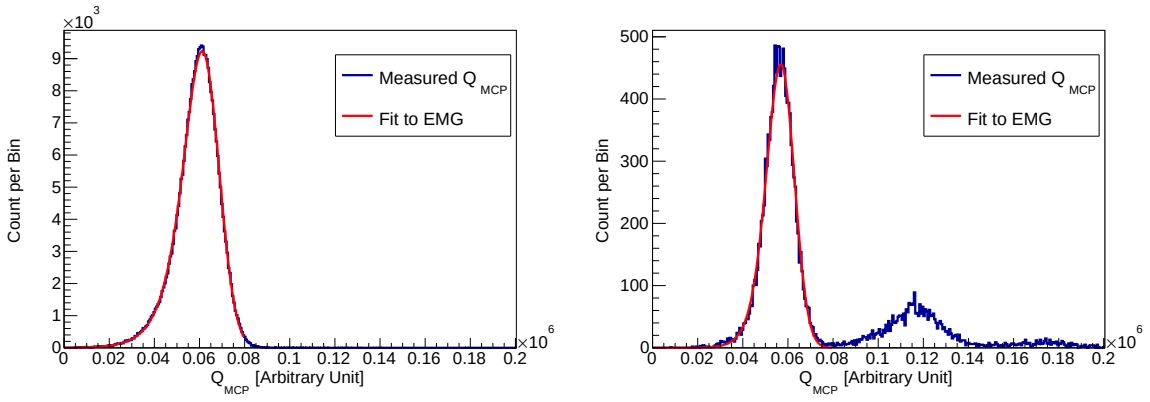

(a) Penning ion (b) Photoion

Figure 4.43: Q_{MCP} spectrum of (a) Penning ions and (b) photoions from the ^{4}He trap. Fits to exponentially-modified Gaussian functions are shown in red.

function with a left tail:

$$f(x) = N_0 \exp\left(\frac{\lambda}{2}(2x - 2\mu + \lambda\sigma^2)\right) \text{Erfc}\left(\frac{x - \mu + \lambda\sigma^2}{\sqrt{2}\sigma}\right) \tag{4.11}$$

where λ, μ, σ and N_0 are fit parameters. The parameter λ describes the inverse tail length. The fit of the Q_{MCP} spectra for Penning ions and photoions from the ^{4}He trap are also shown in Figure 4.43. These fit parameters are used in the studies of the MCP gain versus ion energy and the MCP efficiency described in the following subsections.

The Q_{MCP} peak positions for the cases of ^{6}Li, Penning ions and photoions are all close to one another. The difference among them is less than ∼7%.

4.10.2 Q_{MCP} spectrum versus ion energy

The energy dependence of the Q_{MCP} spectrum for ions with ∼10 keV kinetic energy is studied using the Penning ions and photoions from the ^{4}He trap because their energy is easy to change by tuning the electric field strength of the ion-accelerating field. The electric field strength is scanned from 0.769 kV/cm to 1.731 kV/cm, so that the energy of the ions when hitting the MCP ranges from 7.075 keV to 15.92 keV. For each electric field setting, the Q_{MCP} spectrum in the fiducial area (the center square region) is fit to Equation 4.11 and the fit values of the parameter μ for both Penning ions and photoions are plotted in

Figure 4.44. For the same energy the Penning ions generate larger Q_{MCP} than the photoions do by approximately 7%. This difference roughly tells how differently the MCP responds to different ion species[3], *i.e.* H_2^+ and He^+. The μ-parameter of the Q_{MCP} spectrum increases with the ion energy for both Penning ions and photoions. The change in μ-parameter in the energy range of the recoil ^{6}Li ions from trapped ^{6}He decays is up to 1.6%. Due to the low threshold and low counts at the threshold shown in Figure 4.43, the efficiency variations due to the differences in ion energy and ion species are negligible ($< 0.001\%$).

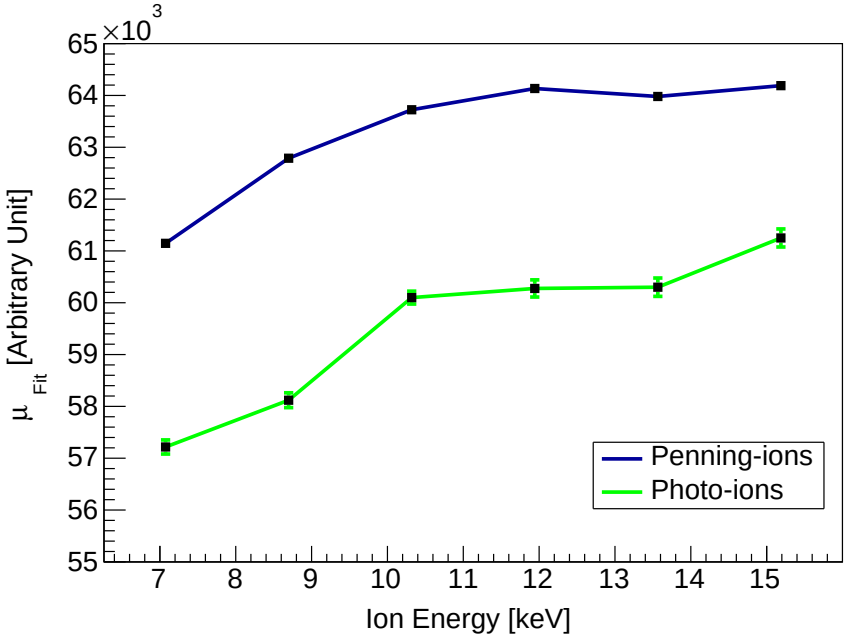

Figure 4.44: Fit value of μ for the Q_{MCP} spectra for different energies of Penning ions and Photoions.

The case for ^{6}Li ions from the non-trapped ^{6}He source is also investigated. To rule out the events generated by β particles, a coincidence trigger between the β telescope and the MCP is implemented. The ion TOF is plotted in Figure 4.45a. In this figure, the timing zero is already adjusted properly (see Section 4.15). The peak near 0 ns corresponds to those events that the β telescope and the MCP are both triggered by fast particles like back-

[3]The compositions of the Penning ions are complex, but the predominant one is H_2^+.

scattered β particles. Therefore, this peak also needs to be ruled out. A cut TOF>10 ns was imposed when generating the Q_{MCP} spectrum for ^{6}Li ions in Figure 4.42.

For the Q_{MCP} versus ion energy study, it is impossible to generate a mono-energetic ^{6}Li ensemble using the non-trapped ^{6}He source. The final energy of the recoil ions has a broad distribution because of the broad decay-position distribution. However, the average ion energy can be modified by applying cuts on the TOF spectrum. We studied the ion energy distribution with three TOF cuts shown in Figure 4.45a. According to the Monte Carlo simulation, the final ion energy distributions with these three TOF cuts are shown in Figure 4.45b.

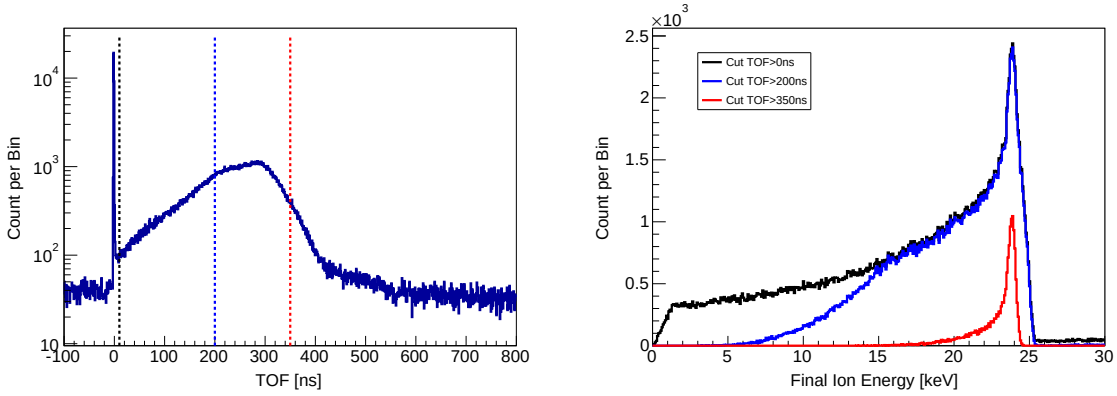

(a) (b)

Figure 4.45: (a) TOF spectrum with cuts indicated. (b) Final recoil-ion-energy distribution with cuts TOF>10 ns, TOF>200 ns and TOF>350 ns.

The Q_{MCP} spectra under conditions 200 ns<TOF<350 ns and 350 ns<TOF<600 ns are plotted in Figure 4.46. In these cases the average final ion energies are 19.19 keV and 22.81 keV respectively. The two Q_{MCP} spectra are fit to the EMG function. The Q_{MCP} peak position (the μ parameter of the EMG function) for the high average ion energy case is larger than the other one by about 4%, which is also negligible concerning the MCP efficiency variation.

In summary, all Q_{MCP} spectra for ions with energy from ~7 keV to ~25 keV fit well to the exponentially modified Gaussian function. The Q_{MCP} peak position increases with

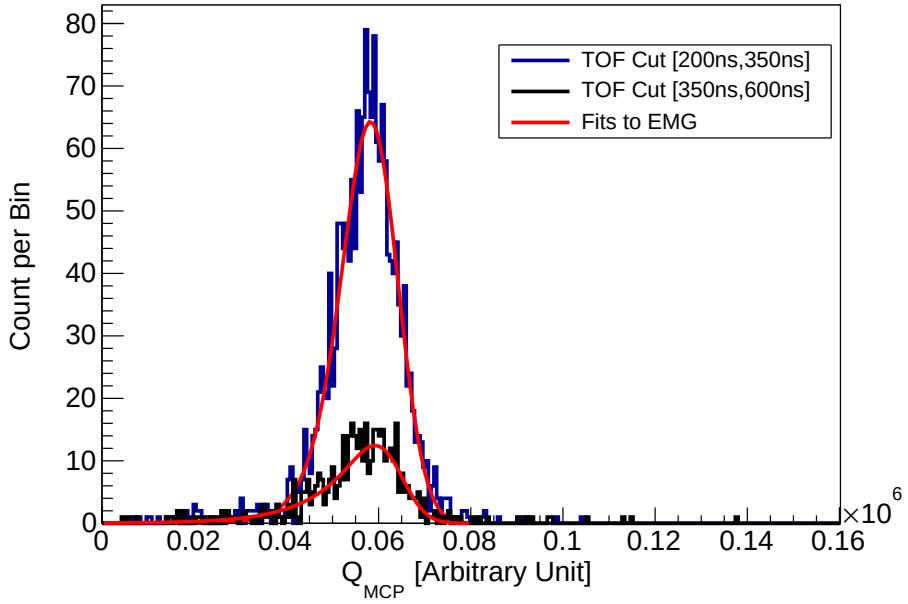

Figure 4.46: Q_{MCP} spectra for two TOF cuts. A coincidence trigger between the β telescope and the MCP is imposed.

the ion energy for one species of particles, but it only increase by ∼5% when the ion energy changes from 7 keV to 15 keV. The Q_{MCP} peak positions for different species of particles vary up to ∼7%. All these changes are negligible concerning the MCP efficiency variation. Furthermore, these changes are about 20% of the FWHM of the Q_{MCP} peak, the Q_{MCP} cannot resolve ion species or ion energy.

4.10.3 Q_{MCP} spectrum versus position

We inspected all Q_{MCP} spectra for α-particles and ^{6}Li ions in each square regions (with the boundaries of the grid lines) of the MCP, and four typical ones are shown in Figure 4.47. It is clear that the average Q_{MCP} values are significantly different from position to position, indicating that the gain is not uniform. All ^{6}Li-ion Q_{MCP} spectra have the EMG function shape. The α-particle Q_{MCP} spectra have a double peak structure in some square regions like the one centered at (−20 mm, −24 mm). Particularly, the α-particle Q_{MCP} spectral

shape in the square region at coordinate (−8 mm, −8 mm) is much broader than that in any other regions. This anomaly is caused by the MCP gain variation versus incident angle, which is discussed in Subsection 4.10.4.

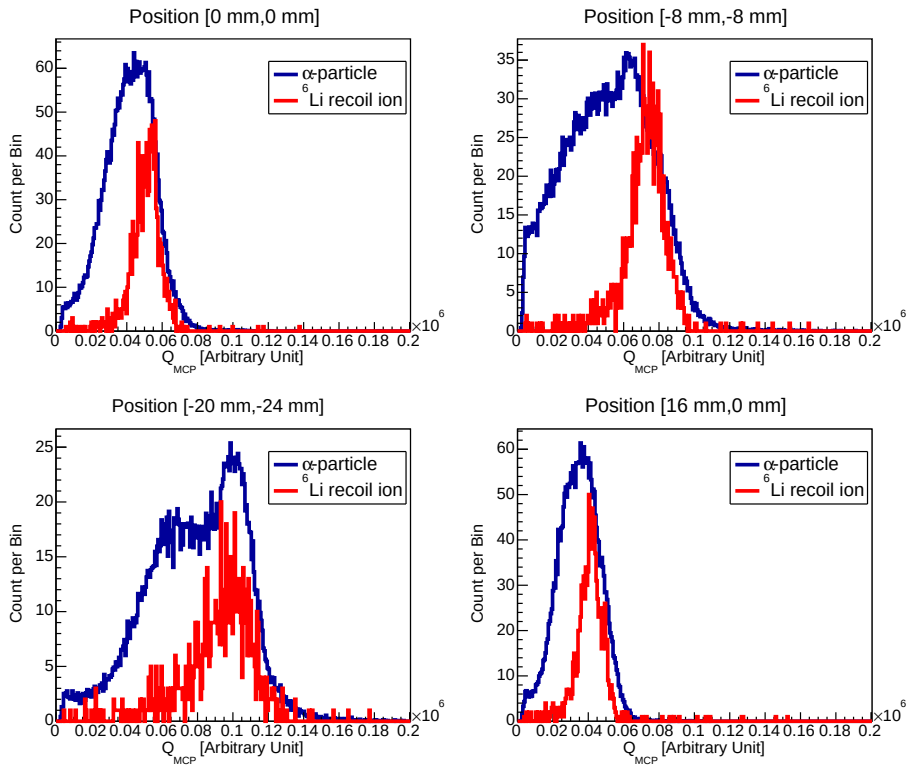

Figure 4.47: Q_{MCP} spectra for α-particles and ^{6}Li ions at four square regions. For the measurement with ^{6}Li a coincidence trigger with the β telescope is imposed.

If we assume that the number of initial electrons generated by the primary particles is the same across the whole MCP, the average Q_{MCP} value is proportional to the MCP gain. To visualize the gain variations over the entire MCP area, the average Q_{MCP} values for α-particles in all active square regions are plotted in Figure 4.48a, and those for ^{6}Li ions are plotted in Figure 4.48b. Despite the spectral shape differences, the average Q_{MCP} values for the α-particles and ^{6}Li ions varies together, following the same trend. The highest gain is about three times the lowest gain. The impact of the gain non-uniformity on the MCP efficiency is discussed in Section 4.12.

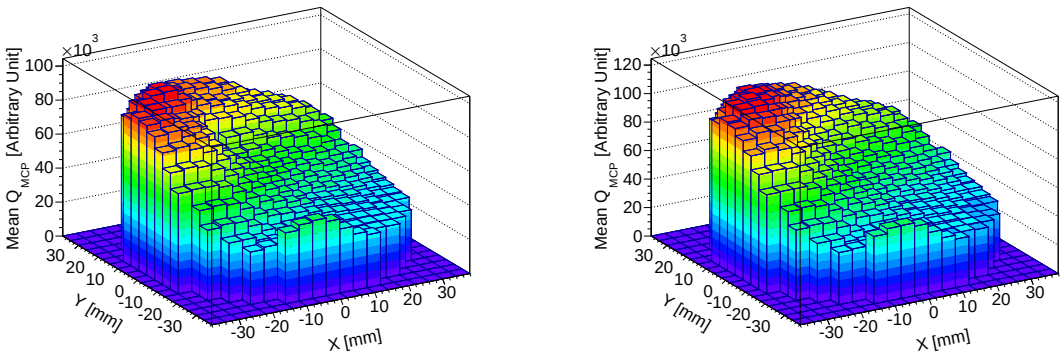

(a) (b)

Figure 4.48: (a) Q_{MCP} average versus position for α-particles. (b) Q_{MCP} average versus position for recoil ^{6}Li ions from non-trapped ^{6}He source.

4.10.4 MCP spectra versus incident angle

The micro-channels in the MCP are at 8° from the normal direction of the MCP surface. Therefore, most of the incoming particles that fall into the channel hit the wall of the channel and generate initial electrons for multiplication. However, if the incoming particle travels nearly parallel to the channel direction, it will undergo fewer collisions with the channel wall and generate fewer initial electrons. Thanks to the chevron configuration of the MCP stack, even if the incoming particle misses the first channel, it still hits the wall of the channel in the bottom layer. However, in this case the gain of the MCP is greatly reduced because half of the channel length doesn't contribute to the multiplication. Therefore, the gain of the MCP is expected to vary substantially versus incident angle when the incoming particles are close to parallel to the channels.

Before explaining the broadened Q_{MCP} spectral shape in the region at (−8 mm, −8 mm), we inspected the distribution of width of the Q_{MCP} spectrum over the whole MCP active area. The *reduced RMS* is defined as the ratio between the RMS and the mean of the Q_{MCP} spectrum. The reduced RMS is sensitive to the local gain non-uniformity, and the smooth variation of the gain is canceled by taking the ratio. The reduced RMS of the Q_{MCP} spectrum for each square region is plotted in Figure 4.49a. The reduced RMS near

(−8 mm, −8 mm) is significantly larger than other regions. We attribute this effect to the gain variation caused by the incident angle. If it is true, then the tracks of the α-particles that hit this region are close to parallel to the channel direction.

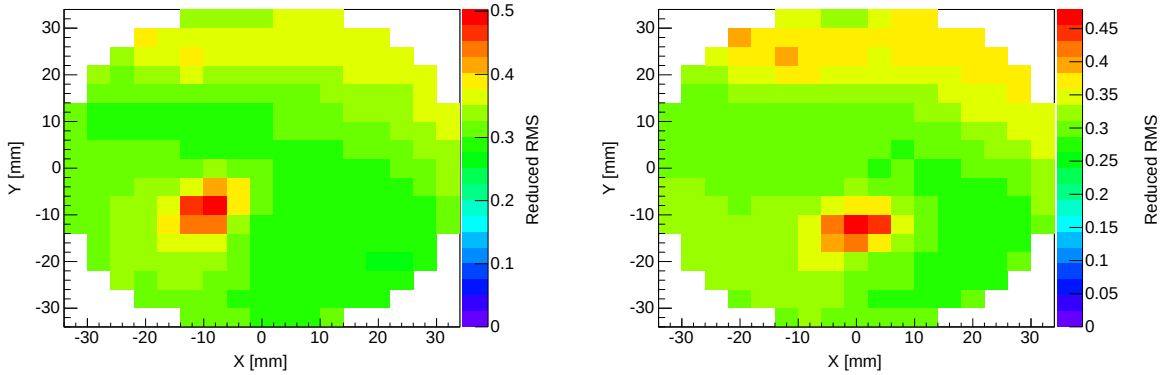

(a) (b)

Figure 4.49: (a) Distribution of the Q_{MCP} reduced RMS. (b) Distribution of the Q_{MCP} reduced RMS after moving the source by 8 mm.

In order to test this explanation, we moved the ^{241}Am source out by 8 mm, and plotted the reduced RMS distribution in Figure 4.49b. After taking into account the rotations of the MCP relative to the chamber and the direction of the magnetic transporter, the source-moving direction is −22.5° from the X direction of the MCP coordinate system. Comparing Figure 4.49a and Figure 4.49b, we found the position of the largest reduced RMS roughly moves in the same way as the source. Therefore, we confirmed that the large reduced RMS is hit-angle related, not intrinsic to the region centered at (−8 mm, −8 mm).

To further inspect the influence of the impact angle on Q_{MCP}, we constructed a 2D histogram of the average Q_{MCP} versus position with finer binning as shown in Figure 4.50. The region near (−8 mm, −8 mm) does have a lower average Q_{MCP} than the neighboring area by ∼50%. According to the study described in Subsection 4.12.2 a gain variation at this level does not affect the efficiency of the MCP. Thus, the MCP gain dependency on the impact angle is not included in the data analysis in Chapter 6.

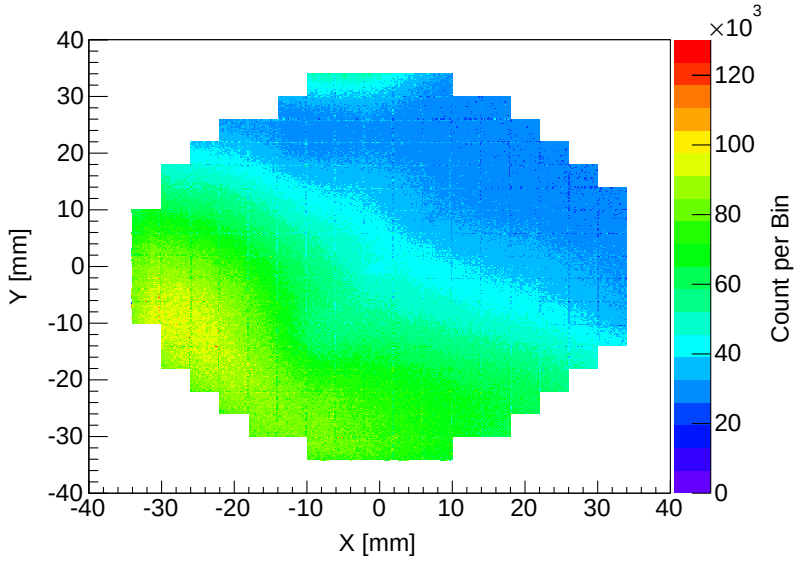

Figure 4.50: Average Q_{MCP} versus position 2D histogram with finer binning.

4.11 MCP position responses to electrons and ions

The position response of the MCP is calibrated using the 5.5 MeV α-particles. It is important to make sure that this calibration is valid for electrons and ^{6}Li ions. In this section the MCP position responses to electrons and ^{6}Li ions are studied. The position calibration using non-trapped ^{6}He source is also introduced.

4.11.1 MCP position response to electrons

To study the MCP response to electrons, we used β particles from the ^{90}Sr source and conversion electrons from the ^{207}Bi source. Calibrations based on the ^{241}Am run were implemented for these two studies. For the study using the ^{207}Bi source, the thin window side of the source is facing the MCP and the coincidence trigger with the scintillator-PMT assembly is required so that the MCP is triggered by the conversion electron while the scintillator-PMT assembly detects the γ ray generated in the same cascade decay. In this way X-rays from the ^{207}Bi source are vetoed. The MCP position spectra for these two cases are shown in Figure 4.51. In Figure 4.51a, the grid lines are visible but blurred. Most of

the β particles penetrate the 50 μm nickel mask, and only those β particles with kinetic energy less than ~175 keV are stopped by the mask. The β-energy spectra of ^{90}Sr and ^{90}Y are continuous, so the low-energy tail results in the blurred grid lines in Figure 4.51a. The conversion electrons from the ^{207}Bi source have energies of 465 keV and 975 keV, and they all penetrate through the mask. Therefore grid lines are not visible in Figure 4.51b.

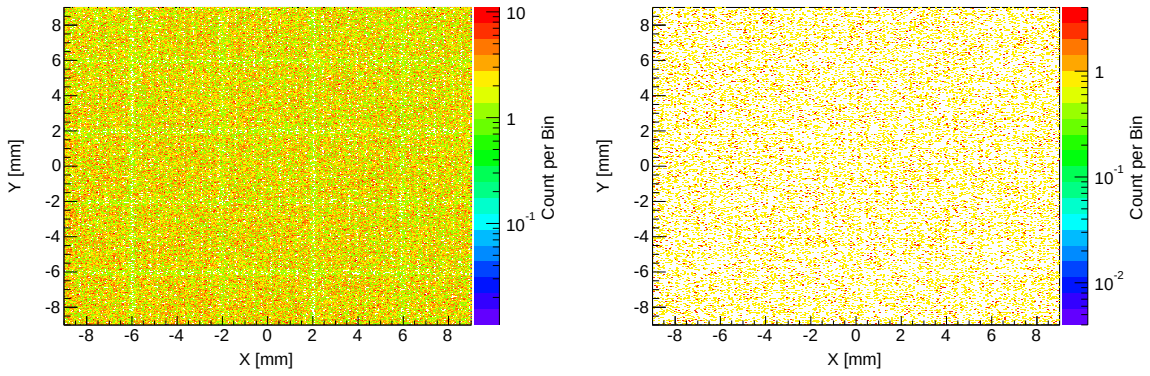

(a) (b)

Figure 4.51: (a) MCP position spectrum for the ^{90}Sr source. (b) MCP position spectrum for the ^{207}Bi source.

Because the contrast of the grid structures in Figure 4.51a is too low, the method developed in Section 4.9 cannot determine the grid line position precisely. Therefore, we projected the MCP position spectrum for the ^{90}Sr source to the X and Y axis as in Figure 4.52 . The positions of the dips correspond to the grid line positions. For both X and Y projections, the dip positions deviate from the standard positions by ~15 μm near the center and up to ~50 μm near the edges. The depth of the dips is proportional to the fraction of blocked β particles. According to Figure 4.52, ~43% of the β particles from the ^{90}Sr source are blocked by the mask. ~43% of the ^{90}Sr-^{90}Y β-energy spectrum corresponds to ~250 keV instead of 175 keV. The extra attenuation is probably due to electron straggling inside the nickel mask. For ^{6}He decay, the β-energy spectrum below 250 keV is only 3% of the whole spectrum. If the β particles are the only particles hitting the MCP, the depth of the dips in Figure 4.52 should be only 3% of the counts nearby.

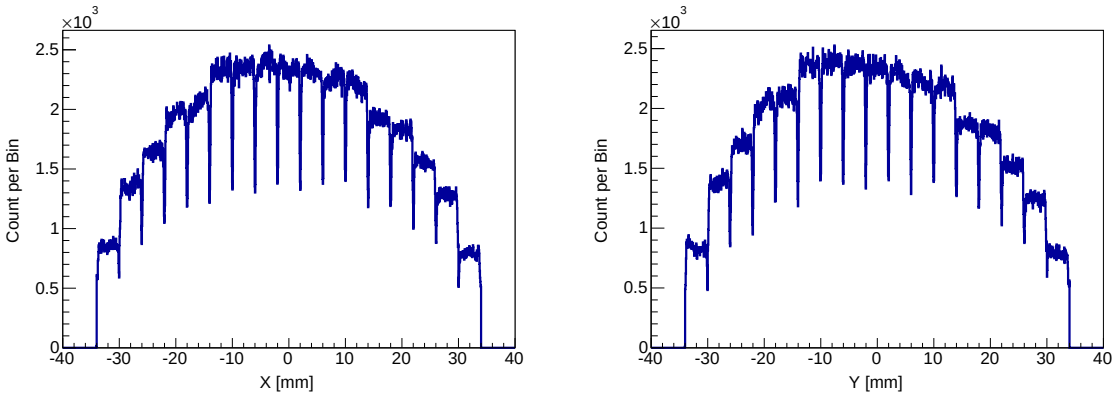

(a) (b)

Figure 4.52: (a) X projection of the MCP position spectra for ^{90}Sr source. (b) Y projection of the MCP position spectra for ^{90}Sr source.

4.11.2 MCP position calibration using the non-trapped ^{6}He source

We constructed the MCP position spectrum when the non-trapped ^{6}He source is introduced to the MOT-2 chamber. In this study no coincidence with the β telescope is imposed, so the events generated by the β particles from the ^{6}He decay are included. Because most of the β particles penetrate through the mask, the contrast of the grid lines (*i.e.* the count density outside the grid area over that inside the grid area) is 6:1, worse than that for α-particles. According to the study in Subsection 4.11.1, 3% of the β particles from the ^{6}He decay are blocked by the mask. Therefore, the β-particle contribution to the grid line shadow is 0.5%, negligible compared to the contribution of the ^{6}Li recoil ions. Then in this case, the calibration algorithm developed in Section 4.9 is still valid. The only difference is that the fit value of B in Equation 4.9 is higher than that in the case of α-particles.

With the full production rate of the ^{6}He, the counting rate of the MCP is ∼90 kHz, and in approximately 15 min, 7.8×10^7events are collected. After applying all calibration procedures described in Section 4.9, we achieved the same accuracy and resolution as those when using α-particles. The distributions of deviations and resolutions are shown in Figure 4.53. To visualize the calibration result, the counterpart of Figure 4.39 for this calibration is plotted in Figure 4.54. As mentioned above, Equation 4.9 fits well to the projection histogram

near the grid line, and the count density inside the grid line region is ∼1/6 of that outside the grid region.

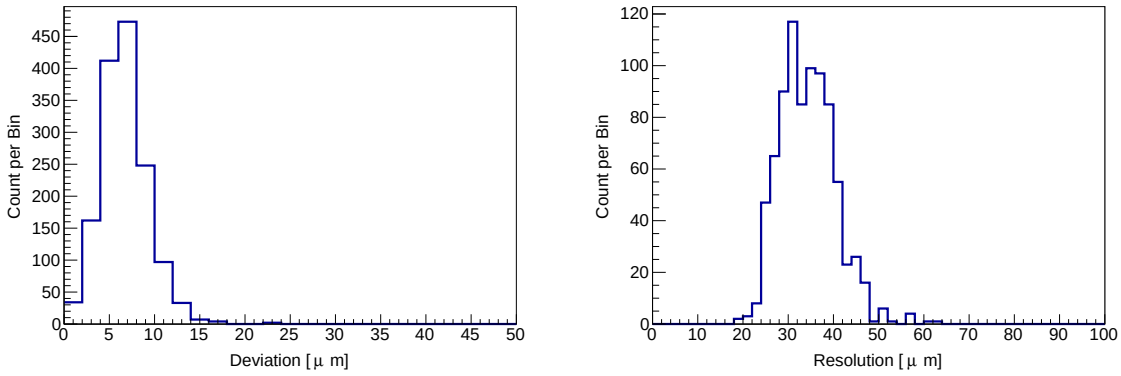

(a) Statistics of deviations (b) Statistics of resolutions

Figure 4.53: Statistics of deviations and resolutions for the calibrated MCP position spectrum of the non-trapped ^{6}He source.

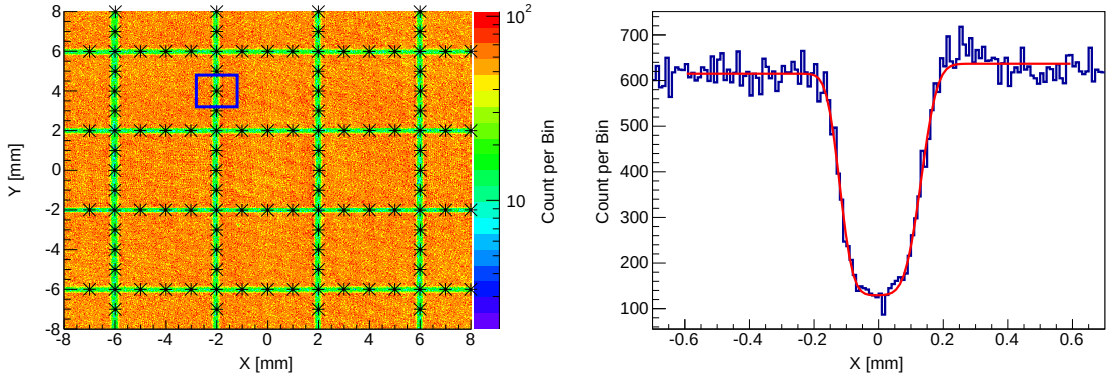

(a) (b)

Figure 4.54: (a)Calibrated MCP position spectrum using non-trapped ^{6}He source. (b) Projection of the region shown in (a) onto the X axis. The red line is the fit-function defined in Equation 4.9.

Furthermore, we inspected the consistency between the calibration using the ^{241}Am source and the calibration using the non-trapped ^{6}He source. We first constructed the cor-

rection functions based on a run with the ^{241}Am source, and then applied these correction functions to the run with the non-trapped ^{6}He source. The procedure described in Subsection 4.9.3 is carried out and the statistics of the deviation and resolution are shown in Figure 4.55. The distribution of the resolution is broader than that of the self-calibration case, but the mean resolution is still $\sim$36 μm. However, the mean deviation becomes 31.89 μm and it distribution is much broader and extends to 100 μm.

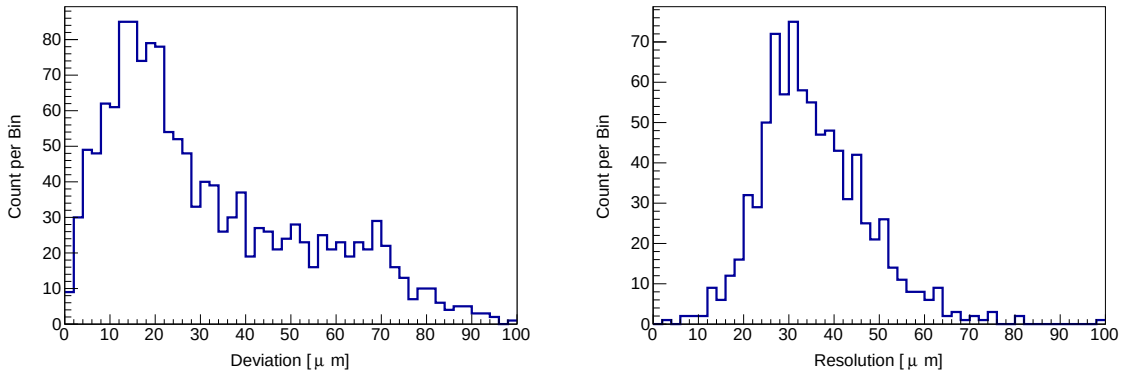

(a) Statistics of deviations

(b) Statistics of resolutions

Figure 4.55: Statistics of deviations and resolutions for the MCP position spectrum of the non-trapped ^{6}He source calibrated based on the ^{241}Am run.

The difference between these two calibration schemes is not fully understood. It could be caused by any differences between 5.5 MeV α-particles and $\sim$10 keV ^{6}Li ions. For example, the α-particles impact deeper than the ^{6}Li ions and this may result in difference pulse shape, and then the timing and position reconstruction are affected. We chose to use the non-trapped ^{6}He source to calibrate the MCP position response during the ^{6}He decay $\beta - \nu$ correlation experiment. First of all, concerning particle type and energy, the ^{6}Li ions from trapped ^{6}He decays are more similar to those from non-trapped ^{6}He decays than to the 5.5 MeV α-particles. Secondly, it is more convenient to use the non-trapped ^{6}He. They are easily introduced to the MOT-2 chamber without the need to break the vacuum, and thus the ^{207}Bi source can be permanently installed on the magnetic transporter to calibrate the β-telescope response every day. Thirdly, the run with non-trapped ^{6}He atoms is also useful

for other calibrations like the MCP efficiency uniformity. One may still be concerned about the β-particle contamination to the calibration in this scheme. In the next subsection, we verified that this calibration scheme is valid for pure ^{6}Li ions.

4.11.3 MCP position response to ^{6}Li ions from the non-trapped ^{6}He source

In this subsection, the MCP position response study is still based on the run with non-trapped ^{6}He source, but the coincidence trigger between the MCP and the β telescope is required. The coincidence trigger rate is about 220 Hz, so it takes about 13 hours to accumulate 10^7 events. Therefore, it is not efficient to use these data to achieve the high-accuracy MCP position response calibration. In this study we use the data from the same run without the coincidence trigger to construct the position correction functions and then apply them to the data with the coincidence trigger. Furthermore, in order to veto the events generated by the back-scattered β particles, a TOF cut 10 ns<TOF<500 ns is imposed.

With all the conditions and calibrations mentioned above applied, the MCP position spectrum is constructed and plotted in Figure 4.56. The contrast of the grid lines is as good as the α-particle spectrum of Figure 4.39a.

However, due to the low statistics it is not possible to determine all grid line cross points and three extra points on each segment with high precision. To inspect whether the calibration using the MCP events generated by both ^{6}Li ions and β particles is still valid for the events generated only by ^{6}Li ions, we project the 2D MCP position spectrum onto the X and Y axis as in Figure 4.57. Then the positions of the dips are determined through a fit to a quadratic function, and the average deviation of the dips from their ideal positions is 8.6 μm in both the X direction and Y direction. This is consistent with the calibration accuracy. Therefore, we infer that the calibration using the non-trapped ^{6}He source without the coincidence trigger with the β telescope is still valid for pure ^{6}Li ions from the non-trapped ^{6}He decays.

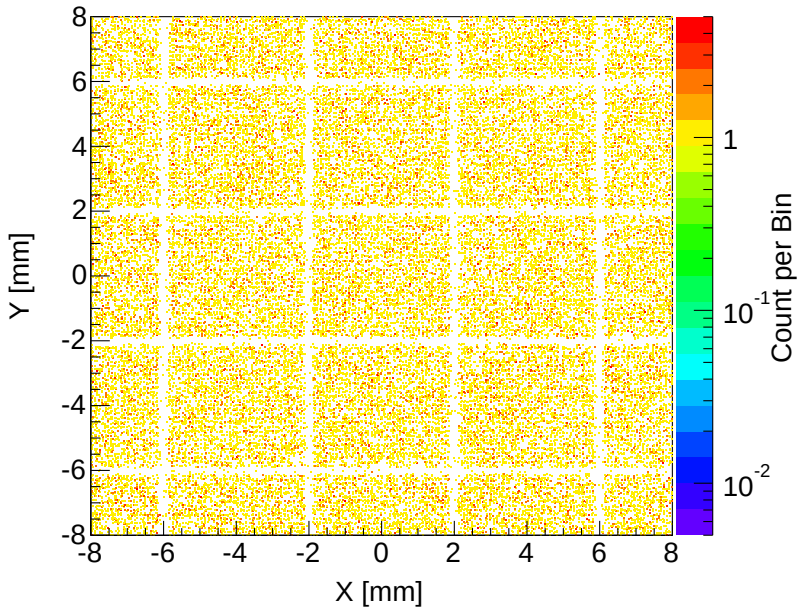

Figure 4.56: MCP Position spectrum with coincidence trigger and TOF cut [10 ns, 500 ns] applied.

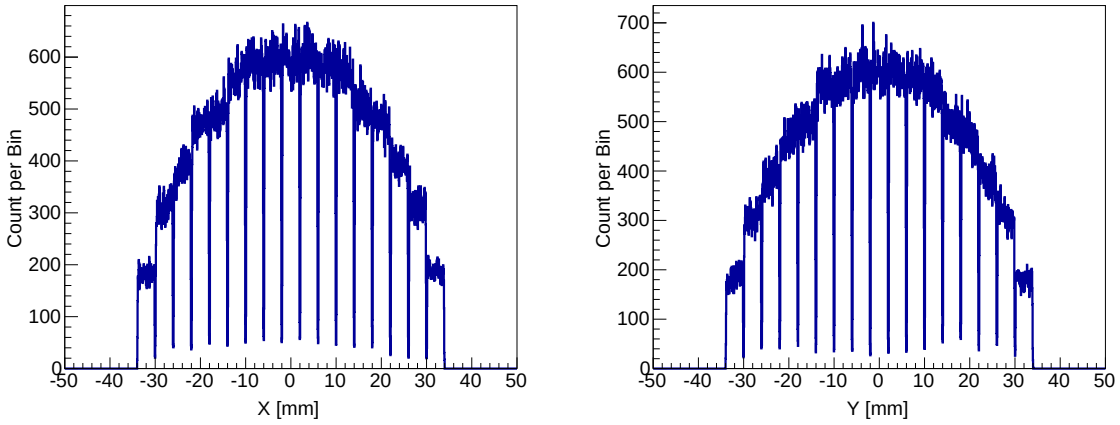

(a) (b)

Figure 4.57: (a) X projection of the MCP position spectra for ^{6}Li ions. (b) Y projection of the MCP position spectra for ^{6}Li ions.

4.12 MCP efficiency measurement

4.12.1 Overall efficiency

The overall efficiency does not affect the TOF spectrum, so it doesn't contribute to the systematic uncertainty of $a_{\beta\nu}$. However, it is still important to verify that the overall efficiency of the MCP is close to the designed value, and to make sure that there is no substantial data loss due to the MCP efficiency. The channel opening area is 50%, so we expect the overall efficiency to be close to 50%.

The ^{241}Am source is held ∼85.0 mm above the MCP, and the solid angle of active area of the MCP (shown in Figure 4.37) is 0.146. The activity of the source is 1 μCi, so the α-particles hit the active area of the MCP at 5.40 kHz. The measured rate of events inside the active area is 2.8 kHz. Thus, the overall efficiency of the MCP is approximately 51.9%, and it is very close to 50% as expected.

4.12.2 Efficiency uniformity

It is important to understand the efficiency uniformity of the MCP. For the decays of trapped ^{6}He atoms, the TOF of the recoil ions and their landing positions are correlated. If the MCP efficiency is not uniform, the TOF spectral shape will be distorted and thus the $a_{\beta\nu}$ extraction becomes inaccurate.

Though many factors can affect the MCP efficiency, like the particle type and incident angle, most of them affect the MCP efficiency through the signal size. If the average signal size in one region is smaller, the event loss due to the threshold is larger so that the efficiency in this region is lower. The average signal size distribution across the MCP is studied using the ^{6}Li ions from the non-trapped ^{6}He source in Subsection 4.10.3. However, the distribution shown in Figure 4.48b is based on the average Q_{MCP}, not the peak value of the fitted EMG function. In order to obtain a better determination of the event loss due to threshold in each region, the Q_{MCP} spectrum in each square region is fitted to the EMG function defined in Equation 4.11. The kept-ratio is defined as:

$$R_{kept} = \frac{\int_{Theshold}^{+\infty} f(Q_{MCP}) dQ_{MCP}}{\int_{-\infty}^{+\infty} f(Q_{MCP}) dQ_{MCP}} \tag{4.12}$$

where the function f is the EMG and its parameters are set to the fit values. This kept-ratio is used as the estimator of the ratio of events above the threshold in that square region. The kept-ratios of all active square regions are plotted in Figure 4.58, and R_{kept} varies across the whole active MCP area by $\sim$0.16%.

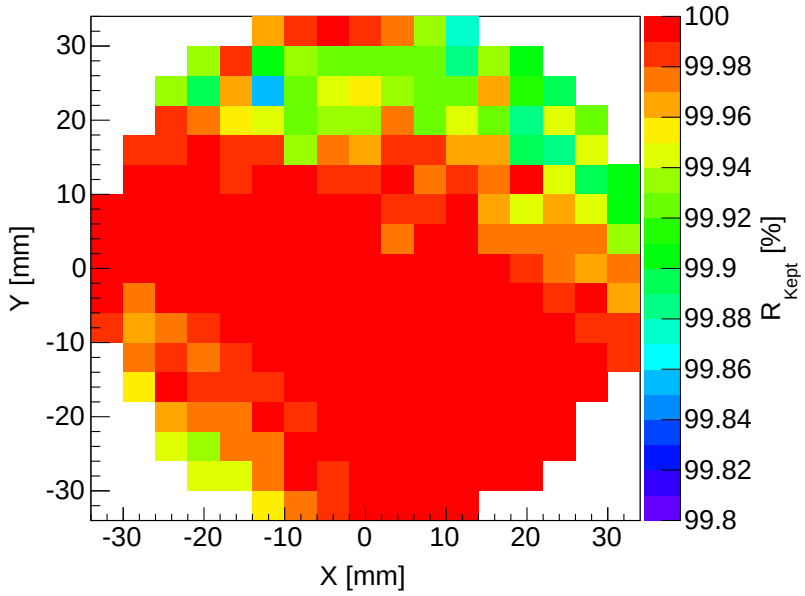

Figure 4.58: R_{kept} for each active square region.

Besides the event loss due to threshold, the MCP efficiency can still depend on other factors. The position resolution of the MCP is larger than its channel size, so it cannot tell whether each channel is working properly. If some channels are inactive due to blocking or damaging, the Q_{MCP} spectral shape is not affected but the MCP efficiency depends on the number of inactive channels in that area. If a big enough dust particle falls on the surface of the MCP, it blocks many channels and usually it is visible on the MCP position spectrum, and they are called *dark points*. One example of dark point is shown in Figure 4.59. During the data taking time for the $a_{\beta\nu}$ measurement four dark points were found, and their positions did not change for the whole data taking period. In the data analysis of the $a_{\beta\nu}$ measurement, the 0.5 mm$\times$0.5 mm area around each dark point is ruled

out, so that these dark points don't affect the $a_{\beta\nu}$ extraction[4].

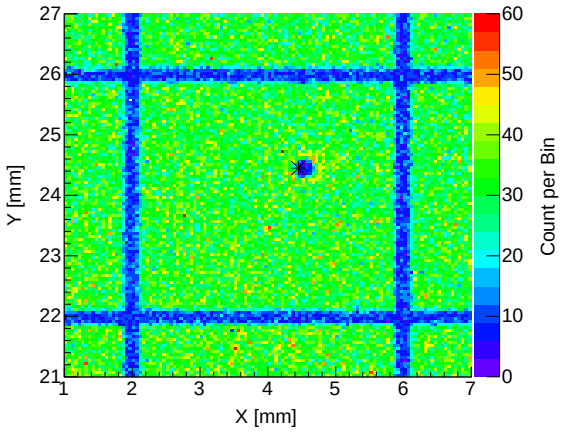

Figure 4.59: One dark point on the MCP. The calibration program determines its position and labels it with "∗".

To estimate the MCP efficiency non-uniformity caused by other reasons like the invisible inactive channels, we compared the measured MCP position spectrum using the non-trapped ^{6}He source without the coincidence trigger with the β telescope and the simulated one under the same conditions. The detailed procedure is described as follows. First the distribution of events generated by β particles is assumed to be uniform. The event density across the whole MCP active area is estimated by averaging the event density inside the grid line shadow. Then this uniform *background* is subtracted from the 2D MCP position spectrum. For each active square region, its efficiency is defined as the ratio between the measured counts and simulated counts inside this area. The highest ratio is normalized to 1, and the relative efficiency map of the MCP is shown in Figure 4.60a. The statistics of the relative efficiencies in different square regions is shown in Figure 4.60b. The distribution of the relative efficiency can be fitted to a Gaussian function, and its standard deviation is 0.85%. The uncertainty of the efficiency of each square region is ∼0.22%, so the efficiency fluctuation from region to region is ∼0.82%. This efficiency fluctuation is much larger than

[4]In the proof-of-principle run, these dark points were not ruled out because they don't affect the result of $a_{\beta\nu}$ at the ∼2% level.

that estimated by Figure 4.58, indicating that the Q_{MCP}-irrelevant factors dominate the MCP efficiency non-uniformity. To estimate the higher limit of the impact of the MCP efficiency non-uniformity on the $a_{\beta\nu}$ extraction, in Chapter 5 and Chapter 6 we will use Figure 4.60a as the MCP efficiency map in the analysis.

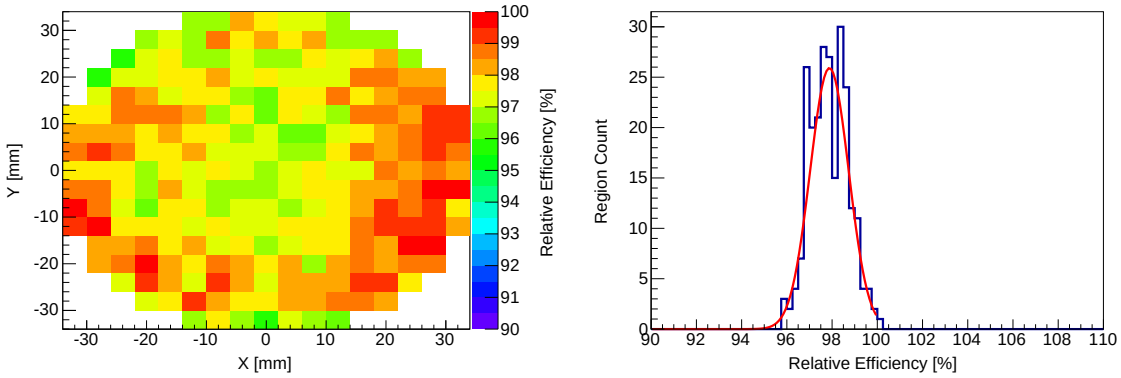

(a) (b)

Figure 4.60: (a) Estimated MCP efficiency map. (b) Statistics of the efficiency in different square regions.

4.13 Calibrations of the Ion-accelerating field and MOT-MCP distance

The ion-accelerating field (the E-field) is calculated by the COMSOL software based on the measured dimensions of the electrode structure and the bias voltages applied to them. The detailed procedures of determining the electrode geometry and the voltages are described in the Subsection 4.13.1 and Subsection 4.13.2, and the E-field calculation is described in Subsection 4.13.3. The MOT-MCP distance is measured using an imaging system described in Subsection 4.13.4. In Subsection 4.13.5, the measurement of the TOF of the nitrogen laser generated photoions is described, and this method provides a consistency check of the modeling of the E-field and the MOT-MCP distance measurement.

4.13.1 Mechanical inspection of the electrode structure

After the MCP system and the electrodes that generate the E-field are all assembled and mounted in position, the distances between electrodes and the thicknesses of the electrodes are measured using standard measuring blocks and micrometers as in Figure 4.61b. The distances between electrodes are measured at the four positions indicated in Figure 4.61a. According to the measurements, the thickness, position and tilting of the electrodes are summarized in Table 4.2. The measured thickness and position of each electrode is fed to the COMSOL program to calculate the E-field. The accuracy of the thickness and electrode spacing measurements is $\sim$25 μm, and the related systematic uncertainty in $a_{\beta\nu}$ is studied using the simulation. Because the tilting is very small, we don't take it into account when generating the E-field for the $a_{\beta\nu}$ extraction, but we studied the systematic uncertainty caused by it. The details of these measurements are listed in Table 4.2.

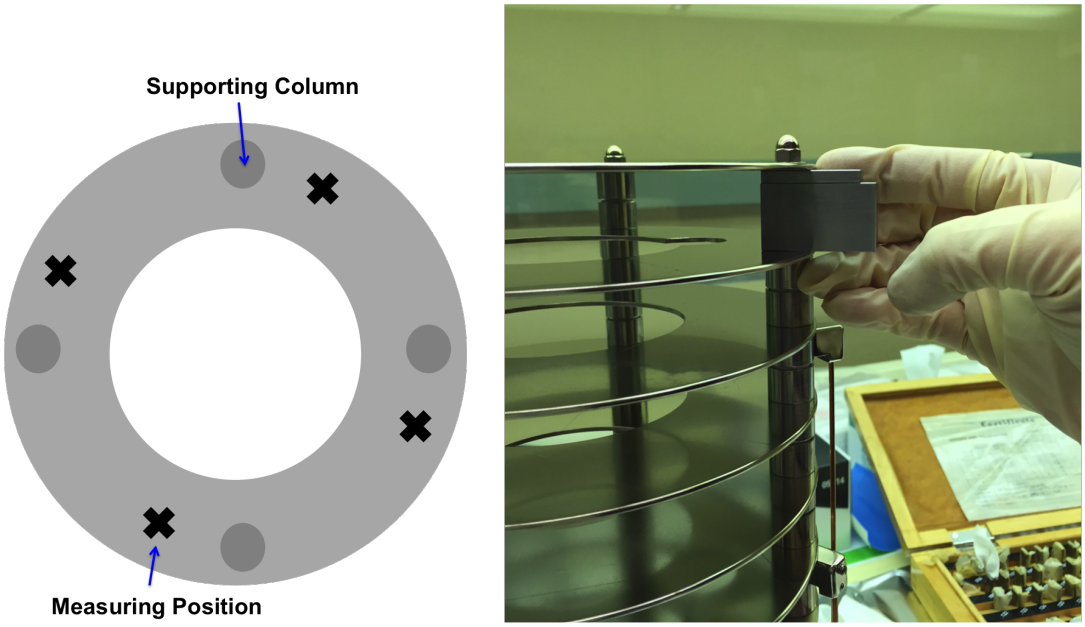

(a) (b)

Figure 4.61: (a) Azimuthal positions where the electrode distances are measured. (b) Stack of measuring blocks inserted between electrode plates.

	Thickness (mm)	Position (mm)	Tilt angle (°)
Electrode 6	1.861	155.864	0.10
Electrode 5	1.854	130.143	0.084
Electrode 4	1.848	104.340	0.056
Electrode 3	1.857	78.491	0.051
Electrode 2	1.835	52.692	0.062
Electrode 1	1.838	26.859	0.041
MCP holder	1.962	0.981	0.009

Table 4.2: The thickness, position and tilting angle (from normal vector to the positive Z direction) of the electrodes.

4.13.2 Voltage calibration

The voltage output of the power supplies and the leakage currents are monitored through the readout system of the power supplies. The accuracy of the voltage output monitor of the power supplies is ∼1%. As shown in Chapter 6, this results in a large systematic uncertainty. In order to achieve a more accurate determination of the voltages on the electrodes, we connect the top electrode to a CPS HVP-250 high-voltage probe. This probe is a voltage divider with input impedance 1 GΩ and voltage ratio 10000:1. Its accuracy is <0.05% from 0 to 50 kV. The output of the probe is connected to a high-accuracy (0.002% for 1 to 10 V range) digital voltmeter (BNC 1201) with 10 GΩ input impedance as required by the CPS HVP-250 probe. The probe draws ∼22 μA when the HV biasing is turned on, and the presence of the probe doesn't affect the output voltage from the power supply.

During the experiment, the output of the probe system is monitored by a LabView program. We observed that the output voltage of the top electrode drifts by up to 5 V during the first hour whenever the setting voltage is adjusted. After this warm-up period, the output fluctuates up to 1.5 V around a constant value. The percentage of both the warm-up drift and the long-term drift is less than 0.025% and it causes negligible systematic uncertainty in the $a_{\beta\nu}$ extraction. To avoid the large drift during the warm-up period,

measurements are usually done 2 hours after the settings to the power supplies are changed.

4.13.3 E-field calculation and optimization

The measured dimensions and positions of the electrode plates are used in the geometry setup of the COMSOL program. Besides the electrode plates, the supporting columns, the chamber wall and the bottom part of the β-telescope chamber are also included in the geometry setup. We calculated the positions of the beryllium window and its holder based on the design drawings of the chamber and the measured distance from the MCP holder (bottom electrode) to the floor of the bottom flange.

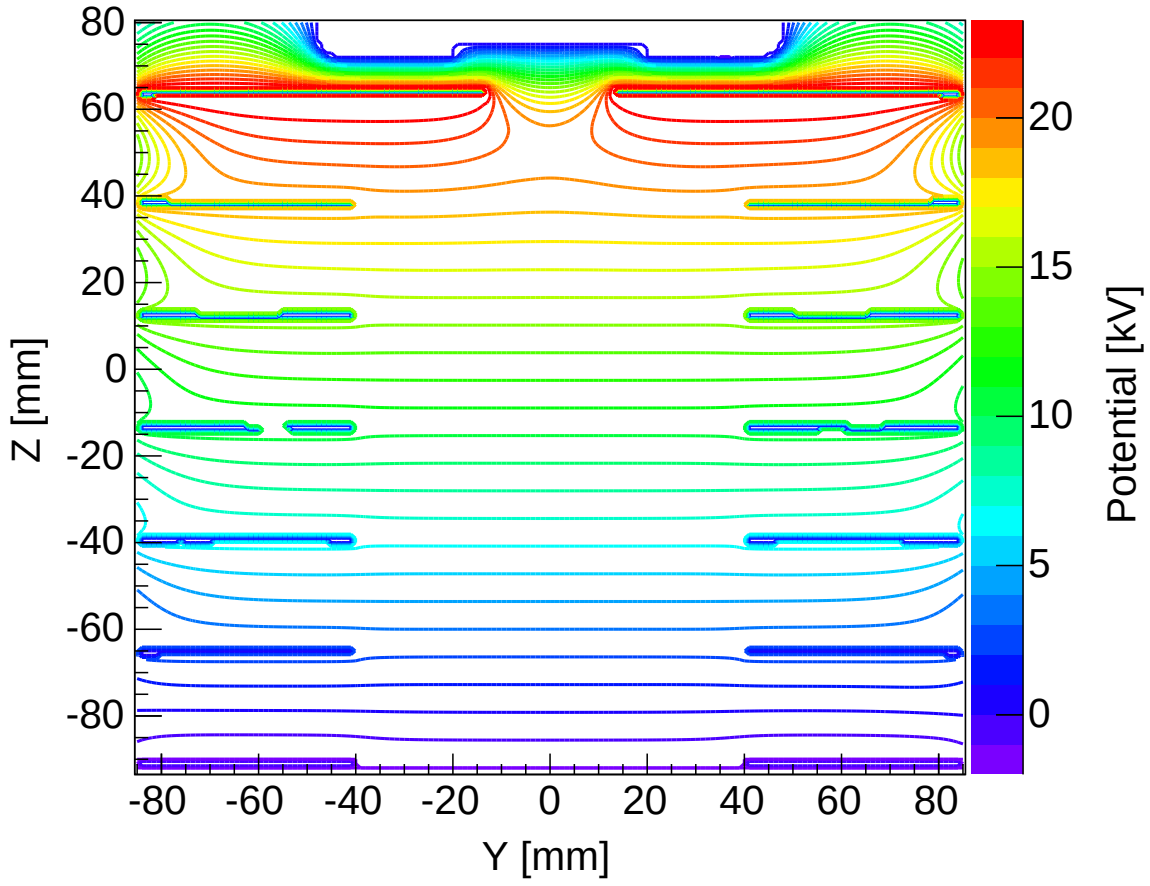

Figure 4.62: Ion-accelerating field equipotential surfaces in the Y-Z plane.

After the geometry is setup in the COMSOL program each conductor volume is set to a potential, and then the electric field is calculated. We output the electric field strengths and potentials to a file at grid points spaced by 1 mm in each dimension. This saved electric field information is used by the ion-tracking program described in Chapter 5. There are many electrode voltage settings being used throughout the whole experiment for different purposes, and the electric fields for these settings are all calculated. Particularly, using the measured geometry setup we optimized the electrode voltage settings so that the electric field is as uniform as possible along the Z axis (from 8 mm above the MOT to the MCP surface). The equipotential surfaces of the optimized field in the Y-Z plane is shown in Figure 4.62. Figure 4.63 shows E_Z as a function of Z when X is kept at 0 and Y is at 0 mm, 5 mm, 10 mm, 15 mm and 20 mm. Along the Z axis (X=0 mm,Y=0 mm) E_Z varies up to 0.64% from the MOT to the MCP, while at 20 mm away from the Z axis E_Z varies up to 1.5%.

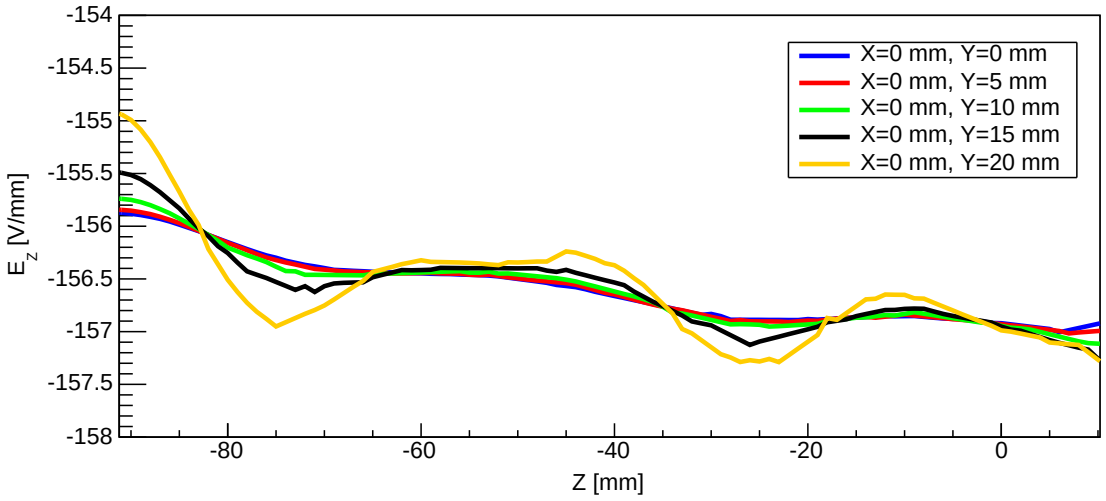

Figure 4.63: E_z as a function of Z at different Y coordinate.

The power supplies are set to the voltages for the optimized E-field. To achieve the accuracy as good as the probe, we connected the probe to each electrode and tuned the setting values so that the probe reads the same voltage as the desired value for the optimized

E-field. During this process, we took into account the warm-up drift effect. Because the drift is repeatable and well defined, we configured the power supply setting so that the stabilized voltage output is the same as the desired value. During the $a_{\beta\nu}$ measurements, the data from the top electrode voltage monitor (by the probe) is used for corrections and the corrected voltages are used to calculate the E-field for generating the fit templates.

4.13.4 Z_{MOT} measurement

An imaging system was constructed to measure the MOT-2 position. A lens is inserted from a view port on the MOT-2 chamber and an iris is mounted to this view port so that the image of the MOT is on the iris plane. One camera is installed and focused on the iris plane. The camera is sensitive to the 1083 nm infrared light scattered from the atoms in the MOT-2. In order to calibrate the camera image for measuring the MOT position and size, we placed a ruler at the MOT position. We machined a ruler which is shown in Figure 4.64a. The top cap fits the inner diameter of the top electrode so that the ruler is held vertically by the top electrode. On the flat surface of the bottom part, grid lines separated by 500 μm are engraved by a laser-cutter. Big circles and half-way tick marks are also engraved in the center region of the grid system so that it is easy to identify the absolute positions on the camera image. The accuracies of both the grid line spacing and the distance between the center of the grid system to the top cap are 25 μm. Combined with the results of the mechanical inspection on the electrode system, the distance between the ruler center to the MCP is well determined. To carry out this calibration procedure, the ruler was placed on the top electrode right after the whole assembly of the MCP and the electrodes is mounted to the MOT-2 chamber. The top of the MOT-2 chamber is temporarily sealed with a blank flange, and then the chamber is pumped to vacuum. We took pictures using the camera with different iris sizes. Figure 4.64b shows a picture with a large iris size. This picture is upside-down due to the imaging system. The biggest engraved circle at the center is visible so that the absolute positions of the grid system in this image is known. However, there is a big distortion in the lower part of the image because this area is too far from the lens principal axis. Therefore, in the following analysis of the iris center and MOT position

determination, the iris size is kept small.

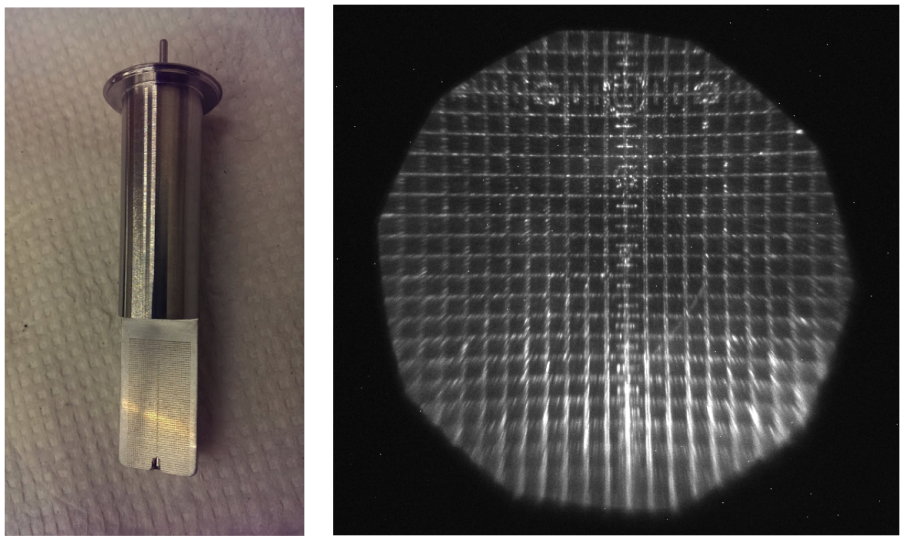

(a) (b)

Figure 4.64: (a) Ruler with engraved grid lines. (b) Ruler image created by the camera.

The camera outputs images in bitmap (bmp) format, and we convert the bitmap images to grey-scale 2D histograms (*i.e.* the content of each bin is the brightness of the pixel). The converted grey-scale histograms for the ruler image is shown in Figure 4.65a. According to the grid structure in this figure, the pixel-index-to-mm conversion is determined to be 48 pixels per mm. The engraved circle shape at (777 , 533) in the pixel space of Figure 4.65a corresponds to the first small engraved circle beneath the largest engraved circle in Figure 4.64b by 4 divisions (or above it by 2 mm in the physical space). Therefore, the ruler center (center of the largest engraved circle shape) is at (777 , 629) in the pixel space of Figure 4.65a. To find the position of the iris center, we choose 10 points (the black dots in the figure) on the edge of the iris in Figure 4.65a, and then fit them to an ellipse (the red curve in the figure). The fitted ellipse center is at (757.3 , 430.7) in the pixel space. Therefore, the center of the iris is 198.3 pixels below the ruler center in the image, and thus 4.131 mm above the ruler center in the physical space.

When measuring the MOT position, we first deplete all atoms in the trap and take a

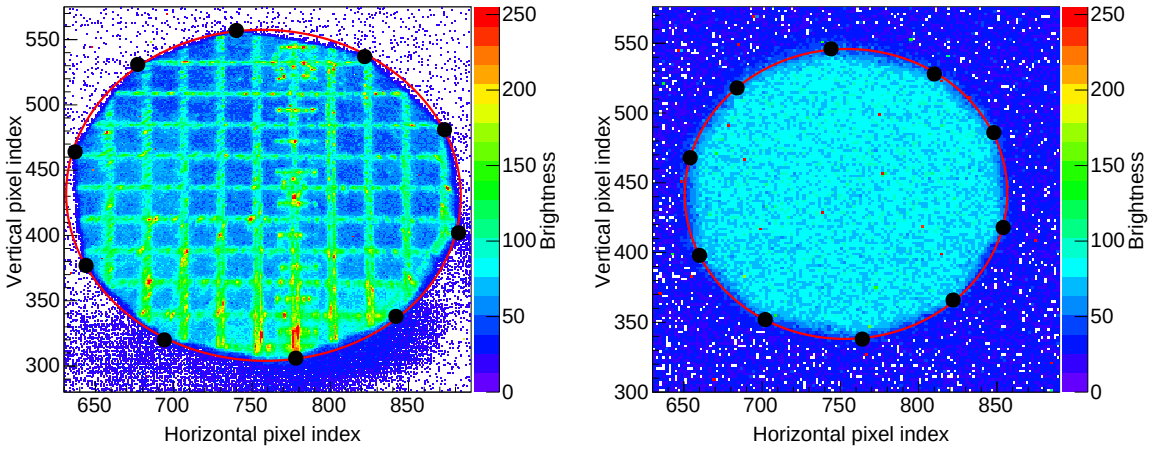

(a) (b)

Figure 4.65: (a) Grey-scale histogram of the ruler image. (b) Grey-scale histogram of the background (no atoms in the MOT).

photo using the camera. This image shows the background generated from light scattered on other surfaces in the chamber. The background image in Figure 4.65b shows clearly the shape of the iris. Similar to the ruler image, we use 10 points on it to fit to an ellipse and determine its center position. Because the iris is firmly attached to the chamber view port, we use the iris center as the reference point for the MOT position measurements.

The background subtracted camera image with the atoms in MOT-2 and its projections onto X and Y axes are shown in Figure 4.66. These projections are fit to Gaussian functions to extract the peak positions and widths. The right-side bump in the Y projection is due to the contribution from the capture period which has a high MOT position and higher photon scattering rate. Therefore this region is excluded from the fit. If this region is included in the fit, the fitted value for the peak position is shifted by 23 μm, and we treat it as the systematic uncertainty due to this tail. The fit results give the MOT position in the pixel space, and combined with the ellipse fit in Figure 4.65b the distance from the MOT to the iris center is determined. Based on the assumption that the iris center does not move during the experiment and the distance from the iris center to the ruler center measured above, the distance from the MOT to the ruler center is known. The mechanical inspection of the

electrode system and the ruler gives the distance between the ruler center to the MCP, and thus Z_{MOT} is determined. Some key measurement results for determining Z_{MOT} are listed in Table 4.3, and the MOT images used in these measurements were taken on October 25h 2015.

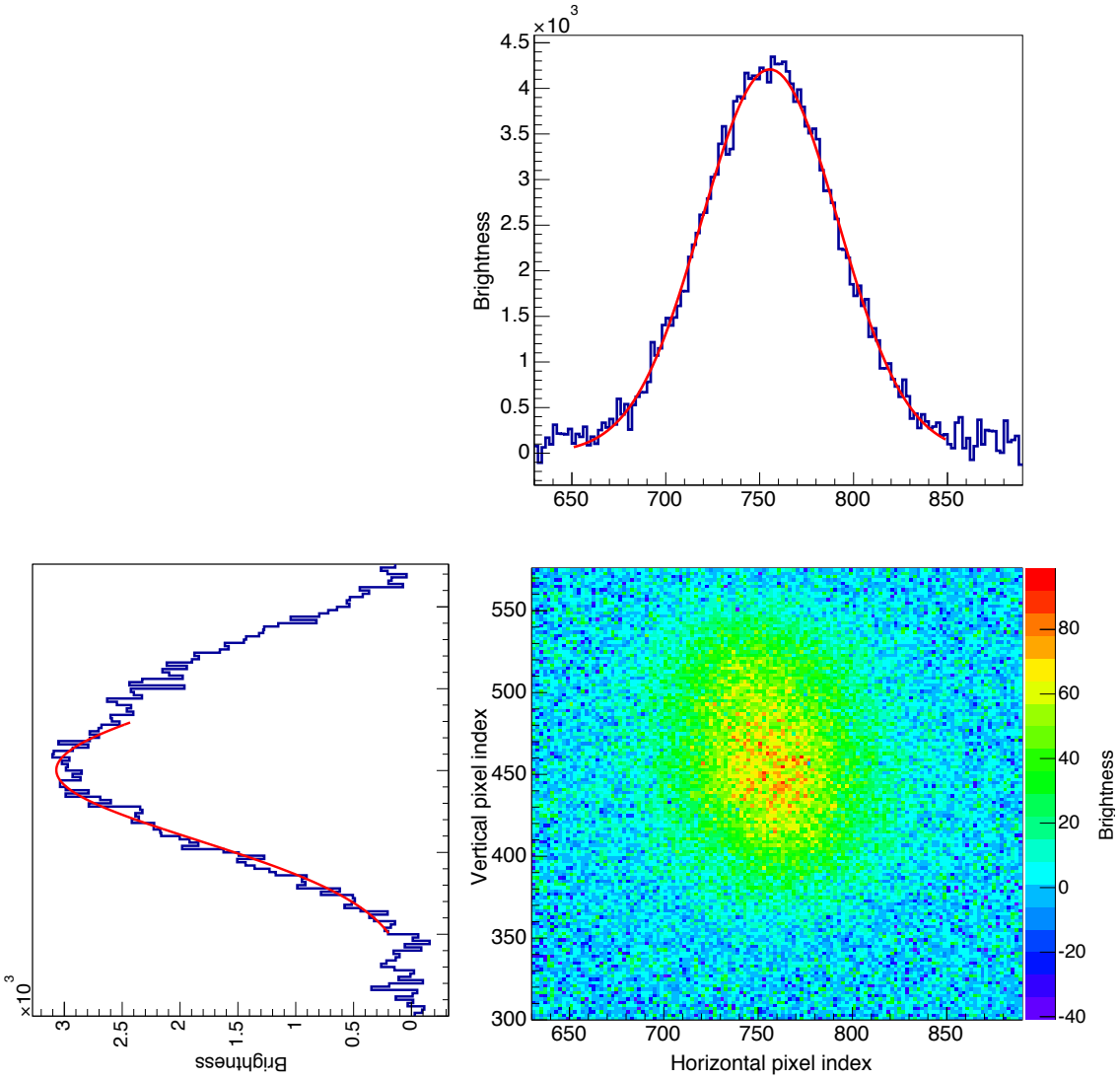

Figure 4.66: Background subtracted grey-scale histogram of the MOT image and its projections onto X and Y axes shown in top and left panels.

	Value (mm)	Uncertainty (mm)
MCP to Electrode-6 top	155.864	0.013
Electrode-6 top to ruler center	−72.283	0.006
Ruler center to iris center	4.131	0.021
Iris center to MOT	−0.173	0.021(stat), 0.023(syst)
Z_{MOT}	87.539	0.033
MOT width (Horizontal)	0.756	0.021
MOT width (Vertical)	0.887	0.021(stat), 0.012(syst)

Table 4.3: Key results for the Z_{MOT} measurement.

4.13.5 Combined calibration of the E-field and Z_{MOT} using the photoion TOF

Based on the measurements described in the previous subsections, the E-field and the Z_{MOT} are well determined. We then use the ion-tracking program described in Section 5.5 to calculated the TOF of photoions from either the ^{4}He or ^{6}He trap. In the simulation, the initial velocity of the photoions are set to zero, and the initial position of each ion is generated according to a 3D-Gaussian distribution centered at the measured MOT position and with the measured width in each direction. The TOF spectrum from the simulation was compared to the measured one in order to test the consistency between different methods. The measured TOF is the time difference between the MCP-back signal and the N_2-Laser signal. However, there is an unknown shift between this measured TOF and the physical TOF due to signal propagating and processing time. To account for this shift, we extract the zero timing by varying the E-field strength as follows. In a uniform electric field with a field strength of E_Z in the Z direction, the measured TOF of a photoion at a distance of Z_{MOT} above the MCP is:

$$\text{TOF} = T_0 + \sqrt{\frac{2MZ_{MOT}}{qE_Z}}, \tag{4.13}$$

where T_0 is the unknown timing shift, M is the ion mass and q is the ion charge. If E_Z is scaled by a factor of k to kE_Z, then TOF$-T_0$ scales as $1/\sqrt{k}$. The scaling of the field can

be done by simply scaling the voltages on all electrodes by the same factor. Therefore, the T_0 can be extracted by fitting the measured TOF values at several field scaling factor (k) values to the function:

$$\text{TOF} = T_0 + \frac{\alpha}{\sqrt{k}}, \tag{4.14}$$

where T_0 and α are free parameters. Relaxing the condition of uniform field, given that the ions are released on the Z axis and according to the symmetry of the system E_X and E_Y vanish along the Z axis, the ions only experience force in the Z direction during the flight. Thus, for any time interval $v_{ion}dt = dz$, where v_{ion} is the ion velocity and z is the distance the ion traveled from the releasing position. The ion velocity v_{ion} can be determined through energy conservation:

$$\frac{1}{2}Mv_{ion}^2 = \int_0^z qE_Z(z')dz', \tag{4.15}$$

and therefore,

$$\text{TOF} = T_0 + \int_0^{Z_{MOT}} \sqrt{\frac{M}{2q\int_0^z E_Z(z')dz'}}dz. \tag{4.16}$$

Although in this case E_Z is a function of z and the function becomes more complicated, if E_Z scales to kE_Z, the TOF still scales with k as in Equation 4.14. Consequently, even in a more realistic E-field like the one described above, Equation 4.14 is valid for fitting the relationship between the TOF and the field scaling factor k.

We measured the ^{4}He photoion TOF spectrum for 5 values of k from 1.0 down to 0.35 with interval 0.1625, and the spectra for these measurements are plotted in Figure 4.67a. The TOF peak values are determined through Gaussian fits and the TOF versus k graph is shown in Figure 4.67b. This graph fits well to Equation 4.14. The fitted value of T_0 is $\sim$5 ns, and its statistical uncertainty is $\sim$0.045 ns. However, during the experiment we observed that the fitted value drifted unto $\pm$0.15 ns from run to run. This might be caused by imperfect scaling of the E-field. Therefore, we assign 0.15 ns systematic uncertainty to the T_0 determination.

The TOF spectrum for $k = 1$ is shifted by T_0 to correct the timing zero shifts, and then it is overlaid with the simulated ^{4}He photoion TOF spectrum as shown in Figure 4.68a.

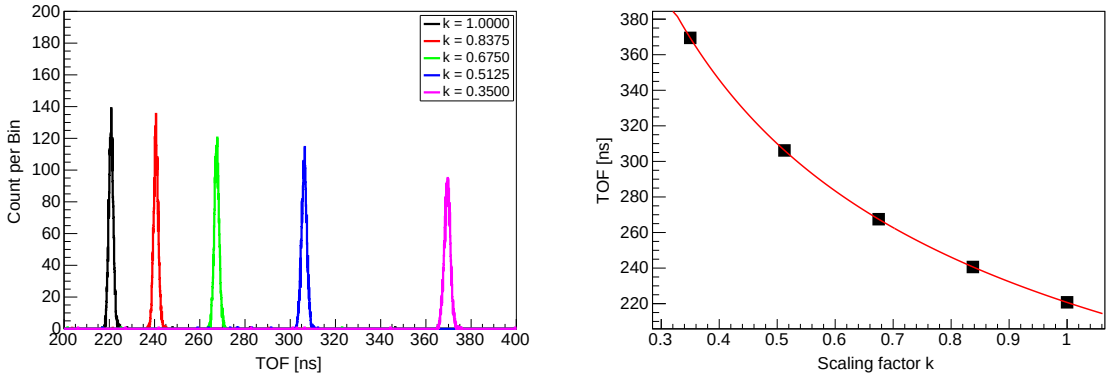

(a) (b)

Figure 4.67: (a) ^{4}He photoion TOF peaks for different E-field scaling factor k. (b) Graph of TOF versus k, fit to Equation 4.14.

The simulated TOF peak position deviates from the measured one by 0.35 ns, while the uncertainties of the TOF positions are 0.02 ns for both the simulation and the measurement. Assuming the E-field is approximately uniform, and using Equation 4.13 one gets

$$\frac{\Delta \mathrm{TOF}}{\mathrm{TOF}} = \frac{1}{2}\frac{\Delta Z_{MOT}}{Z_{MOT}}. \tag{4.17}$$

Therefore, the 0.35 ns discrepancy in photoion TOF peak positions amounts to 0.284 mm discrepancy in Z_{MOT} assuming the E-field calculation and T_0 extraction are accurate. One possible explanation is that the nitrogen laser does not illuminate the whole MOT so the illuminated part of the MOT is the convolution between the MOT profile and the laser beam profile. This may result in a difference between the center of the illuminated part of the MOT and the whole MOT. To test this hypothesis, we changed the Z_{MOT} in the simulation so that the simulated photoion TOF peak position moves to the measured one as shown by the red and blue curves in Figure 4.68b. Then we simulated the photoion TOF peak for ^{6}He and overlaid it with the measured one as shown by the green and black curves in Figure 4.68b. In this case, the discrepancy between the ^{6}He photoion peaks is -0.252 ns. This discrepancy may be caused by the difference in the ^{4}He MOT position and the ^{6}He MOT position, or the nitrogen laser positions for these two measurements, but these hypotheses are not tested using other methods yet.

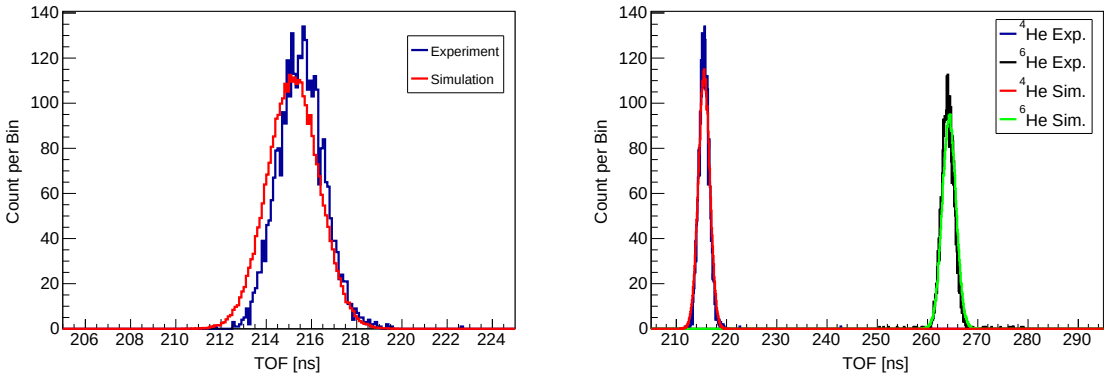

(a) (b)

Figure 4.68: (a) ^{4}He photoion TOF spectrum (timing zero corrected) overlaid with the simulated spectrum. (b) ^{4}He and ^{6}He photoion TOF spectra (timing zero corrected) overlaid with the simulated spectra (Z_{MOT} modified).

In summary, the determination of the E-field, Z_{MOT} and T_0 of the photoion TOF spectrum do not lead to a consistency within the experimental uncertainties. However, the discrepancy in the photoion TOF spectrum is up to 0.350 ns, which amounts to 0.284 mm in Z_{MOT} or 0.32% in the overall E-field strength. These discrepancies are folded into the uncertainties in the E-field and Z_{MOT} and their effects on $a_{\beta\nu}$ extraction are discussed in Chapter 6.

4.14 Horizontal MOT position and shape calibration

While the vertical position and shape of the MOT are measured by the imaging system with the camera, the horizontal position and shape of the MOT are measured directly using the MCP. For both ^{4}He and ^{6}He, Penning ions and photoions can be used to image the MOT on the MCP. The Penning ion image is the MCP 2D position spectrum with no requirements of coincidence with other detectors, and the photoion image requires the coincidence with the N_2-Laser channel. Because the Penning ions originate from the residual gas in the MOT-2 chamber, their temperature is room temperature. Their initial transverse momenta are not negligible for the MOT-width study, so the MOT image on the MCP is broader than the MOT itself. On the other hand, the photoions are at the MOT temperature so their

transverse momenta can be neglected. Nevertheless, the MOT image on the MCP created by the photoions is actually the convolution between the MOT shape and the laser profile. In this section, the details about the MOT position and shape measurement using Penning ions and photoions are discussed. Their pros and cons are compared, and the horizontal position and shape of the MOT are determined based on both methods. In the following subsections, the measurements using the ^{4}He trap are discussed first, and then the same procedure is carried out for the ^{6}He trap. The differences between them are discussed.

4.14.1 Measurements using the ^{4}He MOT

The ^{4}He MOT images using Penning ions and photoions are shown in Figure 4.69. The images are rotated by 22.5° so that the coordinate system coincide with the MOT-2 chamber coordinate system (X direction is the along the push beam). The major part of the MOT image stays inside the center square area on the MCP. The photoion image has lower background because of the coincidence trigger between the MCP and the photo-detector that detects the scattered nitrogen laser photons.

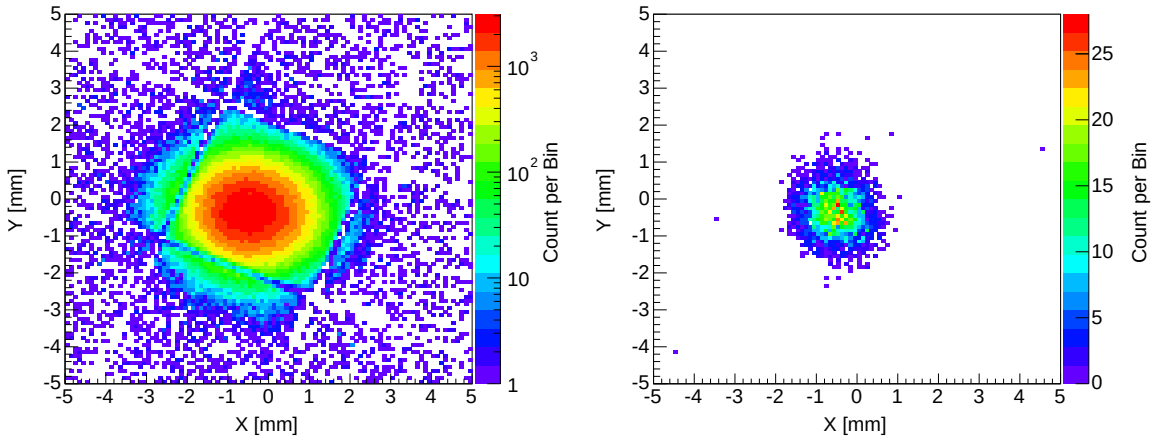

(a) Penning ion (b) Photoion

Figure 4.69: ^{4}He MOT images on the MCP using (a) Penning ions and (b) Photoions.

To study the position and width of the MOT, both of the Penning ion image and the photoion image are projected onto the X and Y axes as shown in Figure 4.70. In order to

reduce the background, we put a cut on Y from -1.8 mm to 1.2 mm when projecting onto the X axis, and vice versa. The peak positions and the widths of the MOT projections are determined through fitting them to the Gaussian function using the recursive algorithm. For each projection histogram, we fit it to the Gaussian function three times in the range from $\mu - 2\sigma$ to $\mu + 2\sigma$, where μ and σ are the fit parameters from the previous fit, and the range of the first fit is the entire histogram range. The fit results converge at the third fit in this study. The uncertainties of the peak positions and widths from the fits are all $\sim$0.011 mm. The results of the fits are listed in Table 4.4.

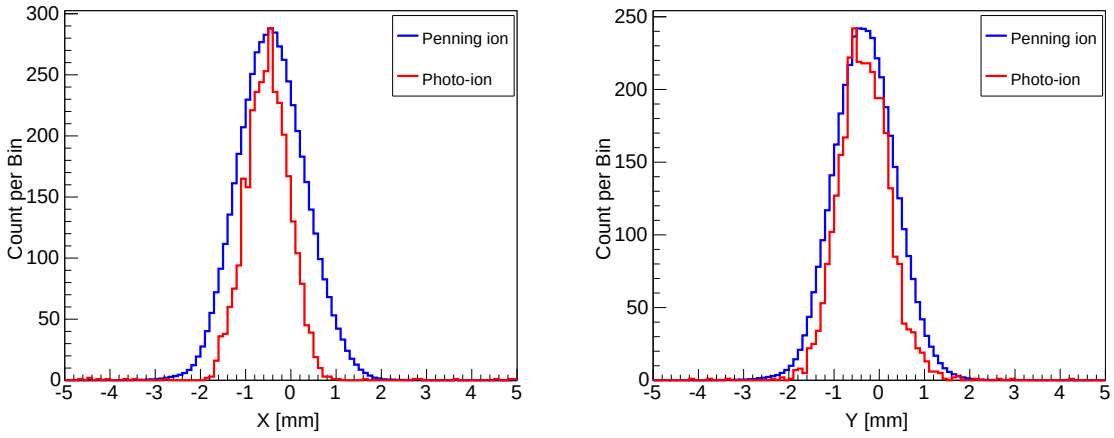

(a) Projection X

(b) Projection Y

Figure 4.70: ^{4}He MOT Penning ion and photoion image projections onto X and Y axes. The differences are caused by the convolution of the laser profile and the atom distribution in the MOT. The difference in Y direction is less because the laser is almost parallel to the Y axis and it is less sensitive to the laser profile.

As shown in Figure 4.70, the photoion peak is narrower than the Penning ion peak. This is caused by the thermal diffusion of the Penning ions during the flight from the MOT to the MCP. The majority of the residual gas is hydrogen so the Penning ions are mainly H_2^+. The $^4He^+$ to H_2^+ mass ratio is 1.98603, and according to Equation 4.16 the TOF of the H_2^+ ion should be $1/\sqrt{1.98603}$ times the TOF of the $^4He^+$ ion, which is $\sim$153 ns. The RMS thermal velocity of the H_2^+ ions in the X or Y direction is 1112.6 m/s at room temperature $\sim$300 K. Therefore, the RMS of the thermal diffusion distance in the X or Y direction is

0.170 mm (σ_{Th}). Therefore, the MOT width in the X or Y directions (σ_X and σ_Y) should be

$$\sigma_X = \sqrt{\sigma^2_{X,Penning} - \sigma^2_{Th}},$$
$$\sigma_Y = \sqrt{\sigma^2_{Y,Penning} - \sigma^2_{Th}}, \tag{4.18}$$

where $\sigma_{X,Penning}$ and $\sigma_{Y,Penning}$ are the fitted Gaussian widths of the Penning ion image projections.

The thermal diffusion of the photoions are negligible because their temperature is more than 3 orders of magnitude lower than room temperature. Ideally, the position and width measured by the photoion projections are the real ones for the MOT. However, due to the convolution between the MOT shape and the laser profile, the photoion image may not represent the real position and shape of the MOT. This explains the differences between the peak positions and widths determined from the Penning ion image projections and the photoion image projections. The differences in the Y direction are less than that in the X direction, because the laser is almost parallel to the Y axis and it probes the MOT along its path uniformly.

4.14.2 Measurements using the ^{6}He MOT

The ^{6}He MOT images using Penning ions and photoions are shown in Figure 4.71. Because the ^{6}Li ions and β particles from the ^{6}He decays also trigger the MCP, the Penning ion image lies on top of the background generated by these particles. Therefore, before making the projection histograms, we subtract a constant from the 2D MCP position spectrum shown in Figure 4.71a so that the background in the projection histograms are close to zero as shown in Figure 4.72.

The procedure for analyzing the projection histograms is the same as that described in Subsection 4.14.1, and the fit results of the peak positions and widths are also shown in Table 4.4. Similar to the ^{4}He MOT image projections, the photoion peaks are narrower and a difference between the Penning ion peak position and the photoion peak position is observed. The comparison of the ^{4}He and ^{6}He MOT images on the MCP is discussed in Subsection 4.14.3.

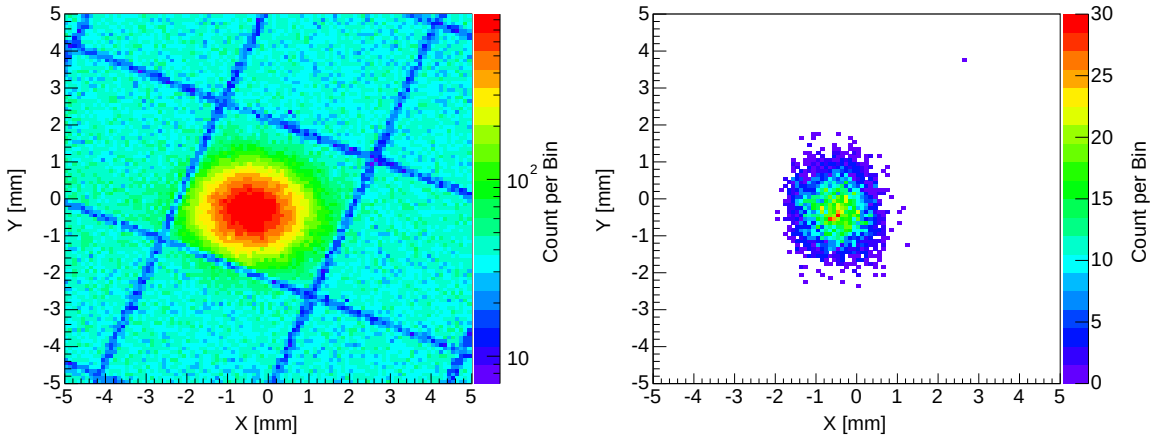

(a) Penning ion (b) Photoion

Figure 4.71: ^{6}He MOT images on the MCP using (a) Penning ions and (b) Photoions.

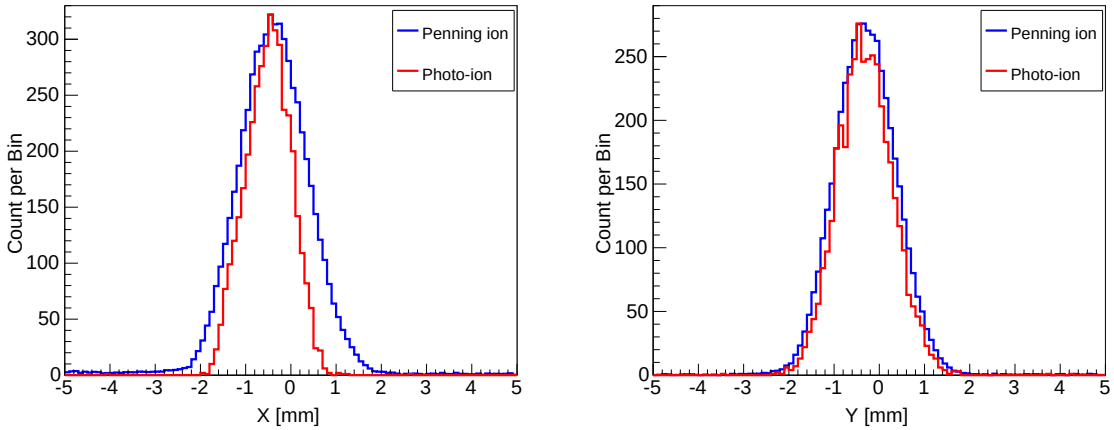

(a) Projection X (b) Projection Y

Figure 4.72: ^{6}He MOT Penning ion and photoion image projections onto X and Y axes.

4.14.3 Discussions on MOT position and width measurements

The MOT position and shape measurement results are summarized in Table 4.4. These measurements are based on the data taken from October 24th 2015 to October 25th 2015.

As discussed above, the photoion measurements are biased by the convolution between

		μ_X (mm)	σ_X (mm)	μ_Y (mm)	σ_Y (mm)
^{4}He	Penning Ion	-0.434 ± 0.012	0.739 ± 0.012	-0.327 ± 0.012	0.671 ± 0.012
	σ_{Th} subtracted		0.719 ± 0.012		0.649 ± 0.012
	Photoion	-0.511 ± 0.010	0.474 ± 0.010	-0.350 ± 0.010	0.518 ± 0.010
^{6}He	Penning Ion	-0.390 ± 0.011	0.750 ± 0.011	-0.311 ± 0.012	0.671 ± 0.012
	σ_{Th} subtracted		0.730 ± 0.011		0.649 ± 0.012
	Photoion	-0.494 ± 0.010	0.541 ± 0.010	-0.325 ± 0.011	0.604 ± 0.011

Table 4.4: MOT position and shape measurement summary.

the MOT shape and the laser profile. The difference between μ_X determined from the Penning ion image and that determined from the photoion image is up to 0.104 mm. A similar size difference may also occur in the Z direction and result in the TOF discrepancy described in Subsection 4.13.5. Therefore, we use the Penning ion measurements to determine the MOT position and shape. The MOT horizontal coordinates are directly μ_X and μ_Y, and the MOT horizontal widths are the σ_{Th} subtracted σ_X and σ_Y calculated using Equation 4.18. These numbers are used in the Monte Carlo simulation to generate the fit templates for the $a_{\beta\nu}$ extraction.

Comparing the positions of the ^{4}He MOT and the ^{6}He MOT, their difference in the Y direction is consistent with their uncertainties, but in the X direction they are different by 0.054 mm (4.5 σ). We observed some power imbalance of the laser beams in the X-Z plane, and this introduces isotope dependent MOT position shift in the X and Z directions. Because of the way the MOT functions, the MOT position difference in the Z direction should be similar to that in the X direction.

The width measurements of the ^{4}He MOT and the ^{6}He MOT are consistent with each other. Because the magnetic field is azimuthally symmetric around the Y axis, the MOT width in the Z direction should be the same as that in the X direction. The ^{4}He MOT widths are compared to the MOT widths determined from the camera image of the ^{4}He MOT. Because the camera is watching the MOT from the 45 $^\circ$ direction in the XY-plane, the

horizontal width seen by the camera is expected to be 0.685 mm. However, the horizontal MOT width in the camera image is 0.756 mm, and the vertical width in the camera is 0.887 mm. Because the image captured by the camera has a contribution from the hot MOT during the capture period, it may appear broadened in the camera image. Therefore, the MOT width determined by the MOT image on the MCP is more reliable, and in the Monte Carlo simulation the Z direction width of the MOT is also set to the σ_X of Equation 4.18, shown in Table 4.4.

In summary, the horizontal MOT position and width are well determined using the images generated by the Penning ions or photoions on the MCP with fitting uncertainty $\sim$0.011 mm. The discrepancies between different methods are less than 0.1 mm, and they are explained by reasons like the convolution between the MOT shape and the nitrogen laser profile. We conclude that the measurements based on the Penning ion image are more reliable, and the Monte Carlo simulations are based on the results from these measurements.

4.15 Timing calibration

There is a delay between the time when the β particles hit the scintillator to the time when the pulse is generated at the anode of the PMT base, mainly due to the electron transport time in the PMT. The cables and amplifiers between the detectors to the DAQ system also add delays. Therefore, the measured TOF, which is the time difference between the MCP-back signal to the PMT signal, has an unknown offset. Furthermore, the resolution of the PMT and the MCP affects the rising edge shape of the recoil ^{6}Li ion TOF spectrum, and subsequently affects the $a_{\beta\nu}$ extraction. In this section, we describe two methods that determine the TOF offset (timing zero) and the resolution of TOF. Besides these, we also investigate the signal-size dependence of the timing for the PMT and the MCP in order to make sure the time readout is independent of the signal size.

As we will see the accuracy of the following measurements don't allow for a determination of the TOF offset to better than 200 ps. This is not enough for an accurate determination of $a_{\beta\nu}$, but these measurements are important to give confidence that our systems are working in the expected manner. On the other hand, this accuracy is good enough for analyses like the charge state distribution and Q-value reconstruction described in Chapter 6.

4.15.1 Timing study using the ^{207}Bi cascade decay

The first excited state of ^{207}Pb, the daughter nucleus from the ^{207}Bi, has a half-life of 130.5 ps. Its decay scheme is shown in Figure 4.73. 84% of ^{207}Bi nuclei decay to the second excited state of ^{207}Pb and then cascade-decay to the ground state through the first excited state. The cascade decay emits one γ ray with 1063.7 keV (or conversion electrons around 975.7 keV) and one γ ray with 569.7 keV (or conversion electrons around 481.7 keV) in coincidence. If one conversion electron hits the MCP while the other γ ray or conversion electron from the cascade decay hits the scintillator, the time difference between the PMT signal and the MCP-back signal is the timing offset due to the delay because the detectors are hit almost at the same time. The decay lifetime is taken into account and then the determined timing offset is adjusted accordingly.

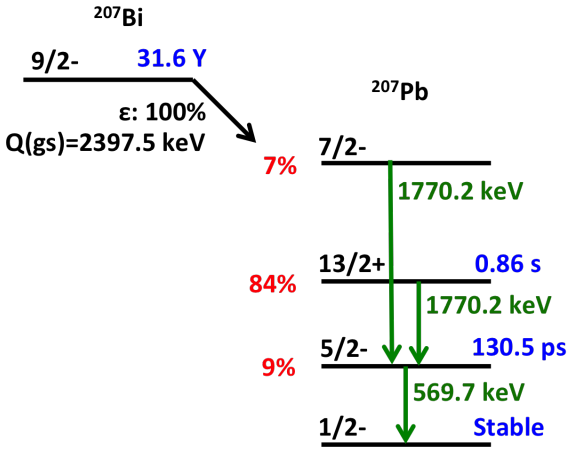

Figure 4.73: ^{207}Bi decay scheme. This scheme is obtained from National Nuclear Data Center [92], Brookhaven National Laboratory.

Because the MWPC has a very low efficiency in detecting γ rays, in this test the MWPC is not included in the analysis. The MCP efficiency for γ ray is also lower, and thus the MCP is mostly triggered by conversion electrons. The TOF spectrum[5] for the ^{207}Bi cascade decay is shown in Figure 4.74. If no conditions are applied to E_β and Q_{MCP} the mean of

[5]Conventionally, we still call the time difference $T_{MCP} - T_{PMT}$ the name *TOF* even though it does not corresponds to the ion flight.

the spectrum is -83.4 ns and the RMS is 1.12 ns. The 2D histograms of E_β versus TOF and Q_{MCP} versus TOF are shown in Figure 4.75. The smearing of TOF becomes larger as E_β goes below 200 keV and the major γ rays from the ^{207}Bi source goes up to about 1 MeV. Therefore, we apply a cut on E_β from 200 keV to 1 MeV in this study as is indicated by the dash-line in Figure 4.75a. The Q_{MCP} versus TOF 2D histogram in Figure 4.75b is constructed under this condition as well. As mentioned in Section 4.10, Q_{MCP} has no strong correlations with the energy of the incoming particles, so we don't put any cuts on Q_{MCP} in this study. The TOF spectrum with the E_β cut is the blue curve in Figure 4.74. It fits nicely to the EMG function with a positive tail:

$$f(x) = N_0 \exp\left(\frac{\lambda}{2}(-2x + 2\mu + \lambda\sigma^2)\right) \mathrm{Erfc}\left(\frac{-x + \mu + \lambda\sigma^2}{\sqrt{2}\sigma}\right). \tag{4.19}$$

After the E_β cut is applied, the RMS of TOF becomes 0.948 ns, smaller than that without the E_β cut. The fit value of the parameter μ is -84.083 ns and the fit value of σ is 0.516 ns.

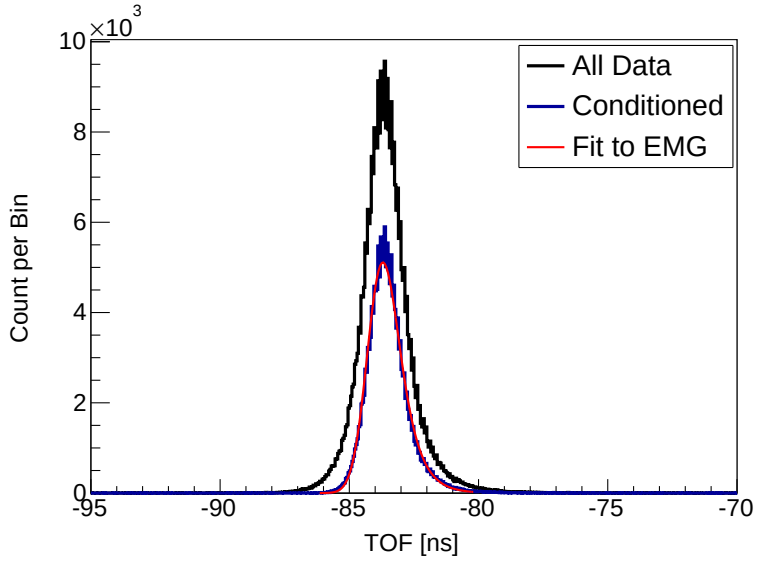

Figure 4.74: TOF spectrum for the ^{207}Bi cascade decay.

In the 2D histograms in Figure 4.75, most events fall into a band vertical to the TOF axis, indication that the dependence of TOF on E_β or Q_{MCP} is weak. In order to investigate this dependency on the sub-nanosecond scale, we project these 2D histograms onto the TOF axis

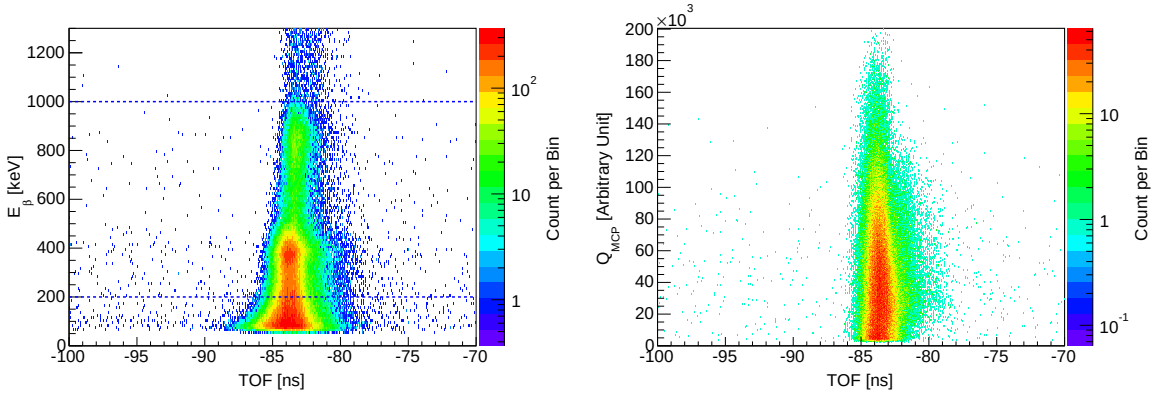

(a) (b)

Figure 4.75: (a) E_β versus TOF 2D histogram. (b) Q_{MCP} versus TOF 2D histogram.

for nine intervals of E_β or Q_{MCP} in the region of interest. These TOF projection histograms are then fitted to Equation 4.19 and the μ parameters are extracted. The deviations of the extracted μ-values (μ_{TOF}) for each interval from the μ_{TOF} of the entire data set are plotted in Figure 4.76, and the horizontal coordinates of the points represent the center of the E_β and Q_{MCP} intervals.

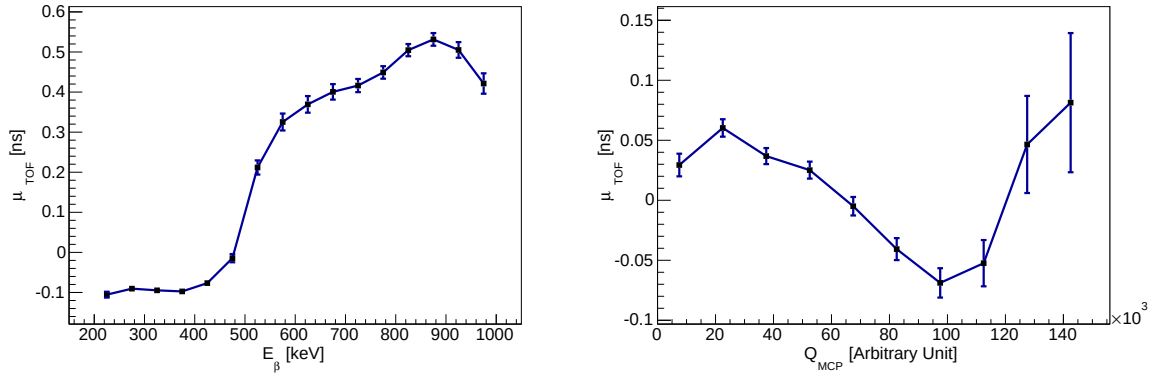

(a) (b)

Figure 4.76: (a) μ_{TOF}-shift versus E_β. (b) μ_{TOF}-shift versus Q_{MCP}. The error bars represent statistical uncertainties only.

As shown in Figure 4.75a there is a sharp rise of the μ_{TOF} by about 450 ps near 500 keV. This can be understood as follows. For the events whose E_β is higher than 500 keV, it is only possible that the 1 MeV γ ray hits the scintillator while the 464 keV conversion electron hits the MCP. Because of the lifetime of the first excited state of ^{207}Pb (188 ps), the MCP should be hit on average 188 ps later than the scintillator. On the contrary, for those events whose E_β is less than 500 keV, the majority of them have the 569.7 keV γ ray hitting the scintillator while the 975.7 keV conversion electron hitting the MCP, and therefore the MCP is hit on average 188 ps earlier than the scintillator. With these decay lifetimes taken into account, the TOF for E_β higher than 500 keV is expected to be 376 ps larger than the TOF for E_β lower than 500 keV. Further more, the speed of the conversion electrons are $v/c = 0.85$ and $v/c = 0.94$ for the 465.7 keV and 975.7 keV electron lines respectively. This increases the TOF difference by 33 ps. Adding all the delays up, the TOF difference for events with E_β larger than 500 keV and lower than 500 keV is expected to be 409 ps. We fit the TOF spectra for E_β in the interval [250 keV ,450 keV] and the interval [550 keV, 750 keV]. The μ_{TOF} is 463 ps higher for the latter one, which agrees with the expected value at the 100 ps scale. Other than this jump in μ_{TOF} around 500 keV, the μ_{TOF} is consistent with a constant versus E_β below 400 keV and above 600 keV, and the drift is up to 150 ps. The average μ_{TOF} for E_β region [600 keV,1000 keV] is -83.714 ns, and this corresponds to the case where the γ ray hits the scintillator and the 465 keV electron hits the MCP. The μ_{TOF} versus Q_{MCP} plot in the right figure of Figure 4.76 shows no clear overall trend, but the overall fluctuation is up to $\pm$150 ps.

In Figure 4.77, there are the plots of the TOF resolutions which is the fitted value of σ in Equation 4.19 for intervals of E_β and Q_{MCP}. For both of them there is a clear descending trend. Therefore it is true that for both the PMT and the MCP larger signal sizes yield better timing resolutions.

As a summary of the timing studies with the ^{207}Bi source, the measured TOF peak position is -83.714 ns for the case where the γ ray hits the scintillator and the 465 keV electron hits the MCP. This number is used in determining the timing-zero position as discussed in Subsection 4.15.4. The jump in the μ_{MCP} versus E_β plot is explained and the timing does not depend on the signal size (*i.e* E_β) when E_β is above 600 keV. However,

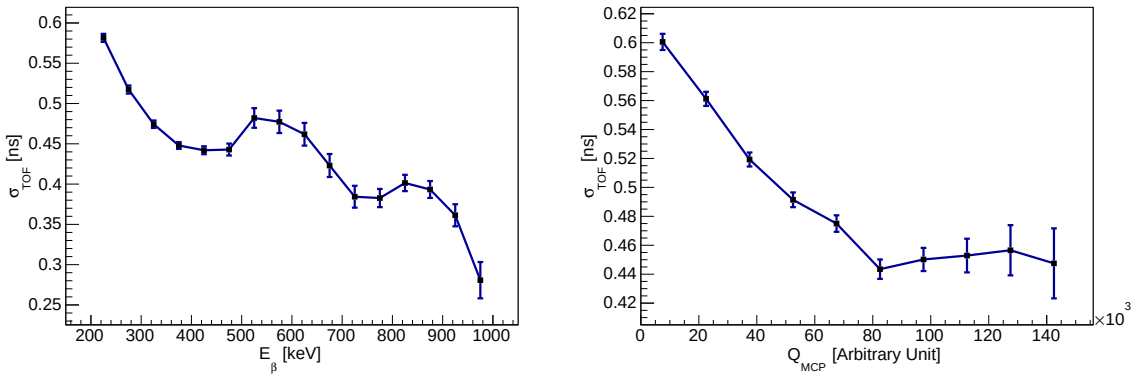

Figure 4.77: Left: TOF resolution versus E_β after correction. Right: TOF resolution versus Q_{MCP} after correction.

the ^{207}Bi source doesn't have intensive radiations with energy higher than 1 MeV, so this method cannot be used to investigate the TOF-E_β relationship at higher energy.

4.15.2 Timing study using the Timing-zero peaks

One striking feature of the triple-coincidence TOF spectrum is that it has sharp peaks near the $TOF = 0$ separated by about 2 ns. The TOF-E_β 2D histogram in the region near these two peaks is shown in Figure 4.78, and this histogram is based on the data taken on October 25th 2015 for over 15 hours with trapped ^{6}He. We call these two peaks the *timing-zero peaks* throughout this thesis. In this subsection, all studies assumes using coincidence trigger between the MCP and the β telescope (including the MWPC). The distortions at the tips of the timing-zero peaks in the 2D histograms are caused by saturation of the DAQ system. This effect is described in detail in Section 4.15.3.

Because these peaks are very close to zero time difference between the PMT trigger and the MCP trigger, these two detectors must be triggered by the same particle that moves close to the speed of light. The time difference between the two peaks corresponds to a 60 cm path length if the particle is traveling at the speed of light. This path length is very close to twice the distance from the MCP to the front of the scintillator. Therefore, we postulate that the left peak is from fast particles hitting the MCP first and then the

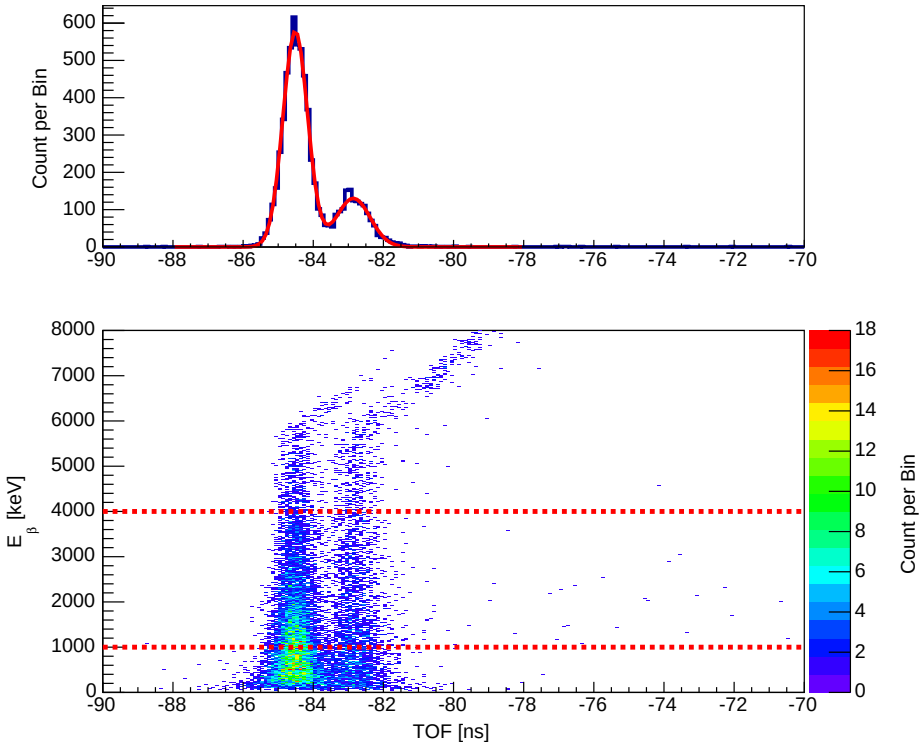

Figure 4.78: TOF-E_β 2D histogram of the timing-zero peaks. The TOF projection of the region between the two red dashed lines (from 1 MeV to 4 MeV) is shown in the upper panel, and the two peaks are fitted to Gaussian functions (red curves).

scintillator, and the right peak is from fast particles hitting the scintillator first and then the MCP. For example, β particles back-scattered from the MCP can contribute to the left peak, and the cosmic rays can contribute to the right peak. The beam related ambient background can create both peaks via Compton scattering and photo-electric effect.

The ratio of the number of events in each peak depends on the environment of the experimental setup. The Figure 4.78 describes the case for trapped ^{6}He source, while the ambient background generated by the accelerator and the ^{6}He production target is also present. In this case the numbers of events in these two peaks are similar, though there are more events in the left peak. By contrast, during the experiment with non-trapped ^{6}He atoms filled in the MOT-2 chamber, the left peak dominates as is shown in Figure 4.79a. This is expected because from some non-trapped ^{6}He atoms below the MCP

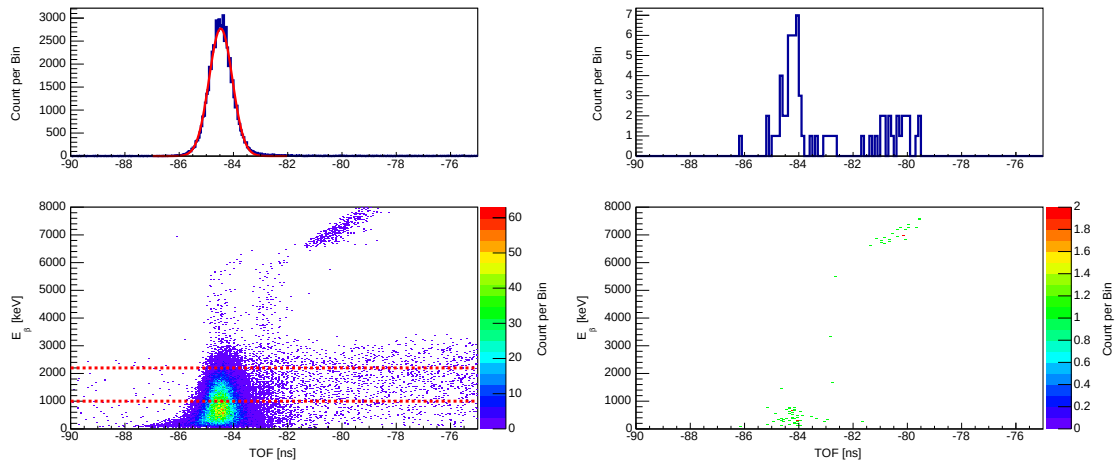

(a) (b)

Figure 4.79: (a) Timing-zero peak for experiment with diffuse ^{6}He source. The TOF projection of the region between the two red dashed lines (from 1 MeV to 2.2 MeV) is shown in the upper panel, and it is fitted to a Gaussian function (red curves). (b) Timing-zero peaks for the ambient background while the deuteron beam is hitting the target. The TOF projection of the whole 2D histogram is shown in the upper panel. Events with $E_\beta =\sim 7000$ keV are from the cosmic rays.

the emitted β particle penetrate through the MCP and then keep flying up and hit the scintillator. In Figure 4.79b the TOF-E_β 2D histogram is plotted for the case with the ambient background[6]. In this case, most of the events are either at the position of the left peak or in the region of cosmic rays[7].

For the left timing-zero peak, most of the incoming particles are stopped in the scintillator, so in principle the PMT readout E_β should equal the full energy of the incoming particle while it is traveling from the MCP to the scintillator if its energy loss in the beryllium window and the MWPC is neglected. This is ideal for studying the TOF shift caused by the velocity difference of the β particles. For the right timing-zero peak, however, there is no well defined correlation between the PMT readout E_β and the energy of the incoming

[6]The ambient background is generated by cosmic rays and γ rays from the accelerator and the production target

[7]The cosmic rays deposit more than 6000 keV energy in the scintillator, but both the energy and timing readings are not accurate because the pulses saturate the ADCs.

particle when it leaves the scintillator, so the velocity of the particle when it is traveling from the scintillator to the MCP is not easy to determine. Therefore, we only show that the right-peak position is approximately correct assuming the particle travels at the speed of light, but don't use it for high precision timing calibration.

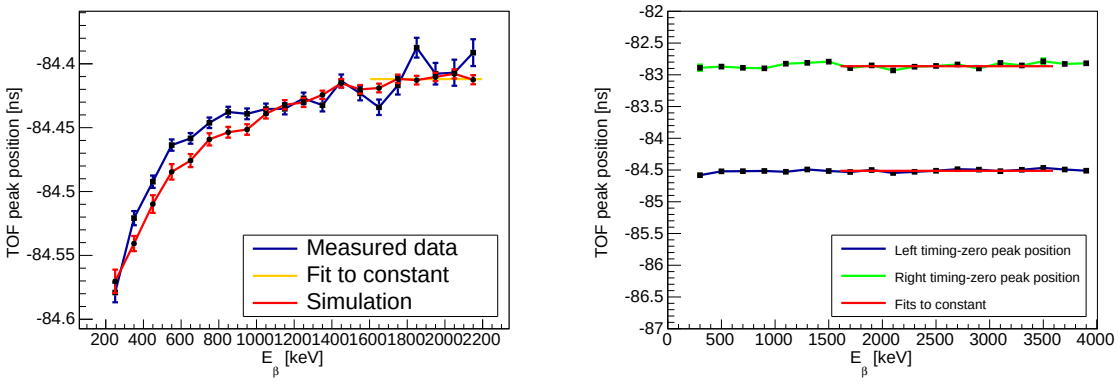

(a) (b)

Figure 4.80: (a) TOF peak shift versus E_β for the left timing-zero peak. (b) TOF peak shift versus E_β for both timing-zero peaks from the trapped ^{6}He data. Both curves are fitted to constant function from 1600 keV to 3500 keV.

The study of TOF shift versus E_β for the left timing-zero peak is done as described in Subsection 4.15.1. The data used here are from the experiment with the non-trapped ^{6}He source. As shown in Figure 4.79a, the TOF spectrum fits well with Gaussian function, so we use Gaussian functions instead of the EMG function to fit the TOF spectra for other E_β range. The β-recoil coincidence TOF spectrum extends into the region of the timing-zero peak, so we limit this study up to E_β=2200 keV below which the number of events outside the timing-zero peaks is negligible. The plot of the TOF peak position versus E_β is shown in Figure 4.80a. Obviously the TOF peak shifts towards smaller values while E_β is becoming smaller. This effect is expected because the velocity of a low-energy β particle is smaller. To confirm this explanation, we ran Monte Carlo simulations and studied the TOF shift caused by variations of electron energy. In the simulation, we shot electrons from the surface of the MCP and registered the energy deposition in the scintillator and the time

when the electron hits the scintillator. Response function of the scintillator-PMT assembly and the timing resolution were applied as described in Chapter 5. The simulated curve of TOF peaks versus E_β is overlaid with the measured on in Figure 4.80a. The measured data agree well with the simulation, and the discrepancies of them at each E_β value are $\sim$20 ps. Therefore we conclude that at the scale of 20 ps there is no TOF shift depending on the value of E_β caused by effects other than the finite velocity of the β particle.

In the E_β region [1600 keV, 2200 keV], the TOF shift caused by the electron velocity is on average 0.018 ns. Neglecting this shift, we fitted the TOF peak-versus-E_β graph in this region to a constant function and the fit value of the constant is -84.412 ± 0.003 ns. We use this value to compare to the left timing-zero peak position determined by other methods in subsection 4.15.4.

We checked whether the timing-zero peaks are still at the same positions when the trapped ^{6}He is used. Because in this case there are enough data in the timing-zero peaks with E_β higher than 2200 keV, the relationship between the TOF and E_β can be studied in a higher energy range. For each E_β segment in Figure 4.78, the 2D histogram is projected onto the TOF axis and we fit this projection histogram to a double-Gaussian function. The positions of the left and right peaks are plotted in Figure 4.80b. In the region [1600 keV, 3500 keV], the TOF peak position of the left timing-zero peak fits to a constant function, and the deviation from this constant fit is up to 0.04 ns. Therefore, in the entire range of interest [200 keV, 3500 keV], there is no TOF shift caused by effects other than the finite β-particle velocity. The right timing-zero peak for the case with trapped ^{6}He source also fits to a constant function in the region [1600 keV, 3500 keV]. The fit results for the left and right timing-zero peak positions are -84.513 ± 0.003 ns and -82.865 ± 0.007 ns. The consistencies between these values and other determinations of the left and right timing-zero peak positions are discussed in Subsection 4.15.4.

The resolution of the TOF is determined by fitting the peak width (parameter σ of the Gaussian function) of the left timing-zero peak. The peak width does change with E_β and their relationship is plotted in Figure 4.81. The data from both the experiment with non-trapped ^{6}He source and the one with trapped ^{6}He source are shown, and the two sets of data agree with each other. This relationship is fitted to an exponential function plus a

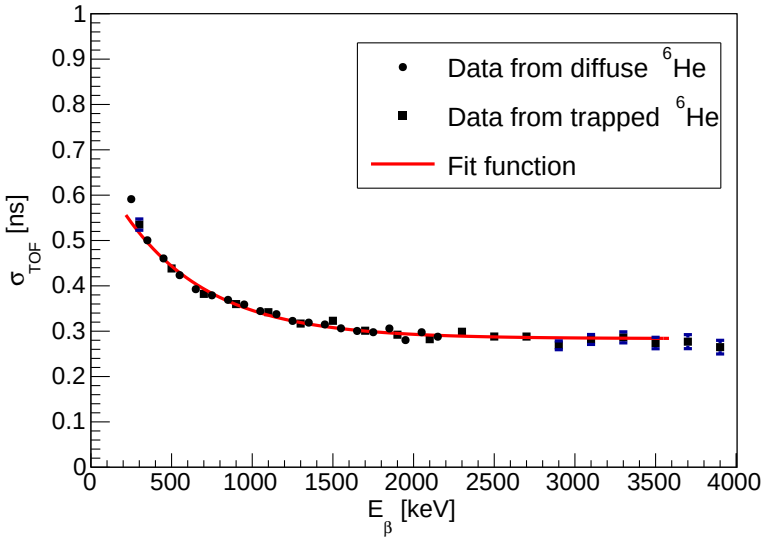

Figure 4.81: TOF resolution versus E_β. The data are fitted to function $\sigma_{TOF} = N \times \exp(-E_\beta/\lambda) + B$ shown in red.

constant

$$\sigma_{TOF} = N \times \exp(-E_\beta/\lambda) + B \tag{4.20}$$

with N, B and λ fitting parameters. The fit value of B is 0.284±0.004 ns, and this represents the TOF resolution for large E_β events. The fit value of λ is 530.1±41.4 keV, which means that if E_β is greater than 530.1 keV, the TOF resolution is very close to the value of B. At the E_β threshold 500 keV (for most of the analyses), the drift of TOF resolution is 0.160 ns. The function of Equation 4.20 with its fit parameters is used in the Monte Carlo simulation to precisely account for the TOF resolution.

4.15.3 DAQ parameters that can affect detector timing

The timing offset of the TOF depends on the CFD settings for the DAQ system, especially the *delay* parameter. Therefore, whenever the DAQ settings for the PMT or the MCP channels are changed, the timing calibration and the MCP position calibration needs to be refreshed.

It is also important to limit the signal sizes for the region of interest within the dynamic ranges of their DAQ channels. For example, the cosmic ray muons pass through the scintillator and deposit over 6 MeV energy in the scintillator, and their PMT pulses saturate the 2.0 V dynamic range of the FASTER digitizer. This saturation affects both the integrated charge readout and the time readout. The TOF versus E_β spectrum for the timing study using the ^{207}Bi source is shown in Figure 4.78 for a larger range of E_β. Clearly the band of events curves to the right if E_β reads larger than 6.5 MeV due to saturation. For the region of interest 200 keV to 4 MeV, the PMT signal size is well below saturation. Moreover, the baseline should also be inspected so that it is stable at zero. A large non-zero baseline distort the timing readout for small signals. Besides this, if the baseline of the signal is not adjusted to zero, the timing is incorrect for small-size signals. Therefore, it is important to tune well the baseline restoration of the DAQ system.

4.15.4 Timing-zero determination

In the previous subsections, the TOF is defined as the time reading difference: $T_{MCP} - T_{PMT}$. For the convenience of the analysis and comparison to simulation, from here on we include the timing zero correction in the definition so that TOF $= T_{MCP} - T_{PMT} - T_{zero}$. Under this definition, the case where TOF=0 corresponds to that the Scintillator and the MCP are hit simultaneously, and the T_{zero} corrects only the delaying caused by the detectors and electronics. In this subsection, we summarize the experiments from previous subsections and determine the value of T_{zero}.

T_{zero} can be determined either using the ^{207}Bi source or the timing-zero peaks of the ^{6}He decay. If using the ^{207}Bi source, we restrict the E_β between 600 keV and 1000 keV. The TOF peak is at -83.714 ns, and it corresponds to the case when the γ ray hits the scintillator and the 465.7 keV electron hits the MCP. To get T_{zero}, one needs to correct for the decay lifetime (-0.188 ns) and the traveling times of the γ ray and electron ($+0.083$ ns). Eventually, the T_{zero} is -83.819 ns using this method. If one uses the timing-zero peaks of the ^{6}He decay (trapped), T_{zero} is the average of T_{0L} and T_{0R}, which is 83.689 ns. The summary of the measurements and T_{zero} extractions are listed in Table 4.5.

$T_{Bi-source}$	-83.714 ± 0.006 ns
T_{0L}	Using trapped ^{6}He: -84.513 ± 0.003 ns Using non-trapped ^{6}He: -84.412 ± 0.003 ns
T_{0R}	-82.865 ± 0.007 ns
Timing-zero	Using the ^{207}Bi calibration: -83.819 ± 0.006 ns Using the ^{6}He calibration: -83.689 ± 0.005 ns

Table 4.5: Summary of the T_{zero} measurements. Uncertainties listed above are statistical only.

There are a few discrepancies in Table 4.5. First of all, using the different sources (non-trapped or trapped ^{6}He) one gets different values of the left timing-zero peak in the TOF spectrum differing, by 0.101 ns. Secondly, the distance between the two timing-zero peaks of the ^{6}He decay TOF spectrum is 1.648 ns, but the calculation based on the distance between the scintillator and the MCP shows that it is 1.462 ns. Finally, the extracted T_{zero} values using the ^{207}Bi source and the ^{6}He source are different by 0.13 ns. All these discrepancies are around 0.1 ns. Actually, there is one big uncertainty in this analysis. The electrons impact deeper into the MCP than the ^{6}Li ions, and they generate initial ionizations at anyplace along the channel. The total electron multiplication and transportation time inside the channel is on the order of $\sim$0.1 ns. In the same way, the γ rays from the ^{207}Bi source also do not only interact with the scintillator on the front surface. These factors add uncertainties to the measured or calculated T_{zero}'s in Table 4.5. The systematic shift caused by assuming the electrons are moving at the speed of light is below 0.022 ns for $E_\beta > 1600$ keV, much smaller than the observed discrepancies discussed above.

In summary, we use the ^{6}He source determined T_{zero} (-83.689 ns) because this method requires no additional calibration runs. This number is accurate to $\sim$0.1 ns. As for the timing resolution, the relationship in Figure 4.81 is used in the Monte Carlo simulation for detector response description. However, the TOF defined above is not the physical time of flight for the recoil ion (T_{ion}), and their relationship is TOF $= T_{ion} - T_e$ where T_e is the time

of flight for the β particle to travel from the MOT to the scintillator. Because it is easier to calculate T_e in the simulation than to determine it in experiments on an even-by-event basis, we calculate the simulated TOF by subtracting T_e from the simulated T_{ion} and extract $a_{\beta\nu}$ by fitting the measured TOF spectrum to the simulated TOF templates. Besides the TOF shift due to the electron speed at low energy, there is no obvious dependence of TOF on the electron energy or Q_{MCP}. Therefore, we introduce no TOF corrections other than T_e in the Monte Carlo simulation.

4.16 Background

4.16.1 Background from non-trapped ^{6}He atoms

During the measurement of $a_{\beta\nu}$ using the trapped ^{6}He, the majority of the background is from the decays of the non-trapped ^{6}He atoms in the MOT-2 chamber. There are many sources of the non-trapped ^{6}He atoms. The trapped atoms escape from the trap due to collisions with the residual gas molecules. During the atom transfer from MOT-1 to MOT-2, not all atoms are captured. ^{6}He atoms also diffuse from the MOT-1 chamber into MOT-2 through the aperture between them, and they can also stream back into MOT-2 from the rough vacuum behind the turbo pump on the MOT-2 chamber. The ^{6}He atoms from all these sources are at room temperature. For the escaped atoms or the non-captured atoms, they are thermalized through collisions with the residual gas or the chamber wall to room temperature. At room temperature, the RMS velocity of a ^{6}He atom is $\sim$1000 m/s, so one atom probes most of the MOT-2 chamber before it decays. Therefore, the distribution of these non-trapped ^{6}He atoms are approximately uniform in the MOT-2 chamber. For the escaped atoms, it takes $\sim$73 μs on average to hit the chamber wall or other elements in the MOT-2 chamber. The probability of decaying in this period is negligible, so these atoms are treated as uniformly distributed.

The contribution of this background needs to be subtracted from the TOF spectrum for the $a_{\beta\nu}$ extraction, and therefore the shape and the normalization of the background TOF spectrum are needed for the background subtraction. The shape measurement is described in this section, while the normalization determination and the background subtraction al-

gorithm are described in Chapter 6.

To measure the TOF spectral shape of the non-trapped ^{6}He decays, we introduced a large amount of non-trapped ^{6}He through the system described in Section 2.3. With the full ^{6}He production, the coincidence trigger rate (between the MCP and the β telescope) is about 220 Hz. However, the MCP single trigger rate is over 90 kHz and the β telescope trigger rate is about $\sim$1 kHz. In this case, it is important to take into account the random coincidences between these two detectors, which means the event triggering the β telescope and the event triggering the MCP are not the same. The TOF spectrum of the non-trapped ^{6}He background for this high rate run is plotted in Figure 4.82 (black curve). The TOF shift due to the timing-zero is already implemented in this spectrum. It is non-physical for a decay to have TOF$<$0 ns or TOF$>$800 ns, so the events in these regions correspond to the random coincidences described above. The number of count per bin in these regions is almost constant. We fit the spectrum to a constant function in the region 1000 ns$<$TOF$<$1400 ns, and the average number of count per bin is 9.98. Assuming that the spectrum of the random coincidence events is also flat in the region 10 ns$<$TOF$<$600 ns (0 is excluded to avoid the timing-zero peak), the random coincidence events are 8.1% of the total, so the signal-to-background ratio is 11.3. These events will introduce a large uncertainty in the background subtraction. To avoid that, one simple method is to reduce the rate. We reduced the production rate so that the coincidence rate for the background TOF measurement is $\sim$30 Hz. The corresponding TOF spectrum is plotted in Figure 4.82 (blue curve). The two histograms are scaled vertically so that their maxima in the region 10 ns$<$TOF$<$600 ns match each other. In this case, the random coincidence count per bin is 1.41. In the region 10 ns$<$TOF$<$600 ns, the signal-to-background ratio is 70. In principle, for a fix period of time the number of valid events (signal) scales linearly with the rate R, but the random coincidence rate (background) scales quadratically with R. Therefore, the signal-to-background ratio scales inversely with R.

In summary, the TOF spectral shape of the background generated by the non-trapped ^{6}He atoms is measured by introducing large amount of non-trapped ^{6}He into the MOT-2 chamber. The higher the rate is, the more the random coincidence events are. Therefore, we keep then coincidence rate $\sim$30 Hz during this measurement. Because this measured back-

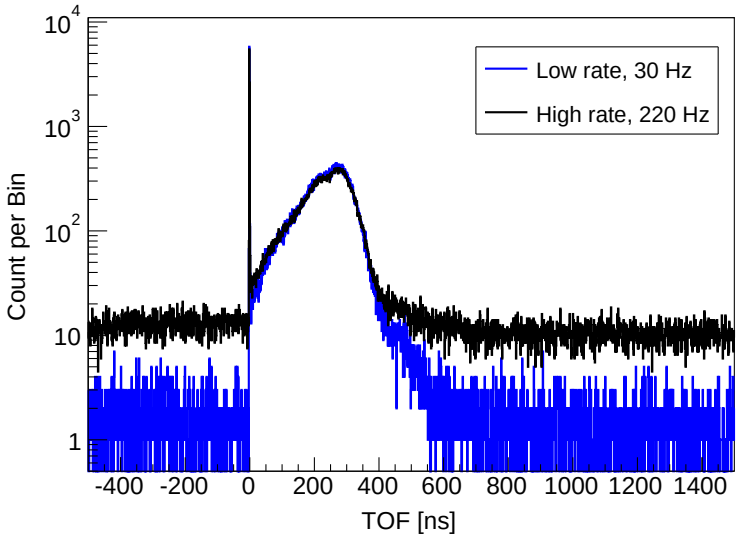

Figure 4.82: TOF spectrum of the background generated by the non-trapped ^{6}He. The blue curve corresponds to the low rate run, and the black curve corresponds to the high rate run.

ground TOF spectral shape will be used directly in the background subtraction procedure, there is no need to use the Monte Carlo simulation to generate this spectrum. However, we still simulate this case in Chapter 5, and this measured spectrum will be used as a standard in estimating how well the simulation can reproduce the measured results.

4.16.2 Background from the ambient radiation

Besides the non-trapped ^{6}He, the ambient radiation from the accelerator and the production target also generates background in all detectors. We measured the rates of each detector and the coincidence rates in presence of only the ambient radiation.

To prevent the produced ^{6}He from diffusing into the experiment region, the gate valve on the 6 inch transfer tube is closed. The trigger rate of the PMT is 8 kHz when the beam is hitting the target. With ^{6}He atoms trapped in MOT-2, the additional rate is less than 10 Hz. The pile-ups between the ambient events and the ^{6}He decay events are negligible. The trigger rate of the whole β telescope (*i.e.* the coincidence trigger between the PMT and the MWPC) is ~0.16 Hz and the E_β spectrum of the ambient radiation is

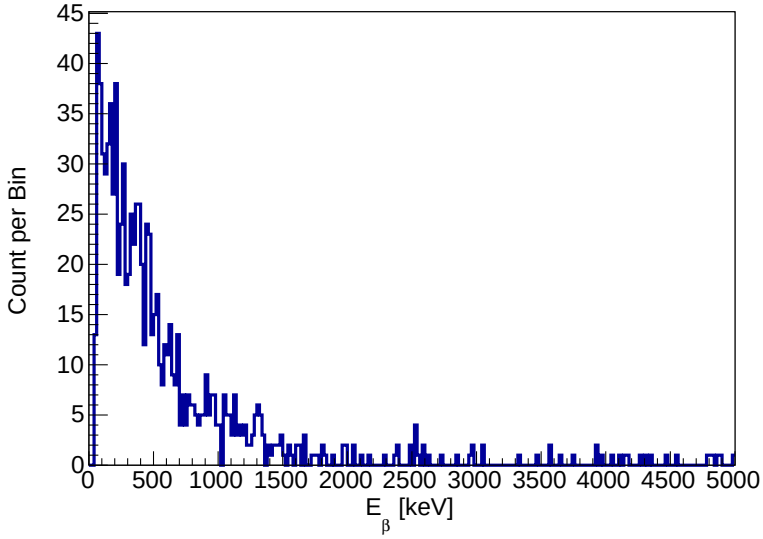

Figure 4.83: E_β spectra for the ambient radiation background when the deuteron beam is hitting the production target. The PMT is read in coincidence with the MWPC but not the MCP. The background caused by the cosmic rays is beyond the E_β range of this figure.

shown in Figure 4.83. With the trapped ^{6}He in the MOT-2, we have achieved $\sim$2 Hz trigger rate in the β telescope. Therefore, the β telescope itself cannot provide a low-background measurement of the ^{6}He β-energy spectrum. The coincidence trigger with MCP is needed to veto the background.

The MCP-β telescope coincidence rate is lower than 0.012 Hz while only the ambient radiation is present. Most of these events are in the timing-zero peaks as shown in Figure 4.79b. During the 1 hour and 40 minutes data taking, there is not a single event detected within the TOF window from 130 ns to 350 ns, so the coincidence rate in this TOF window from 130 ns to 350 ns is lower than 0.00016 Hz. During the $a_{\beta\nu}$ measurement in October 2015, the average coincidence rate is $\sim$1 Hz, so the background generated by the ambient background is negligible.

4.17 Summary of the calibration experiments

This chapter follows the calibration purposes to organize the sections, and some experiments are mentioned multiple times because they serves for more than one calibration purpose. The calibrations are summarized in Table 4.6.

^{55}Fe, MWPC ON	MWPC position, MWPC energy deposition
^{207}Bi, β telescope ON	Scintillator-PMT energy response, MWPC efficiency
^{207}Bi, PMT and MCP ON	Timing-zero
^{90}Sr, β telescope ON	MWPC efficiency
^{90}Sr, MCP ON	MCP signal size, MCP position
^{241}Am, MCP ON	MCP position, MCP signal size, MCP efficiency
Non-trapped ^{6}He, full setup	MCP position, MCP efficiency, MCP signal size, Timing-zero, Background shape
Trapped ^{6}He, full setup	Timing-zero

Table 4.6: Summary of the calibration experiments. Left column indicates the calibration experiment. Right column shows the purpose of each calibration exeperiment.

Chapter 5

THE MONTE CARLO SIMULATION

As mentioned in Chapter 2, in order to extract $a_{\beta\nu}$ we fit the measured ^{6}Li recoil ion TOF spectrum to the templates with $a_{\beta\nu} = \pm 1/3$ generated by the Monte Carlo simulation. Because the detector response functions and fiducial cuts affect the TOF spectrum, it is crucial to model the detector system as close to reality as possible in the simulation. In this chapter, the Monte Carlo (MC) simulation software development is introduced. We use the Monte Carlo simulation to reproduce the spectra from many calibration experiments, and compare the simulated spectra to the measured ones. Through these comparisons, we fix those parameters in the simulation, and estimate how well the simulation matches the real experiment.

5.1 MC simulation software overview

In the MC simulation the decay events are generated according to the decay physics of ^{6}He (or other isotopes for calibration experiments) and source geometry. The decay position and the momenta of the outgoing particles are fed to the β-particle and ion tracking programs. The β-particle tracking program (β tracker) is developed based on the GEANT4 toolkit, and it simulates the transport of the β particle emitted from the decay and records the energy deposition in each volume of the detector system. Besides β particles, the β tracker also tracks photons for calibration purposes. The ion-tracking program (ion tracker) tracks the recoil ions in the E-field calculated by COMSOL (see Section 4.13), and records the TOF, final position and final momentum of the ion. Then the detector responses are implemented in the post-processor, and the recorded energy depositions and hit positions from the β tracker and the ion tracker are converted to detector readouts. These readouts are written to event files for analysis.

There are many adjustable inputs in the simulation program, for example the $a_{\beta\nu}$ value,

the E-field map, detector resolutions and so on. The user interface of the simulation program is command-line style, and one can use shell scripts to run simulations in batch mode. Besides generating fit templates, the MC simulation is also used for studying the sensitivities of $a_{\beta\nu}$ to different systematic effects. This requires frequently changing simulation input configurations. In order to save time, all components of the MC simulation: event generator, β tracker, ion tracker and post-processor, are stand-alone programs that can be executed independently. Therefore, if one changes only the detector response parameters, one need only to re-run the post-processor without the need of re-running the time-consuming GEANT4 based β tracker. The communications between the programs are through files. The event generator is integrated into the β tracker[1], so the β tracker first generates one event, tracks the β particle immediately, and then writes the energy deposition in every part of the detector system into the *Beta-Event File*. Meanwhile, it also writes initial position and velocity of the recoil ion into the *Ion-Info File*. The ion tracker then reads in the *Ion-Info File*, calculate the trajectory of each ion and output the TOF and final momentum of the ion into the *Ion-Event File*. Finally, the post-processor reads in both the *Beta-Event File* and the *Ion-Event File*, implements the detector response functions, and outputs the detector readings to the *Event File* as the final output from the simulation program. The flowchart in Figure 5.1 illustrates the simulation procedures and communications between programs and modules in the MC simulation of ^{6}He decays.

The detector geometry and coordinate system shared by the whole MC simulation program is described in Section 5.2. The detail designs of the event generator, β tracker, ion tracker and post-processor are described in Sections 5.3 through 5.6.

5.2 Detector geometry and coordinate system

In the MC simulation, a global coordinate system is shared by the β tracker, ion tracker and post-processor. The X direction is along the push-beam direction, and the Z direction is vertically upward. The Y direction is chosen so that the coordinate system is right-handed. The origin of the Z axis is at 91.000 mm above the MCP top surface, and the origin of the

[1]The event generator can also run as a stand-alone program and let the β tracker read its output event file and start the following simulation.

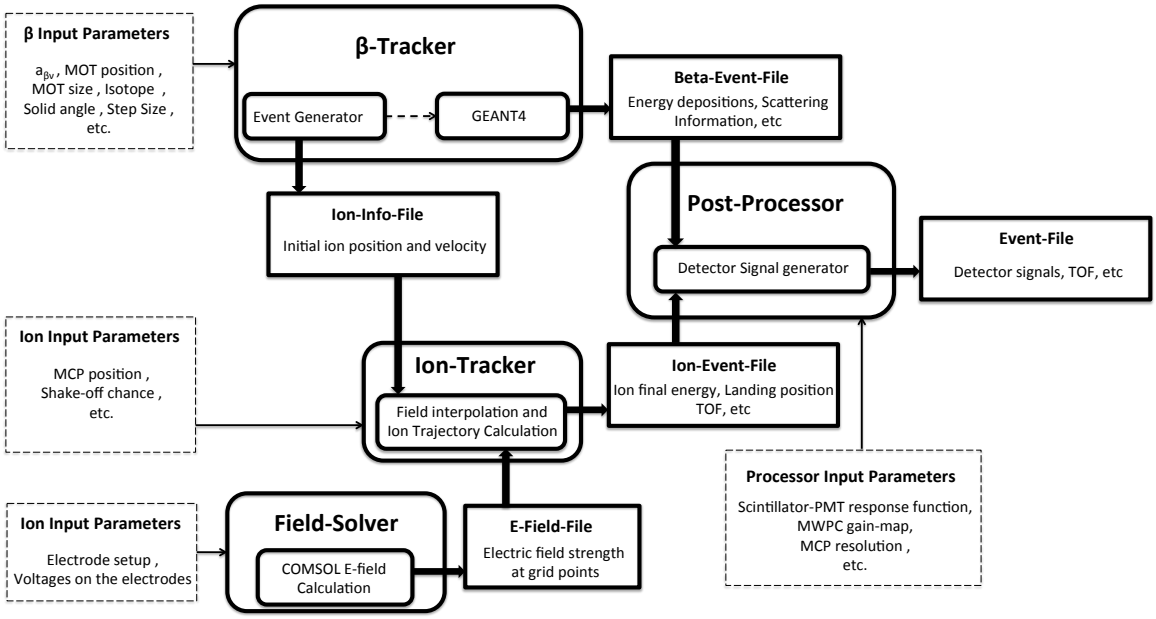

Figure 5.1: MC Simulation Flowchart. Round-corner squares are independent programs (and their internal modules). Sharp-corner squares are data files. Dashed squares are configurations in command lines or script files. Thick arrows indicate data stream into and out of data files. Thin arrows indicate configuring and setting up parameters. Dashed arrows indicate internal communication between modules inside one program.

XY plane is at the center of the MCP mask. The deviation of the electrode structure center to the MCP mask center is neglected.

Both the ion tracker and the β tracker need a detailed description of the detector system geometry. For the E-field calculation, the COMSOL geometry construction is based on the design drawing. The positions of the electrodes are adjusted to match the mechanical inspection results. In the GEANT4 simulation, the geometry of the MOT-2 chamber and the β telescope is simplified. The supporting column of the electrode structure and the supporting structure of the MWPC are not included in the geometry, because these components are well beyond the region of interest. The β particles that hit these components hardly hit the fiducial volume of the MWPC and the scintillator. The detector geometry used in the GEANT4 simulation is shown in Figure 5.2. The positions of the electrodes are also adjusted according to the measurements. The material assignment in the GEANT4

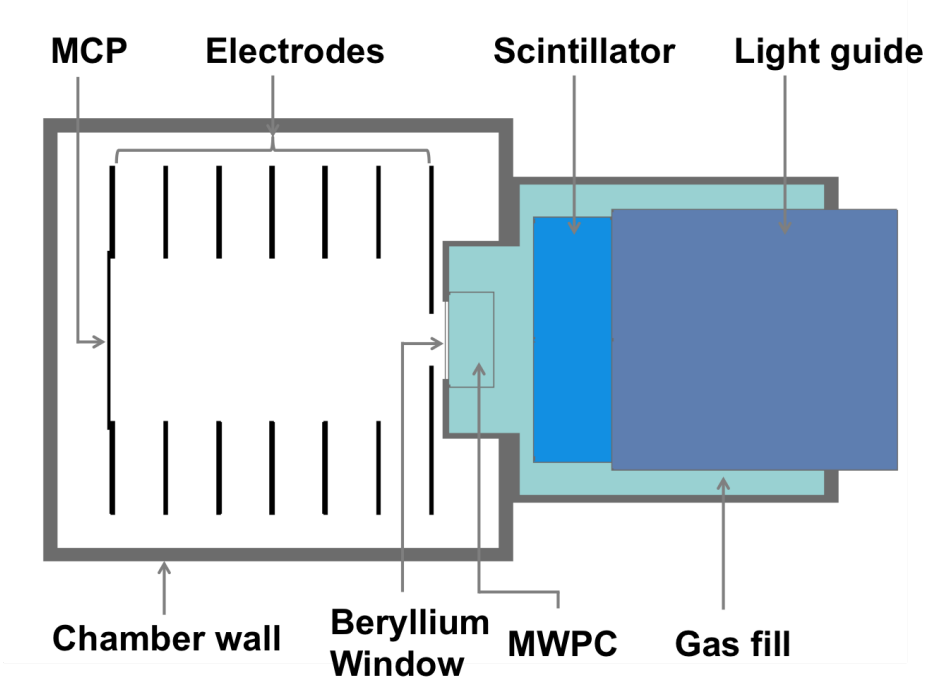

Figure 5.2: Detector geometry in the GEANT4 simulation.

geometry is described in Section 5.4.

Besides the MOT-2 chamber and the detector system, the geometry of the ^{207}Bi calibration source is also described in detail as shown in Figure 5.3. The three layers of the source backing: 50.8 μm platinum, 254 μm stainless steel, and 101.6 μm plastic, are included. It is crucial to include these backing materials in order to generate the correct E_β spectrum in the simulation. The active material on the source is a thin layer of deposition with 5.08 mm diameter. The thickness of the active material is negligible. There is a layer of acrylic cover on the active material, and its area density is 100 μg/cm^2. The energy loss of 500 keV electrons in this layer is $\sim$0.18 keV which is well below our calibration precision, so this layer is also neglected. The geometry descriptions of the ^{90}Sr source and the ^{55}Fe source are not known in detail, so we only have rough descriptions of their geometry. However, the detailed geometry does not affect the ^{55}Fe X-ray energy, and the ^{90}Sr is not used in high-precision calibrations. Therefore, these simplifications are acceptable.

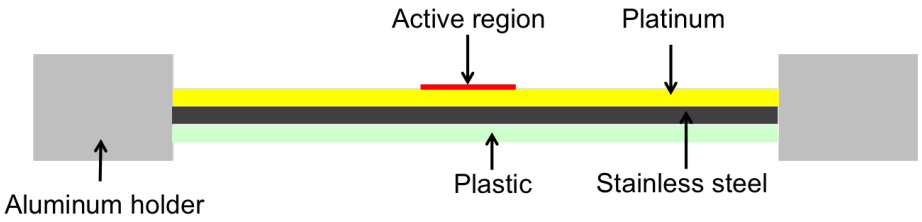

Figure 5.3: Detailed geometry of the ^{207}Bi source.

5.3 Event generator

The event generator is a C++ class that generates the initial positions and momenta of particles for the β-tracking and the ion-tracking programs. It allows the user to select isotopes, position distributions and parameters of the decay physics. This class is compiled into a shared library and linked to both the main function that controls the event generator and the β tracker. The main function reads an input file written by users to configure the event generator. It generates a certain number of events according to the user's request, and writes the information of each event to an output file. Alternatively, the β tracker can be set to use the event generator internally, and users can use the command-line interface of the β tracker to configure the event generator. The event generating function of the generator is called on an event-by-event basis, and the total number of generated events are controlled by the main function or the β tracker.

Currently, the position distribution of the events in the event generator program is either a 3D Gaussian distribution or a uniform distribution in a cylinder. The first one is used to simulate the MOT, and the second one is used to simulate the non-trapped ^{6}He or the calibration sources. The size and center position of these distributions are tunable parameters. To generate events for the photoion studies, only the initial ion positions are generated, while the ion velocity is set to zero. In other cases, the energy distribution of the generated particles depends on the spectrum of the specific isotope. The decay physics of each available isotope is discussed in the following subsections.

5.3.1 ^{6}He decays

When generating the momenta of the β particle and the recoil ion from the ^{6}He decay, we use the 3-body decay phase space. Because the ^{6}He atoms are cold in the MOT-2 compared to the β-decay energy scale, their initial momentum is neglected. Thus the lab frame is the center-of-mass frame of the ^{6}He atom, and in this frame the decay phase space is

$$d\Omega_{\text{3-body}} = \frac{E_e p_e E_\nu^2}{1 + (E_\nu + p_e \cos(\theta_{\beta\nu}))/M_r} dE_e d\Omega_e d\Omega_\nu \tag{5.1}$$

where Ω_e and Ω_ν are the directions of the β particle and the anti-neutrino. (The nomenclature is the same as that in Chapter 1.) In the 3-body decay there are 9 degrees of freedom (*i.e.* 3-momenta of the 3 particles), but due to the conservation of momentum and energy there are 4 constraints and therefore there are only 5 degrees of freedom left: E_β, Ω_e and Ω_ν. E_ν is not independent but given by

$$E_\nu = -(p_e \cos(\theta_{\beta\nu}) + M_r) + \sqrt{(p_e \cos(\theta_{\beta\nu}) + M_r)^2 + 2(Q - E_e)M_r - p_e^2}, \tag{5.2}$$

where Q is the decay Q-value (the mass difference between ^{6}He atom and the ^{6}Li$^+$ ion mass). In these expressions, the ^{6}Li recoil ion is treated as non-relativistic particle, while the β particle and the anti-neutrino are relativistic. Substituting the 3-body decay phase space into the differential decay rate formula (Equation 1.33 in Section 1.2) one gets

$$\frac{d\Gamma_0}{dE_e d\Omega_e d\Omega_\nu} = NF(E_e) \frac{E_e p_e E_\nu^2}{1 + (E_\nu + p_e \cos(\theta_{\beta\nu}))/M_r} \mathcal{M}_0 \tag{5.3}$$

where

$$\mathcal{M}_0 = 1 + b\frac{m_e}{E_e} + a_{\beta\nu}\frac{p_e}{E_e}\cos(\theta_{\beta\nu}), \tag{5.4}$$

and $F(E_e)$ is the Fermi function that corrects the spectrum distortion due to the Coulomb force. The Fermi function is defined in Equation 1.29 in Section 1.2. For ^{6}Li, $Z = 3$ and $\rho = 2.59$ fm [93].

Besides the Fermi function, the recoil order corrections and radiative corrections in addition to the leading order Feynman diagram are included in the simulation. We chose the parametrization of the recoil order corrections following Reference [94]. Adding the

correction terms, $\mathcal{M}_0$ becomes

$$\mathcal{M}_0' = 1 + f_1(E_e) + b\frac{m_e}{E_e} + (a_{\beta\nu} + f_2(E_e))\frac{p_e}{E_e}\cos(\theta_{\beta\nu}) + f_3(E_e)(\frac{p_e}{E_e})^2(\cos^2(\theta_{\beta\nu}) - \frac{1}{3}), \tag{5.5}$$

where the functions f_1, f_2 and f_3 are defined as

$$\begin{aligned} f_1(E_e) &= -\frac{2}{3}\frac{E_0}{M_r}(1 + b' + d') + \frac{2}{3}\frac{E_e}{M_r}(5 + 2b') - \frac{m_e^2}{3M_rE_e}(2 + 2b' + d'), \\ f_2(E_e) &= \frac{2}{3}\frac{E_0}{M_r}(1 + b' + d') - \frac{4}{3}\frac{E_e}{M_r}(3 + b'), \\ f_3(E_e) &= \frac{E_e}{M_r}, \end{aligned} \tag{5.6}$$

and b' and d' are form factors. According to the calculations in Reference [94] and [95] and the measured width of the 3.56 MeV $M1$ transition of ^{6}Li [96], these factors are $b' = 24.7$ and $d = 0.2$.

The radiative corrections are treated similarly to that described in Reference [45] and Reference [97]. In short, the radiative correction to the ^{6}He decay Hamiltonian is divided into the virtual-soft bremsstrahlung part and the hard photon bremsstrahlung part. The virtual and soft bremsstrahlung correction adds two extra terms so that $\mathcal{M}_0'$ becomes

$$\mathcal{M}_{0vs}' = (1 + z_{vs})\mathcal{M}_0' + \widetilde{\mathcal{M}}. \tag{5.7}$$

The $\widetilde{\mathcal{M}}$ is defined as

$$\widetilde{\mathcal{M}} = -\frac{\alpha}{\pi}\frac{1 - \beta^2}{\beta}\mathcal{N}(\beta), \tag{5.8}$$

where α is the fine-structure constant, $\beta = p_e/E_e$, and

$$\mathcal{N}(\beta) = \frac{1}{2}\ln\frac{1 + \beta}{1 - \beta}. \tag{5.9}$$

The z_{vs} is defined as

$$z_{vs} = \frac{\alpha}{\pi}\left(\frac{3}{2}\ln(\frac{m_p}{m_e}) + 2\left(\frac{\mathcal{N}(\beta)}{\beta} - 1\right)\ln(\frac{2\omega}{m_e}) + 2\frac{\mathcal{N}(\beta)}{\beta}(1 - \mathcal{N}(\beta)) + \frac{2}{\beta}L\left(\frac{2\beta}{1 + \beta}\right) - \frac{3}{8}\right), \tag{5.10}$$

where L is the Spence function defined as

$$L(z) = \int_0^z dt \frac{\ln|1-t|}{t}, \tag{5.11}$$

m_p is the proton mass and ω is the soft bremsstrahlung cutoff energy. After the recoil order correction and the virtual-soft bremsstrahlung radiative correction, the differential decay rate is

$$\frac{d\Gamma_{0vs}}{dE_e d\Omega_e d\Omega_\nu} = NF(E_e) \frac{E_e p_e E_\nu^2}{1.0 + (E_\nu + p_e \cos(\theta_{\beta\nu}))/M_r} \left(\mathcal{M}_0'(1+z_{vs}) + \widetilde{\mathcal{M}} \right). \tag{5.12}$$

The hard photon bremsstrahlung term has a completely different kinematics because of the extra photon in the final state. The differential decay rate with the bremsstrahlung photon is given by

$$\frac{d\Gamma_H}{dE_e d\Omega_e d\Omega_\nu dE_\gamma d\Omega_\gamma} = N_H E_\gamma \beta E_e E_\nu (H_0 + a_{\beta\nu} H_1), \tag{5.13}$$

where E_γ is the photon energy, Ω_γ is the direction of the photon and N_H is the constant factor. Because of the photon coupling in this radiative correction term, N_H is smaller than the constant factor N in Equation 5.12 by α. The H_0 and H_1 terms are defined as

$$H_0 = E_\nu \left(-(E_e + E_\gamma) P^2 + \frac{1}{E_e - p_e \cos(\theta_{\beta\gamma})} \right), \tag{5.14}$$

$$\begin{aligned} H_1 = {} & E_\nu p_e \cos(\theta_{\beta\nu}) \left(-P^2 + \frac{1}{E_e E_\gamma - p_e E_\gamma \cos(\theta_{\beta\gamma})} \right) \\ & + E_\gamma E_\nu \cos(\theta_{\nu\gamma}) \left(\frac{E_e + E_\gamma}{E_\gamma (E_e E_\gamma - p_e E_\gamma \cos(\theta_{\beta\gamma}))} - \frac{m_e^2}{(E_e E_\gamma - p_e E_\gamma \cos(\theta_{\beta\gamma}))^2} \right), \end{aligned} \tag{5.15}$$

$$P^2 = \frac{1}{E_\gamma^2} + \frac{m_e^2}{(E_e E_\gamma - p_e E_\gamma \cos(\theta_{\beta\gamma}))^2} - \frac{2E_e}{E_\gamma (E_e E_\gamma - p_e E_\gamma \cos(\theta_{\beta\gamma}))}, \tag{5.16}$$

where $\theta_{\beta\gamma}$ is the angle between the β particle and the bremsstrahlung photon, $\theta_{\nu\gamma}$ is the angle between the anti-neutrino and the bremsstrahlung photon.

The events are generated using the *rejection method* and the right-hand-side of Equation 5.12 as the weight for the events without the bremsstrahlung photon and the right-hand-side of Equation 5.13 for the events with the bremsstrahlung photon. The total decay rates Γ_{0vs} and Γ_H are calculated in Reference [97], and their ratio Γ_H/Γ_{0vs} is 0.03045. Therefore, we first generate a random number with a uniform distribution from 0 to 1. If

the number is less than $\Gamma_H/(\Gamma_{0vs}+\Gamma_H)$, we generate one event with the bremsstrahlung photon. Otherwise we generate one event without the bremsstrahlung photon.

To generate events without the bremsstrahlung photon, we first calculate the maximum value of the weight function (right-hand-side of Equation 5.12). The constant factor N is arbitrary, but needs to be kept as a constant through the whole procedure. Then the direction of the β particle is selected uniformly in the user-defined cone, and the direction of the anti-neutrino is selected uniformly in all directions. The β energy E_β is selected uniformly from m_e to $m_e + E_{end}$ where E_{end} is the largest possible (end-point) kinetic energy of the β particle. E_{end} is calculated based on the 3-body decay kinematics when the neutrino has no energy, and therefore

$$E_{end} = \sqrt{M_r^2 + 2M_r(Q+m_e) + m_e^2} - M_r - m_e. \tag{5.17}$$

After these degrees of freedom are fixed, E_ν is calculated using Equation 5.2, and the ion momentum is calculated using the conservation of momentum. $\cos(\theta_{\beta\nu})$ is calculated using the inner product of the direction vectors of the β particle and the anti-neutrino. In our program, the soft bremsstrahlung cutoff energy ω is chosen to be 1 eV. Then the value of the weight function (W_{0vs}) is calculated based on the values of the parameters mentioned above, and another random number is generated uniformly from 0 to W_{0vs}^{MAX} which is the maximum of the weight function. If this random number is less than the W_{0vs}, this event is kept. Otherwise, this event is rejected.

To generate events with the bremsstrahlung photon, we followed the prescription described in Reference [45]. The weight function for the decay with the hard bremsstrahlung photon (right-hand-side of Equation 5.13) has sharp peaks at $E_\gamma = 0$ and $\theta_{\beta\gamma} = 0$. Therefore, the importance sampling technique is implemented in this procedure to improve the generating efficiency. The importance sampling weight function is chosen to be

$$W_g = \frac{\beta E_e}{2\mathcal{N}(\beta)(E_e E_\gamma - p_e E_\gamma \cos(\theta_{\beta\gamma}))}, \tag{5.18}$$

and the modified weight for event generation is

$$\begin{aligned} W_{Hg} &= N_H \frac{E_\gamma \beta E_e E_\nu (H_0 + a_{\beta\nu} H_1)}{W_g} \\ &= N_H 2\mathcal{N}(\beta) E_\gamma E_\nu (E_e E_\gamma - p_e E_\gamma \cos(\theta_{\beta\gamma}))(H_0 + a_{\beta\nu} H_1). \end{aligned} \tag{5.19}$$

The constant factor is arbitrary, and the maximum of W_{Hg} (W_{Hg}^{max}) is calculated. To carry out the importance sampling, one generates events according to weight function W_g first. The energies and directions of the outgoing particles are generated as follows. The energy and direction of the β particle, direction of the anti-neutrino are selected in the same way as the previous case without the bremsstrahlung photon. For selecting the energy of the photon E_γ, one generates a random number u_1 uniformly from 0 to 1, and then set E_γ as

$$E_\gamma = \omega \exp\left(-u_1 \ln(Cs)\right), \tag{5.20}$$

where $Cs = \omega/(Q - E_\beta)$. For selecting the direction of the photon, one generates another random number u_2 uniformly from 0 to 1, and set $\cos(\theta_{\beta\gamma})$ as

$$\cos(\theta_{\beta\gamma}) = \frac{1 - (1+\beta)\exp(-2\mathcal{N}(\beta)u_2)}{\beta}. \tag{5.21}$$

The azimuthal angle of the photon around the β particle direction is uniformly selected from 0 to 2π. In this calculation, the 3-body decay phase space is not used, so $E_\nu = Q - E_\beta - E_\gamma$, and the momenta of the recoil ion is determined through momentum conservation. Then the rejection method based on the weight function W_{Hg} is carried out. One random number is generated uniformly from 0 to W_{Hg}^{max}. If this random number is less than the calculated W_{Hg} using the particle status generated as above, the event is kept. Otherwise, the event is rejected.

In both cases, with or without the bremsstrahlung photon, if the event is kept, the event generator returns the types, energies and directions of the outgoing particles to the program that calls it, and proceeds to generate the next event. If the event is rejected, the program loops back to the particle energy and direction generation without changing whether or not there is the bremsstrahlung photon. The flowchart of the working procedure of the event generator is shown in Figure 5.4.

The generated β-energy (E_β) spectrum and the recoil-ion-energy spectrum are shown in Figure 5.5. For the recoil-ion-energy spectrum, both cases where $a_{\beta\nu} = -1/3$ and $a_{\beta\nu} = +1/3$ are shown.

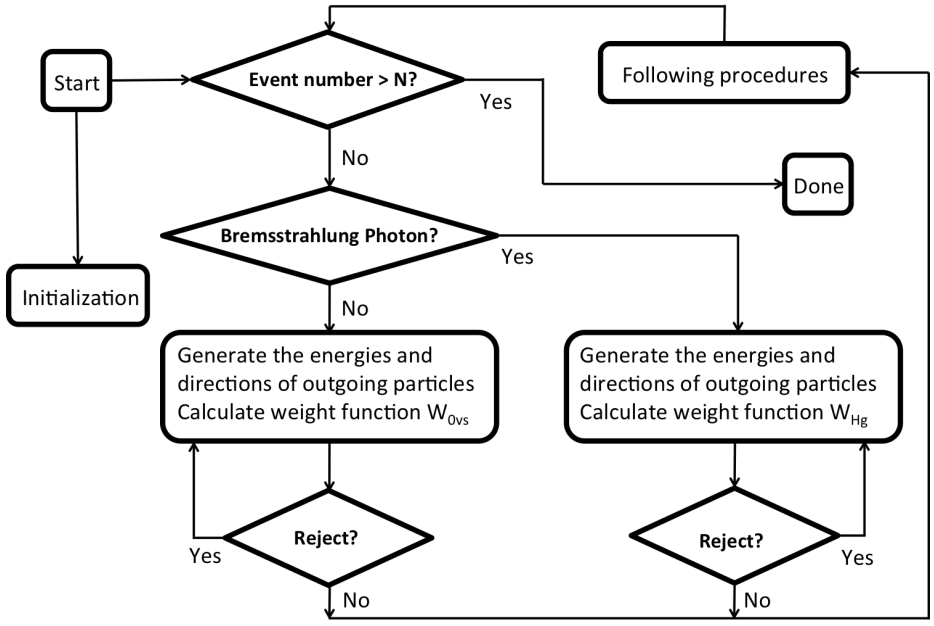

Figure 5.4: Event generator flowchart for generating N events.

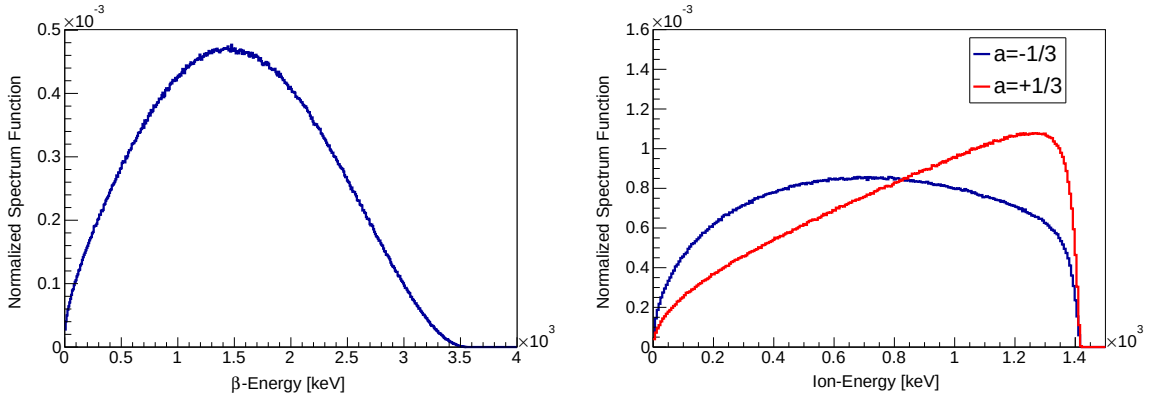

(a) (b)

Figure 5.5: (a) β-Energy spectrum generated by the MC simulation. (b) Recoil-ion-energy spectrum generated by the MC simulation. Blue: $a = -1/3$, Red: $a = +1/3$.

5.3.2 Calibration sources

Three sealed sources: ^{207}Bi, ^{55}Fe and ^{90}Sr are used for the calibration of the β telescope. In the MC simulation, the energy spectrum of the outgoing particles are described as follows.

The conversion electrons from the ^{207}Bi source are used for the high-precision β-telescope energy calibration. However, there are also γ rays emitted from the source, and the intensity of the γ ray is much higher than the conversion electrons. Therefore, detailed descriptions of these outgoing particles are needed. ^{207}Bi decays into ^{207}Pb through electron capture. As shown in Figure 4.73, the daughter nucleus has 3 possible final states, and it subsequently decays to the ground state through emitting γ rays or conversion electrons. If the daughter nucleus starts from the higher two excited states, cascade decays through the $\frac{5}{2}^-$ state will happen. In cascade decays, the emerging particles of both the prompt decay and the following decay are generated as primary particles in an event of the GEANT4 simulation. The energy spectrum and relative intensities are listed in Table 5.1. The initial positions of the outgoing particles are generated uniformly in a cylinder 50 μm in thickness and 5.08 mm in diameter marked in Figure 5.3, and the outgoing particles are emitted uniformly in all directions.

	Prompt Decay			Following Decay			
		Energy [keV]	Intensity [%]		Energy [keV]	Intensity [%]	Half-life [ps]
$\frac{7}{2}^-$	γ	1770.228	6.87	γ	569.698	97.75	130.5
	e^-	1754.367	0.0034	e^-	565.847	1.537	
	e^-	1682.224	0.0238				
$\frac{13}{2}^+$	γ	1063.656	74.5	e^-	553.837	0.442	
	e^-	1059.805	0.44				
	e^-	1047.795	1.84	e^-	481.694	0.111	
	e^-	975.651	7.08				
$\frac{5}{2}^-$	γ	569.698	8.70	-			
	e^-	565.847	0.0099				
	e^-	553.837	0.0393				
	e^-	481.694	0.1368				

Table 5.1: Energy spectrum emerging from the ^{207}Bi source. The half-life listed in the last column is for the intermediate state of the cascade decays.

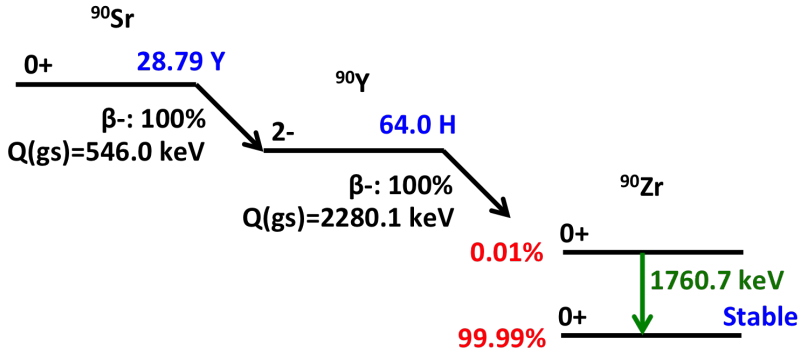

Figure 5.6: Scheme of the ^{90}Sr-^{90}Y-^{90}Zr decay chain. This scheme is obtained from National Nuclear Data Center [92], Brookhaven National Laboratory.

The energy spectrum of the soft X-rays from the ^{55}Fe source is much simpler. The ^{55}Fe decays into ^{55}Mn through electron capture. The daughter nucleus emits two major K-shell X-rays: K_α with 5.895 keV and K_β with 6.49 keV, and their intensity ratio is 8.56 : 1. The X-rays with these two energies are generated with this ratio, and their directions are uniformly distributed in the 4π solid angle.

In the ^{90}Sr source, ^{90}Sr decays into the ground state of ^{90}Y with a half-life 29 years and end-point energy 546.0 keV, and then ^{90}Y decays into the ground state of ^{90}Zr (over 99.99%) with a half-life 64 hours and end-point energy 2280.1 keV. The scheme of the ^{90}Sr-^{90}Y-^{90}Zr decay chain is shown in Figure 5.6. The source we used was already stored long enough so that the secular equilibrium was reached. In this case, the intensity ratio of the two decays is 1:1. We used the spectrum shape described in Reference [98] to generate the energy of the emerging β particles, and their directions are also uniformly distributed in the 4π solid angle.

5.4 β tracker

The β tracker program tracks the generated β particles and γ rays (or X-rays) using the GEANT4 toolkit. This program was developed based on the example *B1* from the GEANT4 (version 4.9.6) package. The program consists of the detector constructor, run manager, primary event generator, step manager, event manager, physics lists, and the messengers. The

detailed work flow is described in the GEANT4 user manual [99], and the event generator was already described in the previous section. Therefore, in this section, we introduce the detector constructor, physics lists, energy deposition in the step manager and the output routine in the event manager.

5.4.1 Detector constructor

We constructed the detector geometry as in Figure 5.2. The materials assigned to the components are listed in Table 5.2.

Chamber wall	G4_STAINLESS-STEEL
Beryllium window	G4_Be
Plastic scintillator	G4_PLASTIC_SC_VINYLTOLUENE
Light guide	G4_PLEXIGLASS
MWPC Gas	Argon (90%) CO_2 (10%) mixuture
Electrodes	G4_STAINLESS-STEEL
MCP	G4_SILICON_DIOXIDE

Table 5.2: Materials used in the GEANT4 simulation.

The MWPC is rotated 30° relative to the MOT-2 chamber coordinate system, so this is also implemented in the GEANT4 geometry. The active MWPC volume is a rectangular box with the base area the same as the anode active area (the area covered by the wires). The height of the active volume (h_{MWPC}) is chosen so that the most probable value of the energy deposition for β particles matches the measurement. This height is larger than the distance between the cathodes. The active volume starts right above the beryllium window and extends to h_{MWPC} above the window.

5.4.2 Physics lists

Because this GEANT4 simulation only involves electrons and photons with energies lower than 10 MeV, the low-energy electromagnetic interaction package is used. We choose to use

the *EmPenelope* modules, and particularly the *Goudsmit-Saunderson multiple scattering model* [100] is activated.

Electrons, positrons and photons are constructed in the GEANT4 physics list. For electrons, registered processes are ionization, Bremsstrahlung, Coulomb Scattering and multiple scattering. For positrons, all the processes for electrons as well as the annihilation are registered. For photons, photo-electric effect, Compton scattering, pair production and Rayleigh scattering are registered.

There are parameters to fine tune the processes in the GEANT4 simulation. The most important one is the secondary particle production range cut. The program stops tracking the newly generated secondary particle with energy too low for it to travel this range in its residing material and deposits its kinetic energy into the residing volume. We set the range cut to 0.1 mm for all volumes except the MWPC. The MWPC range cut is set to 0.05 mm. The second parameter is the step limit for each volume. For the MWPC, we limit the step size to 0.25 mm, and for other volumes we don't limit the step size. Without the limit, the program chooses step sizes adaptively according to the material density, particle energy, distance to boundary and so on.

5.4.3 Energy deposition registry and output routine

In GEANT4, the term *event* is defined as the shower created by the primary particles. The simulation of an event starts from tracking the generated primary particles, and ends when all primary and secondary particles escape or deposit all their energy to the system. For each event and each volume, we created an energy deposition accumulator. In each step of the tracking, the energy loss within this step is added to the energy deposition accumulator for the volume where the particle is at. For each volume, we assigned a *hit flag* to label whether it is hit by the primary particle. At the beginning of an event, all volumes are labeled *not hit*. In each step, the particle residing volume is labeled as *hit* if the particle is primary. This helps identifying events that involve β scattering on electrodes, window holder and so on. There is also a *back-scattering flag* which is labeled *true* if the primary β particle enters and then exits the scintillator volume. At the end of each event, the event

manager summarizes the accumulated energy deposition in each volume and the hit-flags (including the back-scattering flag) in a data structure and then pushed to the output queue.

The MWPC needs special handling beyond registering the energy deposition. The entrance position and the exit position for a primary β particle are identified in the step manager and included in the output data structure. Moreover, we divide the MWPC active volume into *cells*. Each cell is a long rectangular box parallel to the anode wires and each wire sits at the center of the corresponding cell as shown in Figure 5.7. The energy deposition in the hit cell is converted into the number electron-ion pair based on the average ionization energy for the argon-CO_2 mixture. The mean and variance of the ionization position distribution along the wire direction are updated when that cell is hit. To simulate the cathode focusing effect described in Section 4.2, for an ionization happening outside the cathode planes we assume that its coordinate perpendicular to the cathode wire direction is the center position between the adjacent wires. At the end of an event, the number of active cells (which have non-zero energy deposition), the total number of electron-ion pairs and the mean and RMS of the ionization position distribution along the anode wires are included in the output queue.

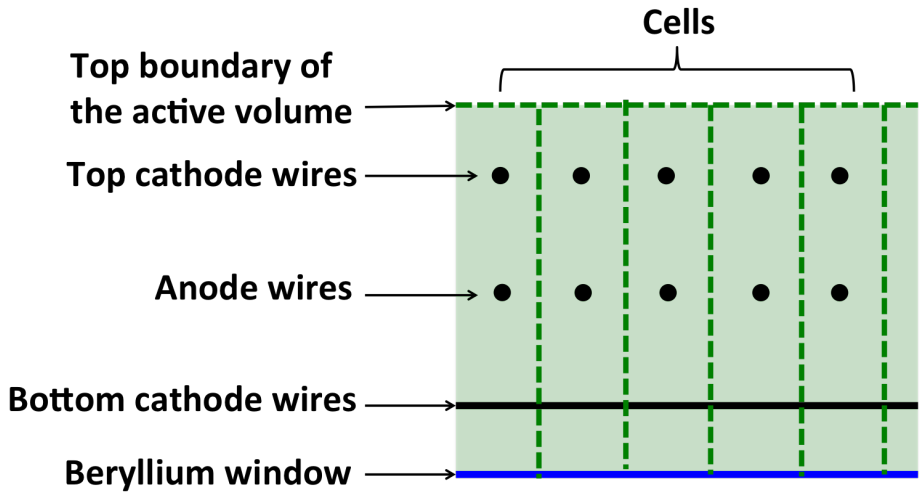

Figure 5.7: Cells of the MWPC.

The event manager also monitors the length of the output queue. Whenever there are

Objects	Percentage with β particles scattered
Collimator	3.0%
Electrodes	0.5%
Beryllium window holder	0.4%
MCP	0.01%

Table 5.3: Percentages of events with β particles scattered. Both the scintillator and the MWPC have non-zero energy deposition.

1000 events stored in the queue, it calls the output function to write the entire output queue to the *Beta Event File* and empties the output queue.

We used the β tracker to estimate the β scattering effects of volumes outside the detection solid angle. Percentages of events with β particles scattered on these objects are listed in Table 5.3. These events all have non-zero energy deposition in the MWPC and the scintillator.

5.5 Ion tracker

The ion tracker reads the *Ion Info File* output by the β tracker and calculates the trajectory of each ion and its TOF in the field generated by COMSOL. It can also read directly from the *Original Event File* when simulating photoions from the MOT. The electric field data file (E-field file) generated by COMSOL contains the electric field strengths on 1 mm spaced grid points. In the ion tracker, the electric field at any given point is determined through linear interpolation of the field strengths at the grid points. The tracking time step is decided adaptively based on the E-field gradient. The ion position and velocity at the end of the time step is determined by solving the Newtonian equation of motion numerically. The E-field strength inside the body of the electrodes are labeled *undefined*. When the ion is right next to the boundary, the program tries to access the E-field strength inside the body of the electrode and fails. In this case, the tracking is terminated. Ions initially generated inside the body of the electrode body are not tracked. When the ion approaches the MCP, *i.e.* in the last step, the distance to the MCP surface is calculated. Then the

time for the ion to travel to the MCP and the final position of the ion are calculated. For every event, the final position, velocity, status (kept or terminated) and the TOF of the ion are written to the *Ion Event File*. We have compared the results from the ion tracker in the electric field for cases in which an analytical solution of the ion trajectory can be solved. The comparison shows negligible difference between the numerically calculated and analytically determined TOF (and final position) of the ion.

One important physics process, electron shake-off, is also simulated in the ion tracker. After the β decay, one or both of the atomic electrons of the $^6Li^+$ ion are shaken off because of the mis-match between the daughter ^{6}Li atomic orbits and the parent ^{6}He atomic orbits. If the electron shake-off happens, the recoil ^{6}Li ion is in charge state 2 or 3. In this case, the acceleration due to the electric force is twice or three times larger than that for charge state 1 ions. The calculation of the probability of shaking off 1 electron is given by Reference [1] as

$$P_{S1} = A + B \cdot E_{ion}, \tag{5.22}$$

where A and B are constants and E_{ion} is the kinetic energy of the recoil ion. According to Reference [1], $A = 0.0942$ and $B = 6.702 \times 10^{-3}$ /keV. It also predicts that the total probability of shaking off 2 electrons is $\sim$2.0%. This is $\sim$100 times higher than the previous calculation [68]. In this experiment, we haven't observed such a high probability. Therefore, the charge state 3 is neglected in the $a_{\beta\nu}$ measurement. The analysis of the recoil charge-state distribution and the verification of Equation 6.17 are discussed in Section 6.9.

5.6 Post-processor and detector responses

The β tracker and ion tracker output data (energy depositions, ion landing positions, and etc.) need to be folded with detector response functions. Therefore, we use the post-processor program to apply detector responses to the data in the *Beta Event File* and the *Ion Event File*, and write the simulated detector readings to the final *Event File*. The input *Beta Event File* and *Ion Event File* need to match, or in other words they are from the same simulation run. In some cases where the simulation purpose is to reproduce the calibration results, one may be only interested in the β telescope or the ion detector, and the unneeded

input file is not read in. The post-processor also reads the detector response configuration file to get the parameters for detector response functions, and it applies different detector responses to one input event and output several files corresponding to the detector response configurations. The detailed detector response simulations are discussed in the following subsections.

5.6.1 MWPC response

As mentioned in Subsection 5.4.3, the number of ionizations, their mean position and position RMS for the activated cells are saved. In the post-processor, we simulate the multiplication and signal generation process for each electron from these ionizations.

Suppose there is one event which has N_w active cells (triggered anode wires), and for the i-th cell there are n_i ionizations with mean X coordinate x_i and X-RMS σ_i. The Y coordinate of these ionizations is the same as the Y coordinate of the wire (center of the cell). For the i-th cell, we simulate the multiplication and signal generation process for every single electron from the ionizations. For the $j-$th electron in this cell, its X coordinate ($x_{i,j}$) is generated from a uniform distribution with mean x_i and RMS σ_i. The final number of electrons $n_{i,j}$ after the multiplication process is generated from an exponential distribution

$$P = \frac{1}{M} exp(-n_{i,j}/M), \tag{5.23}$$

where M is the gain factor which is the product of the average gain factor set by the user and the gain spatial variation adjustment factor determined by the calibration described in Section 4.4. The anode signals created by this electron shower are proportional to the charges collected at the two ends of the charge division chain, and are calculated using the following equations,

$$\begin{aligned} Q_L &= Q_{tot} \times (N_L/21), \\ Q_R &= Q_{tot} \times (N_R/21), \end{aligned} \tag{5.24}$$

where Q_{tot} is the total charge in the electron shower, and $N_L(N_R)$ is the number of capacitors between the triggered wire to the left(right) end of the charge division chain and there are 21 capacitors in total. The signals of the bottom cathode wire groups are calculated based

on the measured distribution mentioned in Section 4.3. This simulation of multiplication and signal generation procedure is done for all ionization electrons and all active cells, and the 2 anode signal values and 6 cathode signal[2] values are accumulated.

After all the cells for this event are simulated, broadenings and noise are added to the signals. The GEANT4 simulation doesn't handle the fluctuation of number of ionizations generated by the incoming particles very well, so we add additional broadening to the number of initial ionizations to get the final signals. The broadening factor B is generated randomly from a Gaussian distribution with mean 1 and standard deviation σ_b where σ_b is a user selected broadening width expressed in percentage (typically $\sim$30%). Then B is multiplied to all anode and cathode signals. Because this factor is common to all signals, the anode signal sum which represents the total energy deposition is broadened but the signal ratios that determine the event position are not affected. Therefore, this broadening does not affect the position resolution. To take into account the electronic noise, we smear the signals in each channel with a gaussian width (corresponding to $\sim$0.01 keV) individually. Because the smearing for each channel is independent from each other, the position resolution worsens. We choose the broadening width, the anode noise and the cathode noise so that the widths of the MWPC energy spectrum and the widths of the peaks in the MWPC position spectrum projections match the measured ones.

Since all signals from the MWPC have their counterparts in the simulation, we applied the same calibration algorithm described in Chapter 4 to the simulated energy and position readouts. The calibration run with the ^{55}Fe source is simulated and the broadening width is chosen so that the 5.9 keV peak matches the measured one. The anode and cathode noises are chosen as described above, and the signal threshold for the cathode wire groups are chosen so that the percentage of events that trigger more than 3 wire groups matches the measured one. The position spectrum of the simulated ^{55}Fe calibration run is shown in Figure 5.8, and the comparison for the energy deposition spectra from the simulation and the experiment is shown in Figure 5.9. These comparisons show that the simulation does a good job at reproducing the main features of the ^{55}Fe data, including the relative intensity

[2]The signals on the top cathode are also calculated, but they are not used for the simulations discussed in this thesis.

of the argon-escape peak and the peak structures in the position spectrum.

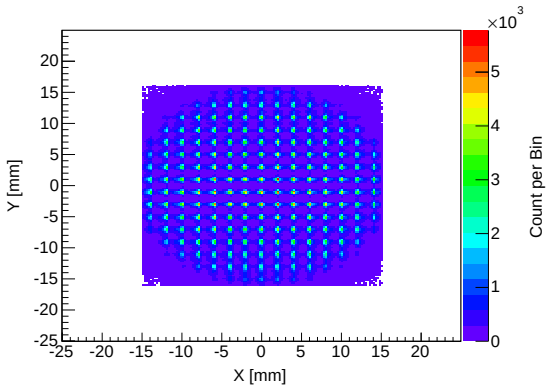

Figure 5.8: Simulated MWPC position spectrum for the ^{55}Fe calibration run.

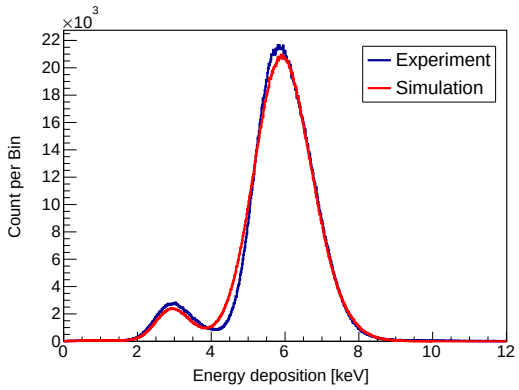

Figure 5.9: Simulated MWPC energy deposition spectrum for ^{55}Fe calibration run.

Using the same parameters (MWPC gain, σ_b and etc.), we simulated the ^{207}Bi calibration. The comparison of the measured and simulated MWPC energy deposition spectra is shown in Figure 5.10a. The peak structures of the MWPC image are reproduced well, but the MWPC energy deposition spectrum does not agree with the measured one well. One possible explanation is that the fluctuations of number of initial electron-ion pairs for X-rays and electrons with ~1 MeV energy are not the same. If it is true, the value of σ_b chosen for the ^{55}Fe simulation does not fit the ^{207}Bi simulation. Therefore, for the simulation of the ^{207}Bi run, we adjusted the value of σ_b to match the simulated MWPC energy deposition spectrum to the measured one. After this adjustment, the simulation agrees well with the experiment as shown in Figure 5.10b. This adjustment does not change the position response of the MWPC, and thus the MWPC image. Using the σ_b value determined by matching the ^{207}Bi run, the simulated MWPC energy deposition spectrum for the ^{6}He decay also matches the measurement (see Figure 6.14).

The MWPC efficiency uniformity in the simulation is also studied and compared to the ^{207}Bi calibration run as shown in Figure 4.18. The measured and simulated MWPC efficiency map do not match perfectly, either. It is possible that the difference is due to simplifications in the signal simulation procedures. For example, the hardware threshold for each cathode ADC are not the same, and the wires are not perfectly parallel. These factors

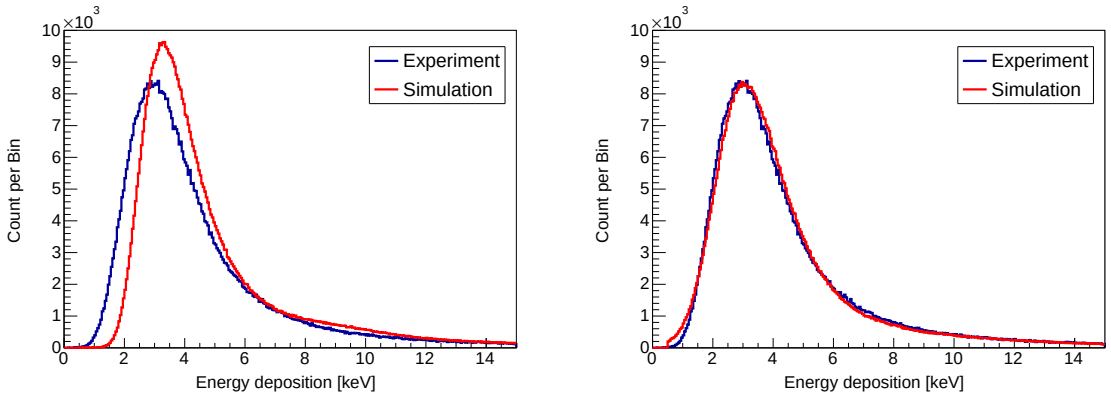

(a) Using broadening from ^{55}Fe calibration

(b) Using broadening from self calibration

Figure 5.10: MWPC energy deposition spectrum comparison for electrons using the ^{207}Bi source. Coincidence triggering with the scintillator-PMT assembly and the condition $E_\beta >$ 700 keV are imposed.

all affect the position and energy reconstruction very little but do affect the efficiency more prominently. One way to match the efficiency maps from simulation to the measured one is to introduce a *weight map*. The weight for each cell is proportional to the efficiency ratio (the measured one over the simulated one). In the simulation, events are rejected or kept according to this weight map. How this weight map affects the $a_{\beta\nu}$ extraction is discussed in Chapter 6, and it turns out not to be a major source of system uncertainties.

5.6.2 Scintillator-PMT assembly response

As mentioned in Section 4.7, the post-processor generates the simulated β-telescope energy $E_{\beta sim}$ read out by Gaussian smearing the energy deposition in the scintillator given by the GEANT4 β tracker based on the response function defined in Equations 4.5 and 4.6. The width for the 975.7 keV peak $\sigma_{975.7}$ is adjusted in a range of $\pm 5\%$ centered at the fitted value of p_2 in Table 4.1, and the spectrum of $E_{\beta sim}$ is constructed for each value of $\sigma_{975.7}$. We renormalize the simulated spectrum so that the integral from 200 keV to 2000 keV is the same as that of the measured spectrum of E_β, and then use the minimum χ^2 method

to determine the best $\sigma_{975.7}$. The χ^2 is defined as

$$\chi^2 = \Sigma_i \frac{(E_\beta[i] - E_{\beta sim}[i])^2}{(\sigma_\beta[i])^2 + (\sigma_{\beta sim}[i])^2} \tag{5.25}$$

where i is the index of the histogram bin. The χ^2 curve over the chosen range of $\sigma_{975.7}$ is shown in Figure 5.11, and by fitting it with a parabola we determined the best fit for $\sigma_{975.7}$. As mentioned in Section 4.7, a variation of $\sigma_{975.7}$ may result in a change of the peak positions of the $E_{\beta sim}$ spectrum, and thus in a change of the calibration result of Equation 4.4. Therefore, we use the iteration procedure sketched in Figure 5.12 to extract the best estimation for $\sigma_{975.7}$ and to calibrate the spectrum. The best fit of $\sigma_{975.7}$, the position of the 975.7 keV peak in the $E_{\beta sim}$ and the minimum χ^2 are stabilized after 3 iterations of the calibration procedure. The $E_{\beta sim}$ spectrum with the stabilized value of $\sigma_{975.7}$ and the E_β spectrum with the stabilized calibration are overlaid on top of each other in Figure 5.13.

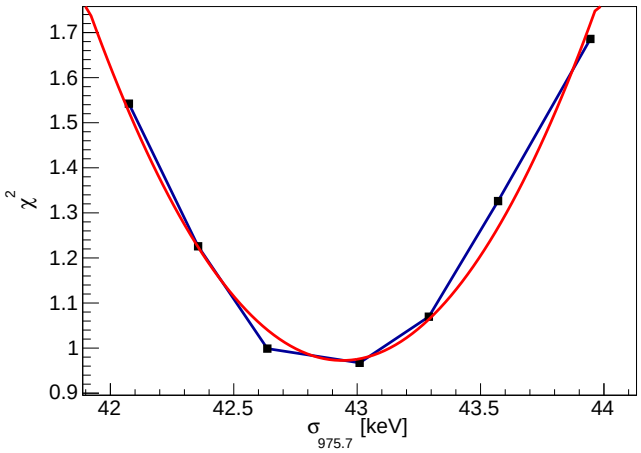

Figure 5.11: χ^2 curve versus $\sigma_{975.7}$.

We confirmed that the tail of each conversion electron line is due to the platinum backing of the calibration source, and the bumps near 500 keV and 1000 keV are from coincidences from the cascade transitions from the daughter nucleus ^{207}Pb. In the GEANT4 simulation, we tried to remove the backing of the calibration source, or turn off the coincidence

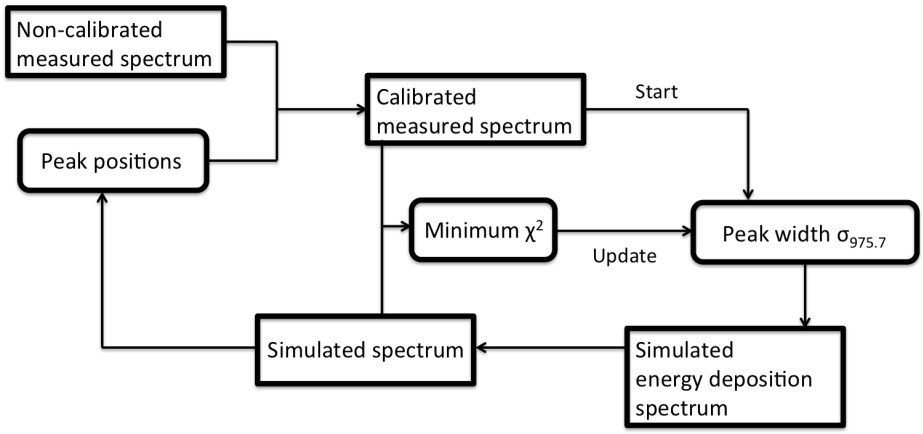

Figure 5.12: Repeated calibration procedure.

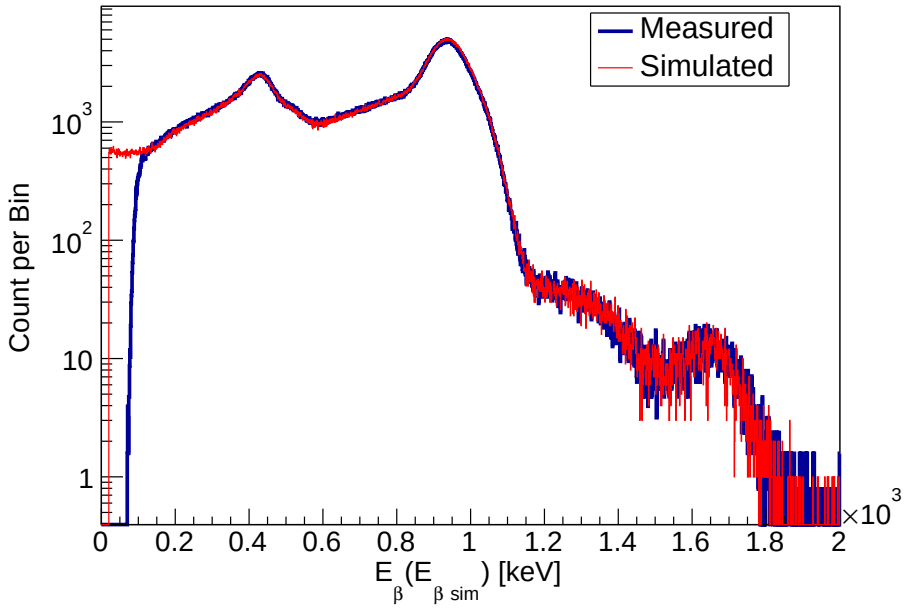

Figure 5.13: The measured E_β spectrum and the simulated $E_{\beta sim}$ spectrum at stabilized condition.

transitions of ^{207}Pb, or simulate only the conversion electrons. The spectra of these three cases are overlaid with the measured E_β spectrum in Figure 5.14. The lack of events near 1300 keV in the green curve indicates that the cause of this bump is the pile-up from two

particles originating from the cascade decays. The disappearance of the tails in both the red and orange curves indicates that the γ rays and the backing of the source are both responsible for the tail. Thus, the γ rays hit the source backing and generate photoelectrons, and some photoelectrons travel upward and hit both the MWPC and the scintillator. This also explains why for those "tail" events the MWPC energy read out is consistent with these events being generated by electrons. Only if all these details are taken into account, the excellent match in Figure 5.13 can be achieved.

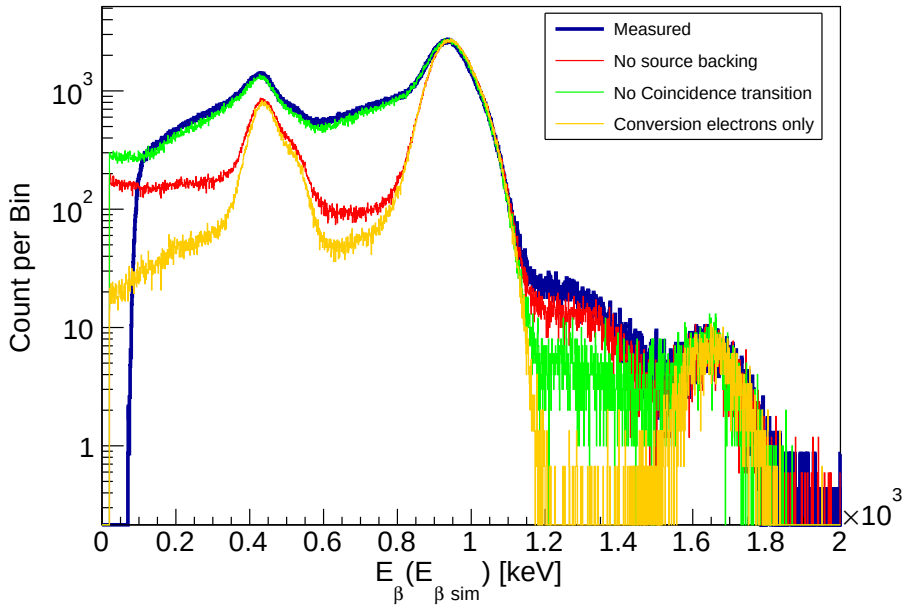

Figure 5.14: The simulated $E_{\beta sim}$ spectra without source backing (Red), without the coincidence transitions of ^{207}Pb (Green), and with only conversion electrons (Orange). These insufficient simulated spectra are overlaid onto the measured E_β spectrum (Blue).

5.6.3 MCP Response

According to the MCP calibration runs described in Chapter 4, there is no obvious granular structure in the position spectrum, and its resolution is also well measured. Therefore, unlike simulating the MWPC, the post-processor applies a 2D Gaussian smearing to the ion landing positions calculated by the ion tracker without simulating the signal generation

process of the MCP anodes. During the calibration runs, we checked the MCP position resolution in different parts of the MCP and found no obvious difference from the center to the edge of the MCP. Therefore, we use the measured position resolution (36 μm) as the Gaussian smearing width for all events.

There is a 21.5° rotation from the MOT-2 chamber coordinate system to the MCP local coordinate system defined by the grid lines of the calibration mask. In the simulation, this rotation is applied to the ion landing position first. Thus in the data analysis software, the ion momentum retrieval algorithm is the same for both the measurement and the simulation. To simulate the calibration mask, the ions that hit the positions covered by the mask grid lines are ruled out. According to the mask manufacturing tolerances, the accuracy of the grid line position and width[3] are 2 μm, much smaller than the MCP accuracy and resolution, so in the simulation the grid lines are at their ideal positions and their width are all 0.25 mm. Furthermore, only the active squares determined from the calibrations are kept in the simulation. Events happening outside the active region are ruled out. The simulated MCP position spectrum for the non-trapped ^{6}He source is shown in Figure 5.15.

The MCP efficiency non-uniformity is simulated by imposing a *weight map* as it is done with the MWPC simulation. One can either use the R_{kept} distribution in Figure 4.58 or the measured efficiency map in Figure 4.60a. The R_{kept} distribution is determined purely from the measurements, but the measured efficiency map does depend on the simulation. One needs to simulate the ion landing position distribution for the non-trapped ^{6}He source assuming uniform MCP efficiency across the whole area. The systematic uncertainty related to the efficiency non-uniformity of the MCP is studied in Chapter 6.

5.6.4 Timing response

After the timing correction described in Subsection 4.15.4, the measured TOF is the time period from the PMT trigger to the MCP trigger, but it is different from the physical TOF (T_{ion}) of the ion by the β-TOF (T_e) from the MOT to the scintillator. The ion tracker calculates T_{ion}, and the β-tracker registers T_e. In the post-processor, the output TOF is

[3]We checked the grid-line positions using a microscope, and root-mean-square of the deviations from the designed positions is ∼5 μm.

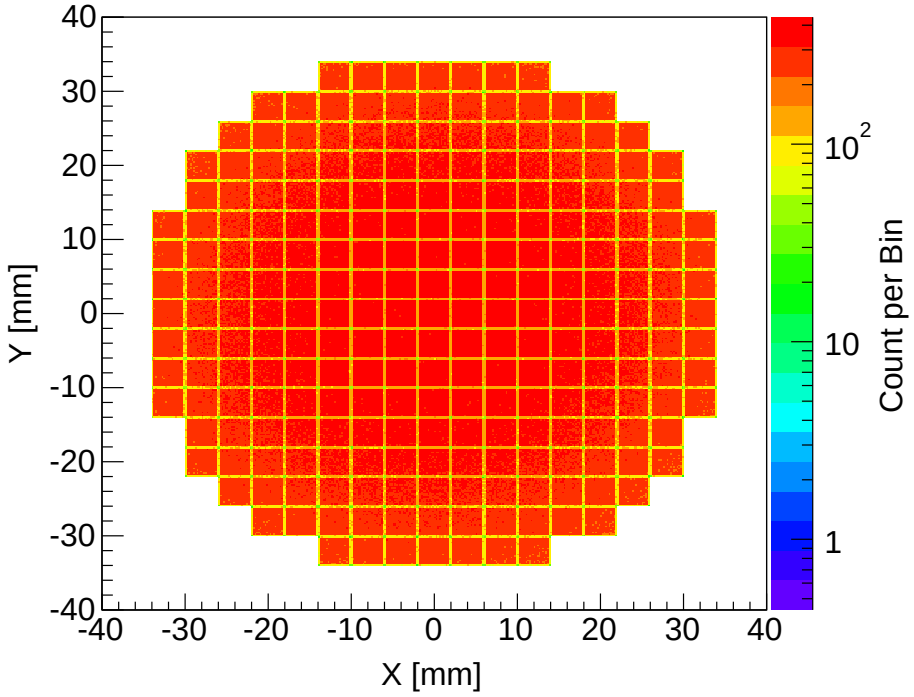

Figure 5.15: Simulated MCP position spectrum for non-trapped ^{6}He source. Shadows of the grid lines are clearly seen.

set to T_{ion}-T_e, and in this way the simulated TOF has the same definition of the measured TOF.

Chapter 6

DATA ANALYSIS

In the previous chapters, the detector system, calibration methods and the MC simulation were introduced. In this chapter the tools for analyzing the data and simulations are introduced. Some important techniques like the Q-value reconstruction, background subtraction and the fit-template construction will be described in detail. Besides the simulation-to-experiment comparisons mentioned in Chapter 5, more comparisons will be discussed to evaluate the goodness of the simulation. Then the sensitivity of $a_{\beta\nu}$ to different systematic effects are studied using the MC simulation and the data analysis software. Finally, the data taking, the $a_{\beta\nu}$ extraction and the analysis of recoil ion charge state distribution are described.

6.1 Data analysis tools

We developed a program to sort events from a data file into histograms and carry out analyses of the histograms. For data files from experiments, there is another program converting the FASTER format data into ROOT format. In this section, the FASTER-to-ROOT conversion program and then the main data analysis program are described.

6.1.1 FASTER-to-ROOT conversion program

The data grouping condition is described in Section 3.6, and in this experiment only the grouped data are written to the FASTER data file. The main data analysis program uses the ROOT toolkit, so in order to facilitate the downstream analysis, we developed a program dedicated to the FASTER-to-ROOT conversion. It also pre-sorts the data and handles coincidence identification.

The program is developed in C++ language and it is linked to the FASTER data interpretation library and the ROOT libraries. The program reads the FASTER event file and

fills ROOT trees according to the coincidence conditions as follows.

- **Scint tree** PMT anode channel triggered
- **MWPC tree** One of the MWPC anode channels triggered
- **Beta tree** PMT anode and one of the MWPC anode channel triggered
- **Double tree** PMT anode and the MCP back channel triggered
- **Triple tree** PMT anode, one of the MWPC anodes and the MCP back channel triggered
- **N2Laser tree** N_2-laser photo-detector channel triggered
- **PMT-Stb tree** Photo-detector for the LED pulses triggered

These trees are not mutually exclusive, so one event may belong to many trees. However, this simplifies the following analysis. For example, for the β-detector energy calibration analysis, only the *Beta tree* needs to be loaded, while the $a_{\beta\nu}$ measurement needs the *Triple tree* alone. Moreover, the program calculates the TOF by taking the difference between the timing readouts of the PMT and MCP back channels, and fills the ROOT trees with the TOF and the absolute PMT timing instead of the original two timing readouts. This also simplifies the following analysis without losing important raw information.

6.1.2 Main data analysis program

The main data analysis program is designed as a multi-functional program for event processing, histogram filling and spectrum fitting. It also integrates the calibration operations including generating the calibration parameters and applying the calibration algorithms. This program can analyze the data from both the experiment or the simulation, and varieties of analysis purposes can be achieved by just writing the input command scripts without hard-coding new functions. It is programmed in C++ and the ROOT toolkit is extensively used in the histogram handling and fitting.

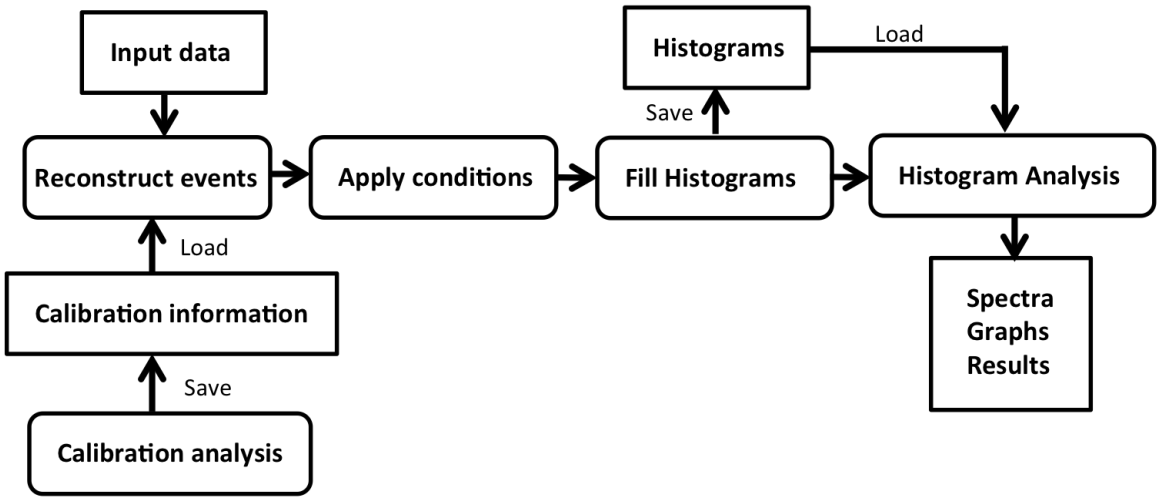

Figure 6.1: Flowchart of the *general procedure* of using the data analysis software.

The *general procedure* of using the data analysis program is described in Figure 6.1. The program reads event files from either an experiment or a simulation, and then calculates meaningful quantities from the raw input data. Calibration algorithms are implemented during this event reconstruction procedure. For example, the program calculates the ion hit position on the MCP from the anode timing readouts, and corrects it using the algorithm described in Subsection 4.9.2. For each event the program tests whether it satisfies all conditions, and then decides whether to fill the histograms. After all events from the input data file are sorted into histograms, the program carries out histogram-analysis functions to perform fitting, comparing, combining and so on. The histograms can be saved to a ROOT file for future use as well, and one may load the saved histograms and carry out the histogram analysis directly without re-processing the input data.

The *general procedure* described above consists of *elementary operations* like reading in the event file, reconstructing events, checking conditions, filling histograms, saving (loading) histograms and so on. The elementary operations also include initializing the histograms, configuring the conditions, loading calibration parameters and other configuring operations. The data analysis program has a master class *Analyzer* that manages the conditions, configurations and histograms in the memory, and each elementary operation is carried out by

one of its member function. The program also has a command-line style user interface (UI) that interprets user's commands and executes the corresponding functions. This design of UI allows users to execute elementary operations one by one or in a batch mode, and thus makes the data analysis program very versatile. Users can fully customize the conditions, histograms, calibrations and so on according to their needs.

The histogram analysis module is a set of member functions of the *Analyzer* class that perform analyses on the histograms. It includes functions like the template fitting for $a_{\beta\nu}$ extraction, background spectrum construction, spectrum comparison and so on. Some functions perform more complicated analyses involving many histograms under different conditions, for example, the timing-zero extraction discussed in Subsection 5.6.2 and the χ^2 minimization procedure described in Subsection 5.6.2. User commands are also constructed for configuring and executing the histogram analysis functions.

The analysis of the calibration runs are also integrated into the analysis program. The purpose of analyzing the calibration runs is to generate parameters needed in the data correction algorithm. The calibration analysis for every purpose is unique to itself, therefore they are all realized by single-purpose hard-coded functions. These functions can be executed by user commands through the UI. These functions output the calibration parameters to the calibration files and assign 2-digit calibration IDs to the file names. Thus in the general procedure, the user can decide which set of calibration parameters to use by choosing the calibration ID. The calibrations are implemented during the event reconstruction process.

6.2 Q-value reconstruction and background suppression

In order to suppress the background events originating from non-trapped ^{6}He atoms in the MOT-2 chamber, we applied a condition on the Q-value reconstructed from the data. In this chapter, Q-value is defined as the sum of the kinetic energies of the outgoing particles from the ^{6}He decay, and its value is expected to be 3.5 MeV. The detector system we build is based on the schematics in Figure 1.10, and thus the neutrino momentum and the Q-value can be reconstructed. To reconstruct the initial momenta of the β particle and the recoil ion, one needs to assume that the decay happens at the MOT center and

the β particle straightly hits the MWPC without being scattered by other materials. The non-uniformity of the E-field, energy loss of the β particles, and the TOF delay caused by the β-particle transportation time are also neglected in the Q-value reconstruction. For the decays originating from the MOT and without β scattering, the reconstructed Q-values are close to 3.5 MeV. However, for the decays outside the MOT or when the β particles are scattered, the Q-values reconstructed under the assumptions above deviate from 3.5 MeV. Therefore, by applying a cut around 3.5 MeV on the reconstructed Q-values, we can suppress events originating from non-trapped ^{6}He atoms or with β scattering.

There is one difficulty in the Q-value reconstruction: a charge state ambiguity. The recoil ions have different charge states due to the orbital electron shake-off, and thus different acceleration in the E-field. Most of the ions in charge state 2 arrive at the MCP earlier than all ions in charge state 1, but there is an overlap between these two groups near TOF=190 ns. The charge states of these events cannot be determined unambiguously from their TOF values. In order to overcome this difficulty, we reconstructed two Q-values, Q_1 and Q_2, assuming the recoil ion has 1 or 2 units of charge respectively. The charge state 3 is neglected due to its low probability except in Section 6.9 where the upper limit of the probability on having the charge state 3 is analyzed.

Because the recoil ion is either in charge state 1 or in charge state 2 but not both, at least one of the reconstructed Q_1 and Q_2 should be close to the physical Q-value, while the other one might be far away from the physical Q-value. To visualize this effect, we constructed the Q_1 vs. Q_2 2D histogram as shown in Figure 6.2. This spectrum is constructed with the E_β threshold set to 500 keV. Clearly most of the events fall within the two bands near $Q_1 = 3.5$ MeV and $Q_2 = 3.5$ MeV. The two bands intercept with each other. It is not surprising because in the TOF vs. E_β 2D histogram the regions of the two charge states also overlap from 193 ns to 200 ns (see Figure 6.3a), and thus in this region the reconstructed values of Q_1 and Q_2 are similar. The overlapping area of the two bands in the Q_1 vs. Q_2 histogram is smaller, because the positions of the MCP and MWPC are added in order to distinguish the two charge states.

As expected, we did observe events with neither Q_1 or Q_2 close to the physical Q-value. These events have one or more of the variables involved in the Q-value construction

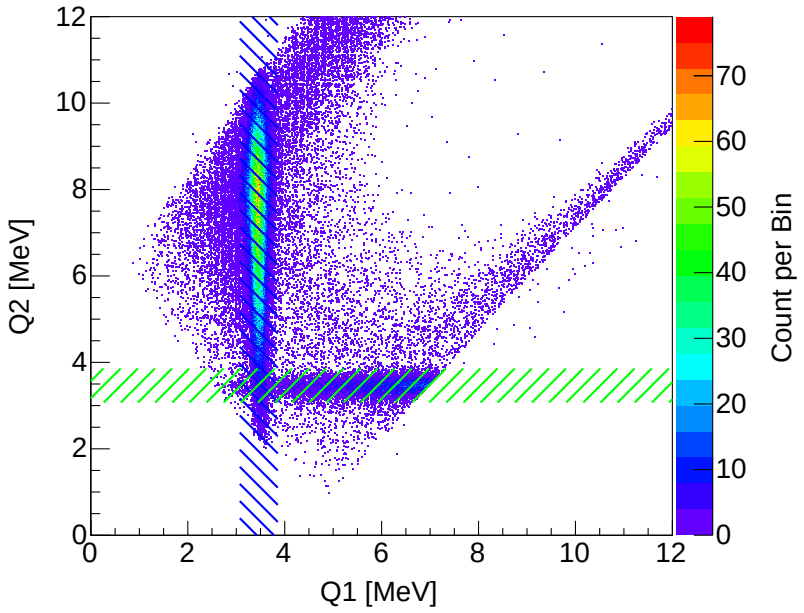

Figure 6.2: Q_1 vs. Q_2 2D histogram. The cut on Q_1 is indicated by the blue shaded area, and the cut on Q_2 is indicated by the green shaded area.

incorrectly determined. Most of them are from the non-trapped ^{6}He decays or with β particles scattered from the electrodes or the window holder. The Q-value cuts we applied is shown by the two shaded bands in Figure 6.2. It requires that either Q_1 or Q_2 is in a region around the physical Q-value 3.5 MeV. These cuts suppress ~90% of the events from non-trapped ^{6}He atoms. We compared the TOF vs. E_β 2D histograms shown in Figure 6.3 before and after the Q-value cuts. The events in the non-physical region[1] are ruled out by the Q-value cuts. Using the Monte Carlo simulation, we find that the Q-value cuts also suppress ~30% of the events with β scattering. Therefore, the Q-value cuts reduce the sensitivity to the background subtraction and the β-scattering effects effectively.

Although the Q-value cuts help ruling out unwanted events, if the cuts are too tight

[1]The physical region is the union of the two triangle regions corresponding to the charge state 1 and charge state 2. For a certain E_β the shortest TOF corresponds to the case where the antineutrino is emitted in parallel with the β particle, and the longest TOF corresponds to the case where the antineutrino is emitted in the opposite direction of the β particle. If the TOF is outside this range, it is not physical for any decays from the MOT with no β scattering.

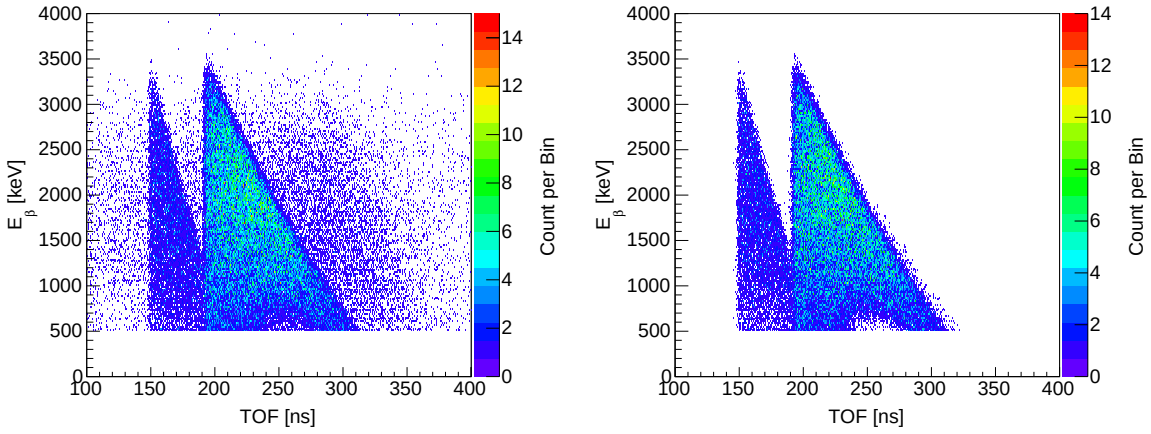

(a) (b)

Figure 6.3: TOF vs. E_β 2D histogram without (a) and with (b) the Q-value cut. In both histograms, the left triangle region corresponds to the charge state 2 and the right triangle corresponds to the charge state 1.

good events will be missed. In order to set a proper cut, we projected the Q_1-vs-Q_2 2D histogram onto the horizontal and vertical axes as shown in Figure 6.4. In order to prevent the interference of events in the charge state 2 when studying the charge state 1, we only project events with $Q_2 > 4$ MeV onto the horizontal axis so the majority of the charge state 2 events are not projected. Same condition is applied to Q_1 when studying the Q_2 projection. We fit the Q_1 peak and Q_2 peak individually to a Gaussian function from 3.3 MeV to 3.7 MeV. The fit results are:

$$Q_1 : \mu = 3.461 \pm 0.0004, \sigma = 0.109 \pm 0.0004 \tag{6.1}$$

$$Q_2 : \mu = 3.469 \pm 0.0015, \sigma = 0.131 \pm 0.0015 \tag{6.2}$$

The means of Q_1 and Q_2 are consistently smaller than the physical value 3.5052 MeV by $\sim$ 44.2 keV. This approximately agrees with the energy loss of the β particle in the beryllium window and the MWPC. To ensure that the Q-value cuts do not affect the good data the cut range is chosen to be from 3.072 MeV to 3.858 MeV, which is equivalent to $\pm 3\sigma$ for the charge state 2 and $\pm 3.6\sigma$ for the charge state 1. According to the Gaussian distribution, the event loss for charge state 1 is 0.03% and that for charge state 2 is 0.27%. The events

in charge state 2 are ∼10% of the total data, so the total data loss is ∼0.06%. Because the Q-value cuts are also applied to the Monte Carlo simulation for generating the fit templates and studying the systematic uncertainties, the event loss through the Q-value cuts does not introduce systematic biases[2].

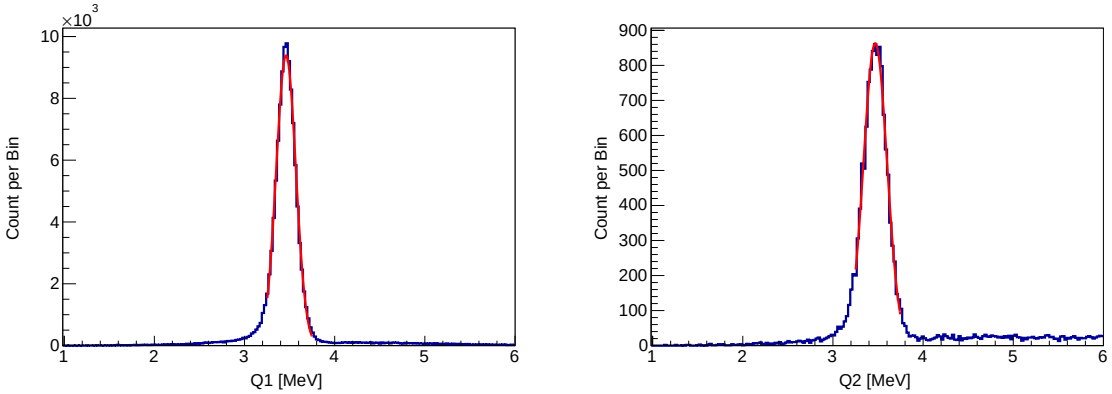

(a) (b)

Figure 6.4: (a) Q_1 and (b) Q_2 spectra. Red curves are the Gaussian fits. The low-energy tails of these peaks are caused by the loss of β-energy due to bremsstrahlung effect or scattering.

6.3 Background spectrum normalization

To account for the remaining background from the non-trapped ^{6}He decays after the Q-value cuts, one needs to know both the shape and the normalization of the background spectrum. The TOF spectrum of the non-trapped ^{6}He source was measured as described in Subsection 4.16.1. Applying the Q-value cuts to the low-rate background run, one obtains the shape of the background spectrum. In this section, we describe the technique of normalizing the background spectrum. One histogram analysis function is dedicated to this task.

For an experimental run with trapped ^{6}He, one calibration run with the non-trapped

[2]Due to the event loss through the Q-value cuts, in theory the sensitivities of the $a_{\beta\nu}$ extraction to the resolutions of the β detector, MCP, etc. becomes larger. However, these changes are too small to be observed at the present level of statistics of the MC simulation.

^{6}He is selected for determining its background spectrum. The experimental setups like the E-field, magnetic field, detector settings are the same for these two runs. The data from the experiment with non-trapped ^{6}He are analyzed with the Q-values reconstructed as if the decays are from the MOT position. The assumed MOT position and uniform electric field strength are the same as those in the data analysis for the trapped ^{6}He run. Two TOF histograms for the non-trapped ^{6}He run are constructed, one without the Q-value cuts and the other with the Q-value cuts. Then the run with trapped ^{6}He is analyzed in the same way with and without the Q-value cuts. For any decay originating from the MOT, the TOF has a lower limit of $\sim$147 ns and a upper limit of $\sim$360 ns, because the recoil ions have a maximum energy of $\sim$1.4 keV. We conclude that those events with TOF$<$147 ns in the trapped ^{6}He analysis without the Q-value cuts are only from the decays of the remaining non-trapped ^{6}He, and this part of the TOF spectrum should have the same shape as that in the non-trapped ^{6}He analysis. Therefore, the TOF spectrum without the Q-value cuts for the non-trapped ^{6}He is scaled by a factor k_B so that its integral in the window from 10 ns to 110 ns matches the integral of the trapped ^{6}He histogram in the same window. The TOF histogram for the trapped ^{6}He and the scaled TOF histogram for the non-trapped ^{6}He are overlaid as shown in Figure 6.5a, and both histograms are without the Q-value cuts. These two spectra agree with each other very well in the region from 0 ns to the rising edge of the charge state 2 TOF spectrum. We use the scaled TOF histogram for the non-trapped ^{6}He as the background spectrum with the correct normalization. In the region of interest, from 140 ns to 320 ns, the integral of the background spectrum is $\sim$1/13 of the integral of the total histogram for this batch of data taken during October 25th 2015. The background ratio depends on the trapping efficiency so it varies from day to day.

Finally, the TOF histogram used for the $a_{\beta\nu}$ extraction is the one with the Q-value cuts imposed. Because the same Q-value reconstruction and Q-value cuts are implemented to both analyses for trapped and non-trapped ^{6}He, the TOF histogram with the Q-value cuts for the non-trapped ^{6}He represents the shape of the background spectrum in the trapped ^{6}He analysis. To correct the background normalization, the TOF histogram with the Q-value cuts for the non-trapped ^{6}He is scaled by the same factor k_B determined above, and then it is used as the background spectrum in the trapped ^{6}He analysis. The TOF

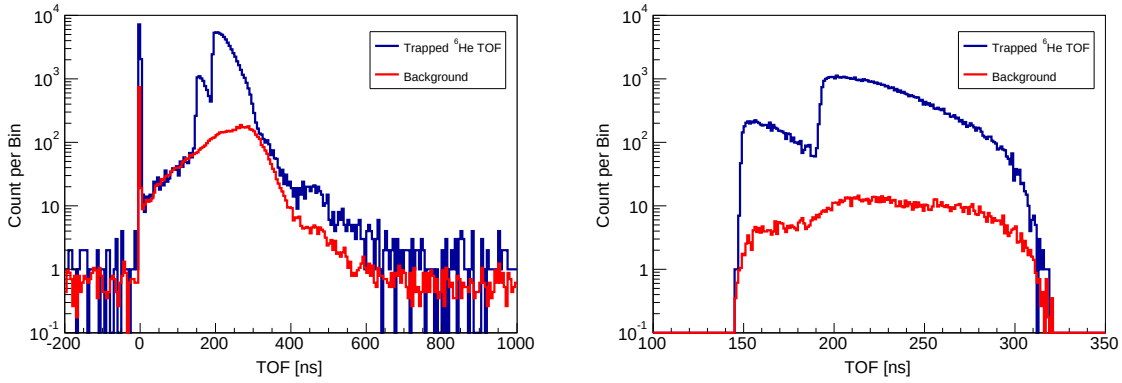

(a) Without Q-value cuts

(b) With Q-value cuts

Figure 6.5: Comparison of the TOF histogram for trapped ^{6}He and its background histogram, with and without the Q-value cuts.

histogram with the Q-value cuts for the trapped ^{6}He and the background spectrum are plotted in Figure 6.5b. After the Q-value cut, in the region of interest the background ratio for this batch of data is ∼1/48. The uncertainty of the background spectrum normalization is dominated by the number of events in the integration window 10 ns to 110 ns. For a run with ∼42000 total counts with the Q-value cuts imposed, the integral of the TOF histogram without the Q-value cuts in the window 10 ns to 110 ns is ∼350. This corresponds to a 5.3% statistical uncertainty of the background spectrum normalization.

6.4 Templates and fit method for the $a_{\beta\nu}$ extraction

As mentioned in Section 2.4, $a_{\beta\nu}$ is extracted by fitting the measured TOF spectrum to the templates generated by the Monte Carlo simulation. The differential decay rate of ^{6}He is a linear function of $a_{\beta\nu}$. After integrating over variables like the 3-momentum of the β particle and the ion landing positions the differential decay rate versus TOF is still a linear function of $a_{\beta\nu}$. This linear relationship holds even after the detector response functions are folded in as long as the detector response functions do not explicitly depend on $a_{\beta\nu}$. Therefore, the most general form of the TOF spectrum (with detector responses folded in)

$F(TOF, S_i, a_{\beta\nu})$ is

$$F(TOF, S_i, a_{\beta\nu}) = \frac{d\Gamma}{dTOF} = F_1(TOF, S_i) + a_{\beta\nu} F_2(TOF, S_i), \tag{6.3}$$

where S_i represents the set of parameters that defines the fiducial region of other variables and the detector response functions. F_1 and F_2 are functions of the TOF that depend on S_i but do not depend on $a_{\beta\nu}$. Therefore, the function F_1 and F_2 can be determined if the value of $F(TOF, S_i, a_{\beta\nu})$ is known for two different $a_{\beta\nu}$ values. For example,

$$F_1(TOF, S_i) = \frac{1}{2}\left(F(TOF, S_i, +\frac{1}{3}) + F(TOF, S_i, -\frac{1}{3})\right), \tag{6.4}$$

$$F_2(TOF, S_i) = \frac{3}{2}\left(F(TOF, S_i, +\frac{1}{3}) - F(TOF, S_i, -\frac{1}{3})\right). \tag{6.5}$$

Therefore, the TOF spectrum expressed in Equation 6.3 can be reformulated as

$$\begin{aligned} F(TOF, S_i, a_{\beta\nu}) = {} & \frac{1}{2}\left(F(TOF, S_i, +\frac{1}{3}) + F(TOF, S_i, -\frac{1}{3})\right) \\ & + a_{\beta\nu}\frac{3}{2}\left(F(TOF, S_i, +\frac{1}{3}) - F(TOF, S_i, -\frac{1}{3})\right). \end{aligned} \tag{6.6}$$

The functions $F(TOF, S_i, +1/3)$ and $F(TOF, S_i, -1/3)$ are generated by the MC simulation, and they are called standard templates $T_{STD+}(TOF)$ and $T_{STD-}(TOF)$. Then the measured TOF spectrum is fitted to Equation 6.6 and $a_{\beta\nu}$ is extracted. Other than $a_{\beta\nu}$, the fit function also has another free parameter T_0 to allow for a time shift. Though the timing zero is determined with accuracy $\sim$0.1 ns, due to the sharp leading edges of the TOF spectrum this 0.1 ns uncertainty in T_0 results in a significant deviation in $a_{\beta\nu}$. Therefore, treating the T_0 as a free fit parameter is appropriate. To account for the background generated by the non-trapped ^{6}He, the background TOF spectrum shown in Figure 6.5b can be either subtracted from the measured TOF of the trapped ^{6}He or added to the fit function. We chose the latter method, because background subtraction may result in negative counts in some bins of the histogram and this issue makes it harder to implement the log-likelihood fit. The normalization of the fit function is fixed so that the integral of the fit function matches the integral of the measured TOF spectrum. In summary, the fit function used in

the $a_{\beta\nu}$ extraction is

$$F_{fit}(TOF) = (N_{exp} - N_B)\frac{(1-3a_{\beta\nu})T_{STD-}(TOF - T_0) + (1+3a_{\beta\nu})T_{STD+}(TOF - T_0)}{(1-3a_{\beta\nu})N_{STD-} + (1+3a_{\beta\nu})N_{STD+}} + B(TOF). \quad (6.7)$$

$B(TOF)$ is the normalized measured background spectrum. N_{exp}, N_B, N_{STD-} and N_{STD+} are the integrals of the measured TOF spectrum, background spectrum, $T_{STD+}(TOF)$ and $T_{STD-}(TOF)$. The $F_{fit}(TOF)$, $T_{STD+}(TOF)$ and $T_{STD-}(TOF)$ all depend on the S_i.

To generate the fitting standard templates $T_{STD+}(TOF)$ and $T_{STD-}(TOF)$, the MC simulation parameters are configured according to the calibration runs described in Chapter 4 and the matching procedures described in Chapter 5. In other words, the parameters S_i used in the simulation should be the same as those used in the experiment. The MOT horizontal coordinates and widths are determined using the Penning ion images of the ^{6}He trap as described in Section 4.14 while taking data for constructing the TOF spectrum (called the *TOF-data*). The vertical coordinate is determined by matching the photoion TOF peak as described in Section 4.13.5. The E-field is calculated in COMSOL using the measured geometry and the voltage settings used in the experiment. The parameters for detector response simulation are tuned to match the spectra from the calibration runs done right before or after the TOF-data taking. The event reconstruction parameters are also set in order to match the simulated spectra to those from the calibration runs. All conditions and the Q-value reconstruction related parameters are set to the same values for the experimental data analysis. The Fierz interference term b is kept at 0 for the $a_{\beta\nu}$ extraction. Then two simulations with $a_{\beta\nu} = +1/3$ and $a_{\beta\nu} = -1/3$ are conducted, and their output data are analyzed. The output TOF histograms of the simulations with $a_{\beta\nu} = \pm 1/3$ are saved as the $T_{STD\pm}(TOF)$ templates. To extract the $a_{\beta\nu}$, these standard templates are loaded to the simulation program and the fitting function described as follows is executed.

First, the analysis program constructs the fit function in Equation 6.7 as a ROOT TF1-type function. During the fit procedure, the fit function is evaluated at the bin centers of the TOF spectrum. The $B(TOF)$ part just returns the corresponding bin content for the given TOF because the background spectrum and the measured TOF spectrum have the same binning configuration. However, T_0 can be any real number so the function T_{STD+}

and T_{STD-} are evaluated at positions away from the bin centers. Therefore, for any given t, T_{STD+} (or T_{STD-}) returns the interpolation of the contents of the adjacent bins nearest to t. The measured TOF spectrum is saved as a ROOT TH1-type histogram, and its *Fit* member function is called to fit the TF1-type function defined above. The log-likelihood fit method is selected because the histogram has many low-count bins. Then the fit result is logged and the fit function and residual histogram are saved. This procedure does not take into account the statistical uncertainties of the templates. Therefore, the statistics of the fitting template and the background spectrum should be good enough so that the statistical uncertainty of each bin is negligible. Practically, we require that the statistical uncertainties of the templates are a factor of 3 smaller than those on the measured spectrum.

To verify whether the fit procedure described above extracts $a_{\beta\nu}$ accurately, we constructed a TOF spectrum with particular values of $a_{\beta\nu}$ and used them as data. For example, for $a_{\beta\nu} = -0.1$ the fit result was $a_{\beta\nu} = -0.0993 \pm 0.0032$. The fit function overlaid with the simulated TOF spectrum and the residual histogram of the fit are plotted in Figure 6.6.

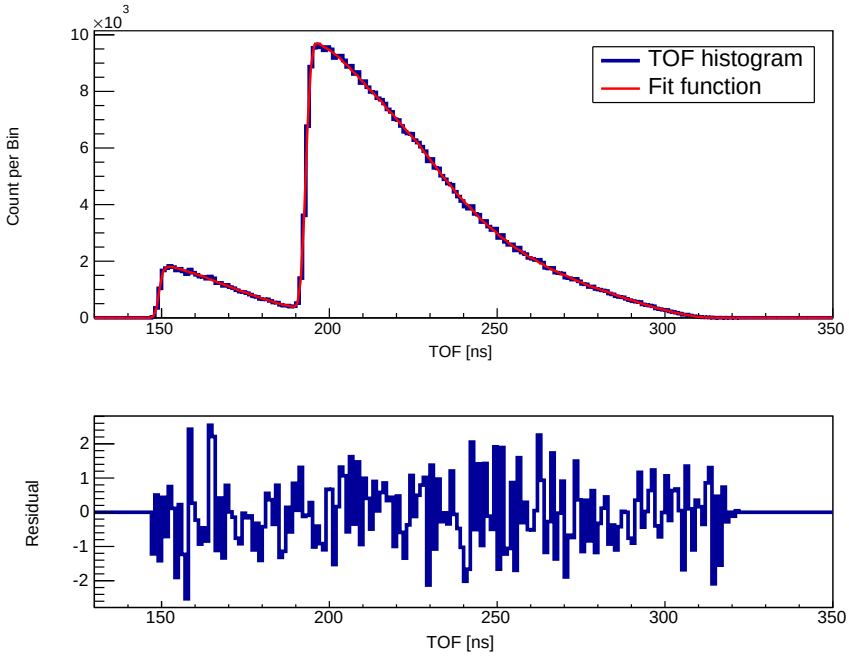

Figure 6.6: Fit to the simulated TOF spectrum with $a_{\beta\nu} = -0.1$. The lower panel shows the residual histogram of the fit.

The fit method described above assumes that the simulation parameter list S_i is the same as that for the experiment. However, the finite precisions of the calibrations cause uncertainties in the parameters S_i. Also, the simulation detector modeling is not perfect. These differences result in deviations of the $a_{\beta\nu}$ extraction, *i.e.* systematic uncertainties of $a_{\beta\nu}$, which are discussed in Section 6.6 and summarized in Section 6.8.

6.5 Comparing the simulations to the experiments

To verify the validity of the MC simulation, we compared several simulated spectra other than the TOF spectrum of the trapped ^{6}He decay to the measured ones. Although the MC simulation is not designed to match these spectra to very high precision, they provide insights in how well the parameter S_i's are controlled. Some comparisons are described in Chapter 5, for example, the E_β and MWPC energy spectrum for the ^{207}Bi source. In this section, more comparisons are shown.

6.5.1 Off-centered ^{207}Bi source

In this test the ^{207}Bi source is placed ∼42 mm away from the center of the MOT-2 chamber by retracting the magnetic transporter. A coincidence trigger between the MWPC and the PMT is required. The position of the ^{207}Bi source is at (29.5 mm, −29.5 mm, 0 mm) in the chamber coordinate system. Based on its position and the geometry of the collimator, the illuminated area on the MWPC is expected to be a circle centered at (−12.2 mm, 3.3 mm) with radius of 16.9 mm in the MWPC coordinate system. The measured and simulated MWPC images are compared in Figure 6.7, and the boundary of the expected illuminated area is marked on both of them. In both the measured and simulated images, the boundary of the illuminated area agrees qualitatively well with the expected one. The events falling in the region outside the expected illuminated area (so-called *shade area*) are caused by β-scattering on the edge of the collimator or large outgoing angle after straggling through the beryllium window. By comparing the simulated and measured event distribution or E_β spectrum in the illuminated area and the shade area, we tested the MC simulation for β-scattering events.

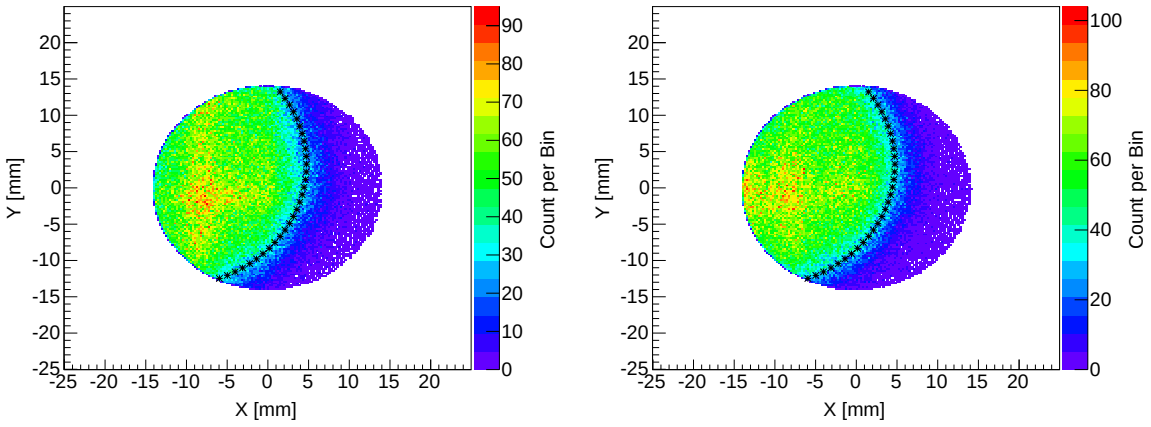

(a) Measurement

(b) Simulation

Figure 6.7: Measured and simulated MWPC image with the boundary of the expected illuminated area marked with the line of "∗". A fiducial cut (14 mm radius cut from the MWPC center) is imposed.

We first compared the event densities as a function of R_c which is the distance to the center of the expected illuminated area (the circle marked as a line of "∗' in Figure 6.7). The simulation-to-measurement comparison for 10 mm $< R_c <$ 26 mm is shown in Figure 6.8. Then the simulated and measured E_β spectra are compared under the condition R_c <16.9 mm (illuminated area) and R_c >16.9 mm (shaded area) as shown in Figure 6.9. In this comparison, the condition E_β >500 keV is imposed for all cases. Both the event density and E_β comparisons show good agreement between the simulation and the measurement.

6.5.2 Non-trapped ^{6}He

In order to simulate the experiment using non-trapped ^{6}He, the event generator is configured to sample the decay positions uniformly in a cylinder with radius 81 mm and vertically from the MCP top surface to the beryllium window holder bottom surface. If one event is generated inside the electrode plates, the event is killed by the ion tracker. The conditions applied to both the measurement and simulation are the same as those for the $a_{\beta\nu}$ measurement using trapped ^{6}He atoms. The background caused by the random coincidences is

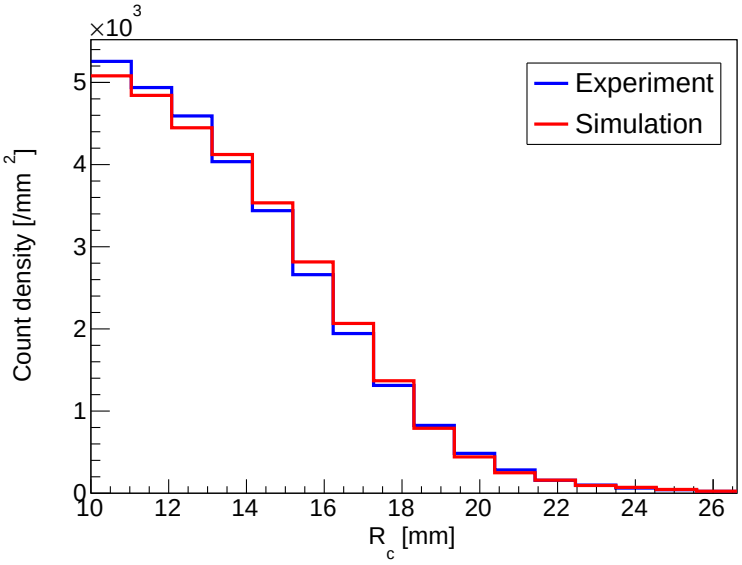

Figure 6.8: Measured and simulated event density as a function of R_c.

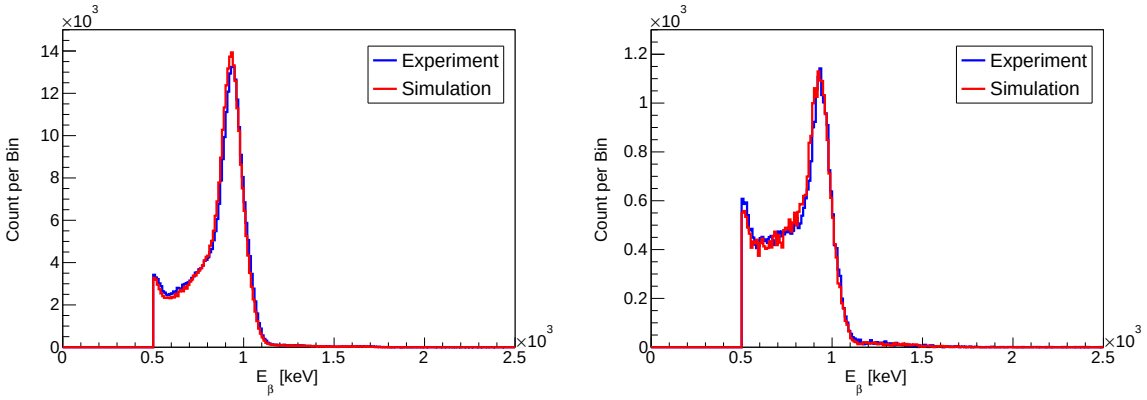

(a) Illuminated area

(b) Shade area

Figure 6.9: Simulation-to-measurement comparisons of the E_β spectrum in (a) the illuminated area and (b) the shaded area of Figure 6.7.

subtracted from the measured TOF spectrum.

The simulation-to-measurement comparison for the TOF spectra is shown in Figure 6.10a, and the E_β spectra are compared in Figure 6.10b. For the TOF spectrum, the simulation agrees with the measurement well in the TOF range from 80 ns to 250 ns. The disagreement

at the low TOF region is due to the loss of MCP efficiency for the very low energy ^{6}Li ions generated near the MCP. Events with high TOF are from the region near the collimator (the last electrode). Out modeling of the beryllium window is not very accurate. For example, the bow due to the differential pressure is not included. This results in a distortion of the E-field in this region and the discrepancy in the TOF-spectrum comparison. However, these details are not important for simulating the decays of trapped ^{6}He atoms located far away from the region of the collimator. The current accuracy of the beryllium window position is good enough for the 1% precision $a_{\beta\nu}$ measurement. The simulated E_β spectrum matches well with the measured one qualitatively with no obvious discrepancies.

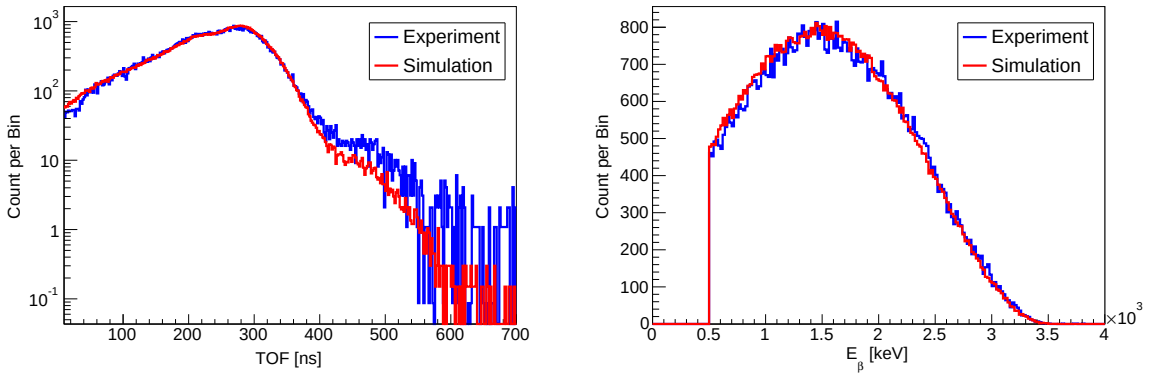

(a) (b)

Figure 6.10: Simulation-to-measurement comparisons for non-trapped ^{6}He decays. (a) TOF spectra (b) E_β spectra

The MCP position spectra from the simulation and the measurement are also compared. It is difficult to visualize the 2D histogram comparison. Instead, we compared the projections of the MCP 2D position spectra in Figure 6.11. The simulation and the measurement also agree with each other well for the MCP position spectrum projections. The positions and widths of the dips that correspond to the mask grid lines also match well. This validates the MCP position calibration and the MCP modeling in the MC simulation.

Finally, we use the MC simulation to inspect the initial event position distribution in the MOT-2 chamber for the non-trapped ^{6}He experiment. Initial positions (with and without

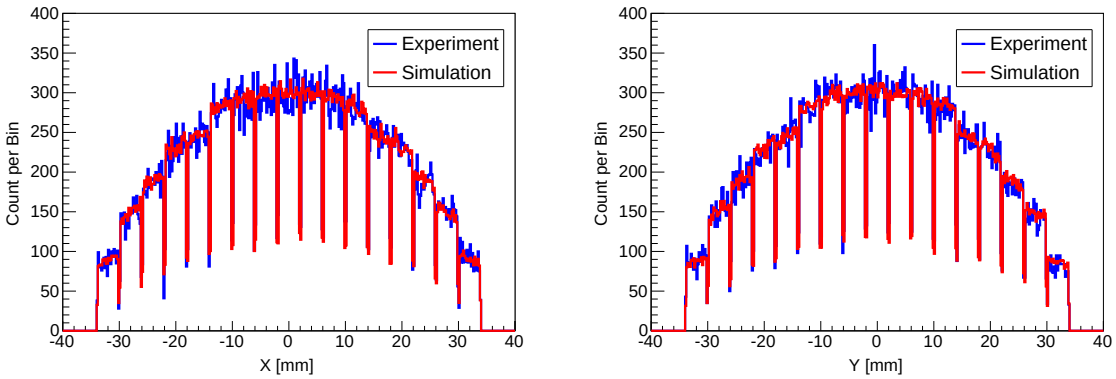

(a) (b)

Figure 6.11: Simulation-to-measurement comparisons of MCP image for non-trapped ^{6}He decays. (a) X projections (b) Y projections

the Q-value cuts) are distributed as shown in Figure 6.12 for events that trigger both the β telescope and the ion detector. Without the Q-value cuts most of the events concentrate near the collimator (the top electrode) because they have a larger β-detection solid angle. The event distribution in the X-Z plane has a collar-shape upper boundary, similar to the shape of equipotential surfaces near that region. ^{6}Li ions generated above this boundary are not energetic enough to overcome the energy barrier and drift to the MCP. With the Q-value cuts applied events happening near the collimator are suppressed.

6.5.3 Trapped ^{6}He

The MC simulation generates fitting templates for the $a_{\beta\nu}$ measurement. It is important to make sure that the MC simulation generates the correct TOF spectra of the trapped ^{6}He decays. By comparing the simulated spectra other than the TOF spectrum (using $a_{\beta\nu} = -1/3$) to the measured ones, one gains knowledge of how well the MC simulation performs for the configuration of interest.

We first compared the β-telescope spectra. The simulation-to-measurement comparison of the E_β spectra for trapped ^{6}He decays is shown in Figure 6.13. The agreement between the simulation and the measurement is good. The spectra have the low-energy threshold at

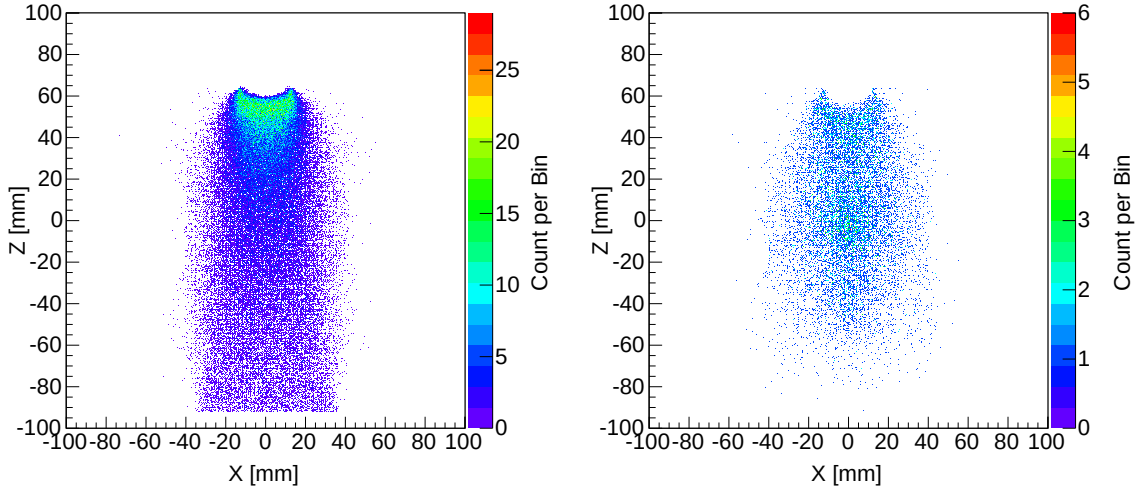

(a) Without Q-value cuts

(b) With Q-value cuts

Figure 6.12: Initial position distribution for non-trapped ^{6}He decays that trigger both the β telescope and the ion detector. Both spectra with and without the Q-value cuts are shown.

500 keV, because this value is chosen to be the standard cut for the $a_{\beta\nu}$ measurement.

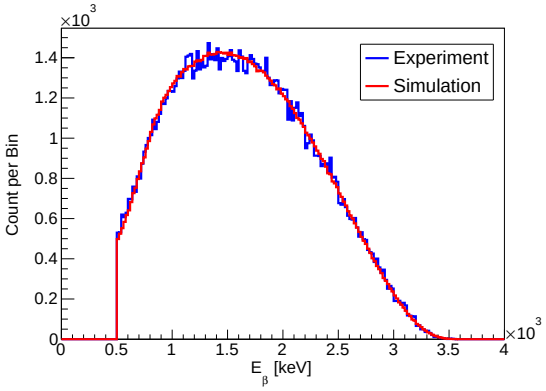

Figure 6.13: Simulation-to-measurement comparison of the E_β spectra for trapped ^{6}He decays.

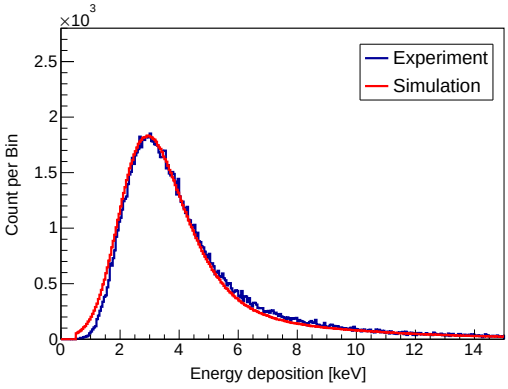

Figure 6.14: Simulation-to-measurement comparison of the MWPC energy deposition spectra for trapped ^{6}He decays.

The MWPC energy spectrum comparison is shown in Figure 6.14, and the comparison of its position spectrum projections are shown in Figure 6.15. The simulated peak positions

and the overall shape of the pedestals for both the X and Y projections match well the measurement. However, there are non-matching details between them. The difference is due to the efficiency non-uniformity of the MWPC, and this effect is studied in Section 6.6. It turns out that its impact on the $a_{\beta\nu}$ extraction is negligible for the 1% measurement. Then the MCP spectrum projections are compared in Figure 6.16, and the simulation agrees well with the measurement.

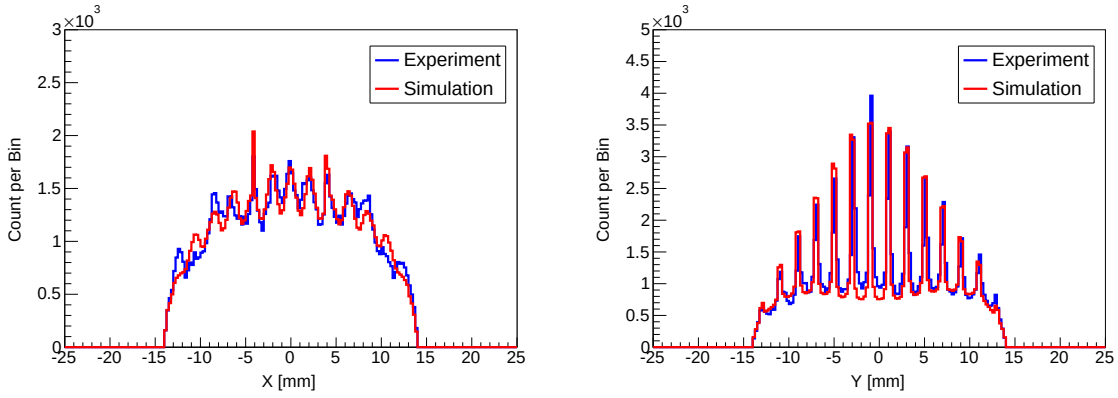

(a) (b)

Figure 6.15: Simulation-to-measurement comparisons of MWPC image for trapped ^{6}He decays. (a) X projections (b) Y projections

The E_β-vs.-TOF 2D histograms from the experiment and simulation are compared in Figure 6.17. The Q-value cuts and background subtraction are implemented in these histograms. To reconstruct the antineutrino momentum and calculate its angle $\theta_{\beta\nu}$ relative to the β momentum, we raised the E_β threshold to 1500 keV to remove the charge state ambiguity. The simulation-to-experiment comparison is shown in Figure 6.18 with both simulations using $a_{\beta\nu} = \pm 1/3$ overlaid. For the measured spectrum, the normalized background spectrum generated by non-trapped ^{6}He decays is subtracted. It is obvious that the measured $\theta_{\beta\nu}$ spectrum deviates from the simulated spectrum with $a_{\beta\nu} = -1/3$. Details of the $a_{\beta\nu}$ determination by fitting the TOF spectrum are discussed in Section 6.8.

To test the background subtraction and Q-value cuts, the Q-value spectrum is further studied. The Q-value projections shown in Figure 6.4 are compared to their corresponding

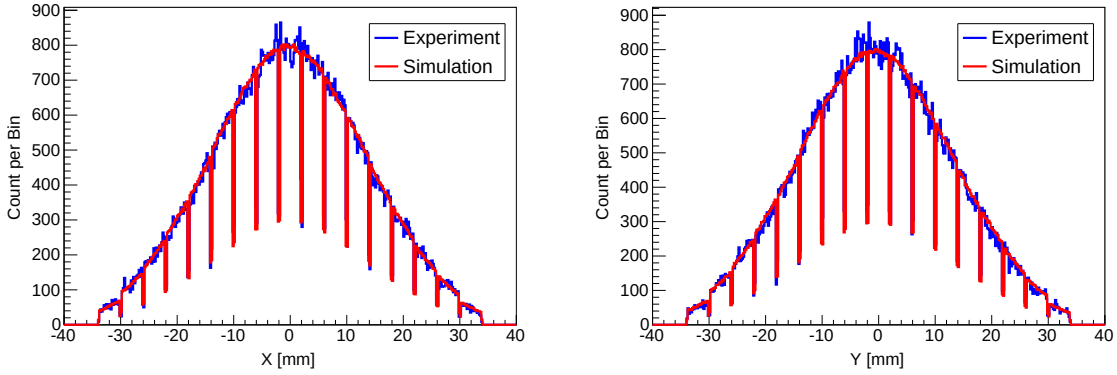

(a) (b)

Figure 6.16: Simulation-to-measurement comparisons of MCP image for trapped ^{6}He decays. (a) X projections (b) Y projections

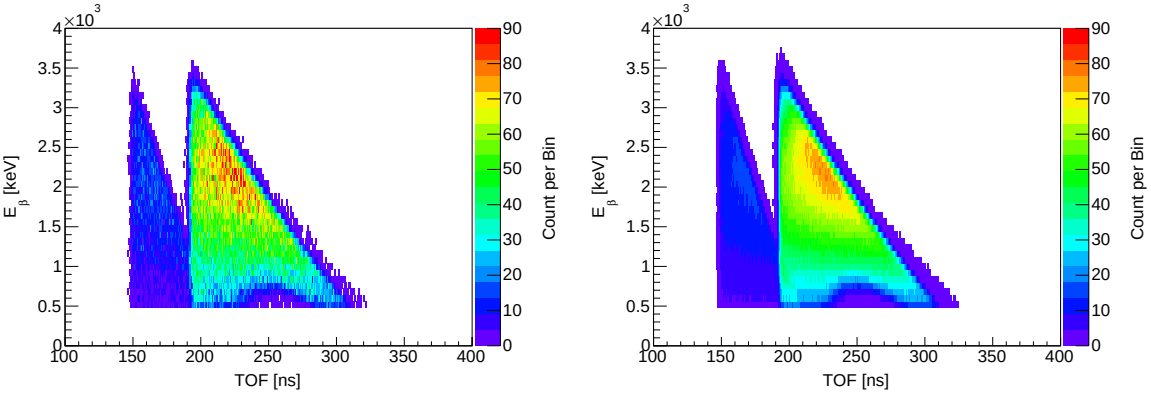

(a) Experiment (b) Simulation

Figure 6.17: Simulation-to-measurement comparison of E_β-vs.-TOF 2D histogram for trapped ^{6}He decays. Normalized background spectrum generated by non-trapped ^{6}He decays are subtracted from the measured spectrum. The simulation histogram is renormalized to the integral of the measured one.

background generated by the non-trapped ^{6}He decays in Figure 6.19, and the background normalizations are determined as described in Section 6.3. The background spectra match those for trapped ^{6}He decays very well in the non-physical regions with higher Q-values. In the non-physical regions with lower Q-values there are extra events in the spectra for

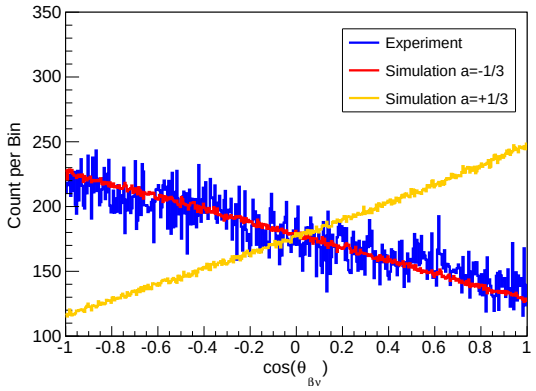

Figure 6.18: Measured and simulated $\cos(\theta_{\beta\nu})$ spectra. The normalized background spectrum generated by non-trapped ^{6}He decays is subtracted from the measured spectrum. The simulated spectrum with $a_{\beta\nu} = +1/3$ is also plotted. The E_β threshold is raised to 1500 keV so that the charge state 1 and charge state 2 are separated in TOF.

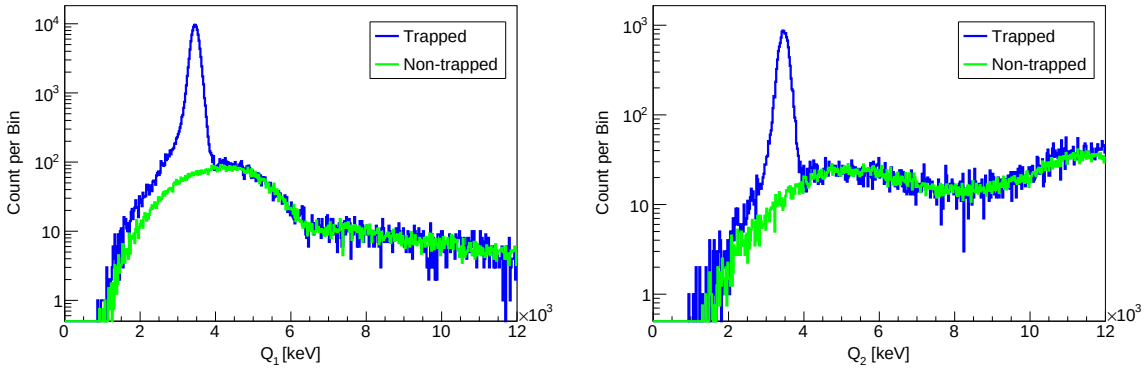

(a) (b)

Figure 6.19: Q-value histograms and their corresponding background generated by non-trapped ^{6}He decays. When constructing the Q_1 histogram, a 4 MeV threshold is imposed on Q_2, and vice versa.

trapped ^{6}He decays. These events may correspond to scattering of β particles, because β particles lose significant amount of energy through scattering, leading to a lower Q-value reconstruction. The simulation-to-measurement comparisons of the Q-value spectra are shown in Figure 6.20 with the background subtraction implemented. The simulations agree

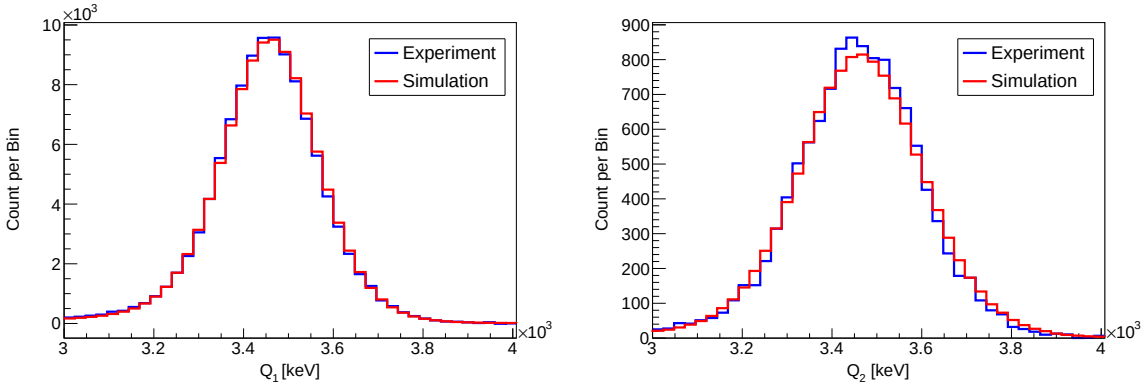

(a) (b)

Figure 6.20: Simulation-to-measurement comparisons of Q-value histograms. Normalized background spectra generated by non-trapped ^{6}He decays for each Q-value are subtracted. When constructing the Q_1 histogram, a 4 MeV threshold is imposed on Q_2, and vice versa.

well with the measurements concerning the Q-values, particularly in the low-Q tails. The simulated Q_1 and Q_2 peak positions agree with the measured ones at the $\sim$2 σ level[3].

Moreover, we studied the TOF spectrum for events ruled out by Q-value cuts. In Figure 6.21a we compared TOF spectra for the trapped and non-trapped ^{6}He decays under *inverse* Q-cuts (meaning keeping only events ruled out by the Q-value cuts). Assuming the background subtraction is correct, in theory the difference between these spectra are caused by events originating from the trapped ^{6}He atoms but with β scattering or incorrectly-determined particle momenta due to other reasons. These events are supposed to be accounted for by the MC simulation. Then we subtracted the backgrounds generated by the non-trapped ^{6}He decays from the TOF spectrum of the trapped ^{6}He decays under the inverse Q-value cuts, and compared it to the MC simulation as shown in Figure 6.21b. The measured and simulated spectra agree with each other well in the TOF region of interest [140 ns, 350 ns]. Extra events at TOF$>$ 350 ns in the measured spectrum are caused by the non-perfect background subtraction in this region as shown in Figure 6.5.

[3]To achieve this agreement, the TOF needs to be corrected by the fitted T_0 values listed in Table 6.38.

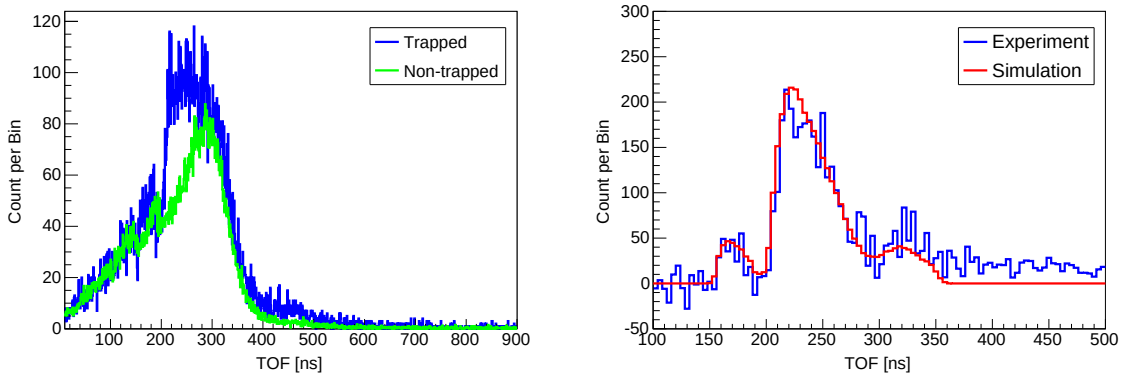

(a) (b)

Figure 6.21: (a)Recoil ion TOF spectrum for the trapped (blue curve) and non-trapped (green curve) ^{6}He decays with inverse Q-value cuts. Spectrum for non-trapped ^{6}He decays is normalized as described in Section 6.3. (b)Simulation-to-measurement comparison of the background-subtracted recoil ion TOF spectrum for the trapped ^{6}He decays with inverse Q-value cuts. The simulation is normalized to the integral of the measured spectrum from 150 ns to 360 ns.

6.6 Sensitivities to systematic effects

Because the TOF spectrum depends on the parameters and conditions S_i in Equation 6.3, the fitted value of $a_{\beta\nu}$ (a_{fit}) is a function of ΔS_i which is the difference between the real value of S_i in the measurement and the value of S_i used for constructing the fit templates. In order to study the relationship between a_{fit} and S_i, we first fix T_0 and expand the log-likelihood function L around its maximum:

$$\Delta L = \frac{\partial^2 L}{\partial a^2}(\Delta a)^2 + \Sigma_i \frac{\partial^2 L}{\partial a \partial S_i}\Delta S_i \Delta a + \Sigma_i \frac{\partial^2 L}{(\partial S_i)^2}\Delta S_i^2, \tag{6.8}$$

where a is short for $a_{\beta\nu}$ in this equation and thereafter in other equations in this section. Obviously, $\Delta a = 0$ maximize L if all $\Delta S_i = 0$, *i.e.* all parameters and conditions for constructing the templates are the same as the ones for constructing the measured TOF spectrum. If $\Delta S_i \neq 0$, the fitted value of a moves by

$$\Delta a_{fit} = -\frac{\Sigma_i \frac{\partial^2 L}{\partial a \partial S_i}}{2\frac{\partial^2 L}{\partial a^2}}\Delta S_i. \tag{6.9}$$

Therefore, to lowest order the fitted value a_{fit} varies with S_i linearly. If the S_i's are all independent, the total systematic uncertainty of $a_{\beta\nu}$ is

$$\sigma_a^{sys} = \sqrt{\Sigma_i (\frac{\partial a_{fit}}{\partial S_i} \times \sigma_{S_i})^2}, \tag{6.10}$$

where σ_{S_i} is the uncertainty of S_i and $\frac{\partial a_{fit}}{\partial S_i}$ is the sensitivity of $a_{\beta\nu}$ to S_i. Practically, the sensitivities are determined through MC simulation. We fixed the fit templates and generated more simulated TOF spectra with lower statistics using different S_i values. For each TOF spectrum, we conducted the template fit and extracted a_{fit}. Then we fit a_{fit} as a function of S_i to a linear function so that the value $\frac{\partial a_{fit}}{\partial S_i}$ is determined. σ_{S_i}'s are determined through calibrations. For some systematic effects like the MWPC efficiency non-uniformity, it is difficult to use one number to quantify this effect. Therefore, we simulated the TOF spectra with and without this effect taken into account, and the difference in a_{fit} is treated directly as the systematic uncertainty generated by this effect, *i.e.* the value of the product $\frac{\partial a_{fit}}{\partial S_i}\sigma_{S_i}$.

However, a_{fit} is too sensitive to T_0 so that with the current accuracy of the T_0 determination, the systematic uncertainty of a_{fit} is much larger than our goal. Therefore, we treat T_0 as a free parameter. In the two-parameter fit, Equation 6.8 becomes

$$\begin{aligned}\Delta L = &\frac{\partial^2 L}{\partial a^2}(\Delta a)^2 + \frac{\partial^2 L}{\partial a \partial T_0}\Delta T_0 \Delta a + \frac{\partial^2 L}{\partial T_0^2}(\Delta T_0)^2 \\ &+ \Sigma_i \frac{\partial^2 L}{\partial a \partial S_i}\Delta S_i \Delta a + \Sigma_i \frac{\partial^2 L}{\partial T_0 \partial S_i}\Delta S_i \Delta T_0 + \Sigma_i \frac{\partial^2 L}{(\partial S_i)^2}\Delta S_i^2.\end{aligned} \tag{6.11}$$

In presence of non-zero ΔS_i, the fitted values of $a_{\beta\nu}$ and T_0 that maximize L move by

$$\Delta a_{fit} = \Sigma_i \frac{\frac{\partial^2 L}{\partial a \partial T_0}\frac{\partial^2 L}{\partial T_0 \partial S_i} - 2\frac{\partial^2 L}{\partial T_0^2}\frac{\partial^2 L}{\partial a \partial S_i}}{4\frac{\partial^2 L}{\partial a^2}\frac{\partial^2 L}{\partial T_0^2} - (\frac{\partial^2 L}{\partial a \partial T_0})^2}\Delta S_i, \tag{6.12}$$

$$\Delta T_{0fit} = \Sigma_i \frac{\frac{\partial^2 L}{\partial a \partial T_0}\frac{\partial^2 L}{\partial a \partial S_i} - 2\frac{\partial^2 L}{\partial a^2}\frac{\partial^2 L}{\partial T_0 \partial S_i}}{4\frac{\partial^2 L}{\partial a^2}\frac{\partial^2 L}{\partial T_0^2} - (\frac{\partial^2 L}{\partial a \partial T_0})^2}\Delta S_i. \tag{6.13}$$

To lowest order, Δa_{fit} is still a linear function of ΔS_i and $\frac{\partial a_{fit}}{\partial S_i}$ is determined in the same way described above for the one-parameter fit. After adding the fit parameter T_0 the sensitivities $\frac{\partial a_{fit}}{\partial S_i}$'s change from their values for the one-parameter fit. For example, the sensitivity to the MOT Z coordinate is greatly reduced in the two-parameter fit.

The results of the sensitivities for all systematic effects studied together with their contribution to the systematic uncertainty of $a_{\beta\nu}$ are shown in Section 6.8.

6.7 Experimental progress and the proof-of-principle run

6.7.1 Overview of the progress from 2013 to 2015

The ^{6}He $\beta - \nu$ correlation experiment started to measure the decays from trapped ^{6}He atoms in 2013. In October 2013 we first observed the PMT-MWPC-MCP triple-coincidence triggers corresponding to ^{6}He decays. The triple-coincidence rate was about 0.1 Hz, and after analyzing the data we found most of them were from the background generated by non-trapped ^{6}He atoms. Also, at this time, the detector system was not fully functional. For example, the MWPC was only active in the center 12 mm $\times$ 12 mm area, and the long light guide was not installed so the PMT needed an additional shim coil to cancel the magnetic field from the MOT. After this run, a second turbo pump on the MOT-2 chamber was installed to prevent ^{6}He back streaming and a shutter between the MOT-1 and MOT-2 chambers was installed as well in order to reduce the number of non-trapped ^{6}He atoms in the MOT-2 chamber. The detector system was further developed in 2014 and the stability of the trapping system was also improved. In October 2014 we observed the triple-coincidence triggers with trapped ^{6}He for the second time. The data rate was $\sim$0.4 Hz but the experiment only lasted for 2 days before the production target was broken. In this run, the signal-to-background ratio was improved to 5:1, and the number of events after the analysis conditions were applied was $\sim$4000. We also started improving the data analysis program using this batch of data as test samples. Many analysis techniques like the Q-value reconstruction were developed. After 3 months of maintenance and improvement of the hardware, in February 2015 we kept the experiment running for four consecutive days with triple-coincidence rate $\sim$0.4 Hz and $\sim$20,000 events (after conditions imposed) were collected. This run showed the feasibility to keep the experiment running in an extended amount of time to collect enough data for the $a_{\beta\nu}$ extraction. However, the high-precision calibrations described in Chapter 4 were not yet developed at that time. For example, the MCP calibration mask was not installed, so the up-to-date calibration could not be carried

out. Therefore, we stopped the data taking and started developing the detector calibration campaign. During the next few months, a new MCP detector with the calibration mask was installed and the geometry of the electrode structures were carefully measured. The calibration methods were developed and tested before July 2015. Since August 2015, the calibrations were fully implemented for all experiments. We ran the experiment in August 2015, but the data rate was still around 0.2 Hz. In September 2015, we improved the trapping efficiency and achieved a data rate of ∼1 Hz. On September 28th, we ran the experiment over night and collected ∼20,000 events. However, the production target failed on the next day because of lithium loss due to over heating. On October 19th, we tried to run the experiment again and improved the data rate to ∼1.4 Hz. From October 24th to 27th, we ran the experiment continuously with an average data rate of 1.4 Hz. On October 25th, the data rate achieved a new record of 2 Hz. This experiment was terminated due to accelerator failure four days later. Within the four days, more than 100,000 events were collected. It is not enough for extracting $a_{\beta\nu}$ to 1%, but it is an important *proof-of-principle* run to test the performance of the hardware and software. The following analysis is based on the data collected during those four days.

For the proof-of-principle run, its data taking and calibration procedures are described in Subsection 6.7.2, and the stability of the calibrations during the four days of data taking are discussed in Subsection 6.7.3. Finally, the conditions imposed in the analysis and important spectra are described in Subsection 6.7.4.

6.7.2 Overview of the data taking and calibration procedure in October 2015

During the four days, the data taking started usually around 6:00 pm in the evening and stopped around 9:00 am on the next day. The production rate and the accelerator control console needed monitoring all the time by the experimenter. The auto-stirring system was activated every 30 min to ensure the lithium coated the target window. The deuteron beam ran at 10 μA, and during the four days, no lithium loss or window breaking were observed. The experimenter was also monitoring the spectra from the on-line analysis of the DAQ system, and reacted promptly if the data rate dropped to zero. A new run in the DAQ

system was started every one or two hours, and the data taken in the previous run were transferred to a data analysis computer for quick analyses. The liquid nitrogen dewar for the discharge source needed to be changed every ∼12 hours. The laser locking, HVs for detectors and the MWPC gas flow needed to be checked every hour to ensure that they are working in good conditions.

Some calibrations were built into the data taken during the overnight runs. For example, the Penning ions from the ^{6}He trap and the photoions generated by the nitrogen laser were hitting the MCP during the data taking time. The timing-zero peaks were always in the data as long as the three detectors were turned on. For other calibrations, like the β-telescope energy calibration and the MCP position calibration, additional dedicated calibration runs were needed. Calibration runs started at the end of data taking period, usually at 8:30 am. First, the non-trapped ^{6}He atoms were delivered to the MOT-2 chamber for MCP position response calibration, background calibration and MCP efficiency uniformity calibration. Then the accelerator was shut down for maintenance during the daytime. Meanwhile, the trap was switched to trapping ^{4}He atoms. The TOF spectrum of the ^{4}He photoions was measured, and the T_0 calibration for the photoion TOF spectrum described in Subsection 4.13.5 was conducted. The MOT picture was taken by the camera after this calibration was done. Then the MOT was turned off, and the ^{207}Bi source was inserted into the MOT-2 chamber for the β-telescope energy calibration for ∼1.5 hours. During the rest of the day, we carried out maintenance on the discharge source and prepared for the data taking in the evening.

Some calibrations like the MWPC position and energy calibrations were done only once three months before this run. These calibrations were either very stable (like the MWPC position calibration) or there is an equivalent monitor during the data run. For example, the peak value of the energy deposition spectrum of the MWPC using the ^{207}Bi source is an indicator of the gain drift. This spectrum was constructed right after the calibration using the ^{55}Fe source. By comparing this spectrum to the spectrum constructed during the calibrations using the ^{207}Bi source right after each experiment, one gets the gain drift from the original calibration using the ^{55}Fe source.

As a summary of the calibrations, we categorize them into the following two types.

- **Infrequent calibrations:** MWPC position (^{55}Fe), MWPC energy (^{55}Fe), MWPC efficiency uniformity, MCP efficiency uniformity, background spectral shape, geometry of the electrode structure, HVs for the E-field.

- **Daily calibrations:** β-telescope energy, MWPC energy drift (^{207}Bi), MCP position, T_0 of the photoion TOF spectrum, timing-zero for the ^{6}Li recoil ion TOF spectrum, MOT position, MOT width.

The infrequent calibrations are stable enough so that there is no need to worry about the stability. The stability of the daily calibrations are described in Subsection 6.7.3.

6.7.3 Stability of calibrations

For the E_β calibration using the ^{207}Bi source, the peak positions corresponding to the 975.7 keV conversion electron line over the four overnight runs are plotted in Figure 6.22. The data from these four calibration runs are analyzed using the same set of E_β calibration parameters. The drift of the 975.7 keV peak position is up to 0.43%. The peak positions of the LED pulser drift up to 0.26% during the overnight runs. For example, the LED pulser peaks for each run on October 25th 2015 are shown in Figure 6.23. Because the 0.26% drift measured by the LED pulser is consistent with the PMT stability determined in Subsection 4.7.1, the calibration accuracy determined in Section 4.7 still holds even if one E_β calibration is applied to the data taken within 12 hours.

The MWPC gain drift is monitored by the peak position of the MWPC energy spectrum. The MWPC energy spectra generated by the ^{207}Bi source or the trapped ^{6}He atoms are almost identical as shown in Figure 6.24a. Their peak positions are determined through fitting the peak region to a Landau distribution and extracting the most probable value. To construct these MWPC energy spectra, a coincidence trigger with the PMT and the condition $E_\beta > 500$ keV was imposed. Because the energy calibration of the MWPC was done in August 2015, we checked whether the MWPC gain drifted significantly since then. The spectra measured on August 14th 2015 and October 24th 2015 are plotted in Figure 6.24b. The peak positions of these two spectra agree with each other at the 1% level.

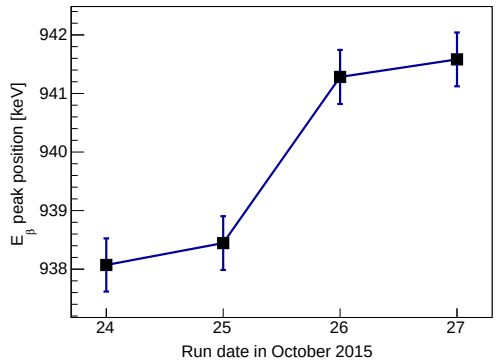

Figure 6.22: Peak positions of the 975.7 keV conversion electron line of the ^{207}Bi source for the four calibration runs.

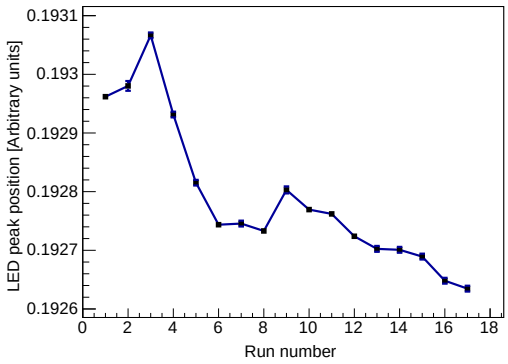

Figure 6.23: Peak positions corresponding to the LED pulses during the run on October 25th 2015.

The peak positions of the ^{207}Bi and ^{6}He MWPC energy spectra for the four overnight runs are plotted in Figure 6.25. For both ^{207}Bi and ^{6}He, the peak positions drifted $\sim$7% during the four days. Within each day, the fluctuation of the peak positions is at the same order. One example is shown in Figure 6.26. However, the gain drift of the MWPC below 10% does not affect the MWPC efficiency significantly and thus is not a significant systematic effect. We didn't correct the gain drift, and instead folded the drift into the uncertainties of the calibration. The systematic uncertainty of $a_{\beta\nu}$ caused by the MWPC gain drift is negligible.

The MOT horizontal positions and widths determined by Penning ions and photoions are shown in Figure 6.27. For the positions determined by the Penning ions, the fluctuations among the four overnight runs are up to $\pm$40 μm, and the widths fluctuates up to $\pm$30 μm. These fluctuations are larger than the statistical error bars shown in Figure 6.27, but they are still at the same level as the discrepancies described in Subsection 4.14.3. Therefore, we use the average position and width determined using the ^{6}He Penning ions to generate the fitting templates, and treat the fluctuations (40 μm for position and 30 μm for width) as additional uncertainties. The fluctuations during each overnight run are also within $\sim$40 μm. (See Figure 6.28 as an example.)

Because the nitrogen laser does not illuminate the MOT homogeneously, the position and

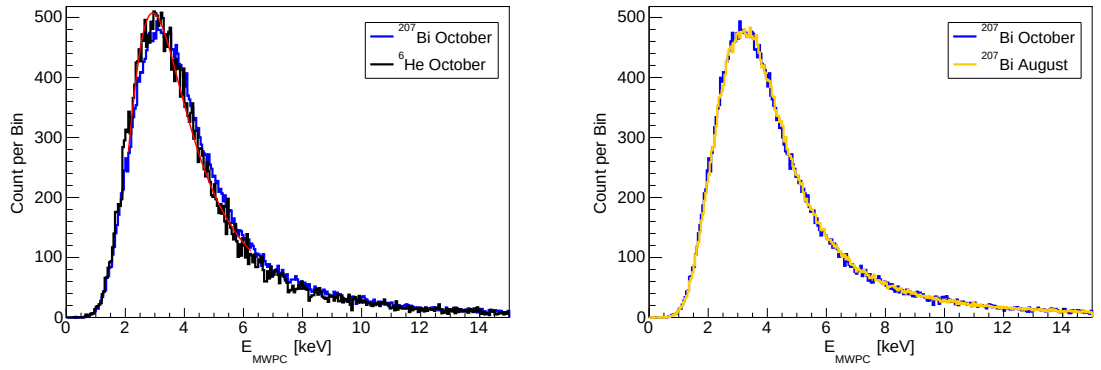

(a) (b)

Figure 6.24: (a) MWPC energy spectrum comparison between using the ^{207}Bi source and trapped ^{6}He atoms. The spectrum for ^{6}He is fitted to a Landau distribution marked in red. (b) MWPC energy spectrum comparison between the October run and the August run. Both of them used the ^{207}Bi source.

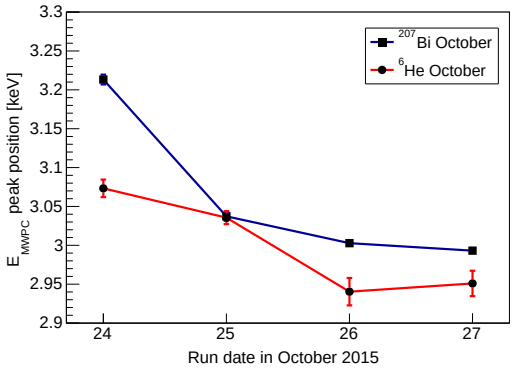

Figure 6.25: Peak positions of the MWPC energy spectra using the ^{207}Bi source for the four calibration runs and using the trapped ^{6}He atoms during the $a_{\beta\nu}$ measurement runs.

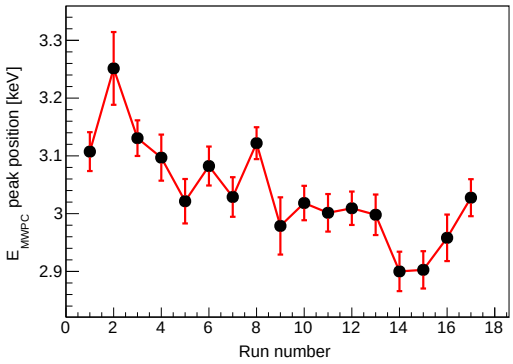

Figure 6.26: Peak positions of the MWPC energy spectra during the $a_{\beta\nu}$ measurement run on October 25th 2015.

width determined by the photoions are biased. The discrepancy between the X coordinate determined by photoions and by Penning ions is ~200 μm. The fluctuations of the position and width determined by the photoions are also ~30 μm, and this indicates that the stability of the nitrogen laser beam and the MOT position should be at the same order. The peak

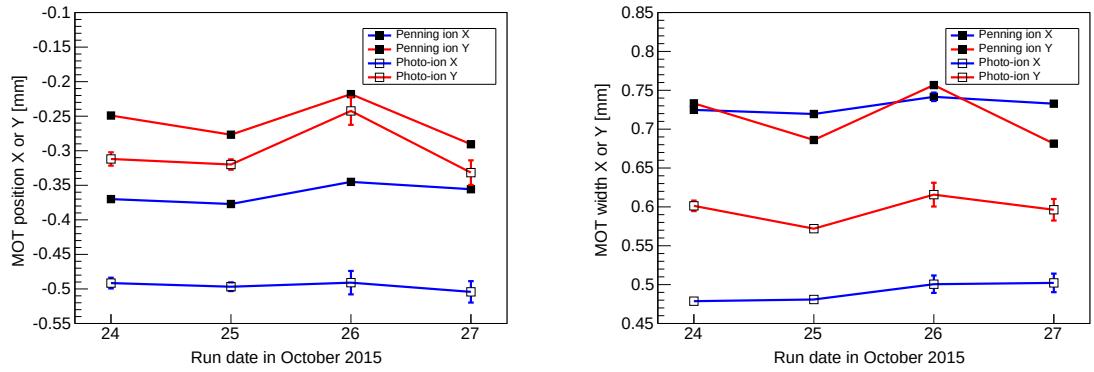

(a) (b)

Figure 6.27: (a) MOT X and Y coordinates determined using Penning ions and photoions. (b) MOT X and Y widths determined using Penning ions and photoions. All error bars are statistical only.

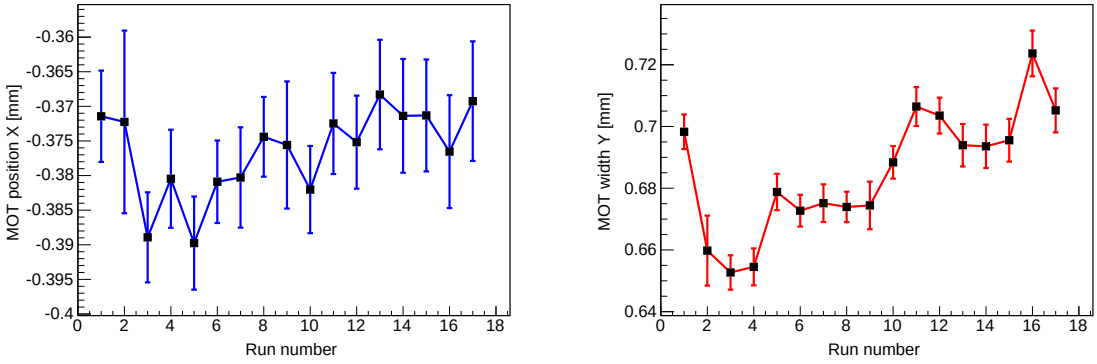

(a) (b)

Figure 6.28: (a) MOT X coordinate determined using Penning ions during the $a_{\beta\nu}$ measurement run on October 25th 2015. (b) MOT Y width determined using Penning ions during the $a_{\beta\nu}$ measurement run on October 25th 2015. All error bars are statistical only.

positions of the ^{6}He photoion TOF spectra during the four overnight runs are plotted in Figure 6.29. The fluctuation is up to 0.1 ns from day to day, and this corresponds to $\sim$70 μm in the MOT Z coordinate. Within each overnight run, the peak positions of the photoion TOF spectrum are consistent with a constant. (See Figure 6.30 as an example.) However,

the MOT Z coordinate determined using the photoion TOF may be different from its true Z coordinate by ∼200 μm as in the X direction. Therefore, the uncertainty of the MOT Z coordinate should be on the order of 200 μm if this method is used.

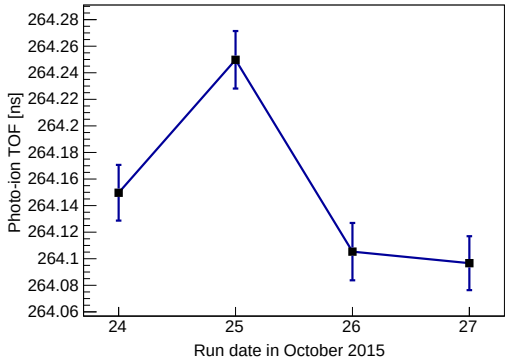

Figure 6.29: ^{6}He photoion TOF peak positions during the $a_{\beta\nu}$ measurement runs.

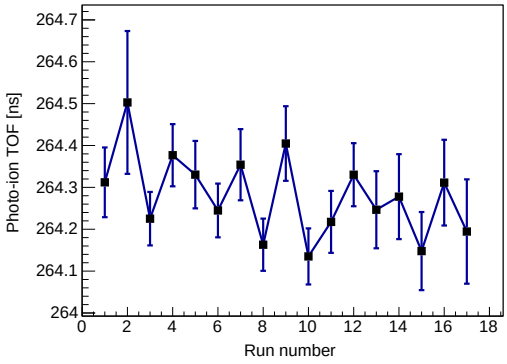

Figure 6.30: ^{6}He photoion TOF peak positions during the $a_{\beta\nu}$ measurement run on October 25th 2015.

The positions of the left and right timing-zero peaks during the four overnight runs are plotted in Figure 6.31. The fluctuations are within ±0.01 ns, and both peaks are consistent with a constant within the statistical uncertainties. This indicates that there is no timing drifts during the experiment.

To monitor the stability of the MCP position calibration, we analyzed the data from the calibration runs using the non-trapped ^{6}He atoms without the requirement of a coincidence trigger with the PMT. The same MCP position calibration parameter set was used in the analysis of all runs, and the MCP position spectra from each run are compared to each other. We found on October 25th 2015, the MCP position spectrum shifted by ∼200 μm in the Y direction and then shifted back on October 26th 2015. In the X direction there is no shift. The comparisons of the X and Y projections of the MCP position spectra taken on October 25th and 26th are shown in Figure 6.32. The mismatching of the dip positions corresponding to the grid lines are clearly seen in Figure 6.32b. We did more tests later after these four measurements and found that this effect happens every one or two days, and the dips shifted only between two possible positions, *i.e.* this effect is discrete. The

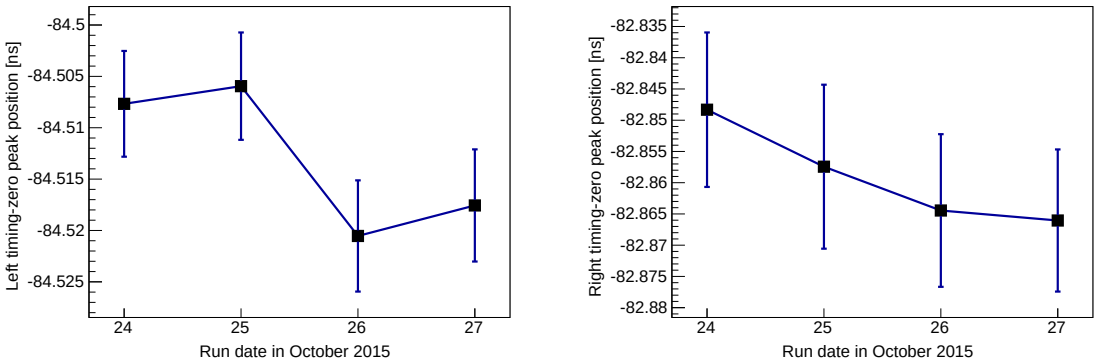

(a) (b)

Figure 6.31: (a) Left timing-zero peak positions during the $a_{\beta\nu}$ measurement runs. (b) Right timing-zero peak positions during the $a_{\beta\nu}$ measurement runs.

reason for this effect is unknown, but the daily calibration takes care of this shift as long as the shift does not happen during the overnight runs. We carefully inspected the MCP position spectra from each overnight run looking for possible shifts. (See Figure 6.33 as an example.) The dip positions for each run were all consistent with the calibration. Then we did this to all sub-runs within one overnight run, and they are all consistent with the calibration as well. Thus, we confirmed that there is no shift during any overnight run.

6.7.4 Conditions and spectra overview

The conditions used in the histogram building when analyzing the data from the proof-of-principle run are listed in Table 6.1. We combined all the data taken from October 24th 2015 to October 27th 2015, and constructed histograms under these conditions. After all conditions are imposed, there are 144,263 events left. The most relevant histograms are shown in Figures 6.34, 6.35, 6.36 and 6.37. Many of them have already appeared in previous sections or chapters. In this subsection we compile them together and organize them into categories. These spectra were also constructed by the RHB on-line data analysis software and were used for checking the stability of the system during data acquisition.

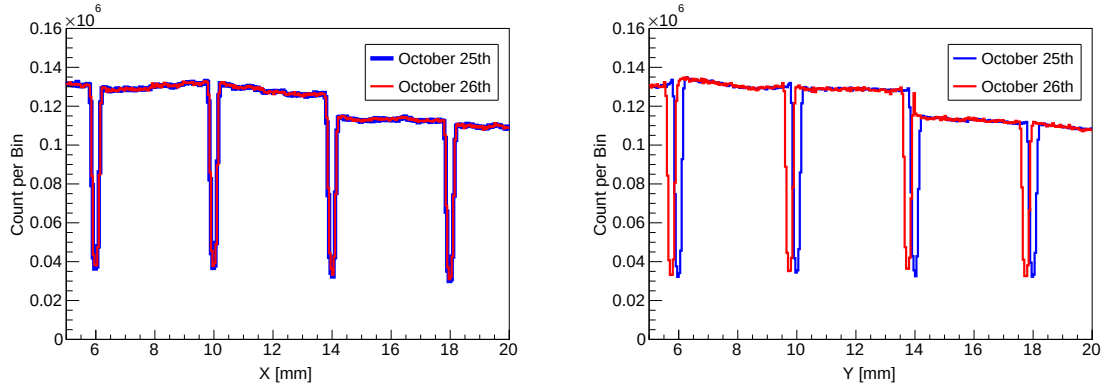

(a) (b)

Figure 6.32: Comparing the X and Y projections of MCP images using non-trapped ^{6}He runs on October 25th and 26th. (a) X projections. (b) Y projections. The timing shift in Y direction is shown in (b).

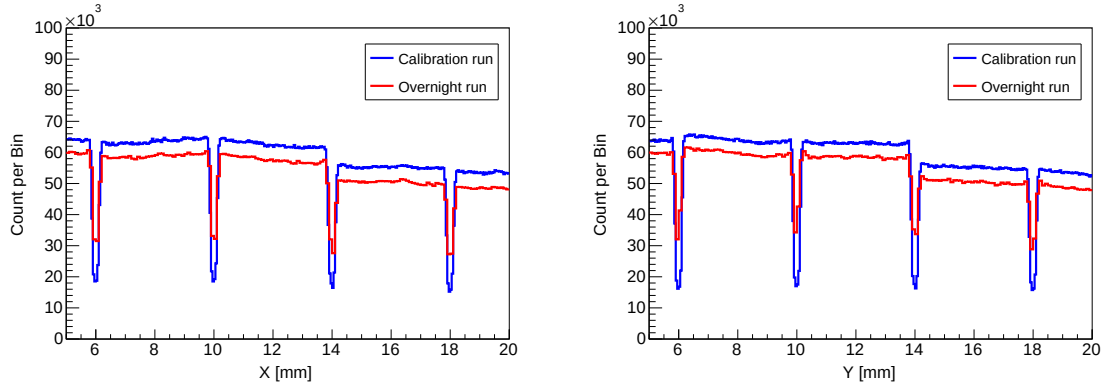

(a) (b)

Figure 6.33: Comparing the X and Y projections of MCP image of the overnight run on October 25th 2015 to those of the corresponding calibration run. (a) X projections. (b) Y projections.

Condition	Value
E_β threshold	500 keV
E_β upper bound	4000 keV
MWPC energy threshold	0.05 keV
Radius on MWPC Image	14 mm
MCP area	built-in calibration
MCP TX_{sum} and TY_{sum} window	7 ns
Push-beam veto time	30 ms
Q-value cut lower bound	3072 keV
Q-value cut upper bound	3858 keV

Table 6.1: Condition imposed on the histogram building.

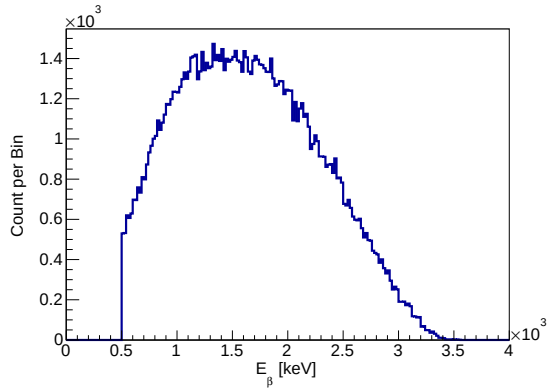

(a) E_β spectrum

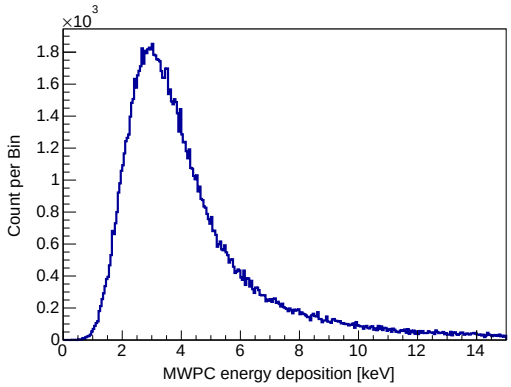

(b) MWPC energy spectrum

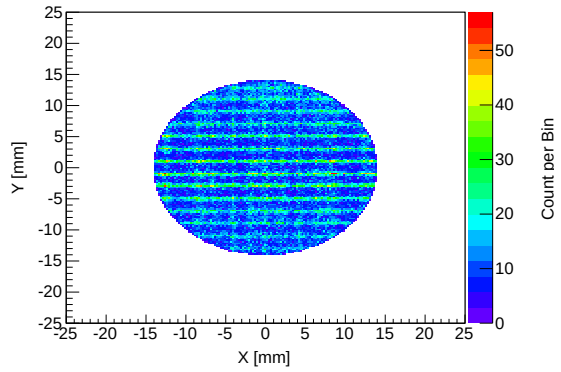

(c) MWPC position spectrum

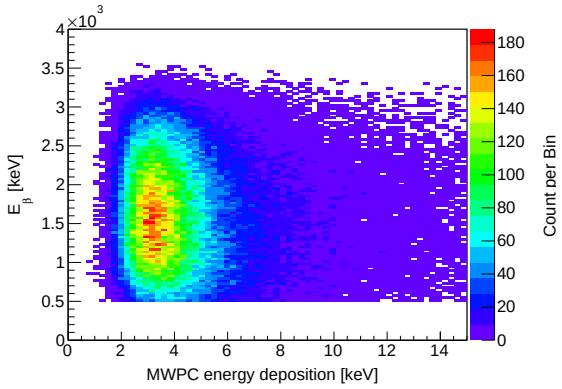

(d) E_β vs. MWPC energy

Figure 6.34: Overview of the β-telescope spectra.

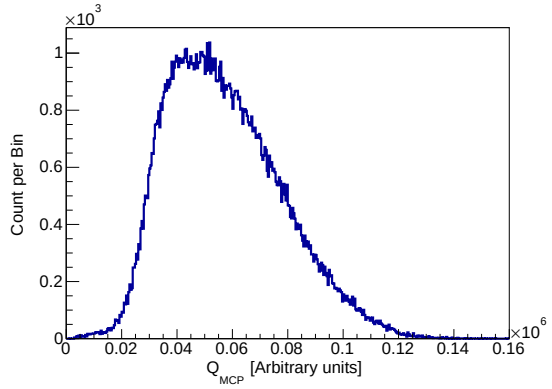

(a) Q_{MCP} spectrum

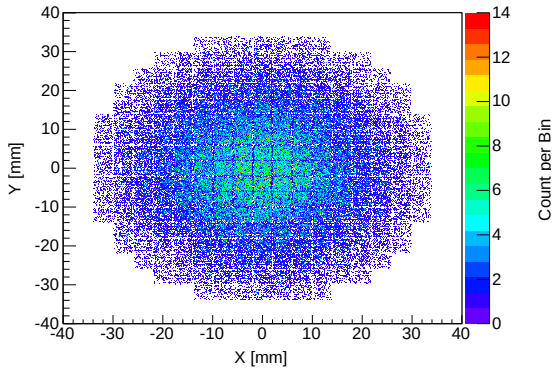

(b) MCP position spectrum

Figure 6.35: Overview of the MCP spectra.

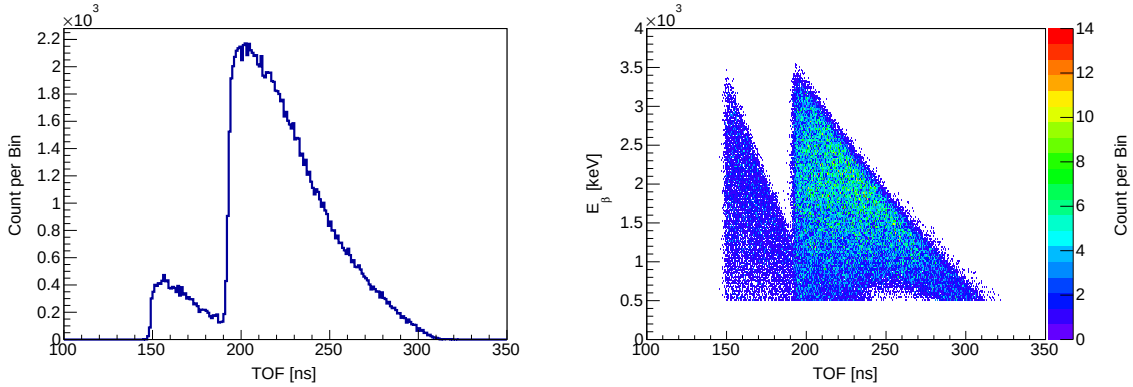

(a) TOF spectrum

(b) E_β vs. TOF

Figure 6.36: Overview of the TOF spectra.

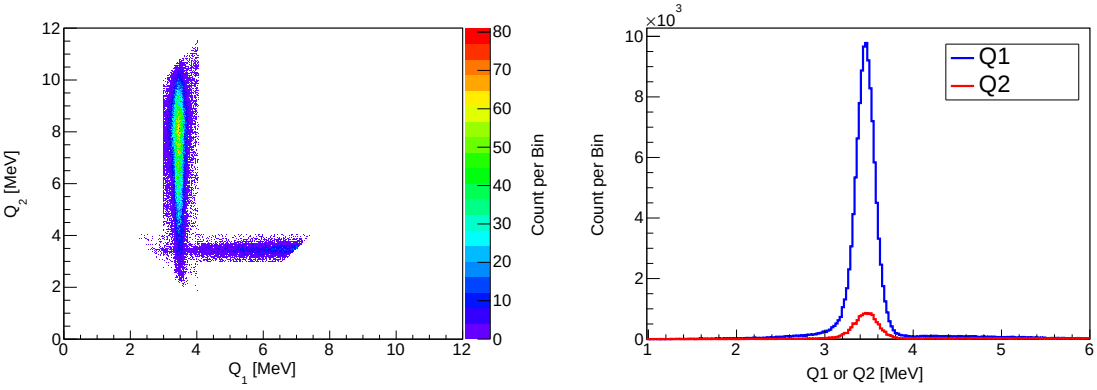

(a) Q_2 vs. Q_1

(b) Q-values of charge state 1 and 2

Figure 6.37: Overview of the Q-value reconstruction spectra.

6.8 $a_{\beta\nu}$ extraction and systematic uncertainty analysis

6.8.1 Fittings of the four runs in October 2015

We attempted to fit the data taken in October 2015. The fitting templates are generated based on the calibration described in Section 6.7.3. Particularly, the MOT parameters (position and widths) in the simulation are set to the average values of the four days' measurements. The fitted functions are overlaid on the measured spectra and the residuals for the data from each day and the combined data set are plotted in Figure 6.38. The fitted value of $a_{\beta\nu}$ and T_0 are listed in Table 6.2.

The statistical uncertainty of the combined fit is ∼2%. However, the fitted value of $a_{\beta\nu}$ is $\sim 4\sigma$ away from the SM expected value $-1/3$. Moreover, the residuals have structures other than pure statistical fluctuations. At this precision and considering the results of previous similar experiments, the discrepancy between this fitted value and the SM expected value is likely caused by systematic effects which are not fully accounted for, like the MOT Z coordinate discrepancies using different methods described in Section 4.14.2.

	$a_{\beta\nu}$	$\sigma_{a_{\beta\nu}}$	T_0 (ns)	σ_{T_0} (ns)	χ^2 per Ndf
October 24th2015	−0.3079	0.0134	−0.432	0.061	209.9/218=0.96
October 25th2015	−0.2957	0.0096	−0.632	0.040	166.5/218=0.76
October 26th2015	−0.2890	0.0220	−0.328	0.103	157.8/218=0.72
October 27th2015	−0.3048	0.0208	−0.389	0.095	205.4/218=0.94
Combined	−0.2993	0.0069	−0.518	0.030	177.4/218=0.81

Table 6.2: Fit results of the runs in October 2015

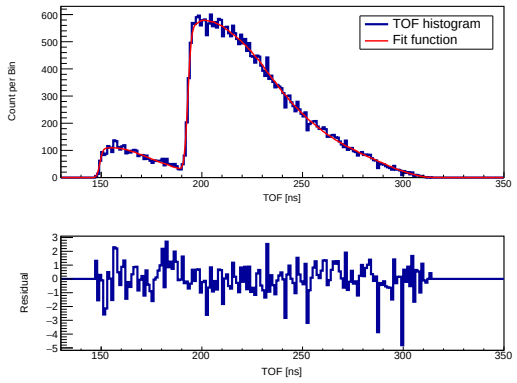

(a) October 24th

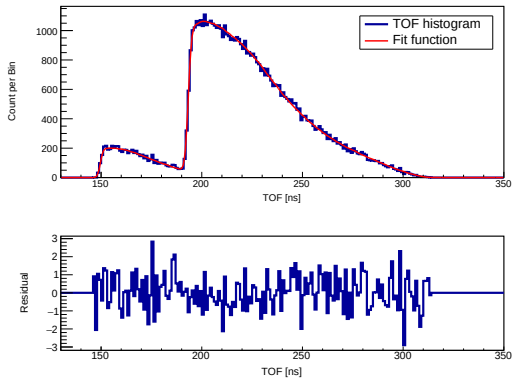

(b) October 25th

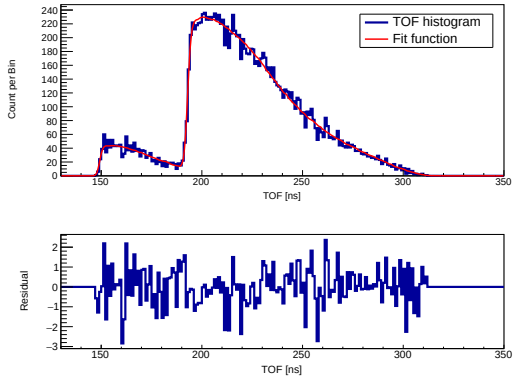

(c) October 26th

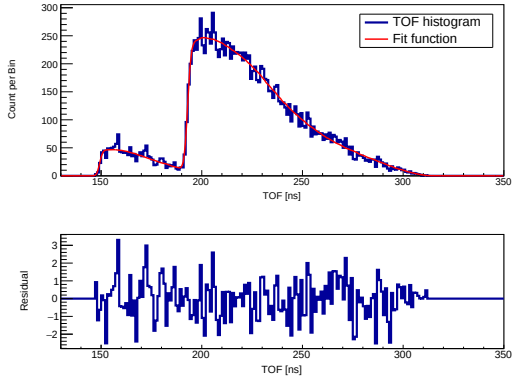

(d) October 27th

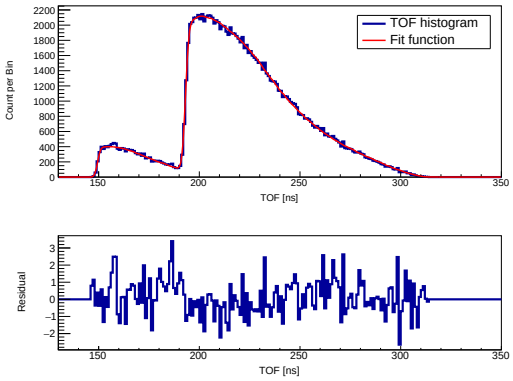

(e) Combined

Figure 6.38: Fitted functions of the TOF spectra and the residual histograms for data from the runs in October 2015 and the combined data set.

6.8.2 Systematic uncertainties

According to the calibrations described in Chapter 4 and in Subsection 6.7.3, some systematic effects are well controlled: the calibrations are accurate and the drifts are well controlled. On the other hand, there are systematic effects that are less understood: there are discrepancies in the results from different calibration methods or there are drifts that are presently not under control. For example, the β-telescope energy readout and the position readout of the MCP are well controlled, but the MOT Z coordinate is less understood. The sensitivities to systematic effects and their contributions to the uncertainty in $a_{\beta\nu}$ are listed in Table 6.3 for the well controlled systematic effects respectively. The well controlled systematic effects amount to an uncertainty of 0.37% in $a_{\beta\nu}$.

S	$(\delta a_{\beta\nu}/\delta S)/a_{\beta\nu}$	δS	$\delta a_{\beta\nu}/a_{\beta\nu}$
E_β threshold	0.023% per keV	2.4 keV	0.05%
MWPC position accuracy	0.8% per mm	0.25 mm	0.2%
MWPC energy threshold	0.14% per keV	0.5 keV	0.07%
MWPC efficiency uniformity		On/Off effect	0.18%
MCP position accuracy	1.7% per mm	0.008 mm	0.014%
MCP efficiency uniformity		On/Off effect	0.07%
Timing resolution	-0.21% per ns	0.035 ns	0.01%
β scattering	2.3%	10%	0.23%
Total			0.37%

Table 6.3: Uncertainties of $a_{\beta\nu}$ from well controlled systematic effects.

For the less understood systematic effects, the sensitivities to them and their contributions to the uncertainty in $a_{\beta\nu}$ are listed Table 6.4. In this table, the anticipated values of the uncertainties of these systematic effects are used. However, currently we observed discrepancies in the calibrations larger than these anticipated values. For example, according to the photoion TOF measurements and the TOF leading-edge position in Figure 6.38, the discrepancy in the Z coordinate of the MOT position is up to 450 μm. The discrepancy in

the long-TOF tail of Figure 6.5a is not explained, therefore it is difficult to estimate the exact uncertainty related to the background subtraction. To resolve these discrepancies we are developing new calibration and analysis projects, such as measuring the TOF spectrum with different signal-to-background ratios. Meanwhile, the code for the MC simulation is under revision for error checking.

S	$(\delta a_{\beta\nu}/\delta S)/a_{\beta\nu}$	δS	$\delta a_{\beta\nu}/a_{\beta\nu}$
MOT Z coordinate	3% per mm	0.05 mm	0.15%
Electrode spacing	8.7% per mm	0.013 mm	0.11%
Voltage accuracy	0.03% per V	0.4 V	0.01%
Background	6.0%	10%	0.6%

Table 6.4: Uncertainties of $a_{\beta\nu}$ from systematic effects that are presently not well under control. The uncertainties of these systematic parameters are anticipated values.

6.9 Charge state distribution analysis

We studied the charge-state distribution of the ^{6}Li recoil ions. The probabilities of shaking off one or two atomic electrons and their dependencies on the recoil-ion energy were extracted. In this analysis, the charge state $q = 3$ is included in the Q-value cuts, and the experimental data were based on the runs from October 24th 2015 to October 27th 2015.

One difficulty we encountered in this analysis is that the TOF regions corresponding to the three charge states overlap with one another as shown in Figure 6.39b. However, the TOF regions of the charge states do not overlap anymore if a higher threshold on E_β is applied. To find the proper E_β threshold that makes the charge states separate we ran a simulation giving equal probability (1/3) to each possible charge state. The resulting E_β-vs.-TOF 2D histogram is shown in Figure 6.39a. We note that using data with E_β >1500 keV events with $q = 2$ are completely separated from events with $q = 1$. In order to separate events with $q = 3$ one needs E_β >2100 keV. The TOF lower boundaries ($T_{lb\ 1} = 190.0$ ns and $T_{lb\ 2} = 146.5$ ns) of charge states $q = 1$ and $q = 2$ and the minimal E_β thresholds for

separating the charge states are labeled by the dashed lines in both the histograms for the simulation and the experiment in Figure 6.39.

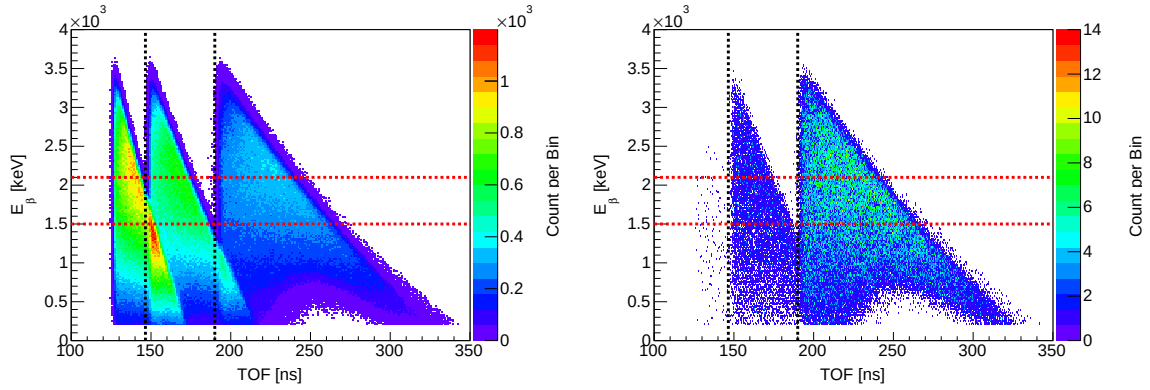

Figure 6.39: E_β-vs.-TOF 2D histograms for data from (a) the simulation assuming equal probabilities for the three charge states and (b) the experiment. The TOF lower boundary positions of the charge state 1 and charge state 2 are indicated by the black lines, and the minimal E_β thresholds needed to separate the charge states are indicated by the red lines.

In the following subsections, the shake-off probability analysis is described in detail, and the choices of E_β thresholds are discussed in each case as well.

6.9.1 Probability of charge state $q = 3$

As discussed above the minimal E_β threshold to separate charge state $q = 2$ and $q = 3$ is 2100 keV. However, applying such high threshold rules out ∼75% of the data and makes the statistics poor. Therefore, in this study, we applied a lower E_β threshold, and used the simulation to determine the *acceptance* which is the percentage of events with $q = 3$ that are below $T_{lb\ 2}$. Then from the measurement we determined the number of events below and above $T_{lb\ 2}$, and corrected these two numbers using the acceptance determined through the simulation.

To measure the percentage of events in each charge state correctly, the apparatus needs to collect all three charge states with equal efficiency. However, with the current size of the MCP, more than 10% of events in the charge state 1 fall beyond the fiducial cut. In

Figure 6.39, the lack of events near TOF=250 ns and $E_\beta < 750$ keV is due to the fiducial cut on the MCP. The larger the E_β is, the smaller amount of energy is carried by the anti-neutrino, and the lower transverse momentum the recoil ion has. Therefore, with a higher E_β threshold the MCP loses fewer events. We chose an E_β threshold at 1000 keV. According to the simulation the event loss due to the finite size of the MCP detector is less than 0.1%. The measured MCP position spectrum is shown in Figure 6.40. Given this E_β threshold the acceptance of the events with $q = 3$ below $T_{lb\ 2}$ is 85.5% according to the simulation.

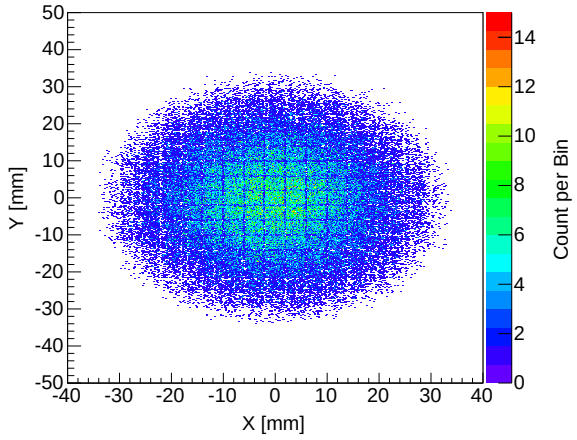

Figure 6.40: Measured MCP position spectrum with E_β=1000 keV.

The TOF spectra with and without the Q-value cuts are plotted in Figure 6.41. The background (from non-trapped ^{6}He decays) spectra are overlaid on top and the normalization of the background is determined with the method described in Section 6.3. The normalization uses the TOF range from 10 ns to 110 ns which is still non-physical when the charge state $q = 3$ is taken into account. In the TOF region where only charge state $q = 3$ is possible to reach, *i.e.* TOF$< T_{lb\ 2}$, the TOF spectrum is dominated by the background.

Without the background subtraction, the number of events with TOF$< T_{lb\ 2}$ is 103±10 assuming Poisson statistics. The integral of the background spectrum in this TOF range is 99.7±6.0. Therefore, after the background subtraction applied, the number of events with TOF$< T_{lb\ 2}$ is 3.3±11.8. Similarly, the number of events with TOF$> T_{lb\ 2}$ after the

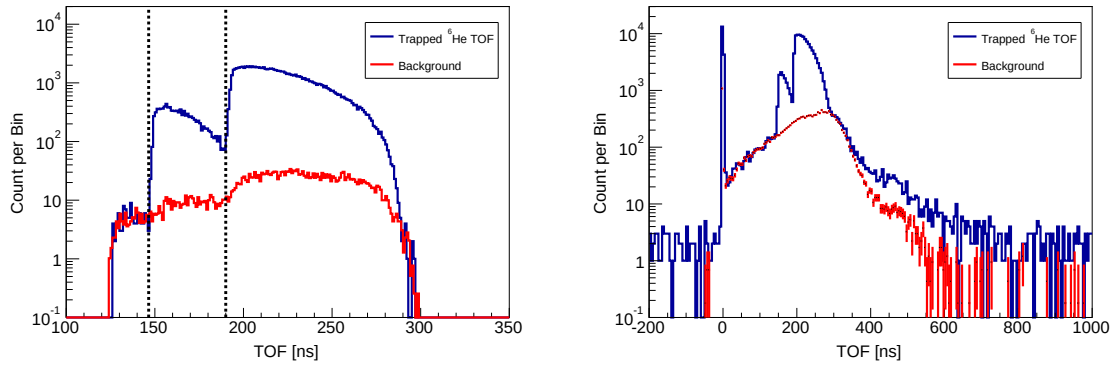

(a) (b)

Figure 6.41: TOF spectra (a) with and (b) without the Q-value cuts. The background spectra (red curves) for each case are overlaid.

background subtraction is 103966±338. Correcting these numbers using the acceptance of events with $q = 3$, the ratio between the number of events with $q = 3$ and those with $q = 1$ or $q = 2$ is

$$\frac{N_3}{N_1 + N_2} = \frac{3.3/0.855}{103966 - 3.3 \times (1/0.855 - 1)} = (0.37 \pm 1.3) \times 10^{-4}, \tag{6.14}$$

where the statistical uncertainty is dominated by the numerator. As discussed above, with a 1 MeV E_β threshold recoil ions in all charge states are fully collected, so the probability ratio of $q = 3$ and $q = 1, 2$ equals the event number ratio determined above, *i.e.* $P_3/(P_1 + P_2) = N_3/(N_1 + N_2) = (0.37 \pm 1.3) \times 10^{-4}$ with nomenclature according to charge state.

Systematic uncertainties caused by the shadow of the mask on the MCP, the non-uniformity of the MCP efficiency and the MOT position, are at most at the level of a few percent. The only simulation-dependent part is the acceptance correction, which is about 15%. Comparing to the statistical uncertainty, these systematic uncertainties are all negligible. Therefore, in the following analysis and discussion, only the statistical uncertainty of $P_3/(P_1 + P_2)$ is taken into account.

Based on this result, we constructed the upper limit of $P_3/(P_1 + P_2)$. Because $P_3 < 0$ is

not physical, the upper limit (L_{up}) is determined by letting

$$\int_0^{L_{up}} Gaus(\mu,\sigma) = 90\% \times \int_0^{+\infty} Gaus(\mu,\sigma), \tag{6.15}$$
$$\mu = 3.71 \times 10^{-5}, \sigma = 1.33 \times 10^{-4},$$

where $Gaus(\mu,\sigma)$ is the Gaussian distribution with mean μ and standard deviation σ. Thus we determined that the upper limit for $P_3/(P_1 + P_2)$ is 2.4×10^{-4} at the 90% confidence level.

6.9.2 Recoil-ion-energy dependency of the probability of charge states $q = 2$ and $q = 1$

To study the recoil-ion-energy dependency of the shake-off probabilities, one needs to reconstruct the initial energy of the recoil ions (E_{Ion}). Therefore, for each event its charge state should be determined with no ambiguity. As shown in the previous subsection, the upper limit of the probability of having an ion with $q = 3$ is at the 10^{-4} level, and the probability of having an ion with $q = 2$ is approximately 10%, ∼3 orders of magnitude higher than that for an ion with $q = 3$. We neglected the charge state $q = 3$ in this subsection. In order to separate the charge state $q = 2$ and $q = 1$, the E_β threshold was set to 1500 keV. Q-value cuts were applied to all histogram constructions in this subsection.

As described in Section 6.2, to reconstruct the initial energy of the recoil ion, we assume that the E-field is uniform and the MOT width is zero. The MOT X and Y coordinates are determined from the Penning ion image measured by the MCP, and its Z coordinate is determined by matching the simulated photo-ion TOF peak position to the measured one. The value of the uniform E-field is chosen so that under this field the photoion peak position matches the measured one. The ^{6}Li recoil ion initial energy distributions for the charge states $q = 1$ and $q = 2$ are shown in Figure 6.42. In this figure, the normalized background spectra for the recoil-ion-energy distributions are plotted as well.

Theoretically, the probability distribution functions (PDFs) of E_{Ion} in the two charge states are

$$F_i(E_{Ion}) = \Phi(E_{Ion}) \times P_i(E_{Ion}) \times Eff_i(E_{Ion}). \tag{6.16}$$

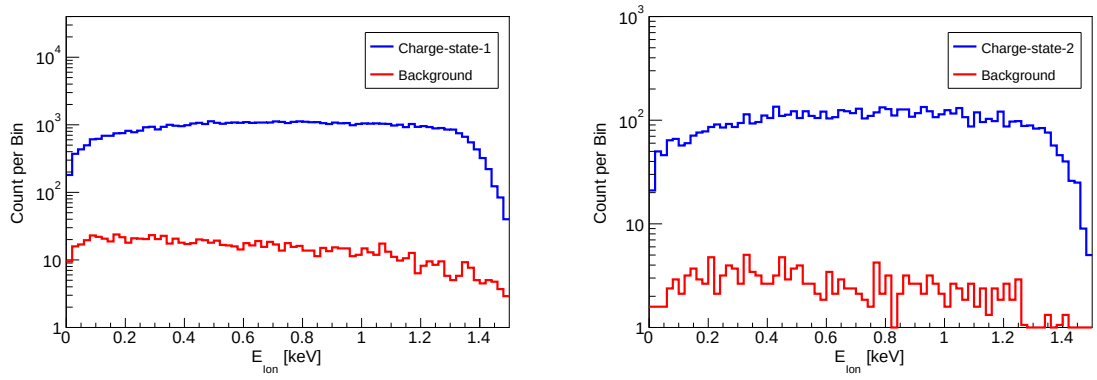

(a) (b)

Figure 6.42: ^{6}Li recoil ion initial energy distributions for (a) the charge state 1 and (b) the charge state 2. Background spectra are plotted in red.

where $i = 1, 2$ indicates the charge state, P_i is the probability of having an ion with $q = i$ as defined in the previous subsection, and $\Phi(E_{Ion})$ represents the part of the PDF that is independent on charge state, while $Eff_i(E_{Ion})$ is the detection efficiency. $\Phi(E_{Ion})$ depends only on the decay dynamics, *i.e.* the value of $a_{\beta\nu}$. $Eff_i(E_{Ion})$ depends on the geometry of the detector system, detector responses and event reconstruction parameters and conditions. According to Reference [1], $P_i(E_{Ion})$ $(i = 1, 2)$ has the form of

$$P_i = A_i + B_i E_{Ion}, \tag{6.17}$$

where A_i and B_i are constants. The goal of this subsection is to extract these constants from the four overnight runs in October 2015.

Taking the ratio of F_2 and F_1, one gets

$$R(E_{Ion}) = \frac{(A_2 + B_2 E_{Ion}) \times Eff_2(E_{Ion})}{(A_1 + B_1 E_{Ion}) \times Eff_1(E_{Ion})}. \tag{6.18}$$

The $\Phi(E_{Ion})$ functions in the numerator and the denominator cancel each other and $R(E_{Ion})$ no longer depend on $a_{\beta\nu}$ explicitly. With the 1500 keV E_β threshold, there is no event loss due to MCP fiducial area for both charge states $q = 1$ and $q = 2$. At the lowest order, we ignored the efficiency non-uniformity of the MCP, the shadow created by the calibration mask, the finite resolutions of each detector and the simplifications of the models like treating

the E-field uniform, *i.e.* letting $Eff_1(E_{Ion})$ and $Eff_2(E_{Ion})$ be identical and cancel each other in Equation 6.18. Because the charge state $q = 3$ is neglected, the sum of $P_1(E_{Ion})$ and $P_2(E_{Ion})$ is 1, and thus Equation 6.18 becomes

$$R(E_{Ion}) = \frac{A_2 + B_2 E_{Ion}}{1 - A_2 - B_2 E_{Ion}}. \tag{6.19}$$

We take the ratio of the measured E_{Ion} spectra (with background subtraction applied) for the charge states $q = 2$ and $q = 1$, and fit the ratio histogram to Equation 6.19 as shown in Figure 6.43. A_2 and B_2 are fit parameters and the fit results are listed in Table 6.5.

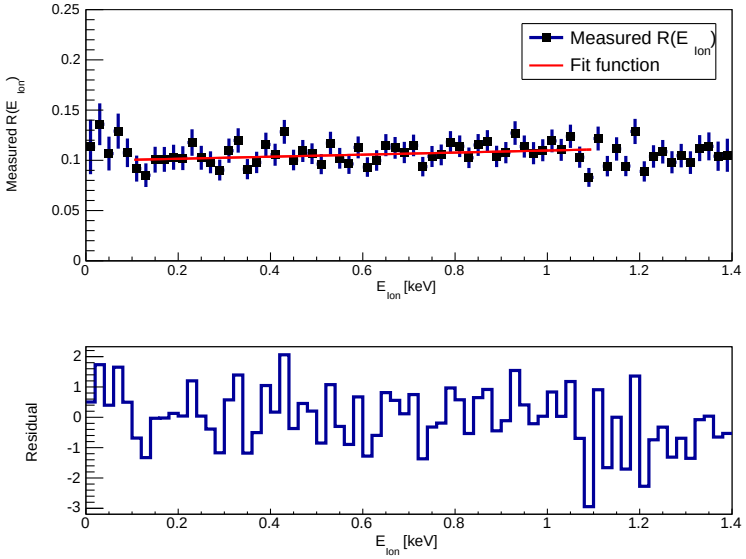

Figure 6.43: Ratio between the E_{Ion} spectra for the charge state 2 and 1, fit to Equation 6.19 in the range 0.1 keV< E_{Ion} <1.1 keV. Residuals are plotted in the lower panel.

In order to understand the bias of the fit results caused by neglecting the efficiency functions $Eff_1(E_{Ion})$ and $Eff_2(E_{Ion})$, we ran simulations with arbitrary values of A_2 and B_2, constructed the histogram of the ratio between the E_{Ion} spectra for each charge state, fit it to Equation 6.19 and extracted A_2 and B_2. For example, the ratio histogram for the simulation with $A_2 = 0.5$ and $B_2 = 0.2$ keV^{-1} is plotted in Figure 6.44, and the fit results are listed in Table 6.6. As shown in this example, Equation 6.19 fits well to the simulated data and the fitted A_2 and B_2 values deviate no more than 1.5% from their input values.

	Value	Uncertainty
A_2	9.1×10^{-2}	3×10^{-3}
B_2 [keV^{-1}]	8.4×10^{-3}	4.5×10^{-3}
χ^2	40.5	
Degree of freedom	48	

Table 6.5: Fit results for A_2 and B_2 in Equation 6.19.

The residual histogram is flat from 0 to 1.2 keV, and the fit region 0.1 to 1.1 keV is chosen to avoid systematic distortions near the ends of the spectrum.

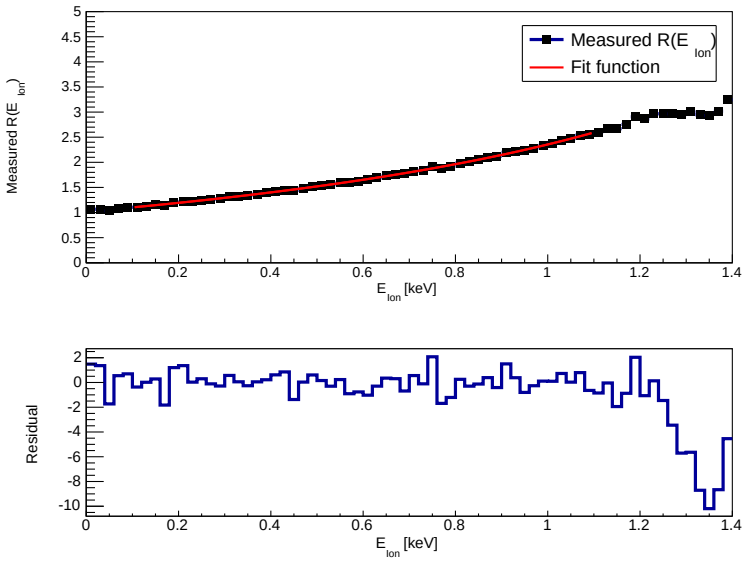

Figure 6.44: Ratio between the simulated E_{Ion} spectra for the charge state 2 and 1, fit to Equation 6.19 in the range 0.1 keV< E_{Ion} <1.1 keV. The residual is plotted in the lower panel.

Furthermore, we studied how the fitted values of A_2 and B_2 deviate from their input values as a function of their input values, and extrapolated the deviations for A_2 and B_2 values set to the measured ones from the experiment. The ratio between the fitted values and the input values, *i.e.* A_2^{Fit}/A_2^{Input} and B_2^{Fit}/B_2^{Input}, at different A_2 and B_2 input values

	Value	Uncertainty
A_2	0.505	8.2×10^{-4}
B_2 [keV^{-1}]	0.197	1.2×10^{-3}
χ^2	28.4	
Degree of freedom	48	

Table 6.6: Fit results for A_2 and B_2 in Equation 6.19 using the simulated data.

as shown in Figure 6.45 and Figure 6.46. As shown in these Figures, all ratios are scattered around 1 within 2% no matter what value A_2^{Input} and B_2^{Input} have. For the fitted values of A_2 and B_2 from the measurement, 2% deviations corresponds to 1.82×10^{-3} for A_2 and 1.68×10^{-4} for B_2. They are all small compared to the statistical uncertainties. Therefore, we treat the 2% deviations as systematic uncertainties. Because the simulation has already taking into account the shadows created by the mask, the realistic E-field, response functions of detectors and so on, the systematic uncertainty extracted above automatically includes the effects caused by these factors at the lowest order. Higher order systematic effects like uncertainties of the E_β threshold or the MCP efficiency non-uniformity are even smaller and thus negligible.

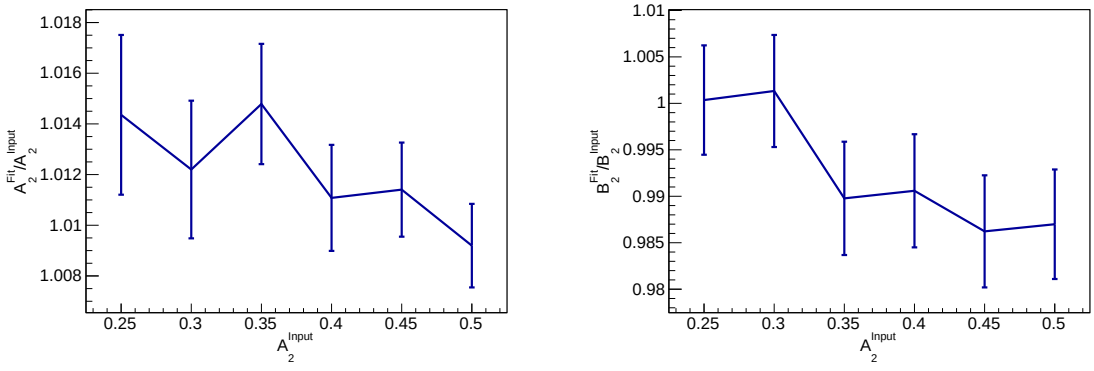

(a) (b)

Figure 6.45: A_2^{Fit}/A_2^{Input} and B_2^{Fit}/B_2^{Input} at 6 A_2 input values. The input value for B_2 is kept at 0.2 keV^{-1}.

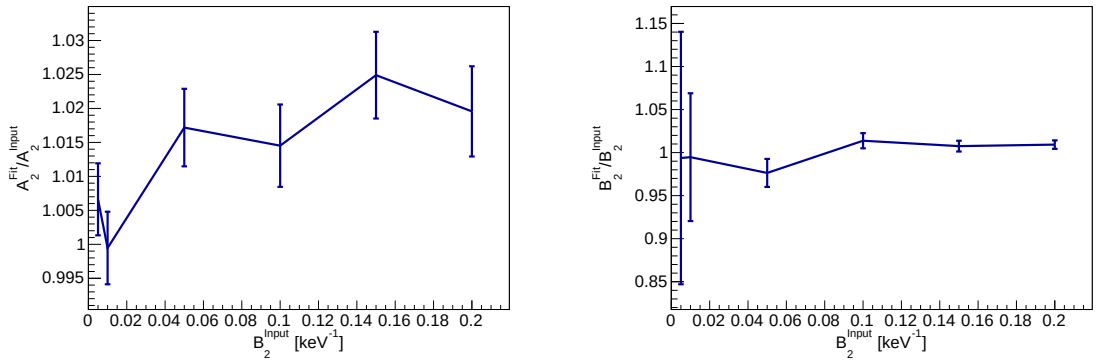

(a) (b)

Figure 6.46: A_2^{Fit}/A_2^{Input} and B_2^{Fit}/B_2^{Input} at 6 B_2 input values. The input value for B_2 is kept at 0.0942 keV^{-1}.

In summary, we extracted the parameters A_2 and B_2 that characterize the E_{Ion} dependency of the probability of shaking off 1 electron. The results are $A_2 = 0.091 \pm^{0.002(sys)}_{0.003(stat)}$ and $B_2 = 8.4 \pm^{0.2(sys)}_{4.5(stat)} \times 10^{-3}$ keV^{-1} .

Chapter 7

CONCLUSION

7.1 The $a_{\beta\nu}$ measurement

7.1.1 Current status of the development

We have constructed a system to measure the $\beta - \nu$ angular correlation coefficient $a_{\beta\nu}$ of the ^{6}He decay using MOT-trapped ^{6}He atoms. The production and trapping system of the ^{6}He are developed, and trapping of more than 200 atoms in the detection chamber was achieved. A detector system that consists of a scintillator-PMT assembly, a MWPC and a MCP was constructed. The responses of the detectors were calibrated to the accuracy capable for a 0.5% level determination of the $a_{\beta\nu}$. However, the calibrations for the timing zero, ion-accelerating field and the MOT position and widths need further inspections and calibrations to achieve a <1% measurement of $a_{\beta\nu}$.

In October 2015, we ran the system for 4 days and more than 140,000 events were observed after all cuts applied in the analysis. The TOF spectra from this data set were fit to the MC simulated fitting templates and the statistical uncertainty of the fitted $a_{\beta\nu}$ value is $\sim$2%. However, the fitted value of $a_{\beta\nu}$ is -0.2993, $\sim 4\sigma$ away from the SM predicted value $-1/3$. This discrepancy is likely caused by systematic effects which are not well understood yet. As a proof-of-principle run, this data set proves that whole system including the data analysis framework is capable to determine $a_{\beta\nu}$ at a precision better than the 10% level, and by comparing the measured spectra to the simulated ones, we confirmed the set of well controlled systematic effects and the less understood ones, which is important for future inspections and developments.

7.1.2 Possible future upgrade for high precision measurements

Presently there are discrepancies in the MOT Z coordinate and the E-field determinations, the immediate need is to inspect the geometry of the electrode system, revise the E-field

calculation and improve the MOT-imaging system. Photoion-TOF measurements are suggested for more voltage settings of uniform and non-uniform fields and more MOT positions. An upgrade of the nitrogen laser generator with shorter pulses and more uniform distribution of the light intensity across the MOT area are helpful for better determination of the MOT Z coordinate using the photoion TOF measurement. Introducing the nitrogen laser pulses into the PMT may also provides another way to calibrate the timing zero.

The validity of the background subtraction algorithm needs more studies to prove. TOF measurements for trapped ^{6}He with different signal-to-background ratios are suggested. Methods of reducing the background generated by non-trapped ^{6}He atoms in the MOT-2 chamber are underdevelopment, so the background subtraction will become less important as it is now.

After all, these projected new measurements requires a stable production and an high-efficiency trapping of ^{6}He atoms. The production system and trapping system need better tuning to achieve this goal.

In the long run, one may use a dipole trap to replace MOT-2 so that the vertical laser beams are not needed. In this way, the β detectors can be brought closer to the MOT to increase the detection solid angle. A new MWPC with a larger active area would also help with increasing the detection solid angle.

7.2 The recoil ion charge state distribution measurement

For trapped ^{6}He atoms in the metastable state, we determined that the upper limit for shaking-off 2 electrons (charge state $q = 3$) in the β decay is 2.43×10^{-4} at the 90% confidence level. The single electron shake-off (charge state $q = 2$) probability is $P_2 = A_2 + B_2 E_{Ion}$ where $A_2 = 0.091\pm^{0.002(sys)}_{0.003(stat)}$ and $B_2 = 8.4\pm^{0.2(sys)}_{4.5(stat)} \times10^{-3}$ keV^{-1}.

These results are compared to the calculated ones in Reference [1]. For the double electron shake-off probability, the calculated probability is 1.86(7)%, two orders of magnitude higher than the probability determined from this experiment. However, the calculated probability is for ^{6}He atoms in the $2\ ^3S_1$ atomic states, while in our experiment the atoms in the MOT are cycling between $2\ ^3S_1$ and $2\ ^3P_2$ states constantly. At the saturation, the populations of the two states are 50% each. In the extreme case that the atoms in the

$2\ ^3P_2$ state do not shake off 2 electrons at all, the calculation still predict that 1% of the total events have 2 shake-off electrons. It still over-predicts the observation by 2 orders of magnitude. For the single electron shake-off probability dependency on E_{ion}, the calculated values for A_2 and B_2 are $A_2 = 0.0942(7)$ and $B_2 = 1.04(6) \times 10^{-3}$ keV^{-1}. In order to compare to the measured ones, the calculations for the $2\ ^3P_2$ state is needed. If ignoring the difference between $2\ ^3S_1$ and $2\ ^3P_2$, the calculated A_2 agrees with the measurement within 1σ, and the difference between the calculated and measured B_2 is 1.6σ.

These measurements are limited by statistics. Higher statistics of trapped ^{6}He data will improve the results discussed above significantly.

Appendix A

DAQ SETTINGS FOR EACH CHANNEL

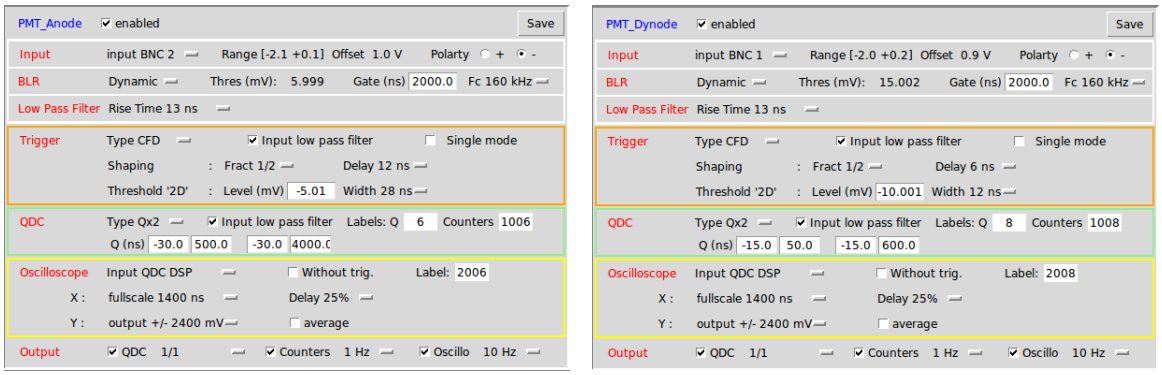

(a) Anode (b) Dynode

Figure A.1: DAQ Settings for PMT channels.

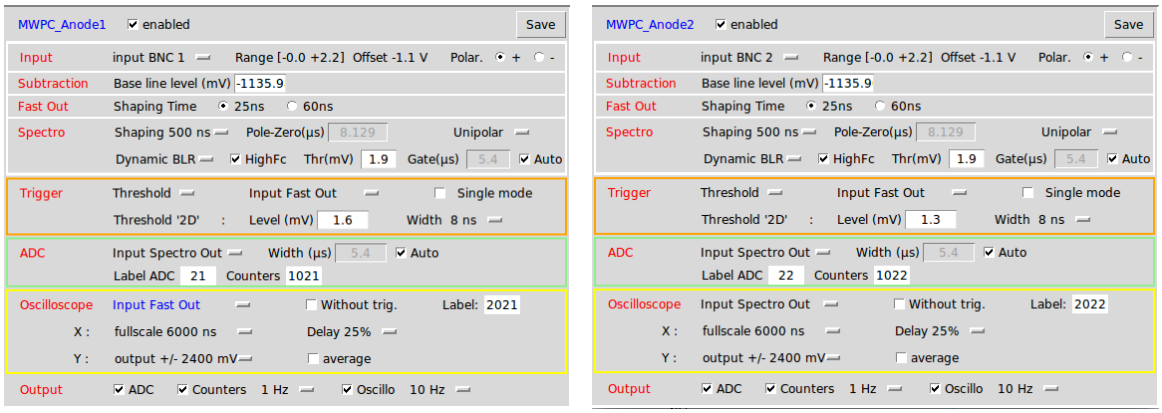

(a) Anode 1 (b) Anode 2

Figure A.2: DAQ Settings for MWPC anode channels.

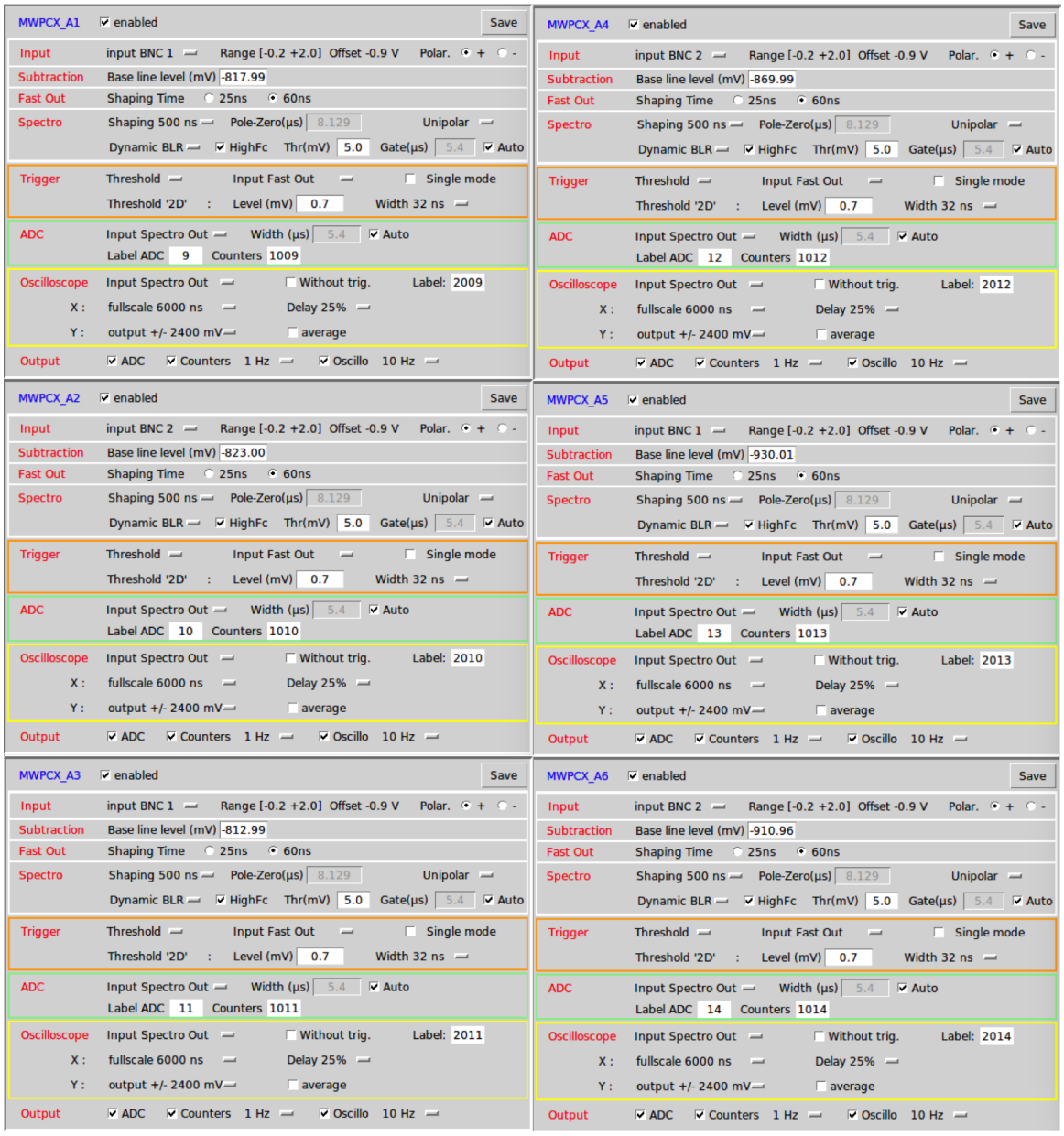

Figure A.3: DAQ Settings for MWPC Canode-X channels.

Figure A.4: DAQ Settings for MWPC Canode-Y channels.

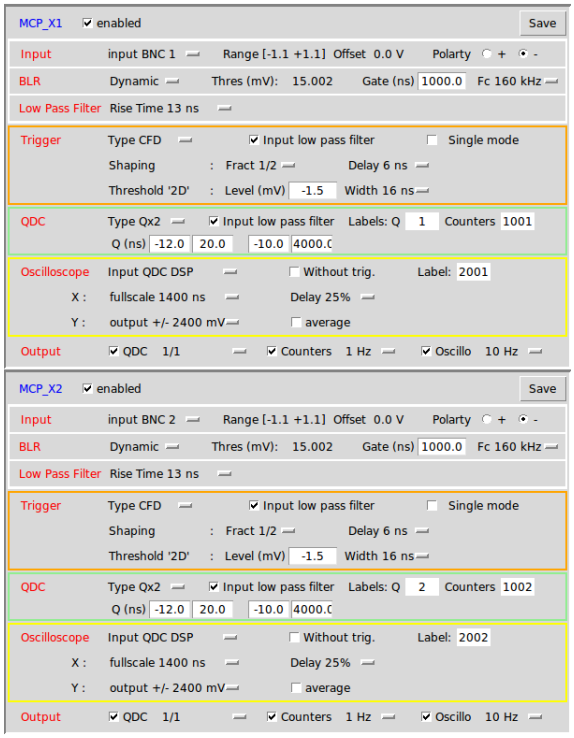

(a) Anode X

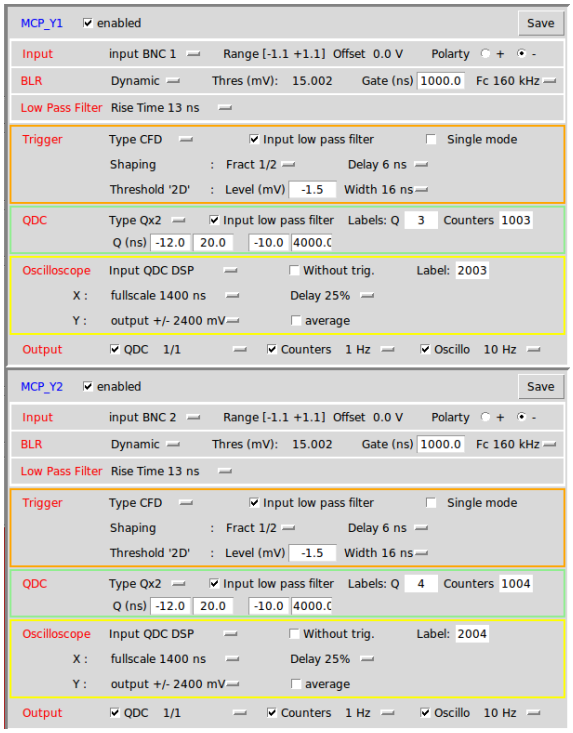

(b) Anode Y

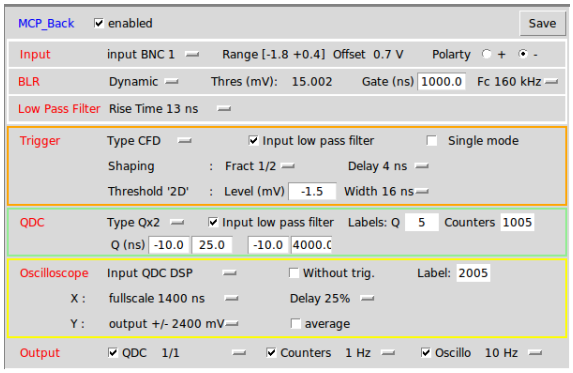

(c) MCP Back

Figure A.5: DAQ Settings for MCP channels.

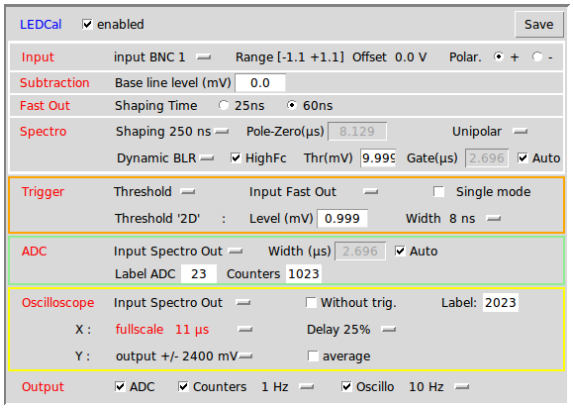

(a) LED

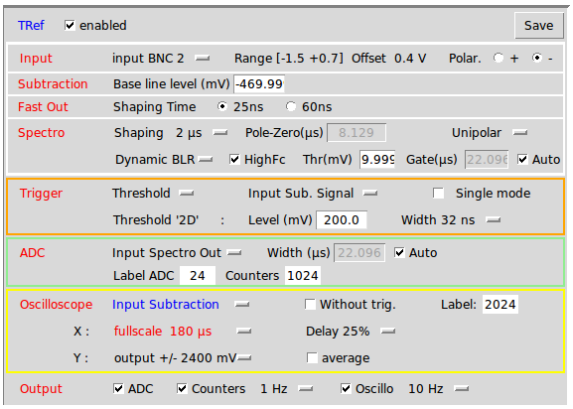

(b) TRef

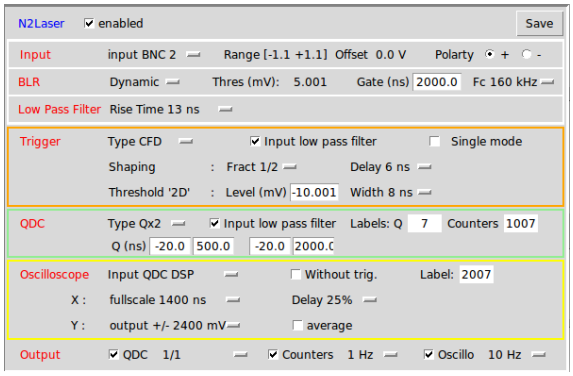

(c) Nitrogen laser

Figure A.6: DAQ Settings for LED, TRef and nitrogen-laser channels.

Appendix B

SCHEMATICS OF MWPC AMPLIFIERS

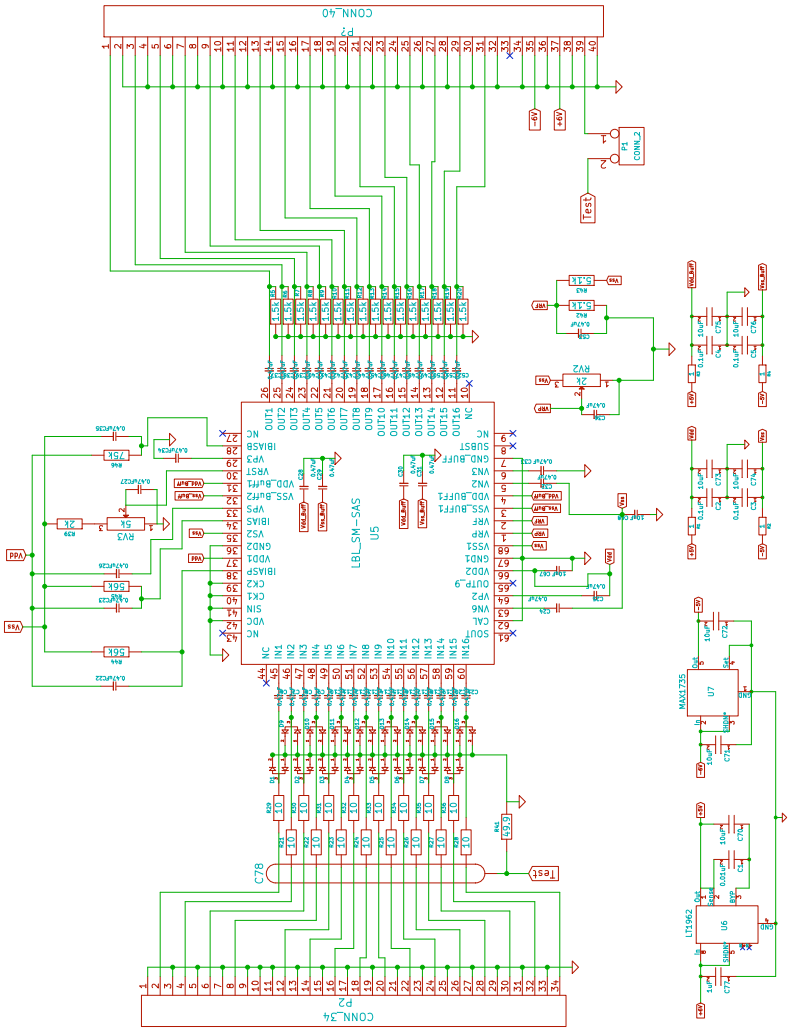

Figure B.1: MWPC cathode amplifier board schematic.

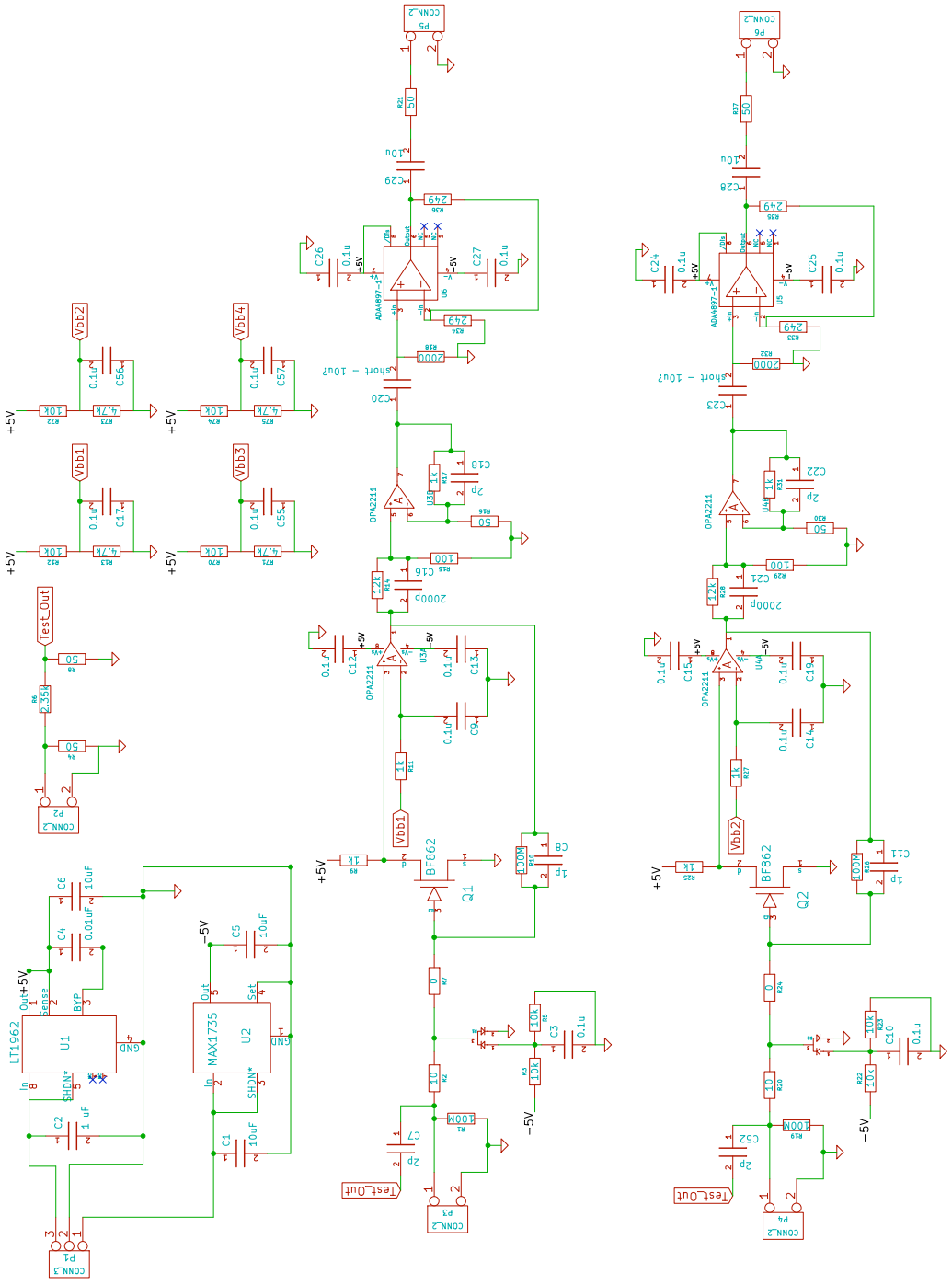

Figure B.2: MWPC anode amplifier board schematic.

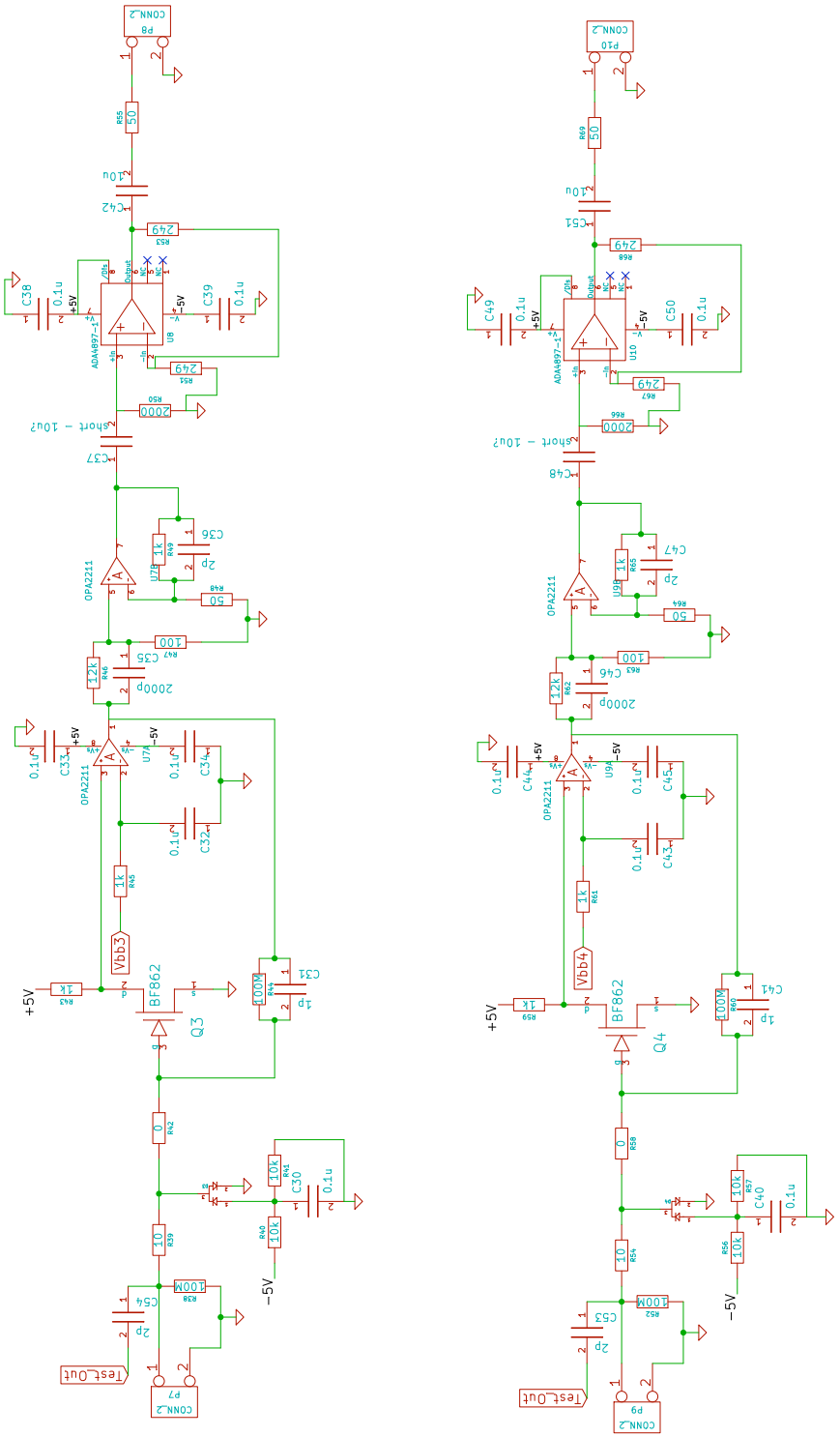

Figure B.3: MWPC anode amplifier board schematic continued.

Appendix C

GRID-FINDING ALGORITHM

To determine the positions of grid-line crossings on the non-calibrated MCP image, we first made initial guesses of them. Because the distortion near the edges are greater than that in the middle region, it is not ideal to use the physical positions of grid-line crossings as the initial guesses. Instead, we project the -6 mm$< Y <6$ mm region of the MCP image onto the X axis, and the -6 mm$< X <6$ mm region to the Y axis. Then the positions of the sharp dips of these two projections as shown in Figure C.1 are determined using local quadrature fits. We use the X coordinates of the local minima of the X-projection as the initial guesses for other grid-line crossings in the same column, and the Y coordinates of the local minima of the Y-projection as the initial guesses for other grid-line crossings in the same row. In the end, only the grid-line crossings with initial guessed positions within a 38.5 mm circle centered at the origin are kept in the analysis.

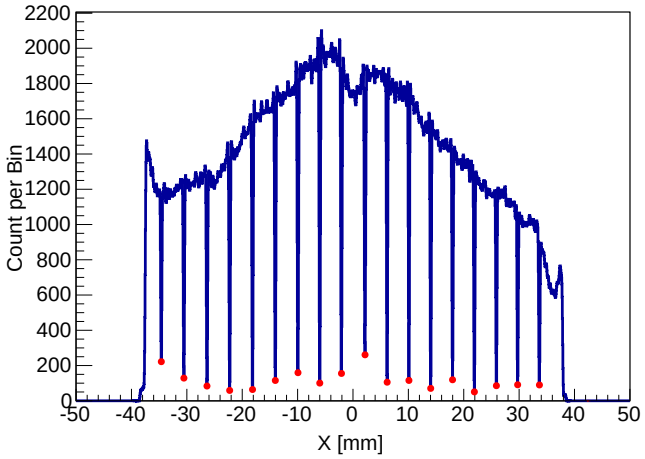

Figure C.1: X-projection of the -6 mm$< Y <6$ mm region of the non-calibrated MCP position spectrum.

For each grid-line crossing, we project a 1.6 mm × 1.6 mm square region centered at its initial guessed position on to X and Y axes, and use the coordinates of the local minima of these projections as the updated coordinates of the grid-line crossing. The local minima are also determined through quadrature fits. Using this method, the accuracy of the determined grid-line crossings is ∼50 μm.

In order to achieve the calibration accuracy at the scale of 10 μm, we fit the projections[1] of the rectangular regions around each grid-line crossings to the function defined in Equation 4.9. If the grid-point is not at the corners, we project the 1.6 mm×0.8 mm rectangular region above and below the grid-point respectively, and average the determined X coordinates of the grid-line segments determined through these projections. The X coordinate of the grid-line crossing is set to the this average. Its Y coordinate is determined in the same way by fitting the projection histograms of the left and right regions. If the grid-point is at a corner, only the two rectangular regions on the inner sides are projected and fitted. Examples of rectangular region selections are shown in Figure C.2.

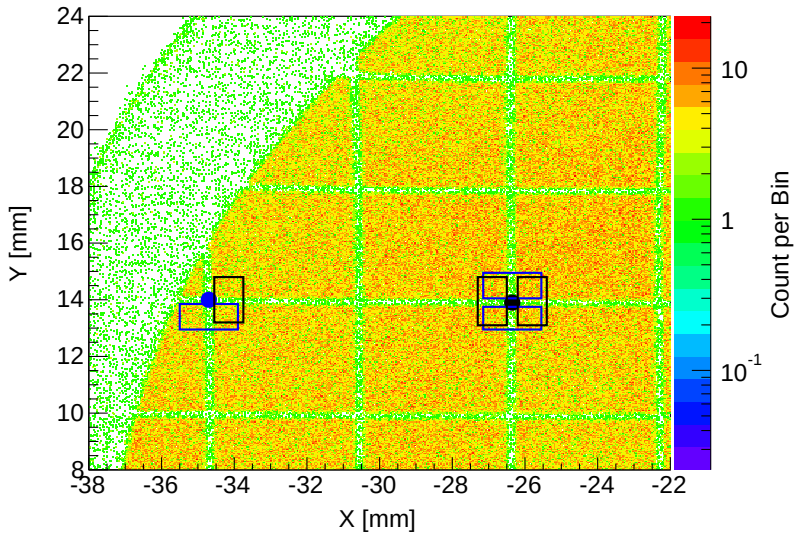

Figure C.2: Projection regions of corner grid-points and non-corner grid-points.

[1]The fits of the projections are similar to the one shown in Figure 4.39b.

LIST OF FIGURES

LIST OF TABLES

BIBLIOGRAPHY

[1] Eva E. Schulhoff and G. W. F. Drake. Electron emission and recoil effects following the beta decay of ^{6}He. *Phys. Rev. A*, 92:050701, Nov 2015.

[2] C. S. Wu, E. Ambler, R. W. Hayward, D. D. Hoppes, and R. P. Hudson. Experimental test of parity conservation in beta decay. *Phys. Rev.*, 105:1413–1415, Feb 1957.

[3] M. Goldhaber, L. Grodzins, and A. W. Sunyar. Helicity of neutrinos. *Phys. Rev.*, 109:1015–1017, Feb 1958.

[4] F. Halzen and A. D. Martin. *Quarks and Leptons: an introductory course in modern particle physics*. John Wiley & Sons, 1984.

[5] G. Aad *et. al.* Observation of a new particle in the search for the standard model higgs boson with the ATLAS detector at the LHC. *Physics Letters B*, 716(1):1 – 29, 2012.

[6] S. Chatrchyan *et. al.* Observation of a new boson at a mass of 125 gev with the CMS experiment at the LHC. *Physics Letters B*, 716(1):30 – 61, 2012.

[7] Peter W. Higgs. Broken symmetries and the masses of gauge bosons. *Phys. Rev. Lett.*, 13:508–509, Oct 1964.

[8] Peter W. Higgs. Spontaneous symmetry breakdown without massless bosons. *Phys. Rev.*, 145:1156–1163, May 1966.

[9] Jeffrey Goldstone, Abdus Salam, and Steven Weinberg. Broken symmetries. *Phys. Rev.*, 127:965–970, Aug 1962.

[10] Barry Holstein. *Weak Interactions in Nuclei*, chapter 4, page 52. Princeton University Press, 1989.

[11] J. C. Hardy and I. S. Towner. Superallowed $0^+ \to 0^+$ nuclear β decays: A new survey with precision tests of the conserved vector current hypothesis and the standard model. *Phys. Rev. C*, 79:055502, May 2009.

[12] M. P. Mendenhall, R. W. Pattie, Y. Bagdasarova, D. B. Berguno, L. J. Broussard, R. Carr, S. Currie, X. Ding, B. W. Filippone, A. García, P. Geltenbort, K. P. Hickerson, J. Hoagland, A. T. Holley, R. Hong, T. M. Ito, A. Knecht, C.-Y. Liu, J. L.

Liu, M. Makela, R. R. Mammei, J. W. Martin, D. Melconian, S. D. Moore, C. L. Morris, A. Pérez Galván, R. Picker, M. L. Pitt, B. Plaster, J. C. Ramsey, R. Rios, A. Saunders, S. J. Seestrom, E. I. Sharapov, W. E. Sondheim, E. Tatar, R. B. Vogelaar, B. VornDick, C. Wrede, A. R. Young, and B. A. Zeck. Precision measurement of the neutron β-decay asymmetry. *Phys. Rev. C*, 87:032501, Mar 2013.

[13] D. Mund, B. Märkisch, M. Deissenroth, J. Krempel, M. Schumann, H. Abele, A. Petoukhov, and T. Soldner. Determination of the weak axial vector coupling $\lambda=g_A/g_V$ from a measurement of the β-asymmetry parameter a in neutron beta decay. *Phys. Rev. Lett.*, 110:172502, Apr 2013.

[14] K.A. Olive et al. (Particle Data Group). Baryon summary tables. *Chin. Phys. C*, 38(090001), 2014 and 2015 update.

[15] Tanmoy Bhattacharya, Vincenzo Cirigliano, Saul D. Cohen, Alberto Filipuzzi, Martín González-Alonso, Michael L. Graesser, Rajan Gupta, and Huey-Wen Lin. Probing novel scalar and tensor interactions from (ultra)cold neutrons to the LHC. *Phys. Rev. D*, 85:054512, Mar 2012.

[16] Franz Osterfeld. Nuclear spin and isospin excitations. *Rev. Mod. Phys.*, 64:491–557, Apr 1992.

[17] J Rapaport and E Sugarbaker. Isovector excitations in nuclei. *Annual Review of Nuclear and Particle Science*, 44(1):109–153, 1994.

[18] G. Martínez-Pinedo, A. Poves, E. Caurier, and A. P. Zuker. Effective g_A in the pf shell. *Phys. Rev. C*, 53:R2602–R2605, Jun 1996.

[19] I.S. Towner. Quenching of spin matrix elements in nuclei. *Physics Reports*, 155(5):263 – 377, 1987.

[20] A. Knecht, R. Hong, D. W. Zumwalt, B. G. Delbridge, A. García, P. Müller, H. E. Swanson, I. S. Towner, S. Utsuno, W. Williams, and C. Wrede. Precision measurement of the ^{6}He half-life and the weak axial current in nuclei. *Phys. Rev. C*, 86:035506, Sep 2012.

[21] Michael E. Peskin. On the trail of the higgs boson. arXiv:1506.08185 [hep-ph].

[22] J. D. Jackson, S. B. Treiman, and H. W. Wyld. Possible tests of time reversal invariance in beta decay. *Phys. Rev.*, 106:517–521, May 1957.

[23] M. González-Alonso and J. Martin Camalich. Isospin breaking in the nucleon mass and the sensitivity of β decays to new physics. *Phys. Rev. Lett.*, 112:042501, Jan 2014.

[24] K. K. Vos, H. W. Wilschut, and R. G. E. Timmermans. Symmetry violations in nuclear and neutron β decay. *Rev. Mod. Phys.*, 87:1483–1516, Dec 2015.

[25] P. Herczeg. Beta decay beyond the standard model. *Progress in Particle and Nuclear Physics*, 46(2):413–457, 2001.

[26] Michael E. Peskin and Daniel V. Schroeder. *An Introduction to Quantum Field Theory.* Westview Press, 1995.

[27] Nathal Severijns, Marcus Beck, and Oscar Naviliat-Cuncic. Tests of the standard electroweak model in nuclear beta decay. *Rev. Mod. Phys.*, 78:991–1040, Sep 2006.

[28] S. Profumo, M. J. Ramsey-Musolf, and S. Tulin. Supersymmetric contributions to weak decay correlation coefficients. *Phys. Rev. D*, 75:075017, Apr 2007.

[29] D.H. Wilkinson and B.E.F. Macefield. A parametrization of the phase space factor for allowed β-decay. *Nuclear Physics, Section A*, 232(1):58–92, 1974.

[30] Nathal Severijns and Oscar Naviliat-Cuncic. Symmetry tests in nuclear beta decay. *Annual Review of Nuclear and Particle Science*, 61:23–46, 2011.

[31] M. Bychkov, D. Počanić, B. A. VanDevender, V. A. Baranov, W. Bertl, Yu. M. Bystritsky, E. Frlež, V. A. Kalinnikov, N. V. Khomutov, A. S. Korenchenko, S. M. Korenchenko, M. Korolija, T. Kozlowski, N. P. Kravchuk, N. A. Kuchinsky, W. Li, D. Mekterović, D. Mzhavia, S. Ritt, P. Robmann, O. A. Rondon-Aramayo, A. M. Rozhdestvensky, T. Sakhelashvili, S. Scheu, U. Straumann, I. Supek, Z. Tsamalaidze, A. van der Schaaf, E. P. Velicheva, V. P. Volnykh, Y. Wang, and H.-P. Wirtz. New precise measurement of the pion weak form factors in $\pi^+ \to e^+\nu\gamma$ decay. *Phys. Rev. Lett.*, 103:051802, Jul 2009.

[32] F. Wauters, A. García, and R. Hong. Limits on tensor-type weak currents from nuclear and neutron β decays. *Physical Review C - Nuclear Physics*, 89(2), 2014.

[33] E. G. Adelberger, C. Ortiz, A. García, H. E. Swanson, M. Beck, O. Tengblad, M. J. G. Borge, I. Martel, H. Bichsel, and the ISOLDE Collaboration. Positron-neutrino correlation in the $0^+ \to 0^+$ decay of ^{32}Ar. *Phys. Rev. Lett.*, 83:1299–1302, Aug 1999.

[34] A. Gorelov, D. Melconian, W. P. Alford, D. Ashery, G. Ball, J. A. Behr, P. G. Bricault, J. M. D'Auria, J. Deutsch, J. Dilling, M. Dombsky, P. Dubé, J. Fingler, U. Giesen, F. Glück, S. Gu, O. Häusser, K. P. Jackson, B. K. Jennings, M. R. Pearson, T. J. Stocki, T. B. Swanson, and M. Trinczek. Scalar interaction limits from the β-ν correlation of trapped radioactive atoms. *Phys. Rev. Lett.*, 94:142501, Apr 2005.

[35] V. A. Wichers, T. R. Hageman, J. van Klinken, H. W. Wilschut, and D. Atkinson. Bounds on right-handed currents from nuclear beta decay. *Phys. Rev. Lett.*, 58:1821–1824, May 1987.

[36] A. S. Carnoy, J. Deutsch, T. A. Girard, and R. Prieels. Limits on nonstandard weak currents from the polarization of ^{14}O and ^{10}C decay positrons. *Phys. Rev. C*, 43:2825–2834, Jun 1991.

[37] C. H. Johnson, Frances Pleasonton, and T. A. Carlson. Precision measurement of the recoil energy spectrum from the decay of He^6. *Phys. Rev.*, 132:1149–1165, Nov 1963.

[38] Vincenzo Cirigliano, Susan Gardner, and Barry R. Holstein. Beta decays and non-standard interactions in the LHC era. *Progress in Particle and Nuclear Physics*, 71:93 – 118, 2013. Fundamental Symmetries in the Era of the LHC.

[39] Tanmoy Bhattacharya, Vincenzo Cirigliano, Saul D. Cohen, Rajan Gupta, Anosh Joseph, Huey-Wen Lin, and Boram Yoon. Isovector and isoscalar tensor charges of the nucleon from lattice QCD. *Phys. Rev. D*, 92:094511, Nov 2015.

[40] J. R. Green, J. W. Negele, A. V. Pochinsky, S. N. Syritsyn, M. Engelhardt, and S. Krieg. Nucleon scalar and tensor charges from lattice QCD with light wilson quarks. *Phys. Rev. D*, 86:114509, Dec 2012.

[41] Gunnar S. Bali, Sara Collins, Benjamin Gläßle, Meinulf Göckeler, Johannes Najjar, Rudolf H. Rödl, Andreas Schäfer, Rainer W. Schiel, Wolfgang Söldner, and André Sternbeck. Nucleon isovector couplings from $N_f = 2$ lattice qcd. *Phys. Rev. D*, 91:054501, Mar 2015.

[42] Aurore Courtoy, Stefan Baeßler, Martín González-Alonso, and Simonetta Liuti. Beyond-standard-model tensor interaction and hadron phenomenology. *Phys. Rev. Lett.*, 115:162001, Oct 2015.

[43] Vincenzo Cirigliano, Martín González-Alonso, and MichaelL. Graesser. Non-standard charged current interactions: beta decays versus the LHC. *Journal of High Energy Physics*, 2013(2), 2013.

[44] David W. Zumwalt. *Developments for the ^{6}He $\beta - \bar{\nu}$ angular correlation experiment.* PhD thesis, University of Washington, 2015.

[45] F. Glück. Order-α radiative correction calculations for unoriented allowed nuclear, neutron and pion β decays. *Computer Physics Communications*, 101(3):223 – 231, 1997.

[46] M. Brodeur, T. Brunner, C. Champagne, S. Ettenauer, M. J. Smith, A. Lapierre, R. Ringle, V. L. Ryjkov, S. Bacca, P. Delheij, G. W. F. Drake, D. Lunney, A. Schwenk, and J. Dilling. First direct mass measurement of the two-neutron halo nucleus ^{6}He and improved mass for the four-neutron halo ^{8}He. *Phys. Rev. Lett.*, 108:052504, Jan 2012.

[47] Brianna J. Mount, Matthew Redshaw, and Edmund G. Myers. Atomic masses of ^{6}Li,^{23}Na,^{39,41}K,^{85,87}Rb, and ^{133}Cs. *Phys. Rev. A*, 82:042513, Oct 2010.

[48] X Flćhard, Ph Velten, E Liénard, A Méry, D Rodríguez, G Ban, D Durand, F Mauger, O Naviliat-Cuncic, and J C Thomas. Measurement of the $\beta-\nu$ correlation coefficient $a_{\beta\nu}$ in the β decay of trapped ^{6}He^{+} ions. *Journal of Physics G: Nuclear and Particle Physics*, 38(5):055101, 2011.

[49] X. Fléchard, E. Liénard, A. Méry, D. Rodríguez, G. Ban, D. Durand, F. Duval, M. Herbane, M. Labalme, F. Mauger, O. Naviliat-Cuncic, J. C. Thomas, and Ph. Velten. Paul trapping of radioactive ^{6}He^{+} ions and direct observation of their β decay. *Phys. Rev. Lett.*, 101:212504, Nov 2008.

[50] J A Behr and G Gwinner. Standard model tests with trapped radioactive atoms. *Journal of Physics G: Nuclear and Particle Physics*, 36(3):033101, 2009.

[51] J.A. Behr, A. Gorelov, K.P. Jackson, M.R. Pearson, M. Anholm, T. Kong, R.S. Behling, B. Fenker, D. Melconian, D. Ashery, and G. Gwinner. Trinat: measuring β-decay correlations with laser-trapped atoms. *Hyperfine Interactions*, 225(1-3):115–120, 2014.

[52] G. D. Sprouse, , and L. A. Orozco. Laser trapping of radioactive atoms. *Annual Review of Nuclear and Particle Science*, 47(1):429–461, 1997.

[53] S. Aubin, E. Gomez, L. A. Orozco, and G. D. Sprouse. High efficiency magneto-optical trap for unstable isotopes. *Review of Scientific Instruments*, 74(10):4342–4351, 2003.

[54] S. N. Atutov, R. Calabrese, V. Guidi, B. Mai, E. Scansani, G. Stancari, L. Tomassetti, L. Corradi, A. Dainelli, V. Biancalana, A. Burchianti, C. Marinelli, E. Mariotti, L. Moi, and S. Veronesi. Cooling and trapping of radioactive atoms: the legnaro francium magneto-optical trap. *J. Opt. Soc. Am. B*, 20(5):953–959, May 2003.

[55] M. G. Sternberg, R. Segel, N. D. Scielzo, G. Savard, J. A. Clark, P. F. Bertone, F. Buchinger, M. Burkey, S. Caldwell, A. Chaudhuri, J. E. Crawford, C. M. Deibel, J. Greene, S. Gulick, D. Lascar, A. F. Levand, G. Li, A. Pérez Galván, K. S. Sharma, J. Van Schelt, R. M. Yee, and B. J. Zabransky. Limit on tensor currents from ^{8}Li β decay. *Phys. Rev. Lett.*, 115:182501, Oct 2015.

[56] S. G. Crane, S. J. Brice, A. Goldschmidt, R. Guckert, A. Hime, J. J. Kitten, D. J. Vieira, and X. Zhao. Parity violation observed in the beta decay of magnetically trapped ^{82}Rb atoms. *Phys. Rev. Lett.*, 86:2967–2970, Apr 2001.

[57] J. A. Behr, A. Gorelov, T. Swanson, O. Häusser, K. P. Jackson, M. Trinczek, U. Giesen, J. M. D'Auria, R. Hardy, T. Wilson, P. Choboter, F. Leblond, L. Buchmann, M. Dombsky, C. D. P. Levy, G. Roy, B. A. Brown, and J. Dilling. Magneto-optic trapping of β-decaying ^{38}K^m, ^{37}K from an on-line isotope separator. *Phys. Rev. Lett.*, 79:375–378, Jul 1997.

[58] N. D. Scielzo, S. J. Freedman, B. K. Fujikawa, and P. A. Vetter. Measurement of the $\beta - \nu$ correlation using magneto-optically trapped ^{21}Na. *Phys. Rev. Lett.*, 93:102501, Aug 2004.

[59] P. A. Vetter, J. R. Abo-Shaeer, S. J. Freedman, and R. Maruyama. Measurement of the β-ν correlation of ^{21}Na using shakeoff electrons. *Phys. Rev. C*, 77:035502, Mar 2008.

[60] J. R. A. Pitcairn, D. Roberge, A. Gorelov, D. Ashery, O. Aviv, J. A. Behr, P. G. Bricault, M. Dombsky, J. D. Holt, K. P. Jackson, B. Lee, M. R. Pearson, A. Gaudin, B. Dej, C. Höhr, G. Gwinner, and D. Melconian. Tensor interaction constraints from β-decay recoil spin asymmetry of trapped atoms. *Phys. Rev. C*, 79:015501, Jan 2009.

[61] G. Li, R. Segel, N. D. Scielzo, P. F. Bertone, F. Buchinger, S. Caldwell, A. Chaudhuri, J. A. Clark, J. E. Crawford, C. M. Deibel, J. Fallis, S. Gulick, G. Gwinner, D. Lascar, A. F. Levand, M. Pedretti, G. Savard, K. S. Sharma, M. G. Sternberg, T. Sun, J. Van Schelt, R. M. Yee, and B. J. Zabransky. Tensor interaction limit derived from the α-β-$\overline{\nu}$ correlation in trapped ^{8}Li ions. *Phys. Rev. Lett.*, 110:092502, Mar 2013.

[62] S. Van Gorp, M. Breitenfeldt, M. Tandecki, M. Beck, P. Finlay, P. Friedag, F. Glück, A. Herlert, V. Kozlov, T. Porobic, G. Soti, E. Traykov, F. Wauters, Ch. Weinheimer, D. Zákoucký, and N. Severijns. First $\beta - \nu$ correlation measurement from the recoil-energy spectrum of penning trapped ^{35}Ar ions. *Phys. Rev. C*, 90:025502, Aug 2014.

[63] A. Knecht, D.W. Zumwalt, B.G. Delbridge, A. García, G.C. Harper, R. Hong, P. Müller, A.S.C. Palmer, R.G.H. Robertson, H.E. Swanson, S. Utsuno, D.I. Will, W. Williams, and C. Wrede. A high-intensity source of ^{6}He atoms for fundamental research. *Nuclear Instruments and Methods in Physics Research, Section A: Accelerators, Spectrometers, Detectors and Associated Equipment*, 660(1):43–47, 2011.

[64] A. Knecht, R. Hong, D. W. Zumwalt, B. G. Delbridge, A. García, P. Müller, H. E. Swanson, I. S. Towner, S. Utsuno, W. Williams, and C. Wrede. Precision measurement of the ^{6}He half-life and the weak axial current in nuclei. *Phys. Rev. Lett.*, 108:122502, Mar 2012.

[65] C. Couratin, Ph. Velten, X. Fléchard, E. Liénard, G. Ban, A. Cassimi, P. Delahaye, D. Durand, D. Hennecart, F. Mauger, A. Méry, O. Naviliat-Cuncic, Z. Patyk, D. Rodríguez, K. Siegień-Iwaniuk, and J-C. Thomas. First measurement of pure electron shakeoff in the β decay of trapped $^{6}He^{+}$ ions. *Phys. Rev. Lett.*, 108:243201, Jun 2012.

[66] C. Couratin, X. Fabian, B. Fabre, B. Pons, X. Fléchard, E. Liénard, G. Ban, M. Breitenfeldt, P. Delahaye, D. Durand, A. Méry, O. Naviliat-Cuncic, T. Porobic, G. Quéméner, D. Rodríguez, N. Severijns, J.-C. Thomas, and S. Van Gorp. Electron shakeoff following the β^{+} decay of trapped $^{35}Ar^{+}$ ions. *Phys. Rev. A*, 88:041403, Oct 2013.

[67] N. D. Scielzo, S. J. Freedman, B. K. Fujikawa, and P. A. Vetter. Recoil-ion charge-state distribution following the β^{+} decay of ^{21}Na. *Phys. Rev. A*, 68:022716, Aug 2003.

[68] L. Wauters and N. Vaeck. Study of the electronic rearrangement induced by nuclear transmutations: A B-spline approach applied to the β decay of ^{6}He. *Phys. Rev. C*, 53:497–500, Jan 1996.

[69] T. A. Carlson, Frances Pleasonton, and C. H. Johnson. Electron shake off following the β^{-} decay of He^{6}. *Phys. Rev.*, 129:2220–2226, Mar 1963.

[70] A.J.Koning and D.Rochman. Evaluated nuclear data file (ENDF), URL: http://www-nds.iaea.org/exfor/endf.htm, 2015.

[71] GEometry ANd Tracking: a toolkit for the simulation of the passage of particles through matter URL: geant4.cern.ch.

[72] H. J. Metcalf and P. van der Straten. *Laser Cooling and Trapping*. Springer, 1999.

[73] C. J. Foot. *Atomic Physics*. Oxford University Press, 2005.

[74] S. S. Hodgman, R. G. Dall, L. J. Byron, K. G. H. Baldwin, S. J. Buckman, and A. G. Truscott. Metastable helium: A new determination of the longest atomic excited-state lifetime. *Phys. Rev. Lett.*, 103:053002, Jul 2009.

[75] T.M. Ito, R. Carr, B.W. Filippone, J.W. Martin, B. Plaster, G. Rybka, and J. Yuan. A multiwire proportional chamber for precision studies of neutron decay angular correlations. *Nuclear Instruments and Methods in Physics Research Section A: Accelerators, Spectrometers, Detectors and Associated Equipment*, 571(3):676 – 686, 2007.

[76] Ichita Endo, Tatsuo Kawamoto, Yoshinari Mizuno, Takashi Ohsugi, Takashi Taniguchi, and Tohru Takeshita. Systematic shifts of evaluated charge centroid for the cathode read-out multiwire proportional chamber. *Nuclear Instruments and Methods in Physics Research*, 188(1):51 – 58, 1981.

[77] F. Sauli. Principles of operation of multiwire proportional and drift chambers. *CERN Report*, 77-09, 1977.

[78] A. Pullia, W.F.J. Muller, C. Boiano, and R. Bassini. Resistive or capacitive charge-division readout for position-sensitive detectors. *Nuclear Science, IEEE Transactions on Nuclear Science*, 49(6):3269–3277, Dec 2002.

[79] Richard S. Wolff. Measurement of the gas constants for various proportional-counter gas mixtures. *Nuclear Instruments and Methods*, 115(2):461 – 463, 1974.

[80] R A Ryan, F Wauters, F E Gray, P Kammel, A Nadtochy, D Peterson, T van Wechel, E Gross, M Gubanich, L Kochenda, P Kravtsov, D Orozco, R Osofsky, M H Murray, G E Petrov, J D Phillips, J Stroud, V Trofimov, A Vasilyev, and M Vznuzdaev. Design and operation of a cryogenic charge-integrating preamplifier for the MuSun experiment. *Journal of Instrumentation*, 9(07):P07029, 2014.

[81] E. Beuville, P. Barale, F. Bieser, W. Hearn, S.R. Klein, M.A. Lisa, T. Noggle, H.G. Ritter, C. Vu, and H. Wieman. A low noise amplifier-shaper with tail correction for the star detector. In *Nuclear Science Symposium and Medical Imaging Conference Record, 1995., 1995 IEEE*, volume 1, pages 562–565 vol.1, Oct 1995.

[82] M. Anderson, F. Bieser, R. Bossingham, D. Cebra, E.L. Hjort, S.R. Klein, S. Kleinfelder, C.Q. Vu, and H. Wieman. A readout system for the STAR time projection chamber. *Nuclear Instruments and Methods in Physics Research Section A: Accelerators, Spectrometers, Detectors and Associated Equipment*, 499(2–3):679 – 691, 2003. The Relativistic Heavy Ion Collider Project: RHIC and its Detectors.

[83] V. A. Andreev, T. I. Banks, R. M. Carey, T. A. Case, S. M. Clayton, K. M. Crowe, J. Deutsch, J. Egger, S. J. Freedman, V. A. Ganzha, T. Gorringe, F. E. Gray, D. W. Hertzog, M. Hildebrandt, P. Kammel, B. Kiburg, S. Knaack, P. A. Kravtsov, A. G. Krivshich, B. Lauss, K. R. Lynch, E. M. Maev, O. E. Maev, F. Mulhauser, C. Petitjean, G. E. Petrov, R. Prieels, G. N. Schapkin, G. G. Semenchuk, M. A. Soroka, V. Tishchenko, A. A. Vasilyev, A. A. Vorobyov, M. E. Vznuzdaev, and P. Winter. Measurement of muon capture on the proton to 1% precision and determination of the pseudoscalar coupling g_P. *Phys. Rev. Lett.*, 110:012504, Jan 2013.

[84] Photonis website URL https://www.photonis.com.

[85] Roentdek - Handels GmbH. *MCP Delay Line manual*, 2011.

[86] Fast acquisition system for nuclear research URL: http://faster.in2p3.fr.

[87] Cathy Fontbonne. *FASTER-QDC-TDC MODULE USER MANUAL.* LPC Caen, 2013.

[88] Cathy Fontbonne. *FASTER-ADC MODULE USER MANUAL.* LPC Caen, 2012.

[89] Garfield - simulation of gaseous detectors URL: http://garfield.web.cern.ch/garfield/.

[90] Glenn F. Knoll. *Radiation Detection and Measurement.* John Wiley and Sons, Inc., 3rd edition, 1999.

[91] J. Egger, D. Fahrni, M. Hildebrandt, A. Hofer, L. Meier, C. Petitjean, V.A. Andreev, T.I. Banks, S.M. Clayton, V.A. Ganzha, F.E. Gray, P. Kammel, B. Kiburg, P.A. Kravtsov, A.G. Krivshich, B. Lauss, E.M. Maev, O.E. Maev, G. Petrov, G.G. Semenchuk, A.A. Vasilyev, A.A. Vorobyov, M.E. Vznuzdaev, and P. Winter. A high-pressure hydrogen time projection chamber for the mucap experiment. *The European Physical Journal A*, 50(10), 2014.

[92] National nuclear data center URL: http://www.nndc.bnl.gov.

[93] I. Angeli and K.P. Marinova. Table of experimental nuclear ground state charge radii: An update. *Atomic Data and Nuclear Data Tables*, 99(1):69 – 95, 2013.

[94] Frank P. Calaprice. Second class interactions and the electron-neutrino correlation in nuclear beta decay. *Phys. Rev. C*, 12:2016–2021, Dec 1975.

[95] Barry Holstein. *Weak Interactions in Nuclei*, chapter 7, page 235. Princeton University Press, 1989.

[96] J.C. Bergstrom, I.P. Auer, and R.S. Hicks. Electroexcitation of the 0^+ (3.562 MeV) level of ^{6}Li and its application to the reaction ^{6}Li(γ, $\pi+$)^{6}He. *Nuclear Physics A*, 251(3):401 – 417, 1975.

[97] F. Glück. Order-α radiative correction to ^{6}He and ^{32}Ar β decay recoil spectra. *Nuclear Physics A*, 628(3):493 – 502, 1998.

[98] J.J. Devaney. The beta spectra of $^{90}_{38}$Sr and $^{90}_{39}$Y. *Los Alamos National Laboratory Technical Report*, DE86001226(LA-10467-MS), 1985.

[99] Geant4 Collaboration. *Geant4 User's Guide for Application Developers*, 2012.

[100] S. Goudsmit and J. L. Saunderson. Multiple scattering of electrons. *Phys. Rev.*, 57:24–29, Jan 1940.